THE UNIVERSITY OF MICHIGAN

COLLEGE OF ENGINEERING
Department of Aerospace Engineering
High Altitude Engineering Laboratory

Technical Report

THE REFLECTANCE AND SCATTERING OF SOLAR RADIATION BY THE EARTH

Fred L. Bartman

ORA Project 05863

under contract with:

NATIONAL AERONAUTICS AND SPACE ADMINISTRATION
CONTRACT NO. NASr-54(03)
WASHINGTON, D.C.

administered through:

OFFICE OF RESEARCH ADMINISTRATION ANN ARBOR

February 1967

This report was also a dissertation submitted in partial fulfillment of the requirements for the degree of Doctor of Philosophy in The University of Michigan, 1967.

ACKNOWLEDGMENTS

The author wishes to thank all of the many people who have assisted him in this study. The advice, and help of Professor Edward S. Epstein, Chairman of the Doctoral Committee, is particularly appreciated. The author is also grateful to Professors Leslie M. Jones, Robert M. Howe, Lawrence L. Rauch, and Aksel Wiin-Nielsen, for serving as members of the Committee and for their help and suggestions during the course of the work.

The constant interest and encouragement of Professors Wilbur Nelson and L. M. Jones in the early stages of the work, before the Committee was formed, are also gratefully acknowledged.

The help of all my colleagues in the High Altitude Engineering Laboratory in carrying out preparations and field operations for the balloon flight measurements is also acknowledged. Of these, the work of Mr. Michael Surh, on radiometer calibration, and Messrs. Leo W. Carls, Paul A. Titus, Wan Y. Lee, and David Hartzig on field operations and radiometer data processing is particularly appreciated.

The financial support received from the National Aeronautics and Space Administration under Contract NASr-54(03) is also gratefully acknowledged. Numerous discussions of radiometer calibrations and the manner of interpretation of radiometer data with Dr. William Nordberg, Mr. William Bandeen and other members of the Staff of Goddard Space Flight Center, and of Mr. Frank Malinowski of Santa Barbara Research Corporation have also been very helpful.

TABLE OF CONTENTS

	Page
LIST OF TABLES	v
LIST OF ILLUSTRATIONS	vii
NOMENCLATURE	xiv
ABSTRACT	xxiii
CHAPTER	
I. INTRODUCTION	1
II. DEFINITIONS	5
A. The Geometry of Scattering and Reflection	5
B. Reflectance	5
C. Scattering Angle	10
D. Earth's Albedo	11
E. Planetary Albedo, Bond's Definition	16
III. A REVIEW OF RESEARCH RELATED TO EARTH'S ALBEDO	23
A. Earth's Albedo from Measurements of Earthlight on the Moon	23
B. Earth's Albedo Measurements from Satellites and Spacecraft	25
C. Reflectance of the Earth's Surface	27
D. The Reflectance of Clouds	28
E. The Scattering of Solar Radiation by Air Molecules and Aerosols	28
F. Estimates of Earth's Albedo	33
G. Discussion: Models of the Earth for Albedo Purposes	33
IV. BALLOON FLIGHT MEASUREMENTS OF EARTH REFLECTANCE	36
A. Introductory Notes	36
B. The Balloon Flight Measurement System	37
C. Radiometer Measurements: Calibration and Interpretation	43
1. Calibration of the radiometers	43
2. Interpretation of the radiometer data	57
D. Data Obtained on Three Flights	63
1. The 2 June, 1962 Balloon Flight	63
2. The 26 June, 1963 Balloon Flight	78
3. The 10 March, 1965 Balloon Flight	84
E. Discussion of Data Obtained	93
1. Nonisotropic earth reflectance	100
2. The wavelength dependence of earth reflectance	101

TABLE OF CONTENTS (Continued)

CHAPTER		Page
V.	A MODEL OF THE EARTH FOR ALBEDO PURPOSES	107
	A. Geometrical Characteristics	107
	B. Physical Characteristics	108
	C. Illustrative Example	110
VI.	CONCLUSIONS AND SUGGESTIONS FOR FURTHER RESEARCH	124
	A. Conclusions	124
	B. Further Research	126
APPENDIX A.	EARTH'S ALBEDO FROM MEASUREMENTS OF EARTHLIGHT ON THE MOON	128
	1. The Work of Danjon	128
	2. The Work of Bakos	131
	3. The Work of Dubois	137
APPENDIX B.	EARTH'S ALBEDO MEASUREMENTS FROM SATELLITES AND SPACECRAFT	140
	1. The Low Resolution Measurements	140
	2. The Medium Resolution Measurements	158
	3. The Mariner 2 Measurements	183
APPENDIX C.	REFLECTANCE OF THE EARTH'S SURFACE	187
	1. Spectral Reflectance	187
	2. Angular Distribution of Reflectance	200
	3. Total Directional Reflectance	209
APPENDIX D.	THE REFLECTANCE OF CLOUDS	218
	1. Spectral Reflectance	218
	2. Angular Distribution of Reflectance	218
	3. Total Directional Reflectance	219
APPENDIX E.	THE SCATTERING OF SOLAR RADIATION BY AIR MOLECULES AND AEROSOLS	225
	1. Molecular Scattering	225
	2. Aerosol Scattering	232
	3. Summary	237
APPENDIX F.	ESTIMATES OF EARTH'S ALBEDO	238
APPENDIX G.	DESCRIPTION OF COORDINATE SYSTEMS USED	249
REFERENCES		250

LIST OF TABLES

Table		Page
1.	Earth's Albedo From Measurements of Earthlight on the Moon	24
2.	Earth's Albedo Measurements From Satellites and Spacecraft	26
3.	Summary of Reflectance Data For Earth Surface Features	29
4.	Summary of Reflectance Data for Clouds	30
5.	Summary of Data for Molecular and Aerosol Scattering	32
6.	Summary of Earth Albedo Estimates	34
7.	Cloud Cover Viewed by Radiometer, 2 June 1962 Balloon Flight	63
8.	Theoretical F-1 MRIR Reflectance Measurements	104
9.	Illustrative Example, Values of η'_{jk}	117
10.	Illustrative Example, Values of ζ'_{jk} For GHA = 180.3° (0000 GMT)	118
11.	Illustrative Example, Values of ζ'_{jk} For GHA = 0.23° (1200 GMT)	119
12.	Illustrative Example, Values of $\sum_i$ For GHA = 180.3° (0000 GMT)	120
13.	Illustrative Example, Values of $\sum_i$ For GHA = 0.23° (1200 GMT)	121
14.	Earthshine Photometer Stations	132
15.	Longitudinal Variation of Cloud Cover	135
16.	Monthly Variations of the Brightness of the Earthshine	135
17.	Values of Absorptivity for Various Coatings	142
18.	Nominal Characteristics of Tiros Radiometer Channels 3 and 5	160
19.	Nominal Characteristics of F-4 MRIR (0.2-4.0-Micron Channel)	168
20.	Final Seasonal and Annual Values of Long- and Short-Wave Radiation	182

LIST OF TABLES (Concluded)

Table		Page
21.	Bidirectional Luminous Reflectance of Terrain Backgrounds for Moderately High Sun	203
22.	Bidirectional Luminous Reflectance of Terrain for Low Sun Angles	206
23.	Bidirectional Luminous Reflectance of Terrain Backgrounds Under Overcast	207
24.	Dependence of Cloud Total Reflectance on Underlying Surface	223
25.	Wavelength Dependence of Normal Optical Thickness of Earth's Molecular Atmosphere Above Sea Level	230
26.	Reflectance of Solar Radiation, %	240
27.	Data Used to Obtain Albedo of Northern Hemisphere	243
28.	Seasonal Distribution of Planetary Albedo Components Due to Atmosphere Scattering and Ground Reflectance	245

LIST OF ILLUSTRATIONS

Figure		Page
1.	Geometry of reflection and scattering.	6
2.	Distribution of reflected radiation for a perfectly diffuse (Lambert) reflector.	9
3.	Distribution of reflected radiation for imperfectly diffuse reflector. $1/\pi\ \rho(\theta_o,\phi_o,\theta,\phi)\cos\theta$ is plotted for three angles of incidence: 0°, 40°, and 60°.	10
4.	Geometry for calculating earth's albedo.	12
5.	Planetary albedo-geometrical relations.	17
6.	Comparison of Danjon's phase function with that of a perfectly diffuse homogeneous earth.	25
7.	Balloon flight configuration.	39
8.	Balloon gondola used on 2 June, 1962 balloon flight.	39
9.	Airborne telemetry unit and instrument programming unit mounted in gondola.	41
10.	Inside mobile telemetry ground station.	42
11.	Instrument operation program for 10 March, 1965 ballon flight.	44
12.	Calibration sources.	46
13.	TIROS #103A radiometer channel 5 (0.55-0.75-micron) calibration curves.	50
14.	TIROS #103A radiometer channel 3 (0.2-5.5-micron) calibration curves.	51
15.	Calibration curves for 0.55-0.85-micron channel of F-1 MRIR radiometer.	53
16.	Calibration curves for 0.2-4.0-micron channel of F-1 MRIR radiometer.	54
17.	SBRC F-4 MRIR calibration, 0.2-4.0-micron channel.	55
18.	University of Michigan F-4 MRIR calibration data, 0.2-4.0-micron channel.	56

LIST OF ILLUSTRATIONS (Continued)

Figure		Page
19.	Weighting function, $H_{s\lambda}\phi'_{\lambda}$ for 0.55-0.75-micron channel of TIROS #103A radiometer.	59
20.	Weighting function, $H_{s\lambda}\phi'_{\lambda}$ for 0.2-6.0-micron channel of TIROS #103A radiometer.	60
21.	Weighting function, $H_{s\lambda}\phi'_{\lambda}$ for 0.55-0.85-micron channel of F-1 MRIR radiometer.	61
22.	Weighting function, $H_{s\lambda}\phi'_{\lambda}$ for 0.2-4.0-micron channel of F-4 MRIR radiometer.	62
23.	Altitude-time curve for 2 June, 1962 balloon flight.	64
24.	Trajectory for 2 June, 1962 balloon flight.	64
25.	Photographs of cloud cover for 2 June, 1962 balloon flight.	65
26.	Bidirectional reflectance of stratocumulus clouds, ρ' for 0.55-0.75-micron channel of TIROS #103A radiometer, 2 June, 1962 balloon flight.	67
27.	Bidirectional reflectance of stratocumulus clouds, ρ' for 0.2-5.5-micron channel of TIROS #103A radiometer 2 June, 1962 balloon flight.	68
28.	Bidirectional reflectance of stratocumulus clouds as a function of scattering angle, average values.	70
29.	Comparison of experimental measurements of bidirectional reflectance of stratocumulus cloud with theoretical single scattering pattern of water cloud model.	71
30.	Model of bidirectional reflectance pattern of stratocumulus cloud.	72
31.	Total directional reflectance of a stratocumulus cloud as a function of solar angle of elevation.	74
32.	Reflectance diagram, ratio ρ'_3/ρ'_5 vs. ρ'_5 for 2 June, 1962 balloon flight. All data taken above complete overcast or broken to scattered cloud conditions.	75
33.	Reflectance ratio vs. time for 2 June, 1962 balloon flight.	77
34.	Altitude-time data and trace of balloon trajectory for 26 June, 1963 balloon flight.	79

Figure		Page
35.	Reflectance diagram, ratio ρ_3'/ρ_5' vs. ρ_5' for 26 June, 1963 balloon flight, TIROS #103A radiometer.	80
36.	Reflectance diagram ratio ρ_3'/ρ_5' vs. ρ_5' for 26 June, 1963 balloon flight, NIMBUS MRIR F-1.	81
37.	Reflectance ratio vs. time for 26 June, 1963 balloon flight, TIROS #103A radiometer.	82
38.	Reflectance ratio vs. time for 26 June, 1963 balloon flight, NIMBUS MRIR F-1.	83
39.	Altitude vs. time curve for 10 March, 1965 balloon flight.	85
40.	Ground trace of balloon trajectory for 10 March, 1965 balloon flight.	86
41.	Polar coordinate system for bidirectional reflectance diagrams.	88
42.	Bidirectional reflectance diagram obtained at 0832-0836 CST on 10 March, 1965 balloon flight. θ_o = 72.2-71.5°, pressure altitude = 20.0-16.5 mb.	89
43.	Photos of model of 0832-0836 CST bidirectional reflectance pattern. θ_o = 72.2-71.5°.	91
44.	Bidirectional reflectance of snow-covered earth and atmosphere in principal plane, 10 March, 1965 balloon flight. θ_o = 72.2-71.5°.	92
45.	Bidirectional reflectance diagram obtained at 0855-0909 CST on 10 March, 1965 balloon flight. θ_o = 68.3-66.0°, pressure altitude = 9.0-8.5 mb.	94
46.	Photos of model of 0855-0909 CST bidirectional reflectance pattern. θ_o = 68.3-66.0°.	95
47.	Bidirectional reflectance of snow covered earth and atmosphere in principal plane, 10 March, 1965 balloon flight. θ_o = 68.3-66.0°.	96
48.	Bidirectional reflectance diagram obtained at 1109-1116 CST on 10 March, 1965 balloon flight. θ_o = 50.5-50.0°, balloon pressure altitude = 8.5-8.3 mb.	97
49.	Photos of model of 1109-1116 CST bidirectional reflectance pattern. θ_o = 50.5-50.0°.	98

Figure		Page
50.	Bidirectional reflectance of snow covered earth and atmosphere in principal plane, 10 March 1965 balloon flight. θ_o = 50.5-50.0°.	99
51.	Directional reflectance of stratocumulus cloud as a function of sun elevation angle (r is true directional reflectance, r' is result obtained for average of bi-directional reflectance for radiometer nadir angles of 0-45°).	102
52.	Reflectance diagram demonstrating spectral dependence of earth reflectance.	105
53.	Spectral reflectance curve of earth measured through clear skies from balloon over South Dakota, 26 June, 1963.	106
54.	Land, ocean, and snow covered areas of the earth, 23 December.	113
55.	Mean cloudiness of the earth, 23 December.	114
56.	Illustrative example: values of α_i.	115
57.	Average albedo in integration ring k vs θ_k.	122
58.	Images in cat-eye photometer.	128
59.	Variation of the brightness of the earthshine.	139
60.	Schematic diagram of satellite orbiting the earth.	148
61.	Typical black sensor and mirror temperature observations during a TIROS IV orbit.	149
62.	View of the earth and the precessing TIROS IV orbital plane.	154
63.	Comparison of the meridional variation of albedo for two precessional cycles.	156
64.	Comparison of the meridional variation of albedo for March, April, and May with data of London.	157
65.	Diagram indicating principle of operation of a channel of the TIROS five-channel radiometer.	159
66.	Effective spectral response of channels 3 and 5 of TIROS five-channel radiometer.	161

Figure		Page
67.	The scan patterns of the TIROS medium resolution radiometer.	163
68.	Optical arrangement of NIMBUS five-channel radiometer (MRIR).	164
69.	Relative characteristic response, ϕ'_λ, of 0.55-0.85-micron channel of F-1 MRIR.	165
70.	Relative characteristic response, ϕ'_λ, of 0.2-4.0-micron channel of F-1 and F-4 MRIR instruments.	166
71.	Field of view contours of the 0.2-4.0-micron channel of the F-4 MRIR.	167
72.	TIROS VII: 0.55-0.75-micron channel quasi-global map averages.	175
73.	TIROS VII: 0.55-0.75-micron channel albedo, June-July-August 1963.	177
74.	TIROS VII: 0.55-0.75-micron channel albedo, September-October-November 1963.	178
75.	TIROS VII: 0.55-0.75-micron channel albedo, December 1963-January-February 1964.	179
76.	TIROS VII: 0.55-0.75-micron channel albedo, March-April-May 1964.	180
77.	TIROS VII: 0.55-0.75-micron channel albedo, June 1963-May 1964.	181
78.	Reflectance curves for soils and rocks.	188
79.	Diffuse reflectance of representative types of desert surfaces.	189
80.	Spectral distribution of reflected energy for minerals and rocks.	190
81.	Reflectance of NAA standard granite.	191
82.	Spectral reflectance coefficients. (1) sand; (2) soil; (3) asphalt; (4) brick; (5) concrete.	192
83.	Bidirectional reflectance of sand ($\theta_o = 53°$) and black loam soil ($\theta_o = 78.5°$) at different wavelengths.	194

Figure		Page
84.	Spectral reflectance curves for vegetation.	195
85.	Spectral albedo of different vegetation: (1) sudan grass; (2) maize; (3) clover; (4) lucerne grass (June), (5) lucerne grass (July).	196
86.	Evolution of spectral reflection of a leaf during the growing season.	198
87.	Spectral albedo of a water surface (measured over a lake with depth of 60 to 70 cm).	199
88.	Spectral albedo of the snow cover in clear weather, 28 March, 1963. The Leningrad Region dry snow.	201
89.	Bidirectional reflectance of various types of soil at different angles of incidence. λ = 0.643 micron.	202
90.	Bidirectional reflectance of green grass turf at different angles of incidence. λ = 0.643 micron.	205
91.	Bidirectional luminous reflectance in the principal plane for water of infinite depth.	208
92.	Measured luminance of a snow surface.	210
93.	Total reflectance of various types of soil.	211
94.	Dependence of total reflectance of clay soil on its surface condition.	212
95.	Total reflectance of vegetation.	214
96.	Total reflectance of water basins.	215
97.	Variation of total reflectance of sea surface as a function of sun angle under stratus clouds.	216
98.	Change in total reflectance of snow cover with time.	217
99.	The spectral albedo for middle layer clouds.	218
100.	Intensity functions for water cloud illuminated by 0.45-micron radiation.	220
101.	Intensity functions for water cloud illuminated by 0.70-micron radiation.	221
102.	Total reflectance of coastal stratus cloud as a function of cloud thickness.	222

Figure Page

103. Dependence of cloud total reflectance on cloud thickness and cloud type. 224

104. Distribution of intensity of light emerging from the top of the atmosphere and of the skylight in the principal plane. Sun elevation 53°, optical thickness τ = 1.0, surface albedo A = 0, 0.25, and 0.80. 228

105. Surface albedo (Fresnel case) and ratio of upward flux (Fresnel case) to upward flux (Lambert case) for non-absorbing, homogeneous, plane parallel atmosphere with Rayleigh scattering. 229

106. Relative intensity of outward radiation for Rayleigh atmosphere with red clay surface. 231

107. Relative intensity of outward radiation for Rayleigh atmosphere with white quartz sand surface. 233

108. Sky and earth radiance, for an atmosphere with optical depth 0.4, surface albedo 0.2 (Lambert), and aerosol scattering with five times as much forward as back-scattering. 236

109. The seasonal distribution of planetary albedo (%). 245

NOMENCLATURE

a	Radius of the earth
a, b	Constants indicating beginning and end of satellite's orbit through earth's shadow
A	Anti-source
A	Albedo, earth's albedo
A'	Apparent earth's albedo for incomplete bidirectional reflectance
$\overline{A}$	Average earth's albedo
A_a	Albedo of atmosphere
A_{au}, A_{av}, A_{ai}	Albedo of atmosphere in ultraviolet, visible, and infrared, respectively
A_c	Albedo of clouds
A_{cu}, A_{cv}, A_{ci}	Albedo of clouds in ultraviolet, visible, and infrared respectively
A_e	Albedo of earth surface
A_{eu}, A_{ev}, A_{ei}	Albedo of earth's surface in ultraviolet, visible, and infrared, respectively
A_u, A_v, A_i	Albedo of earth in ultraviolet, visible, and infrared, respectively
$A_{v\lambda}$	Spectral distribution of earth's albedo in the visible region of the spectrum
A_λ	Spectral albedo

$A'_{0-0.7}$	Photometric albedo (actually includes ultraviolet) for a clear sky
A_r	Area of radiometer aperture
A, B, C	Variables used to replace terms in complicated expressions
C	Brightness of sunlit crescent of moon
C	% cloud cover. Also weighted % cloud cover
C, C_m, C_c, C_t	Constants
Ch	Channel
Cos*ϕ	Geometrical weighting function for solar radiation incident on an area viewed from a satellite
dm	The mass of a scattering element
ds	An element (of area) of a reflecting surface
D	Danjon's photometric albedo
E	East
E	Brightness of earthlight on moon
$f_o(\lambda)$	Spectral energy distribution of standard source
$f_\oplus(\lambda)$	Spectral distribution of earth radiation
$f_1(\lambda)$	Empirical solar continuum according to Minnaert
$f_2(\lambda)$	1-F, where F is the Fraunhofer line blanketing coefficient
$f_3(\lambda)$	Wavelength dependence of over-all reflectivity of earth
$F(\eta)$	Lunar phase function
$f_\lambda(\alpha)$	Function proportional to earth's phase function
H	Heat capacity of sensor
H	Irradiance, watts cm^{-2}

H_A	Solar irradiance absorbed in the atmosphere with normal cloud cover
H_λ	Spectral irradiance, watts cm^{-2} $micron^{-1}$
H_s	Solar irradiance, watts cm^{-2}
$H_{s\lambda}$	Solar spectral irradiance, watts cm^{-2} $micron^{-1}$
H'_s	Solar irradiance at the earth's surface with a clear sky
H''_s	Solar irradiance at the earth's surface with normal cloud cover
h	Vertical distance between bottom of balloon and point of its maximum diameter
h_s	Sun's hour angle
h(t)	Satellite sensor degradation correction factor
i	Angle of incidence
I_{dd}	Radiation transmitted diffusely through the atmosphere, reflected at the earth's surface and transmitted diffusely through the atmosphere
I_{dD}	Radiation transmitted diffusely through the atmosphere, reflected at the earth's surface and transmitted directly back through the atmosphere
I_{Dd}	Radiation transmitted directly through the atmosphere, reflected at the surface, and transmitted diffusely back through the atmosphere
I_{DD}	Radiation transmitted directly through the atmosphere, reflected at the surface, and transmitted directly through the atmosphere
I_s	Radiation backscattered by the atmosphere, never reaching the earth's surface
I_o	Photoelectric current produced by a standard source
$I_\oplus$	Photoelectric current produced by earth radiation
I_1, I_2	Photometer images
I_1	Intensity of earthshine
I_2	Intensity of sunlit portion of the moon

k	A constant
k_λ	Coefficient used in Bond's definition of planetary albedo
k_λ	Mass scattering coefficient
K	Conductivity of hemisphere support rod
K_1, K_2, K_3	Constants
ℓ	Length of load line in balloon train
$M_{o\lambda}$	The magnitude difference of the apparent brightness of the earth at full phase as viewed from the moon and the brightness of the sun at 1 Astronomical Unit
$M_E - M_c$	The magnitude difference of the sunlit crescent of the moon and the earthlit portion of the moon
$M_E - M_s$	The magnitude difference of the apparent brightness of the earth as viewed from the moon and the brightness of the sun at 1 Astronomical Unit
n	Index of refraction
$n(r)$	Number of particles with size in range r to r + dr
N	Number density
N	North
N	Radiance, watts cm^{-2} $ster^{-1}$
N_c	Radiance of diffuse calibration source, watts cm^{-2} $ster^{-1}$
N'_c	Effective radiance of calibration source, watts cm^{-2} $ster^{-1}$
N_s	Radiance of surface reflecting solar radiation, watts cm^{-2} $ster^{-1}$
N'_s	Effective radiance of surface reflecting solar radiation, watts cm^{-2} $ster^{-1}$
$N_{c\lambda}$	Spectral radiance of diffuse calibration source, watts cm^{-2} $ster^{-1}$ $micron^{-1}$
N_λ	Spectral radiance, watts cm^{-2} $ster^{-1}$ $micron^{-1}$
P_1, P_2	Intensity functions of different polarizations
P_s	Total power incident on the illuminated hemisphere of the earth watts

$p(\cos\beta)$	Phase function in scattering theory
p_λ	Geometrical albedo
q_λ	Phase integral
$Q(\alpha)$	Function proportional to earth's phase function
r	Maximum radius of balloon
r	Radius of a scattering particle
r	Specular reflectance calculated with the Fresnel formula
$r(\theta_o,\phi_o)$	Directional reflectance, the fraction of radiation incident from direction (θ_o,ϕ_o) which is reflected
$r\ (\theta_o,\phi_o)$	Spectral directional reflectance
$\overline{r\ (\theta_o,\phi_o)}$	Spectral directional reflectance measured under conditions of natural illumination
$r'(\theta_o,\phi_o)$	Apparent directional reflectance when using measurements up to 45°
$\overline{r}(\alpha,t)$	Weighted average reflectance of planet for phase angle α and time t
R.A.	Right ascension of satellite orbit
$R_{o\lambda}$	The magnitude difference of the apparent brightness of the earth at full phase at 1 A.U. and the brightness of the sun at 1 A.U.
$\overline{R}_{E-S}$	The mean distance of the earth from the sun
$\overline{R}_{p-s}$	The mean distance of a planet from the sun
R'	The responsivity of the radiometer detector
R_ℓ	Thermal radiation emitted by the earth and its atmosphere, watts cm^{-2}
R_r	Radiation reflected from the surface of the earth, watts cm^{-2}
R_s	Direct radiation from the sun, watts cm^{-2} (the solar constant)
R(R,70)	Correction factor, response at 70°F divided by response at T°F
S	South
S	Source

S	Brightness of sun
$S_{\oplus}$	Brightness of earth as seen from spacecraft, footcandles
S_o	Footcandle output of standard source
t	Time
T_1, T_2	Two consecutive sensor temperatures, ^oK
$\overline{T}$	Average sensor temperature, ^oK
T	Temperature, ^oK
T_B	Temperature of black sensor, ^oK
T_m	Temperature of mirror, ^oK
$\overline{T}_m$	Average temperature of mirror, ^oK
T_s	Temperature of shielded sensor, ^oK
T_T	Temperature of sensor with Tabor surface, ^oK
T_w	Temperature of white sensor, ^oK
V_c	Radiometer voltage when viewing calibration source
V_s	Radiometer voltage when viewing surface reflecting solar radiation
V	Volts
W	West
W	Radiant emittance, watts cm^{-2}
W_λ	Spectral radiant emittance, watts cm^{-2} $micron^{-1}$
Z	Altitude
Z	Zenith
α	Size parameter (used in scattering theory)
α	Phase angle
$\alpha_i(\zeta;\eta;t)$	Coefficients of basic bidirectional reflectances
α_ℓ	Absorptivity of spherical shell sensor for thermal radiation
α_s	Absorptivity of spherical shell sensor for solar radiation

β	The solid angle subtended by the earth as viewed from a satellite
β	Scattering angle measured from incident ray extended to scattered ray
δ	Depolarization factor of air
δ	Declination of satellite
δ_s	Declination of sun
Δ	The mean distance of the moon from the earth
Δm	Magnitude difference
ε_ℓ	Emissivity of spherical shell sensor for thermal radiation
ζ	Longitude of a point on the surface of a planet, as viewed from earth
ζ'	Longitude of a point on the surface of the earth
η	Colatitude of a point on the surface of a planet, as viewed from earth
η'	Colatitude of a point on the surface of the earth
η	Phase angle of the moon as viewed from earth
η_1	Reflectance of earthshine area of moon
η_2	Reflectance of sunlit area of moon
θ_o	Zenith angle of sun
θ	Zenith angle of radiance or reflected ray, and nadir angle of observation
λ	Wavelength, microns
μ	Micron
ν	Wave number, cm^{-1}
ν^*	A constant
π	3.141596...
ρ	Air density
$\rho_\lambda(\theta_o,\phi_o,\theta,\psi,\zeta;\eta;t)$	Bidirectional reflectance at a point $(\zeta;\eta')$ on the earth's surface

$\rho(\theta_o,\phi_o,\theta,\phi)$	Bidirectional reflectance, fraction of radiation incident from direction (θ_o,ϕ_o) which is reflected in direction (θ,ϕ)
$\rho_\lambda(\theta_o,\phi_o,\theta,\phi)$	Spectral bidirectional reflectance
$\rho_{\lambda i}(\theta_o,\phi_o,\theta,\phi)$	Basic bidirectional reflectances for use with albedo model of earth
ρ'	Effective average bidirectional reflectance of a surface as measured by a radiometer
ρ''	Effective bidirectional reflectance corrected for degradation of satellite sensor
ρ'''	Effective bidirectional reflectance corrected so that radiation balance is obtained
ρ_G	Surface albedo
ρ	Average bidirectional reflectance over bandwidth of radiometer channel
ρ_3',ρ_5'	Effective bidirectional reflectance of radiometer channel's 3 and 5
θ_s (min)	Minimum zenith angle of sun (at local noon)
$\sigma = \frac{a}{R}$	Radius of the earth divided by the distance of the earth from the sun
σ	Stefan-Boltzmann Constant
τ	Optical thickness
ϕ	Azimuth angle of reflected or scattered ray
$\phi_\lambda(\alpha)$	Phase function at wavelength λ
ϕ_λ	Effective spectral response of a channel of a radiometer
ϕ_λ'	Relative spectral response of a channel of a radiometer
ϕ_v	Response function of the eye
$\phi_{s\ II}$	Response function of the s II photo emissive surface multiplied by transmission function of objective lens
ϕ_o'	Azimuth angle used for integration over sunlit hemisphere of earth measured counterclockwise from north

ϕ_o	Azimuth angle of sun's ray extended, measured counterclockwise from north
$\psi = \phi - \phi_o$	Azimuth angle of reflected or scattered ray measured counterclockwise from principal plane
Ω	Solid angle
$\sum_i, \sum_j, \sum_k$	Summation over i, j, k, respectively
I	Night portion of satellite orbit
II	Sunrise and sunset portion of satellite orbit
III	Daylight portion of satellite orbit

ABSTRACT

The basic objective of this study is to provide a complete analysis of the physical and observational problems associated with the determination of the earth's albedo. There are two main results of this analysis: One is the conclusion that, insofar as the reflectance of solar radiation is concerned, the earth is a nonhomogeneous body with its various regions having different diffuse, wavelength dependent reflectance functions. The second is a statement of the geometrical-physical characteristics of a precise model for the calculation of earth's albedo.

The nature of the earth's reflectance is explored by means of precise definitions, a complete survey and critical analysis of existing research results, and new earth reflectance data obtained by radiometer measurement on three high altitude balloon flights. The precise model is obtained by careful detailed application of the precise definitions.

First, the nature of the reflectance of a surface element is considered in terms of spectral bidirectional reflectance. Directional reflectance and total reflectance quantities are defined. The geometrical nature of scattering is reviewed. Then earth albedo is defined precisely in terms of the time dependent spectral bidirectional reflectance of all areas of the earth's sunlit hemisphere. The astronomer's definition of planetary albedo, Bond's definition, is considered. The Bond albedo is then expressed as a function of the time dependent spectral bidirectional reflectance. It is concluded that, for a rotating planet such as the earth, the Bond albedo is not the same as the precise albedo, except for the case of a homogeneous planet having isotropic (diffuse) reflectance.

Information about the nature of earth's reflectance is presented by means of summaries of results in several different areas of albedo research:

a. The classical earth albedo experiment of Danjon.
b. Spacecraft and satellite measurements.
c. Measurements of the reflectance of earth's surface features.
d. Theoretical studies of the scattering of solar radiation by clouds, the clear earth's atmosphere and aerosols.
e. Estimates of earth's albedo made in connection with earth's heat balance studies.

These summaries show that the earth is a nonhomogeneous reflector of solar radiation. Reflectance functions for soil and rock, vegetation, ocean, snow and ice, and scattering functions for clouds, clear air and aerosols are complex, nondiffuse and wavelength dependent. Time varia-

tions, diurnal and seasonal, are much in evidence. In spite of this, the model used by experimenters for satellite data interpretation is usually a homogeneous earth with diffuse reflectance. Wavelength dependence is also often neglected. The need for a more precise model becomes apparent.

New data obtained with radiometers flown on high altitude balloons is presented and discussed. The balloon flight measurement system is described. The geometry of the measurements is shown to be precisely that which yields bidirectional reflectance or scattering patterns. Calibration curves are shown for the radiometers used. The method of interpretation of data as bidirectional reflectance is explained. Data from three balloon flights is presented.

Data from a flight on 2 June, 1962 shows the reflectance or scattering of solar radiation from low stratus clouds over farmland. The scattering pattern obtained is shown to agree qualitatively with theoretical results for single scattering from a water cloud with realistic particle size distribution, with large backscattering, very large forward scattering and indications of a fogbow at about 136°. Directional reflectance calculated from the scattering pattern for varying solar zenith angles, give a maximum total directional reflectance of 85% for zero solar zenith angle, a minimum of 58% at 40° solar zenith angle and 63% at 85° zenith angle, in good agreement with other experimental data. The data also show that cloud reflectance has relatively small spectral variations whereas under broken cloud conditions over South Dakota farmland in June, a rather large spectral variation is obtained, with spectral reflectance at 0.55-0.75 micron being much less than at 0.2-4.0 microns.

The spectral variations of earth reflectance noted above are confirmed by measurements made with two radiometers on 26 June, 1963. Reflectance of high cumulus clouds shows a spectral variation similar to that of low stratus.

Bidirectional reflectance data for partially snow covered earth, under clear sky conditions on 10 March, 1965, shows large backscattering and extremely large forward scattering for large solar zenith angles and an almost diffuse pattern with an indication of a small specular component for a smaller zenith angle. Directional reflectance is 35% for 72° solar zenith angle, 36% for 67°, and 30% for 50°.

Using the above data it is shown that errors of 10% in earth's albedo and 20% in directional reflectance could be produced in satellite data obtained with incomplete geometrical sampling, analyzed under the assumption of perfectly diffuse reflectance. Also, it is noted that

narrow band, 0.55-0.75 micron, data cannot be used instead of wide band, 0.2-4.0 microns, data for earth's albedo without appropriate corrections.

The geometrical-physical nature of the model is indicated using the precise model of earth's albedo with basic time dependent bidirectional reflectance functions. The procedure for calculation of earth's albedo is indicated and an illustrative example is worked out. It is noted that a much more complete geographical-climatological study is essential to complete the model.

I. INTRODUCTION

It is universally accepted that an understanding of the heat budget of the earth is fundamental for a better understanding of the world's weather processes. Thus a very important meteorological parameter is the earth's heat balance, which can be expressed as the difference between the incident solar energy and the outgoing radiant energy which, in turn, is the sum of the reflected solar radiation and emitted thermal radiation.

The reflected solar radiation (or albedo) which is one of three factors involved in the earth's heat balance, has been the subject of considerable interest, study, and conjecture. It is not only important for local and global, short- and long-term estimates of heat balance, but for the study of various problems in bioclimatology, light physiology, visibility, and aerial surveying as well.

The measurement of reflected solar radiation is best done from outside the earth and its atmosphere. Such measurements became feasible with the development of satellite technology, and some have already been made.[1,2] However, the methodology of these measurements has not yet been perfected. For example, the analysis of data obtained is usually carried out using a simple model of the earth based on three assumptions.

a. The reflectance (i.e., albedo) of the earth is isotropic (diffuse) in nature.

b. The reflectance of the earth is independent of wavelength. This is equivalent to the assumption that the spectral distribution of reflected solar radiation is equal to that of the incident solar radiation.

c. The method of sampling data from the satellite does not produce any error or bias in the result. This assumption would be valid only if the earth's surface were perfectly homogeneous.

It is surprising, at first that these assumptions are used. A brief survey of the literature on the reflectance of surface features and scattering by the atmosphere and clouds reveals evidence to the contrary, i.e., earth reflectance and scattering are nonisotropic and wavelength dependent. Also the earth and its atmosphere are obviously not homogeneous. A further search shows, however, that the precise model, nonhomogeneous with nonisotropic wavelength dependent reflectance has not been formulated and studied. Thus the need for using it in applications is not obvious and the method of applying it is not available for use. Indeed, it is appropriate to say that the lack of validity of the above three assumptions is obvious, but ignored, in the interpretation of satellite measurements of reflected solar radiation.

This paper is a limited study leading to the mathematical formulation of a precise model of the earth for albedo purposes, considering only the first part (a) of the two parts which are necessary for a complete study:

a. The geometrical-physical aspects of the reflectance of a surface, scattering by the clear atmosphere and clouds, and the reflectance of the earth as whole.

b. The geographical-meteorological aspects as a function of time and location on the earth.

The main part of the study is contained in Sections II-V, each of which treats a distinct phase of the subject.

In Section II, the nature of the reflectance of a surface element is considered in terms of the spectral bidirectional reflectance. Directional reflectance and total reflectance quantities are then defined. The geometrical nature of scattering is indicated and the definition of scattering angle reviewed. Next earth albedo is defined precisely in terms of the time dependent spectral bidirectional reflectance of all

areas of the earth's sunlit hemisphere. Finally the astronomer's definition of planetary albedo, Bond's definition, is considered and is shown to be identical to the precise albedo, for a rotating planet such as the earth, only when the planet is homogeneous with isotropic reflectance.

Section III contains summaries of results already obtained in several areas of albedo research:

a. The classical earth albedo experiment of Danjon.

b. Albedo measurements made from Explorer VII, the TIROS meteorological satellites and the Mariner 2 (Venus) spaceprobe.

c. Experimental data regarding the nature of the reflectance of earth surface features (soil, rock, vegetation, snow, and ocean).

d. Theoretical studies of the scattering of solar radiation by clouds and the clear earth's atmosphere.

e. Estimates of earth's albedo which have been made in connection with heat balance studies.

Section III is completed with a discussion of the approximate nature of the models of earth's albedo implicitly used by astronomers, meteorologists, and spacecraft experimenters. The need for a more precise model is indicated.

Section IV is devoted to a discussion of new measurements of earth reflectance made on high altitude balloon flights with instruments of the exact same design as those flown on the TIROS and NIMBUS meteorological satellites. Instrument calibrations and the interpretation of results are considered. Possible errors are indicated. Resulting data from three balloon flights demonstrating the spectral dependence and non-isotropic nature of the reflectance of partially snow covered earth and of the scattering of radiation from clouds are presented. The bidirectional reflectance patterns which were obtained are shown to compare

favorably with the limited theoretical data which are available. The data are then used to indicate the error that might be made in values of earth's albedo obtained by analysis of satellite reflectance data which is assumed to be isotropic. The unique opportunity of making measurements of reflectance with balloon borne instruments gave impetus to the whole investigation of albedo. Also these measurements have been applied directly to the precise model of albedo described in Section V.

Section V indicates the nature of a precise model of the earth for albedo purposes. The geometrical-physical characteristics of the model are discussed, and the method of calculating earth's albedo for a given model is outlined. It is suggested that suitable models based on a geographical-meteorological study be made for at least one day in each month of the year and that studies of these models be made as outlined above. A simple approximate model of the earth, incorporating some non-isotropic features is considered for the purpose of illustrating the technique. Detailed calculations are made and the results are discussed. It is hoped that the formulation of a precise albedo model may prove to be one of the more significant outcomes of the study.

Conclusions and suggestions for further research are contained in Section VI. Experimental techniques, methods of data interpretation, and limitations of the results of each area of research summarized in Section III are given in detail in Appendices A-F. Appendix G contains a summary of the four different coordinate systems used in this paper.

II. DEFINITIONS

A. THE GEOMETRY OF SCATTERING AND REFLECTION

The geometry of scattering and reflection is illustrated by Figure 1. Q is the point at which reflection or scattering takes place. SQ is the ray from the radiation source; in this case, the sun. QR is the reflected or scattered ray. In this example the incident ray is coming from the east at a low elevation angle, the ray QR is going west-north-west at a high elevation angle. The plane SQZ is called the principal plane and the plane SQR is called the scattering plane. The incident ray is defined by the polar coordinates (θ_o,ϕ_o), where θ_o is the zenith angle and ϕ_o the azimuth angle measured counterclockwise from the north direction to the extended principal plane. The reflected or scattered ray is measured by its polar coordinates (θ,ϕ). The angle ψ is equal to $\phi-\phi_o$. QS is the direction to the source; it has coordinates θ_o, and $\psi = 180°$. The direction QA to the antisource has coordinates $\theta = 180-\theta_o$ and $\psi = 0$. Where $\psi = 0$ or $180°$, for a reflected or scattered ray, the principal plane and scattering plane coincide. β is the scattering angle.

B. REFLECTANCE

Definitions of reflectance[3,4] that will be used in this study are as follows.

If ds is an element of a reflecting surface at Q in Figure 1, (θ_o,ϕ_o) are the zenith and azimuth angles of the incident radiation and (θ,ϕ) are the zenith and azimuth angles of a reflected ray, then the radiance in the direction (θ,ϕ) is given by:

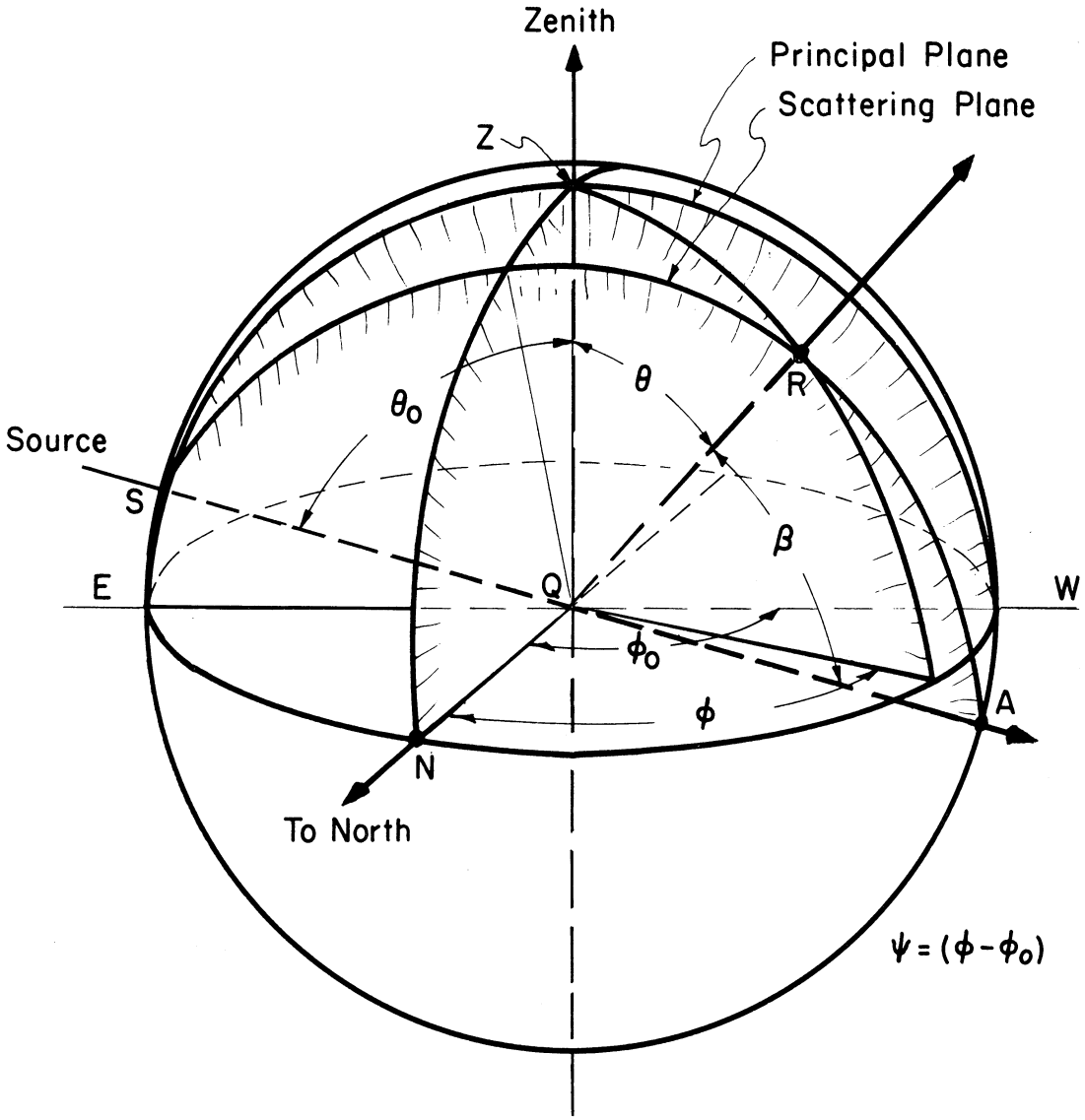

Figure 1. Geometry of reflection and scattering.

$$N(\theta_o,\phi_o,\theta,\phi) = \frac{1}{\pi}\rho(\theta_o,\phi_o,\theta,\phi)\cos\theta\ H\ \cos\theta_o\ \rho(\text{watts cm}^{-2}\ \text{ster}^{-1}) \quad (1)$$

where H is the irradiance from the direction (θ_o,ϕ_o) in watts cm^{-2} and $\rho(\theta_o,\phi_o,\theta,\phi)$ is the bidirectional reflectance, i.e., the fraction of radiation incident from the direction (θ_o,ϕ_o) which is reflected in the direction (θ,ϕ).

The total amount of reflected radiation from the element of area ds is given by the integral over the upper hemisphere, i.e.,

$$Wds = \int_{\phi=0}^{2\pi}\int_{\theta=0}^{\frac{\pi}{2}} N(\theta_o,\phi_o,\theta,\phi)\ \sin\theta\ d\theta\ d\phi\ \cdot\ ds \quad (2)$$

The directional reflectance $r(\theta_o,\phi_o)$, defined as the fraction of incident radiation which is reflected is

$$r(\theta_o,\phi_o) = \frac{W\cdot ds}{H\cos\theta_o\ ds} \quad (3)$$

$$r(\theta_o,\phi_o) = \frac{1}{\pi}\int_{\phi=0}^{2\pi}\int_{\theta=0}^{\frac{\pi}{2}} \rho(\theta_o,\phi_o,\theta,\phi)\cos\theta\sin\theta\ d\theta\ d\phi \quad (4)$$

For perfectly diffuse (Lambert) reflectance, we have:

$$\rho(\theta_o,\phi_o,\theta,\phi) = \rho = \text{constant} \quad (5)$$

and from (4) above:

$$r(\theta_o,\phi_o) = \rho = r = \text{constant} \quad (6)$$

Thus for perfectly diffuse reflectance, the directional reflectance is equal to the bidirectional reflectance, and each of these quantities is a constant.

Reflectance is a function of wavelength as well as direction. Spectral dependence is indicated by the subscript λ, thus:

$\rho_\lambda(\theta_o,\phi_o,\theta,\phi)$ = spectral bidirectional reflectance.

$r_\lambda(\theta_o,\phi_o)$ = spectral directional reflectance.

The reflectance without a subscript is the average reflectance over a range of wavelengths. This quantity is also called a total reflectance. Thus, for example the average or "total" directional reflectance over a range of wavelength λ_1 to λ_2 is given by:

$$r\,(\theta_o,\phi_o) = \frac{\int_{\lambda_1}^{\lambda_2} r_\lambda(\theta_o,\phi_o)H_\lambda\, d\lambda}{\int_{\lambda_1}^{\lambda_2} H_\lambda\, d\lambda} \qquad (7)$$

where H_λ is the spectral irradiance, watts cm^{-2} $micron^{-1}$.

Note that average reflectance is a function of the spectral distribution of the incident radiation as well as the nature of the reflecting surface. Thus average reflectance quantities measured with one spectral distribution may not necessarily be used as average reflectances for another spectral distribution.

Figure 2 shows the distribution of reflected radiation for a perfectly diffuse (Lambert) reflector. The quantity plotted is $\frac{1}{\pi}\ \rho_\lambda(\theta_o,\phi_o,\theta,\phi)\cos\theta$. Note that the distribution of reflected radiation is the same for all angles of incidence, i.e., $\rho_\lambda(\theta_o,\phi_o,\theta,\phi) = \rho$ =

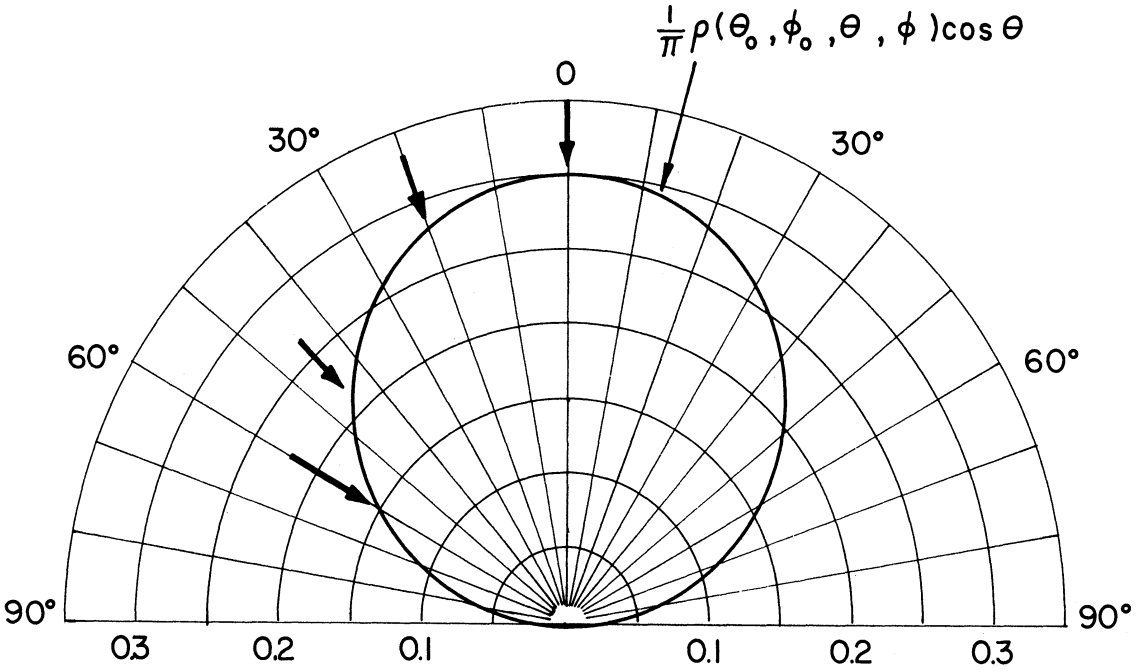

Figure 2. Distribution of reflected radiation for a perfectly diffuse (Lambert) reflector.

constant. For this illustration, $\rho = 0.94$ and, therefore $\frac{1}{\pi}\rho = 0.3$.

Figure 3 shows the distribution of reflected radiation for a nondiffuse reflector. $\frac{1}{\pi}\rho_\lambda(\theta_o,\phi_o,\theta,\phi)\cos\theta$ is plotted for three different angles of incidence. In this case the reflector has a fairly large specular component, and is similar to some distributions which have been measured for glazed snow (see Appendix C).

In Figures 2 and 3, the distribution of reflected radiation has been shown only for the plane of incidence (in Figure 1, the plane SZQ determined by the normal to the reflective surface and the incident ray). Complete specification of the distribution requires similar plots for all vertical planes, i.e., the distribution over the hemisphere.

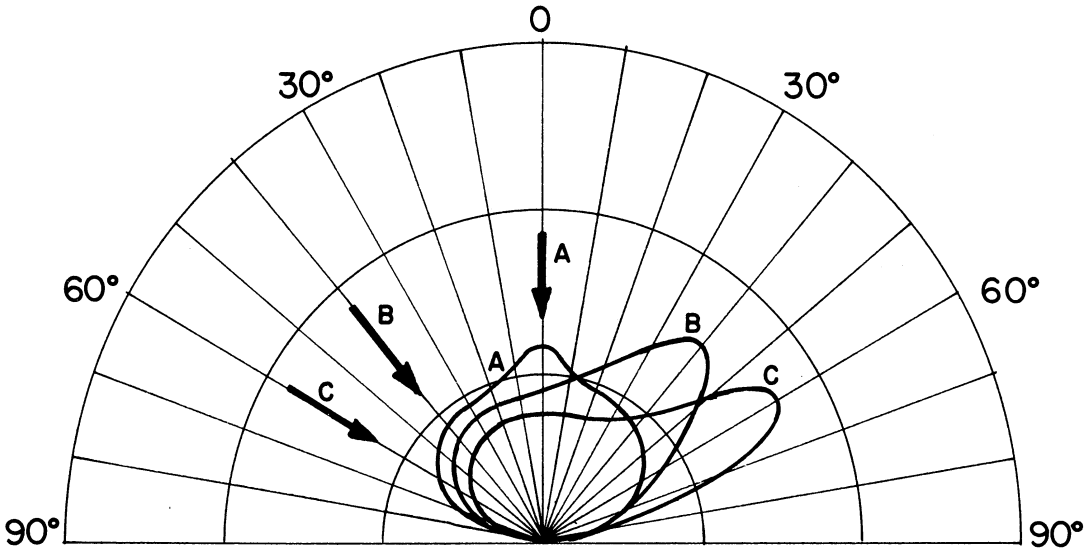

Figure 3. Distribution of reflected radiation for imperfectly diffuse reflector. $1/\pi\ \rho(\theta_o,\phi_o,\theta,\phi)\ \cos\theta$ is plotted for three angles of incidence: 0°, 40°, and 60°.

Ideally such a complete hemispherical plot should be obtained for each wavelength in the range of consideration. Then, finally a hemispherical plot of bidirectional reflectance should be obtained for each spectral distribution of interest.

C. SCATTERING ANGLE

In the study of scattering phenomena, it is the scattering angle β (see Figure 1) which is significant.[5] The angle β is related to the zenith and azimuth angles of the incident ray (θ_o,ϕ_o) and of the scattered ray (θ,ϕ) by the equation

$$\cos\beta = \sin\theta_o \sin\theta \cos\psi - \cos\theta_o \cos\theta \qquad (8)$$

where $\psi = \phi-\phi_o$

Radiation will be scattered from a scattering center (such as Q in Figure 1) into all directions, into the lower hemisphere as well as the upper hemisphere. Once the scattering pattern has been determined for $0 \leq \beta \leq 180$, the radiance in any direction can be specified.

D. EARTH'S ALBEDO

The geometrical relations that apply to a discussion of earth's albedo are illustrated by Figures 4a and 4b. In Figure 4a the earth is shown with the upper hemisphere illuminated by the sun. The earth's axis of rotation is the line NS shown in a position corresponding to summer in the northern hemisphere. The coordinate system (θ_o, ϕ_o') is fixed by the position of the sun. $\theta_o = 0$ is a direction pointing at the sun and ϕ_o' is measured counterclockwise from the north direction (as viewed from above) in a plane at right angles to the sun's rays. (Note that ϕ_o in Figure 1 was measured in a plane normal to the zenith direction.)

Figure 4b shows the difference between the angles ϕ_o and ϕ_o'. Note that ϕ_o' is measured counterclockwise from north at the subsolar point s, whereas ϕ_o is measured counterclockwise from north at the point of reflectance Q. η' is the colatitude of the point Q, δ_s is the declination of the sun, and h_s is the sun's hour angle with respect to the point Q.

The solar spectral irradiance at time t on a surface normal to the sun's rays is:

$$H_{s\lambda}(t) \quad \text{watts cm}^{-2} \text{ micron}^{-1}$$

The total solar irradiance is:

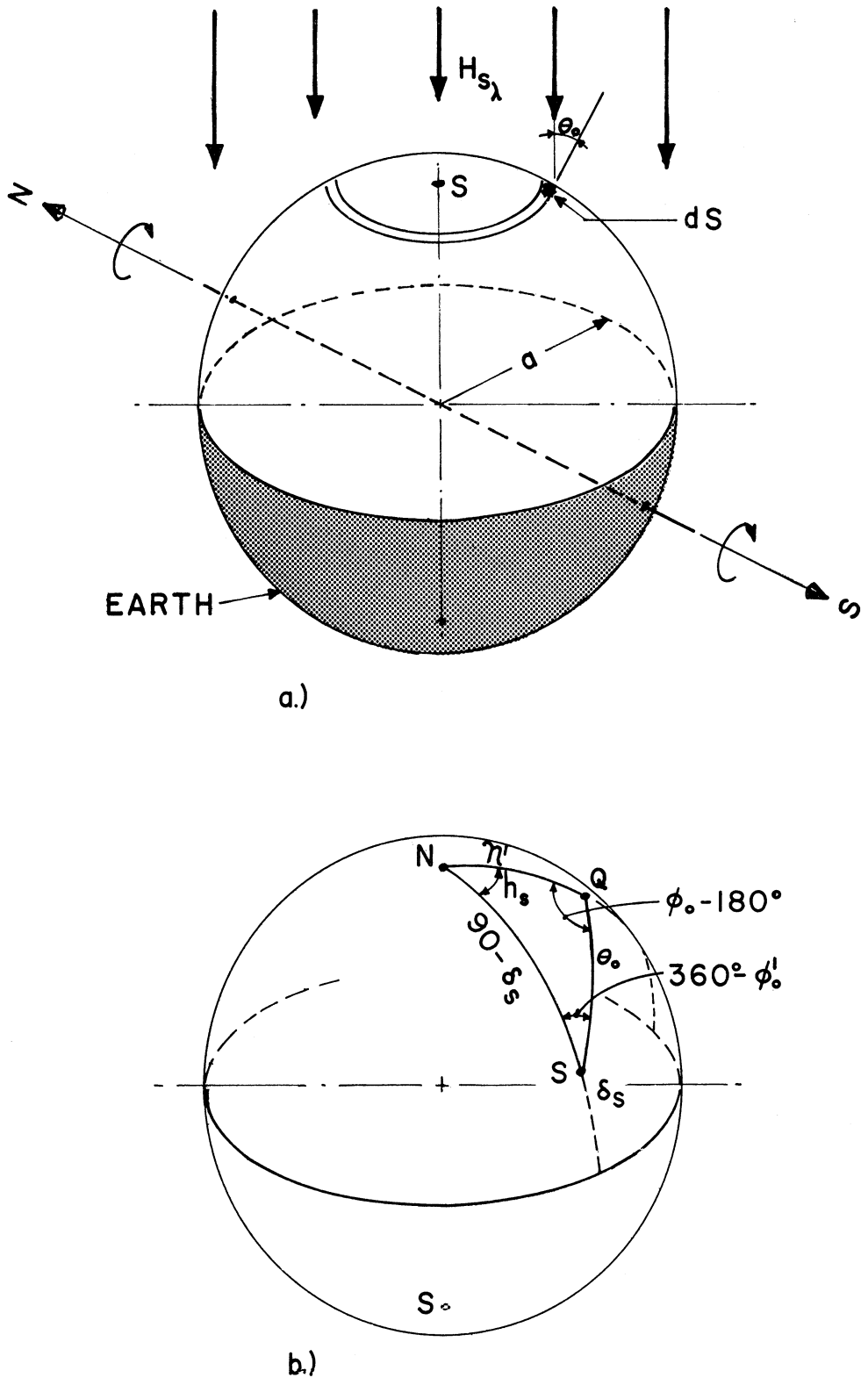

Figure 4. Geometry for calculating earth's albedo.

$$H_S(t) = \int_0^\infty H_{S\lambda}(t)d\lambda \quad \text{watts cm}^{-2} \tag{9}$$

The numerical value of $H_s(t)$ varies inversely as the square of the distance from the sun. Its mean value over a period of a year (the solar constant[6]) is 0.1395 watts cm^{-2}. During the year values of $H_s(t)$ vary over a range of 0.965 to 1.035 times the solar constant.

The solar radiant power falling on an element of area ds is:

$$H_s(t) \cos \theta_o \cdot ds = \int_0^\infty H_{s\lambda}(t) \cos \theta_o \cdot ds \cdot d\lambda \quad \text{(watts)} \tag{10}$$

The element of surface area ds on the surface of the earth is given by:

$$ds = a^2 \sin \theta_o \, d\theta_o \, d\phi'_o \tag{11}$$

and the total power incident on the illuminated hemisphere of the earth is:

$$P_s(t) = \int_{\phi'_o=0}^{\pi} \int_{\theta_o=0}^{\frac{\pi}{2}} H_s(t) \cos \theta_o \, a^2 \sin \theta_o \, d\theta_o \, d\phi'_o$$

$$P_s(t) = \pi a^2 \cdot H_s(t) = \pi a^2 \int_0^\infty H_{s\lambda}(t) \, d\lambda \tag{12}$$

The portion of the earth's surface which lies in the area ds is continuously changing because the earth is rotating on its axis. Note also that the azimuth angle of the incident ray varies with θ_o, ϕ'_o, i.e., is $\phi_o(\theta_o, \phi'_o)$. Thus the spectral reflectance of the area is changing as a function of time; i.e., we have the bidirectional spectral reflectance:

$$\rho_\lambda(\theta_o,\phi_o,\theta,\phi,t) \tag{13}$$

and the directional spectral reflectance

$$r_\lambda(\theta_o,\phi_o,t) = \frac{1}{\pi}\int_{\phi=0}^{\pi}\int_{\theta=0}^{\frac{\pi}{2}} \rho_\lambda(\theta_o,\phi_o,\theta,\phi,t)\cos 0 \sin\theta\, d\,\theta\, d\phi \tag{14}$$

The power reflected from the earth at the wavelength λ is:

$$\int_{\phi_o'=0}^{2\pi}\int_{\theta_o=0}^{\frac{\pi}{2}} r_\lambda(\theta_o,\phi_o,t)\, H_{s\lambda}(t)\cos\theta_o \cdot a^2 \cdot \sin\theta_o \cdot d\theta_o \cdot d\phi_o' \tag{15}$$

The total power reflected from the earth is:

$$\int_{\lambda=0}^{\infty}\int_{\phi_o'=0}^{2\pi}\int_{\theta_o=0}^{\frac{\pi}{2}} r_\lambda(\theta_o,\phi_o,t)H_{s\lambda}(t)a^2\cos\theta_o \sin\theta_o\, d\theta_o d\phi_o' d\lambda \tag{16}$$

and the earth's albedo at time t is

$$A(t) = \frac{\displaystyle\int_{\lambda=0}^{\infty}\int_{\phi_o'=0}^{2\pi}\int_{\theta_o=0}^{\frac{\pi}{2}} r_\lambda(\theta_o,\phi_o,t)H_{s\lambda}(t)\cos\theta_o \sin\theta_o\, d\theta_o d\phi_o' d\lambda}{\pi\displaystyle\int_0^{\infty} H_{s\lambda}(t)\, d\lambda} \tag{17}$$

Usually it is the average value of earth's albedo over a period of time which is of interest, i.e.,

$$\overline{A} = \frac{1}{t_2 - t_1}\int_{t_1}^{t_2} A(t)\, dt \tag{18}$$

Note that the albedo represents an integration over many variables, i.e., $\theta_o, \phi_o, \theta, \phi, \lambda$. We can show this explicitly by the equation:

$$A(t) = \frac{\int_{\lambda}\int_{\theta_o}\int_{\phi_o'}\int_{\theta}\int_{\phi} \rho_\lambda(\theta_o,\phi_o,\theta,\phi,t)H_{s\lambda}(t)\sin\theta_o\cos\theta_o\sin\theta\cos\theta d\theta_o d\phi_o' d\theta d\phi d\lambda}{\pi^2 \int_{\lambda=0}^{\infty} H_{s\lambda}(t)d\lambda} \tag{19}$$

In this equation (θ_o,ϕ_o') are measured in the coordinate system shown in Figure 4a with the direction θ_o pointing towards the sun, whereas (θ,ϕ) are measured in the coordinate system illustrated in Figure 1, with the direction $\theta = 0$ pointing towards the zenith, normal to the element of area ds.

From the above definition (Equation (19)), we see that a precise specification of earth's albedo requires that we know the bidirectional reflectance $\rho\ (\theta_o,\phi_o,\theta,\phi,t)$ at every point θ_o,ϕ_o' of the sunlit portion of the earth.

The average albedo of the earth over some time interval is given by integrating (averaging) over:

1. All directions of reflectance

   $$0 \leq \theta \leq \frac{\pi}{2} \qquad 0 \leq \phi \leq 2\pi.$$

2. All parts of the sunlit portion of the earth

   $$0 \leq \theta_o \leq \frac{\pi}{2} \qquad 0 \leq \phi_o \leq 2\pi.$$

3. The entire range of wavelengths of the solar spectrum (usually $0.2\mu \leq \lambda \leq 4.0\mu$), with weighting function $H_{s\lambda}(t)$.

4. Over the desired period of time t.

In practice, a complete knowledge of $\rho_\lambda(\theta_o,\phi_o,\theta,\phi,t)$ is not possible. As a result, any calculation of earth's albedo is an approximation to

the true value obtained by making some assumption about the nature of $\rho_\lambda(\theta_o,\phi_o,\theta,\phi,t)$.

Note: In the above, the azimuth angle $\psi = \phi - \phi_o$ could have been used wherever ϕ has been used, i.e., we could have written $\rho_\lambda(\theta_o,\phi_o,\theta,\psi)$ instead of $\rho_\lambda(\theta_o,\phi_o,\theta,\phi)$ and could have integrated over ψ instead of ϕ. Thus Equation (19) would be

$$A(t) = \frac{\int_\lambda \int_{\theta_o} \int_{\phi_o'} \int_\theta \int_\psi \rho_\lambda(\theta_o,\phi_o,\theta,\psi,t) H_{s\lambda}(t) \sin\theta_o \cos\theta_o \sin\theta \cos\theta \, d\psi \, d\theta \, d\phi_o' \, d\theta_o \, d\lambda}{\pi^2 \int_\lambda H_{s\lambda}(t) \, d\lambda} \qquad (19a)$$

E. PLANETARY ALBEDO, BOND'S DEFINITION

The work of astronomers on the determination of the albedo of planets has resulted in a definition of planetary albedo[7] which is an approximation to the definition of earth's albedo given in the last section. This definition of planetary albedo, suggested by Bond and adopted by H. N. Russell,[8] serves for the calculation of a planet's albedo from photometric observations of the planet from another planet.

The geometrical relations that apply to the discussion are shown in Figures 5a and 5b. Figure 5a shows a planet illuminated by the sun. S, p, and E represent, respectively, the centers of the sun, the planet, and the earth, from which measurements of the planet's albedo can be made (a similar geometry would apply for measurements of earth's albedo from the moon). The angle α is called the phase angle.

If the reflectance of the planet in the direction α is given by $k_\lambda \, \phi_\lambda(\alpha)$, where $\phi_\lambda(\alpha)$, the phase function, has maximum value $\phi_\lambda(0) = 1$, and if it is assumed that the reflectance has the same value in all

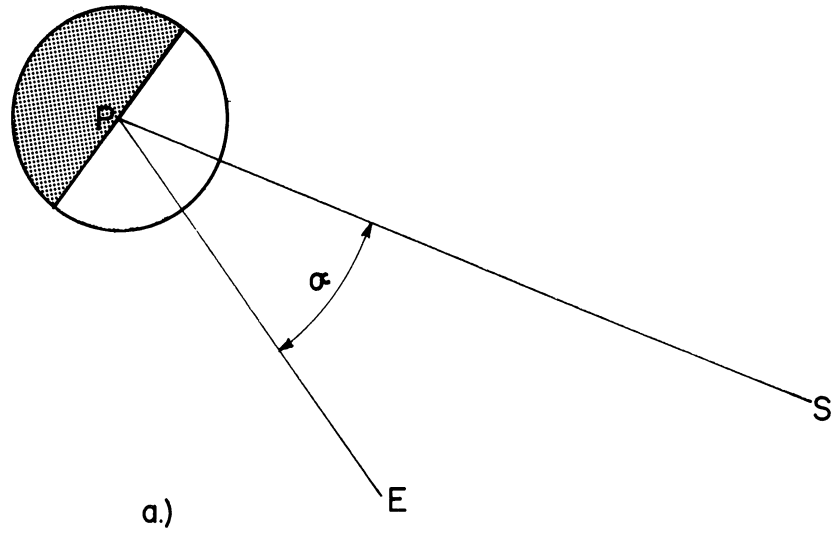

a.)

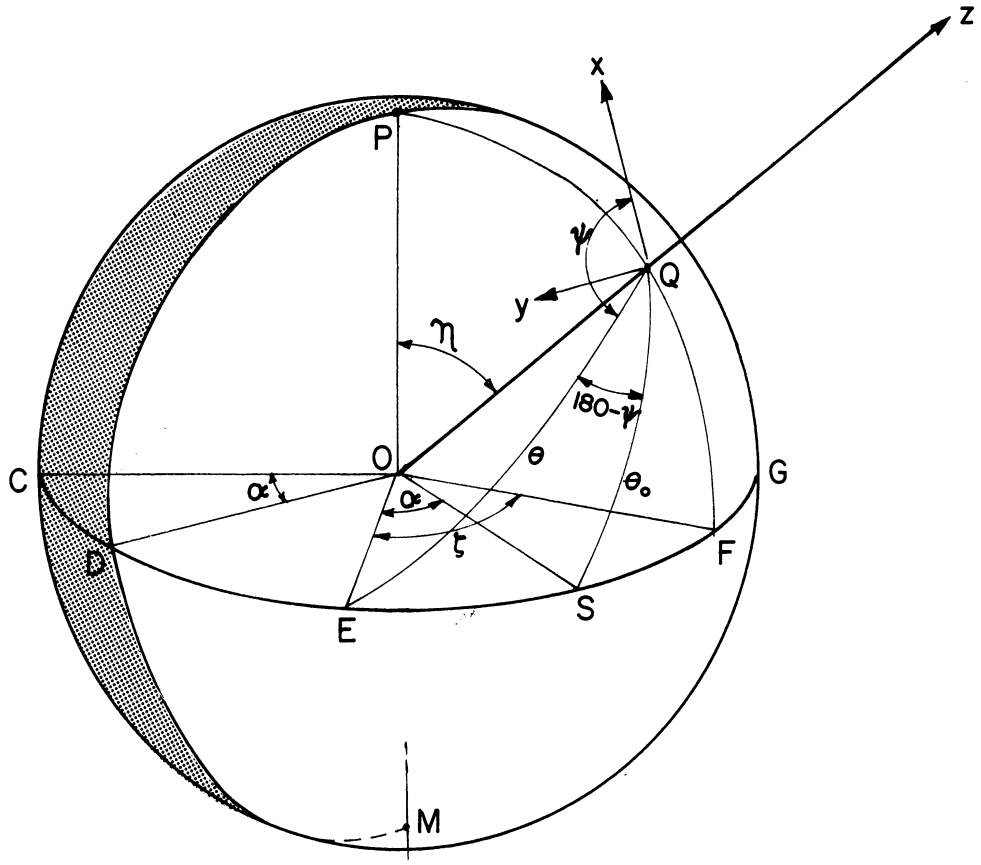

b.)

Figure 5. Planetary albedo-geometrical relations.

directions on the cone of half angle α formed by rotating PE about PS then the spectral albedo of the planet is given by the definition of Bond:

$$A_\lambda = 2\, k_\lambda \int_0^\pi \phi_\lambda(\alpha) \sin \alpha \, d\alpha \qquad (20)$$

The intensity of light reflected from the planet at the phase angle α can be calculated with the help of the geometrical relations shown in Figure 5b. The planet is shown as viewed from some point in space. The portion PCMD of the hemisphere shown is in shadow. OS is the sun's direction, OE, the direction to the observation point. For any point Q on the planet's surface, θ_o is the zenith angle of incidence, the azimuth angle of incidence is ϕ_o. The reflectance angles are θ and ψ, α is the phase angle of the observation.

The coordinate system which will be used for integration over the planetary surface has the equatorial circle CESG and the meridian circle PEM as reference circles. The meridian circle of the point Q on the surface is PQF. The coordinates of the point Q are the longitude ζ and the colatitude η.

The angles of incidence and reflection are related to the angles α, ζ, and η by:

$$\cos \theta_o = \sin \eta \cos(\zeta - \alpha) \qquad (21)$$

$$\cos \theta = \sin \eta \cos \zeta \qquad (22)$$

$$\cos \psi = \frac{\cos \theta \cos \theta_o - \cos \alpha}{\sin\theta \sin \theta_o} \qquad (23)$$

$$\sin \psi = \frac{\sin \alpha \cos \eta}{\sin \theta \sin \theta_o} \qquad (24)$$

We can derive the equation for the Bond planetary albedo as follows. Assuming:

1. That the surface of the planet is homogeneous and constant in its characteristics for the time interval required to make measurements over all phase angles α,
2. The earth is at a constant distance Δ from the planet during this time interval,
3. The planet is at a constant distance $\bar{R}_{p-s}$ from the sun during this time interval,

the spectral albedo is:

$$A_\lambda = \frac{\text{Total reflected solar radiation at wavelength } \lambda}{\text{Total incident solar radiation at wavelength } \lambda}$$

and

$$A_\lambda = \frac{2\pi \int_0^\pi f_\lambda(\alpha)\, \Delta^2 \sin\alpha \, d\alpha}{\pi \cdot a^2 \cdot H_{s\lambda} \, \frac{\bar{R}^2_{E-S}}{\bar{R}^2_{p-s}}}$$

$$= \frac{2 \cdot \Delta^2 \cdot \bar{R}^2_{p-s}}{a^2 \cdot \bar{R}^2_{E-S}} \int_0^\pi \frac{f_\lambda(\alpha)}{H_{s\lambda}} \sin\alpha \, d\alpha \qquad (25)$$

where a is the mean radius of the planet

H_s is the spectral irradiance of the earth by the sun at mean distance $\bar{R}_{E-S}$.

$f_\lambda(\alpha)$ is the spectral irradiance of the earth due to solar radiation reflected from the planet.

Note that the equation just written agrees with the Bond definition of spectral planetary albedo

$$A_\lambda = 2\, k_\lambda \int_0^\pi \phi_\lambda(\alpha)\, \sin\alpha\, d\alpha \tag{26}$$

if

$$k_\lambda \phi_\lambda(\alpha) = \frac{\Delta^2 \cdot \bar{R}^2_{p-s}}{a^2 \cdot \bar{R}^2_{E-S}} \frac{f_\lambda(\alpha)}{H_{s\lambda}} \tag{27}$$

The total albedo of the planet can then be obtained from:

$$A = \frac{\int_0^\pi A_\lambda\, H_{s\lambda} d\lambda}{\int_0^\infty H_{s\lambda}\, d\lambda} \tag{28}$$

The relation between $f_\lambda(\alpha)$ which appears in the expression for the Bond albedo can be related to $\rho_\lambda(\theta_o,\phi_o,\theta,\psi,t)$ on the planet as follows: The spectral solar irradiance of one cm^2 of surface on the planet at a mean distance $\bar{R}_{p-s}$ from the sun is:

$$H_{s\lambda} \frac{\bar{R}^2_{E-S}}{\bar{R}^2_{p-s}} \cos\theta_o$$

The spectral radiance of this area, due to reflectance of the solar radiation, is:

$$\frac{1}{\pi} \rho_\lambda(\theta_o,\phi_o,\theta,\psi,t) H_{s\lambda} \frac{\bar{R}^2_{E-S}}{\bar{R}^2_{p-s}} \cos\theta_o \cos\theta$$

The spectral irradiance of one cm^2 of surface at the earth (normal to the earth-planet direction) is $\frac{1}{\Delta^2}$ times this last quantity. Thus the spectral irradiance at the earth due to the portion of sunlit hemisphere of the planet which is viewed from the earth is:

$$f_\lambda(\alpha) = \frac{1}{\pi}\frac{a^2}{\Delta^2}\frac{\bar{R}^2_{E-S}}{\bar{R}^2_{p-s}} H_{s\lambda} \int_{\eta=0}^{\pi}\int_{\zeta=\alpha-\frac{\pi}{2}}^{\frac{\pi}{2}} \rho_\lambda(\theta_o,\phi_o,\theta,\psi,t)\cos\theta_o\cos\theta\sin\eta d\eta d\zeta \tag{29}$$

Substituting for $f_\lambda(\alpha)$ in Equation (26), we obtain:

$$A_\lambda = \frac{2}{\pi}\int_{\alpha=0}^{\pi}\int_{\eta=0}^{\pi}\int_{\zeta=\alpha-\frac{\pi}{2}}^{\frac{\pi}{2}} \rho_\lambda(\theta_o,\phi_o,\theta,\psi,t)\cos\theta_o\cos\theta\sin\eta\sin\alpha d\alpha d\eta d\zeta \tag{30}$$

and finally substituting from (21) and (22):

$$A_\lambda = \frac{2}{\pi}\int_{\alpha=0}^{\pi}\int_{\eta=0}^{\pi}\int_{\zeta=\alpha-\frac{\pi}{2}}^{\frac{\pi}{2}} \rho_\lambda(\theta_o,\phi_o,\theta,\psi,t)\cos\zeta\cos(\zeta-\alpha)\sin^3\eta\sin\alpha d\alpha d\eta d\zeta \tag{31}$$

Equation (31) indicates that the Bond planetary albedo represents a measurement to which only certain selected values of bidirectional reflectance $\rho_\lambda(\theta_o,\phi_o,\theta,\psi,t)$ contribute. It is obtained by integrating over:

1. All phase angles, α.
2. That part of the sunlit portion of the planet which can be seen from the observation points at the angles α.
3. A period of time at least as great as the time required to achieve all phase angles $0 \leq \alpha \leq \pi$.

Finally, we note that the Bond albedo is an approximation in that it assumes that the reflectance of the planet in any direction at angle α to the line OS (see Figure 5b) is the same as that measured at the phase angle α in the direction OE. This may accidentally be so; otherwise this assumption is valid for a rotating planet such as the earth only if the surface of the planet is homogeneous with perfectly diffuse reflectance, i.e., only if $\rho_\lambda(\theta_o,\phi_o,\theta,\psi,t) = \rho_\lambda$, a constant. In this

very special case, the Bond definition (31) and the precise definition of albedo (19a) will yield the same result, $A_\lambda = \rho_\lambda$, and the phase function $\phi_\lambda(\alpha)$ becomes:

$$\phi_\lambda(\alpha) = \frac{\sin\alpha + (\pi-\alpha)\cos\alpha}{\pi} \qquad (32)$$

III. A REVIEW OF RESEARCH RELATED TO EARTH'S ALBEDO

A. EARTH'S ALBEDO FROM MEASUREMENTS OF EARTHLIGHT ON THE MOON[9-13]

Part of the moon's surface facing the earth, which is not directly illuminated by the sun, is illuminated by light reflected to the moon by the earth. Although this part of the moon is only feebly illuminated, it is visible during most of the month. Measurements of this faint "earthlight" can be used to calculate earth's albedo in the visible according to Bond's definition of planetary albedo. Measurements of this type have been made and reported on by Danjon,[9] Dubois,[10] Bakos[11] and others.

Details of the experimental technique and the method of data analysis are discussed in Appendix A. The results obtained are summarized below in Table 1, which indicates a long-term average photometric albedo of 0.40 and demonstrates that the proper model of the earth for albedo purposes has the following characteristics:

1. It is nonhomogeneous as indicated by diurnal variations and a reflectance of continental areas greater than of ocean areas.
2. Its albedo is spectrally dependent as demonstrated by the relatively large spectral variation over the small wavelength range already measured.
3. Its reflectance is of a nondiffuse nature. Comparison of the Danjon phase function with that corresponding to the ideal diffuse rose (Figure 6) shows this to be so.

TABLE 1

EARTH'S ALBEDO FROM MEASUREMENTS OF EARTHLIGHT ON THE MOON

Photometric Albedo (λ = 0.554 micron)

10-Year average[a]	A_λ = 0.40
Yearly averages[b]	$0.37 < A_\lambda < 0.44$

Phase Function (λ = 0.554 micron)[a]

$$\phi_\lambda(\alpha) = 2.512^{-\left[1.30\,\frac{\alpha}{100} + 0.19\,\left(\frac{\alpha}{100}\right)^2 + 0.48\,\left(\frac{\alpha}{100}\right)^3\right]}$$

Spectral Variation[b]

λ	0.467	0.544	0.606
A_λ	0.48	0.39	0.315

Seasonal Variations[a,c,d]

Albedo Maxima: Spring and Fall
Albedo Minima: Summer and Winter

Diurnal and Other Variations

1. Diurnal variation with maximum albedo over Asian continent. Probably due to higher average cloud cover over Asia.[c]
2. Reflectance of continental areas must be greater than that of ocean areas.[c]
3. Earthshine approaches maximum as a minimum activity of the solar cycle approaches and then decreases rapidly right after the minimum of solar activity.[d]

Limitations of Technique

1. Accuracy limited by light scattering in earth's atmosphere and measurement over only a limited range of phase angles.
2. Measurements made from within 28.5° of the plane of the earth's equator. It would be desirable to measure from other directions in space as well.
3. Measurements made over only a small portion of the spectrum (0.467-0.606 micron) instead of 0.2-4.0 microns.
4. Telescopes used in measurements of Danjon[9] and Dubois[11] were located in France and their data do not necessarily apply to the earth as a whole.[12] New measures at other longitudes are necessary.

---

[a] Danjon.[9]

[b] Angstrom,[13] from Danjon's data.

[c] Bakos.[10]

[d] Dubois.[11]

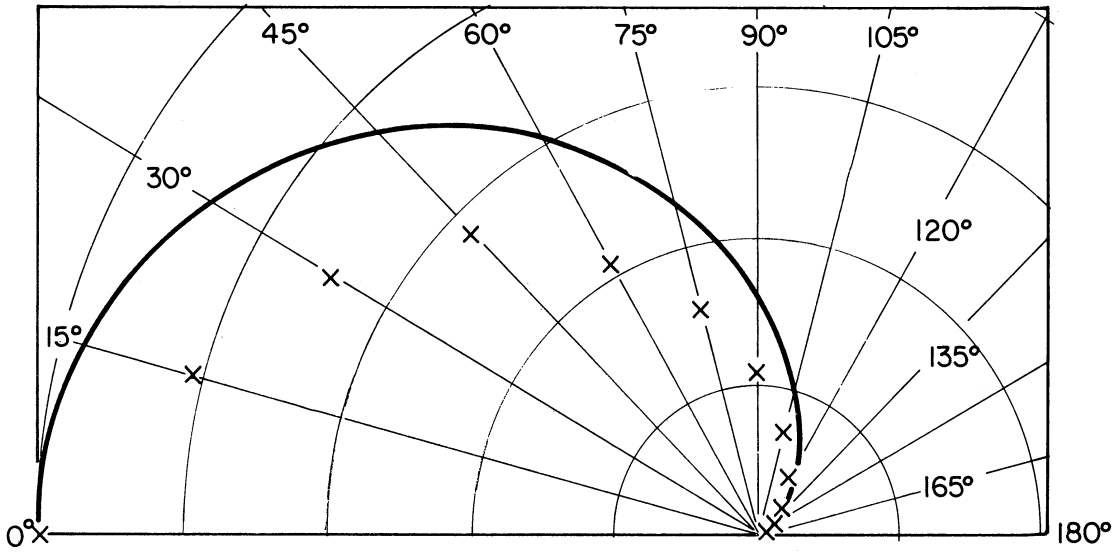

$$\text{——}: \phi(\alpha) = \frac{\sin\alpha + (\pi - \alpha)\cos\alpha}{\pi}$$

$$\text{x}: \phi(\alpha) = 2.512^{-\left[1.30\left(\frac{\alpha}{100}\right) + 0.19\left(\frac{\alpha}{100}\right)^2 + 0.48\left(\frac{\alpha}{100}\right)^3\right]}$$

Figure 6. Comparison of Danjon's phase function with that of a perfectly diffuse homogeneous earth.

B. EARTH'S ALBEDO MEASUREMENTS FROM SATELLITES AND SPACECRAFT[14-29]

Measurements of earth reflectance (or earth albedo) have been made from the Explorer VII satellite,[14] the TIROS and NIMBUS meteorological satellites[1,15] and the Mariner 2 spacecraft[16] on the flight to Venus.

The instruments used were of several types, differing in spatial and spectral resolution, and providing measurements of different significance. Details of the experimental techniques and data analysis problems are discussed in Appendix B. The results obtained are summarized in Table 2. Long-term average values of earth albedo of 32-35% are in-

TABLE 2

EARTH'S ALBEDO MEASUREMENTS FROM SATELLITES AND SPACECRAFT

Earth's Albedo

6-Month average[a]	A = 0.35
1-Year average[b]	A = 0.322

Phase Function

Some data in reasonable agreement with Danjon's phase function.[c]

Spectral Variation

No data

Seasonal Variations

Albedo maxima: Spring[a] and/or Fall[b]

Latitude Variations[a,b]

Meridional profiles averaged over the globe show slight maxima at the equator, minima at the subtropical belts and increasing values with latitude up to 60° latitude.

Diurnal and Other Variations[c]

1. Diurnal variation with bright spot in Atlantic near eastern South America.
2. Semiperiodic 5-6 day variation.
3. Reflectance of land areas 1.41 times greater than reflectance of ocean areas.

Limitations of the Satellite and Spacecraft Experiments

1. Isotropic (diffuse) reflectance assumed.[a,b]
2. An earth, homogeneous, in constant latitude belts is assumed.[a,b]
3. Sampling errors are ignored.[a,b]
4. Data limited to 60°N-60°S.[a,b]
5. Annual albedo adjusted to fit heat balance estimated from 8-12μ channel data.[b]

---

[a] House[2]

[b] Bandeen, et al.[1]

[c] Wildey[16]

dicated. Additional data supporting the nonhomogeneous nature of the earth's reflectance is indicated, although in two of the experiments[1,2] data is analyzed as though the earth is homogeneous in constant latitude belts. Earth reflectance is generally assumed to be diffuse in the analysis of satellite experiments; thus, appreciable errors may be introduced into the data.

C. REFLECTANCE OF THE EARTH'S SURFACE[30-46]

Although it is possible to define the reflectance of a surface element quite precisely in terms of the spectral bidirectional reflectance $\rho_\lambda(\theta_o,\phi_o,\theta,\phi)$, it is an extremely rare case for which we have sufficient information about this quantity. In order to calculate the reflectance of a given surface element we must not only know $\rho_\lambda(\theta_o,\phi_o,\theta,\phi)$ for all values of wavelength, incident direction, and direction of reflection but must also know the spectral and directional distribution of the incident radiation as well. Knowledge of the latter is often as difficult to come by as is knowledge of former.

The earth's surface is not homogeneous, it is composed of many different types of materials which can (after Kon drat' yev[30]) be divided into four general classes, i.e.,

1. Soils and rocks
2. Vegetation
3. Water basins
4. Snow and ice

Appendix C is a summary of earth surface reflectance data. Data on spectral dependence, angular distribution of reflectance, total reflection, dependence on conditions of illumination, and dependence on other parameters, i.e., roughness, time of day, growing season, etc.,

have been gathered together in this appendix in the form of figures and tables, with interpretation of the data as necessary.

A condensed summary of this data is contained in Table 3, leaving no doubt that the earth's surface, in itself, is nonhomogeneous with nondiffuse spectrally dependent reflectance.

D. THE REFLECTANCE OF CLOUDS[47-52]

The reflectance of clouds is an extremely important factor in the evaluation of earth's albedo, since as much as 75% of the reflected solar radiation may be due to cloud reflectance. It is difficult to obtain accurate reflectances to apply to a practical situation, since cloud reflectance depends on so many factors, i.e., cloud type, cloud thickness, cloud height, the reflectance of the earth beneath the cloud and solar elevation angle.

Again detailed cloud reflectance data has been compiled. It is contained in Appendix D. Spectral reflectance, angular distribution of reflectance, and total reflectance are discussed. A condensed summary is contained in Table 4. As far as clouds are concerned, a proper model of the earth for albedo purposes is nonhomogeneous with nondiffuse spectrally dependent reflectance.

E. THE SCATTERING OF SOLAR RADIATION BY AIR MOLECULES AND AEROSOLS[53-70]

Solar radiation from the sun decreases in intensity as it passes through the "clear" (hazy or noncloudy) sky. This decrease in intensity, called "extinction," is due to scattering and to absorption by aerosols and the molecular gases. The absorbed energy may appear later as thermal radiation and is not of concern as far as earth's albedo is concerned. Some of the scattered energy is returned to space directly after single

TABLE 3

SUMMARY OF REFLECTANCE DATA FOR EARTH SURFACE FEATURES

	Spectral Characteristics	Angular Distribution of Reflectance	Total Reflectance
Soils and Rocks	1. increasing to 1 micron 2. decreasing above 2 microns 3. moisture decreases reflectance	1. backscattering and forward scattering 2. sand has large forward scattering 3. loam has small forward scattering	1. 5-45% 2. moisture decreases reflectance by 5-20% 3. smooth surfaces have higher reflectance 4. diurnal variation, maximum reflectance for small sun angles
Vegetation	1. small below 0.5 micron 2. a small maximum bump at 0.5 to 0.55 micron 3. chlorophyll absorption at 0.68 micron 4. sharp increase at 0.7 micron 5. decrease above 2 microns 6. depends on growing season	1. backscattering 2. small forward scattering	1. 5-25% 2. diurnal effects, maximum reflectance for small angles 3. marked annual variation
Water Basins	1. maximum at 0.5-0.7 micron 2. depends on turbidity and waves	1. large back and forward scattering	1. small reflectance 2. diurnal variation maximum for small sun angles 3. depends on turbidity and waves
Snow and Ice	1. decreases slightly with increasing wavelength 2. large variability depending on purity, wetness, physical condition	1. diffuse component plus mirror component 2. mirror component increases with increasing angle of incidence	1. variable 25-80% 2. 84% in antarctic 3. 74% Ross Sea ice 4. 30-40% White Sea ice

TABLE 4

SUMMARY OF REFLECTANCE DATA FOR CLOUDS

Spectral Characteristics	Angular Distribution of Reflectance	Total Reflectance
1. Constant from 0.2 micron to about 0.8 micron	1. Pronounced forward scattering with smaller backscattering	1. 10-80%
2. Decreasing with wavelength above 0.8 micron showing water vapor absorption bands	2. Minimum for scattering angles of 80-120°	2. Varies with cloud type, cloud thickness, and type of underlying surface
	3. Fogbow for scattering angle of 143°	

scattering, or ultimately after multiple scattering by air molecules and aerosols and/or reflection from earth surface features and scattering from clouds. It is this radiation, scattered and reflected back out into space which constitutes the earth's albedo.

The complete scattering problem, which involves multiple scattering by air molecules and aerosols plus reflection from earth surface features and scattering from clouds, is not solved in all of its detail and is even difficult to formulate. However, various approximations to the problem have been considered and a large volume of literature discussing various aspects of the problem does exist. The results of a search of the literature are given in Appendix E. A condensed summary, is given in Table 5. Although it cannot be said that solutions for the real atmosphere exist, it is apparent that such scattering is wavelength dependent with large forward scattering effects, i.e., bright horizons decreasing in intensity with decreasing solar zenith angle. A clear atmosphere itself would contribute approximately 7% to the earth's albedo.

Although the main factors determining the nonhomogeneity of the earth are clouds, land, and sea areas, it is possible that differences in aerosol content from one part of the atmosphere to another also contribute to this characteristic.

The nondiffuse nature of reflectance of the earth's surface features and clouds will be somewhat modified by the passage of the reflected radiation through the atmosphere. In addition, the atmospheric scattering will add to the nondiffuse nature because of the basic nonisotropic nature of the scattering process.

TABLE 5

SUMMARY OF DATA FOR MOLECULAR AND AEROSOL SCATTERING

	Spectral Characteristics	Angular Distribution	Total Radiation Scattered Back Out into Space
Molecular Scattering	λ^{-4} Law (blue earth)	1. Forward and backscattering producing bright horizons. 2. Brightness of horizon decreases with increasing zenith angle.	Contribution to earth's albedo of about 7%
Aerosol Scattering	Wavelength dependence not as strong as for molecular scattering	Very strong forward scattering.	

The spectral dependence of the reflectance of earth surface features will be combined with the spectral dependence of the scattering processes to determine the overall spectral albedo of the earth.

F. ESTIMATES OF EARTH'S ALBEDO[71-87]

The information discussed above, the measurements of earthlight reflected from the moon, the satellite and spacecraft measurements of reflected solar radiation, the reflectance of earth's surface features, and the scattering of solar radiation by air molecules, aerosols and clouds, all contribute to our knowledge of the nature of the earth's albedo, however, they do not serve to precisely define its value.

Attempts to synthesize available information into an average value of earth's albedo have been made by meteorologists interested in the heat valance of the earth. Details of some of these are contained in Appendix F. Table 6, taken from Angstrom,[13] with London's data added,[71] summarizes these attempts. Note that modern estimates of earth's albedo (since 1948) fall in the range of 0.33-0.38, compared with values estimated from satellite and spacecraft measurements of 0.32-0.35.

G. DISCUSSION: MODELS OF THE EARTH FOR ALBEDO PURPOSES

It is apparent from the above summary, that several models of the earth are being used for albedo purposes. Astronomers use a model which differs from that of meteorologists. Spacecraft experimenters use a still different model.

The measurements of the astronomers are interpreted in terms of Bond's definition of planetary albedo. Photometric (visible) albedo only is discussed. This definition assumes that the earth has a homogeneous surface with perfectly diffuse reflectance; however, the phase function ob-

TABLE 6

SUMMARY OF EARTH ALBEDO ESTIMATES

Author	Year	Clouds	Ground + Atmosphere	Planetary Albedo	Photometric Albedo
Abbot & Fowle[72]	1908	0.65		0.37	
Aldrich[50]	1919	0.78	0.17	0.43	
Simpson[73]	1928	0.74	0.17	0.43	
Baur & Philips[74]	1934	0.72	0.085	0.415	
Fritz[75]	1948	0.47-0.52	0.17	0.347	0.39[a]
Houghton[76]	1954	0.55	0.135	0.34	
London[71]	1957	0.50	0.134-0.173	0.35	
Angström I[13]	1962	0.46	0.195	0.33	0.39[a]
Angström II[13]	1962	0.55	0.195	0.38	0.43

[a]Danjon later changed this value to 0.40.

tained and the diurnal and seasonal variations noted are not consistent with this assumption.

The model of the earth considered by meteorologists considers only meridional variations. Equatorial symmetry is assumed on a yearly average basis. Seasonal variations are considered but diurnal and yearly variations are not.

The satellite measurements of House[2] and Bandeen[1] used the meteorologists model having meridional variations only, with the additional assumption of diffuse reflectance. Seasonal variations were noted.

It seems to be quite obvious that a more precise model of the earth should be used for albedo purposes. This model should allow for diurnal seasonal and annual variations, and should consider the spectrally dependent nondiffuse nature of the reflectance and scattering of solar radiation by the earth and its atmosphere.

Additional new data, obtained on high altitude balloon flights, demonstrating the nonisotropic nature of the earth's reflectance will be presented in the next section. Finally the nature of a precise model of the earth for albedo purposes will be indicated.

IV. BALLOON FLIGHT MEASUREMENTS OF EARTH REFLECTANCE

A. INTRODUCTORY NOTES

Radiometers of the same type as the five channel radiometers flown on the TIROS and NIMBUS satellites have been flown on a series of high altitude balloon flights by members of The University of Michigan's High Altitude Engineering Laboratory, as a part of a research and development program in support of the NASA Goddard Space Flight Center's (GSFC) Meteorological Satellite Program.

The philosophy of this ballon flight test program is the following. Perhaps the most important factor in the interpretation of the data measured by a radiometer (actually any instrument used for scientific data gathering) is an intimate detailed knowledge of its operational characteristics, a thorough understanding of which is best obtained by frequent, careful calibrations. Ideally, the calibrations would be made under the same environmental conditions as experienced by the instrument when it is used for data taking, i.e., for these radiometers, under near space conditions. Also, it is desirable to make calibrations both before and after flight data are obtained, and indeed, if possible, during the flight. This was not possible for the satellite-borne radiometers during the early phases of the meteorological satellite program and accordingly, the balloon flight program was initiated for this purpose.

The TIROS five-channel radiometer 103A and the NIMBUS MRIR F-1 and F-4 radiometers have been flown a number of times on high altitude balloon flight tests. The results of an extensive series of calibrations of the visible channels of these instruments are discussed in technical reports.[27,88]

Additional benefits have been obtained on those occasions when measurements were made simultaneously by instruments on the balloon and by similar measurements on a satellite orbiting overhead, since a comparison of balloon and satellite measurements can help in the interpretation of the satellite measurements. Some of these results have also been reported.[22,89]

Finally, the radiation measurements made by these instruments are of great interest in themselves for what they tell us about atmospheric radiation processes. Of particular interest for this paper are the measurements of scattered and reflected solar radiation which help to show the nonhomogeneous nature of the earth as a reflector of solar radiation and also show the nonisotropic wavelength dependent nature of the reflectance of the earth's atmosphere and surface.

The data that will be presented was obtained on three balloon flights. The dates of these flights and the radiometers used for the measurements on these flights are:

2 June 1962	TIROS #103A Five-Channel Radiometer
26 June 1963	TIROS #103A Five-Channel Radiometer NIMBUS F-1 MRIR
10 March 1965	NIMBUS F-4 MRIR

B. THE BALLOON FLIGHT MEASUREMENT SYSTEM

A typical balloon flight configuration for the radiometer test flights is shown in Figure 7. The gondola which carries the radiation measuring instruments hangs at the end of a long load line, the length, ℓ, of which is determined by the requirement that the sun shine directly on the gondola at all times of the flight. Thus the length used is slightly greater than the value of ℓ given by:

$$\frac{r}{\ell+h} = \tan\theta_s \text{ (min)}$$

where θ_s(min) is the zenith angle of the sun at local noon. Typical values of r, h and ℓ which have been used are 100, 92, and 250 feet, respectively. In addition to the payload recovery parachute and flashing red light shown in the figure, other balloon control equipment may be hung on the load line. The radiometers, power supplies, control devices, auxiliary measuring sensors, and telemetry equipment are carried in the gondola.

Figure 8 is a photograph of the balloon gondola used on the 2 June 1962 balloon flight, shown suspended from the back of the launching truck. The TIROS five-channel radiometer projects from the balloon gondola on the left and a 70 mm aerial camera, boresighted with the radiometer, is on the right. Another 70 mm camera, looking vertically downward, is in the front of the gondola.

The TIROS radiometer and its associated camera were mounted on the ends of a horizontal shaft. When the shaft was rotated, the field of view of the radiometer and camera moved in a conical scan (60° cone half angle) across the surface of the earth from horizon to horizon.

At the top of the gondola was a circular ring with a set of photocells for the measurement of the azimuth of the shaft with respect to the sun. The sun's azimuth and elevation are known accurately as a function of time.

The geometry of the radiation measurements is exactly that shown in Figure 1, so that when measurements are made, information about bi-directional reflectance patterns, or scattering patterns, is obtained.

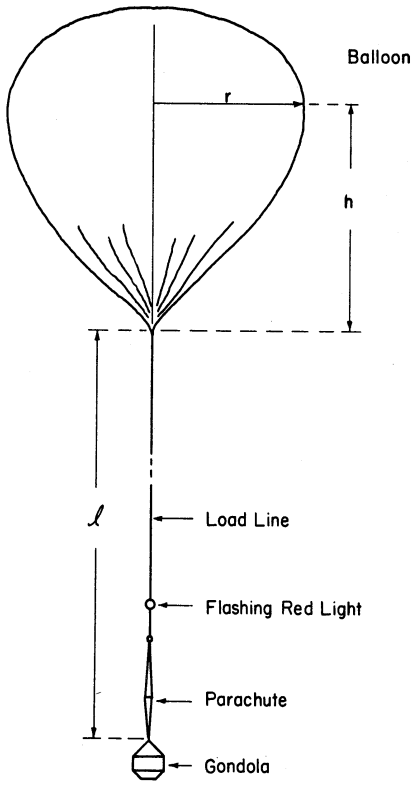

Figure 7. Balloon flight configuration.

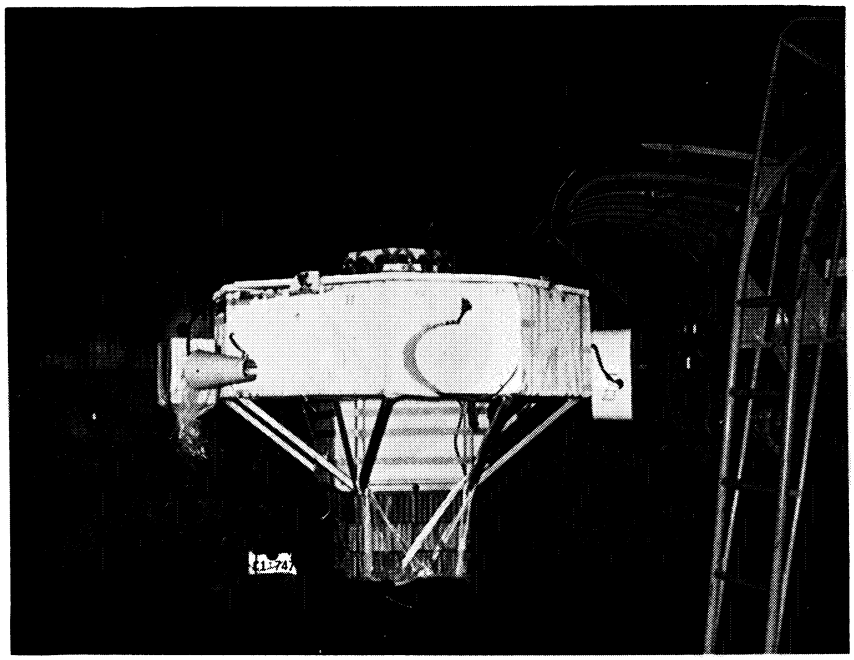

Figure 8. Balloon gondola used on 2 June, 1962 balloon flight.

The instrument arrangements for the other balloon flights was similar to that shown in Figure 8. When the NIMBUS MRIR was used, it was mounted on the gondola in such a fashion that, with a motionless gondola, it would scan the earth from horizon to horizon, in a vertical plane. When the gondola rotates, its azimuth data must be considered in the calculation of reflectance and scattering patterns.

The balloon gondola does not hang vertically beneath the balloon during the ascent portion of the flight. However as it approaches its float altitude and begins to move with the wind, it assumes a position vertically beneath the balloon and provided its suspension system has been adjusted properly, a well defined coordinate system is obtained.

An FM-FM telemetry system was used to transmit data to a mobile telemetry ground station. The airborne portion of the system consists of up to about 12 voltage controlled oscillators, a mixing amplifier, a two watt transmitter and a crossed dipole antenna system. The telemetry ground station is built into a bus. Antennas and a pre-amplifier are located on the roof of the bus, and receivers, FM discriminators, direct writing recorders, tape recorders, A-D conversion equipment with paper tape punch and flexowriter print out, WWV receiver, and standard time code generator are located inside of the bus. The airborne unit and ground station are shown in Figures 9 and 10 respectively.

The airborne antenna is mounted in a horizontal plane, beneath a horizontal reflector, under the balloon gondola and radiates quite uniformly in all directions below and to the side of the balloon gondola. The maximum range of the telemetry is determined by the horizon as viewed from the gondola. When the balloon is at 115000 feet altitude,

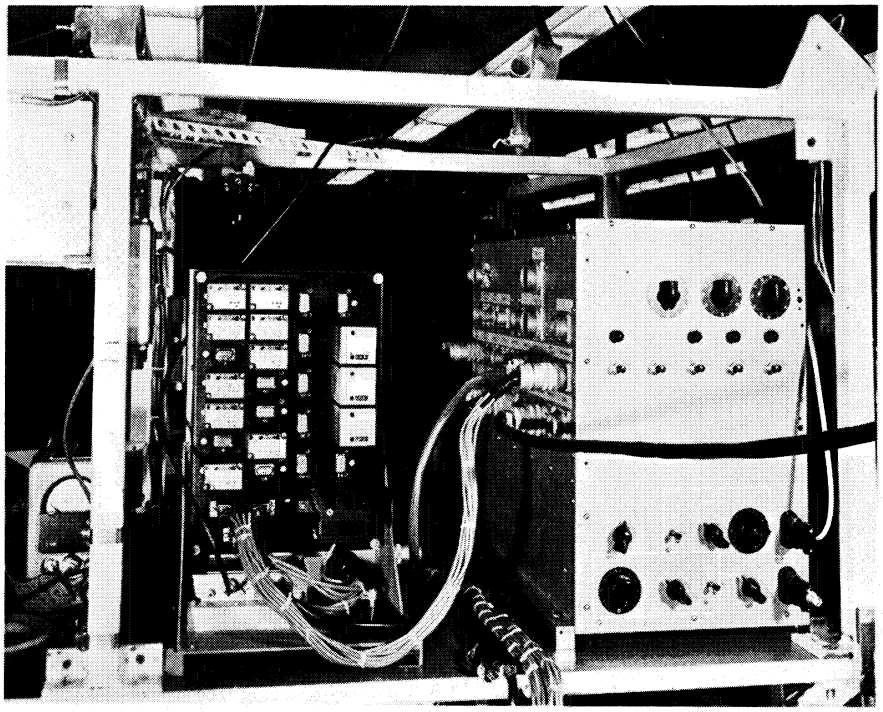

Figure 9. Photograph of airborne telemetry unit and equipment programming unit.

the horizon is about 425 miles away. With the ground station built into a bus, the length of a flight, for which data can be received, is increased by moving the bus along the road in the same direction as the balloon is traveling. Data can be received and recorded without difficulty as the bus moves over modern roads at speeds up to 50 mph. When the bus is moving, a corner reflector, steerable in azimuth from inside the bus, is used. When the bus is standing still, a bifilar helical antennae can be used on top of the bus.

The accuracy of the telemetry system is about 0.5% of full scale for low frequency signals of the radiometer type. This accuracy is checked and maintained by two independent 5-point calibration units with which the telemetry system is calibrated at 5-minute intervals before, after, and throughout the flight. This 0.5% accuracy in the telemetry

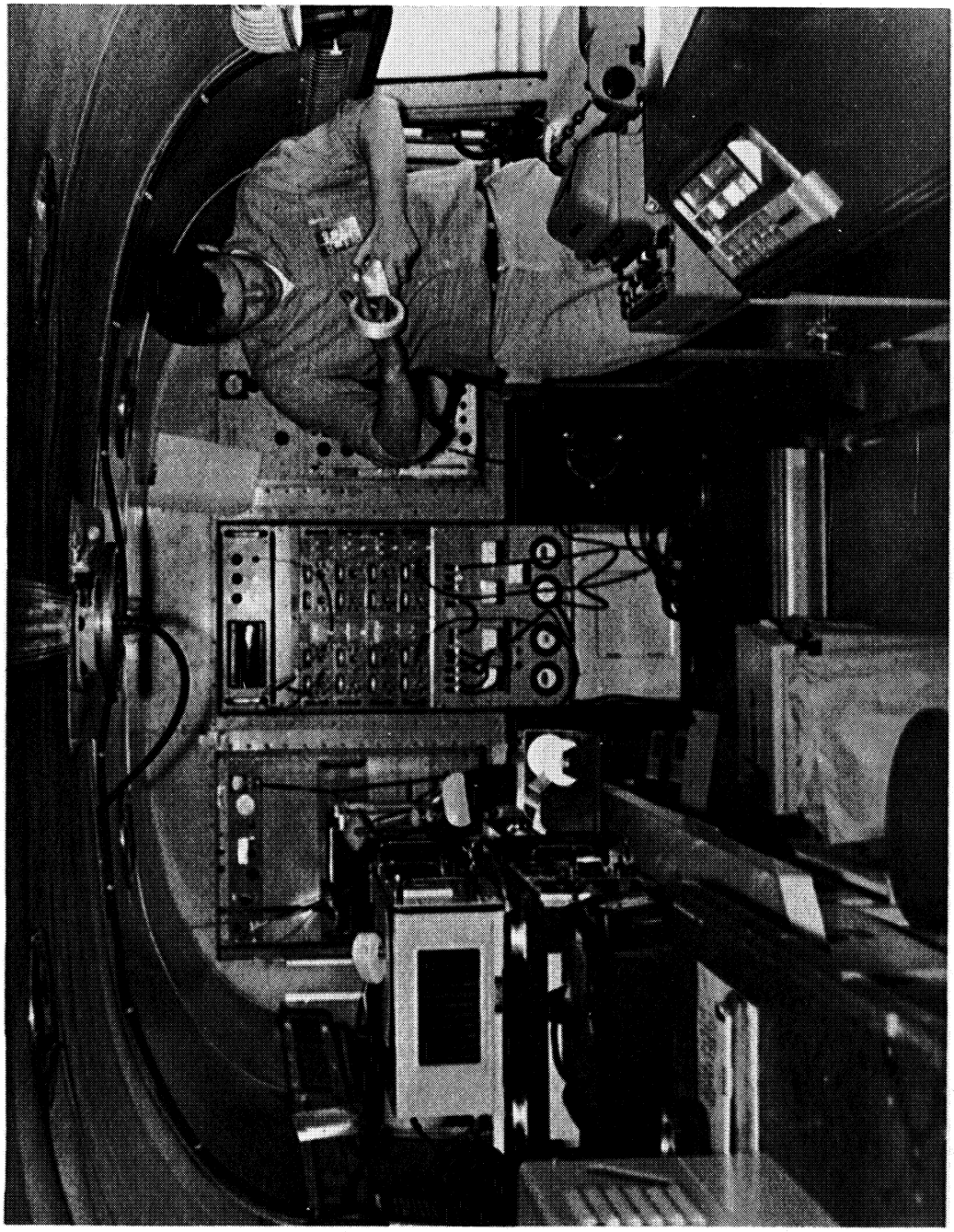

Figure 10. Inside mobile telemetry ground station.

is better than the accuracy of calibration of the radiometer and thus does not significantly limit the data accuracy.

An electrical control system for equipment on the balloon gondola, deriving a program of electrical signals for operation of all equipment on the gondola from a basic timing unit, is also carried on the gondola. One of these systems is also shown in Figure 9. A typical flight program is outlined schematically in Figure 11. The time sharing of signals on each telemetry channel is indicated. Housekeeping functions which are monitored are indicated in the lower portion of the figure.

The basic power supply for the balloon gondola is a number of sets of Yardney silver cell batteries, with solid state voltage regulators where necessary. The mobile telemetry ground station has two 5 kw, gasoline motor driven 60-cycle generators. Commercial power can be used when the bus is standing still.

C. RADIOMETER MEASUREMENTS: CALIBRATION AND INTERPRETATION

1. Calibration of the Radiometers

The method of calibrating the TIROS and NIMBUS medium resolution radiometers is discussed in Appendix B. A calibration curve is made from pairs of values of radiometer output voltage, V_c, and values of the effective radiance of the calibration source, N'_c, where:

$$N'_c = \int_0^\infty N_{c\lambda} \phi_\lambda \, d\lambda$$

Usually, the interpretation of radiometer voltage readings is made in terms of % reflectance

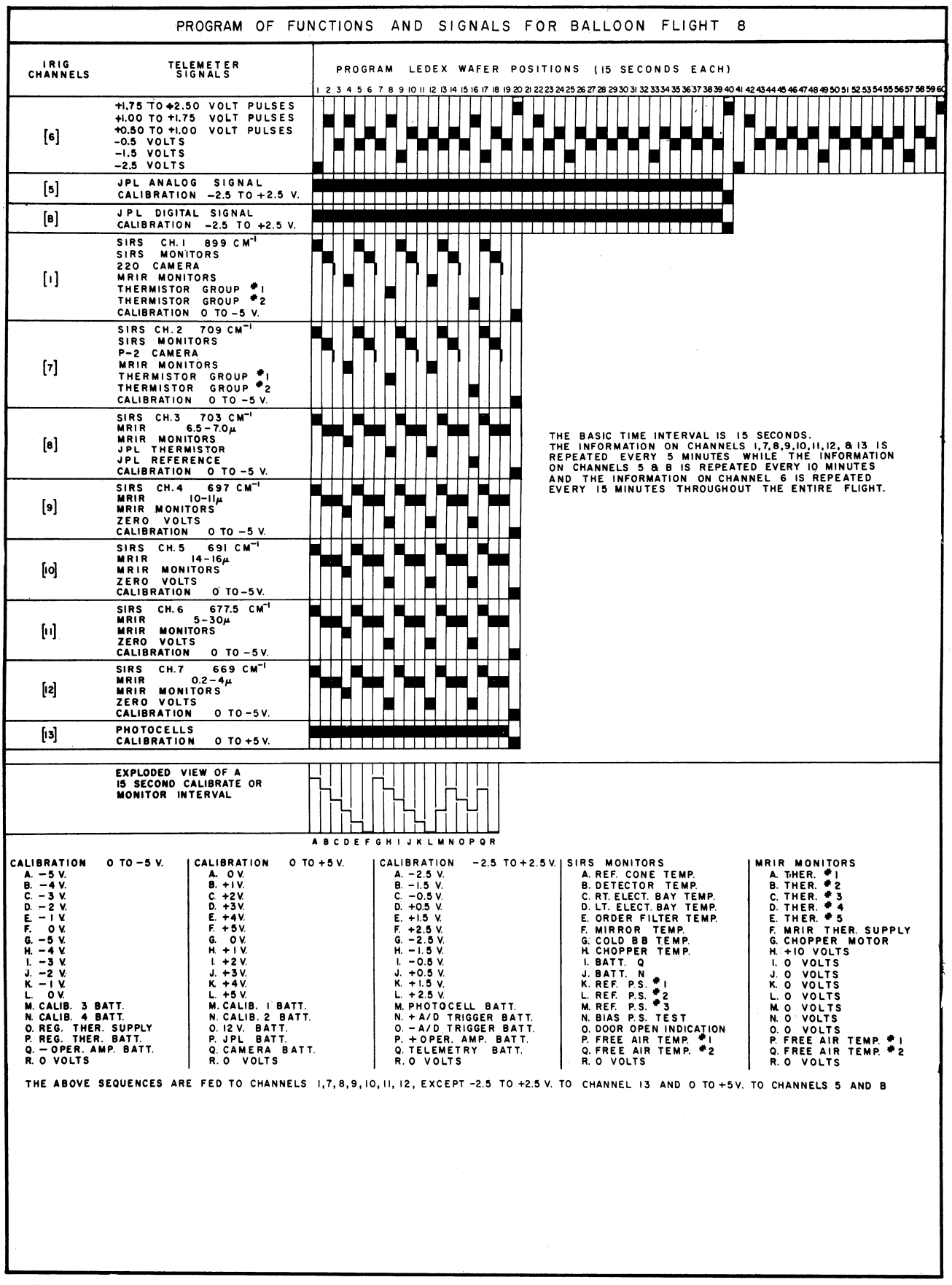

Figure 11. Instrument operation program for 10 March, 1965 balloon flight.

$$\rho' = \frac{N'_c}{N'_s(100\%)} = \frac{\int_0^\infty N_{c\lambda}\phi_\lambda d\lambda}{\frac{1}{\pi}\int_0^\infty H_{s\lambda}\phi_\lambda d\lambda} \qquad (33)$$

Thus it is necessary to know accurately the value of $N_{c\lambda}$ of the source over the spectral range of the channels (0.2-4.0 microns). In addition, the source should have uniform radiance $N_{c\lambda}$ over the entire area within the radiometer field of view. The intensity of the source should be variable in magnitude, so that values of N'_c covering the necessary range can be obtained. At any intensity setting, the source should be stable for a length of time suitable for the calibration.

The sources for the calibration of the visible channels of the three radiometers used for the balloon flight measurements are described in detail in technical reports.[27,88,90] The sources (a,b,c,d,e) are shown schematically in Figure 12.

Source a was developed at NASA GSFC for TIROS radiometer calibration. Source b is used at the Santa Barbara Research Center (SBRC) for NIMBUS MRIR calibrations. Sources c, d, and e have been used for calibrations at The University of Michigan, and represent a development sequence to arrive at the most suitable source e. The characteristics, advantages, and disadvantages of each source are given in the technical reports noted above.

Calibrations of each radiometer were carried out several times over a long interval of time during which the balloon flights were made. This calibration data is given in Figures 13 to 18.

Calibration curves for the TIROS radiometer #103A are shown in Figures 13 and 14. The data was taken at GSFC in 1961 and 1962 with source a, and at The University of Michigan in 1964 with source e.

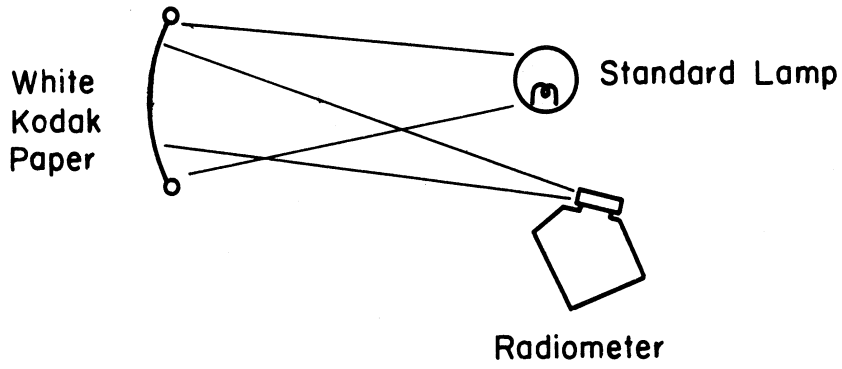

a.) GSFC CALIBRATION SOURCE

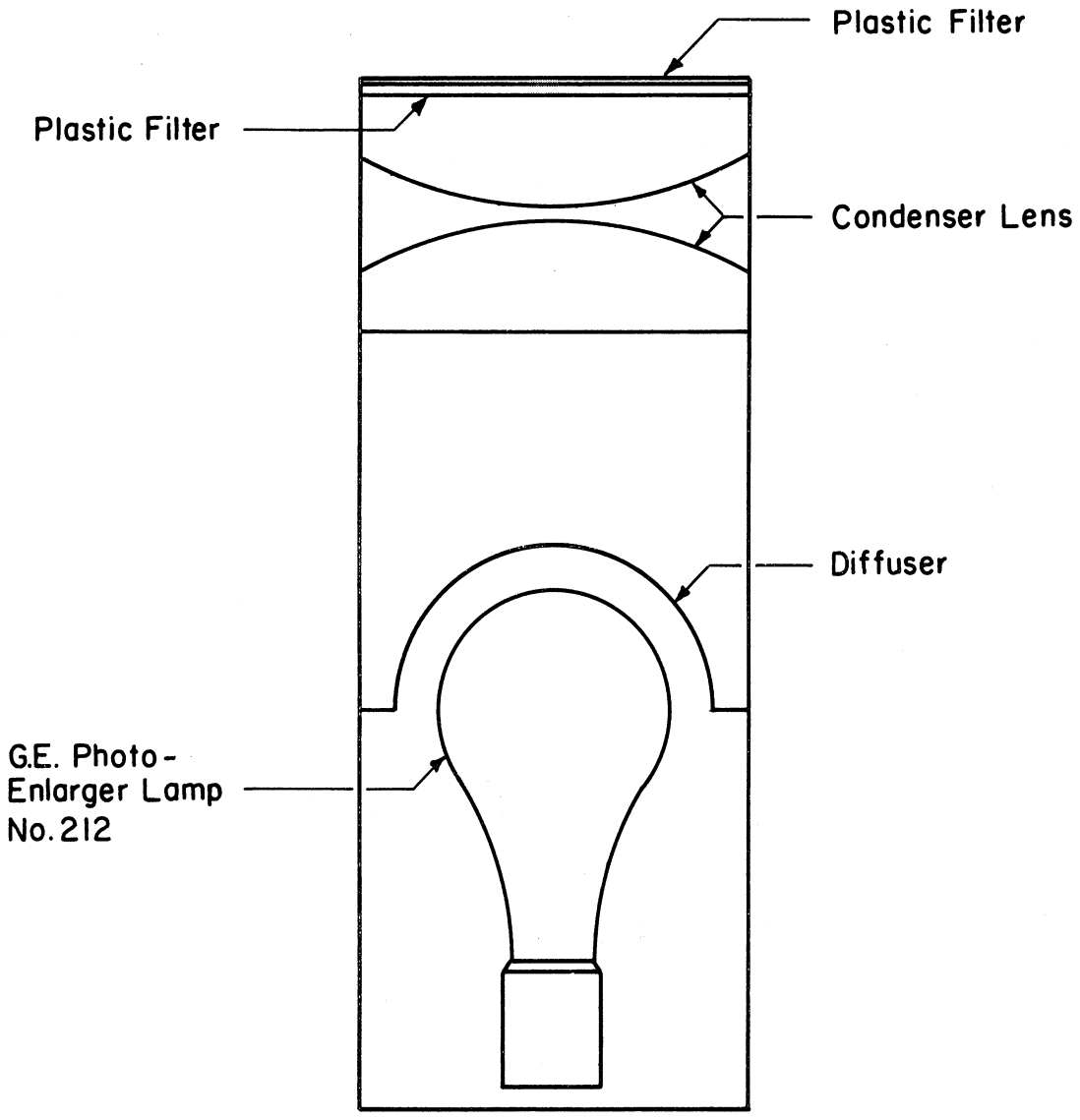

b.) SBRC CALIBRATION SOURCE

Figure 12. Calibration sources.

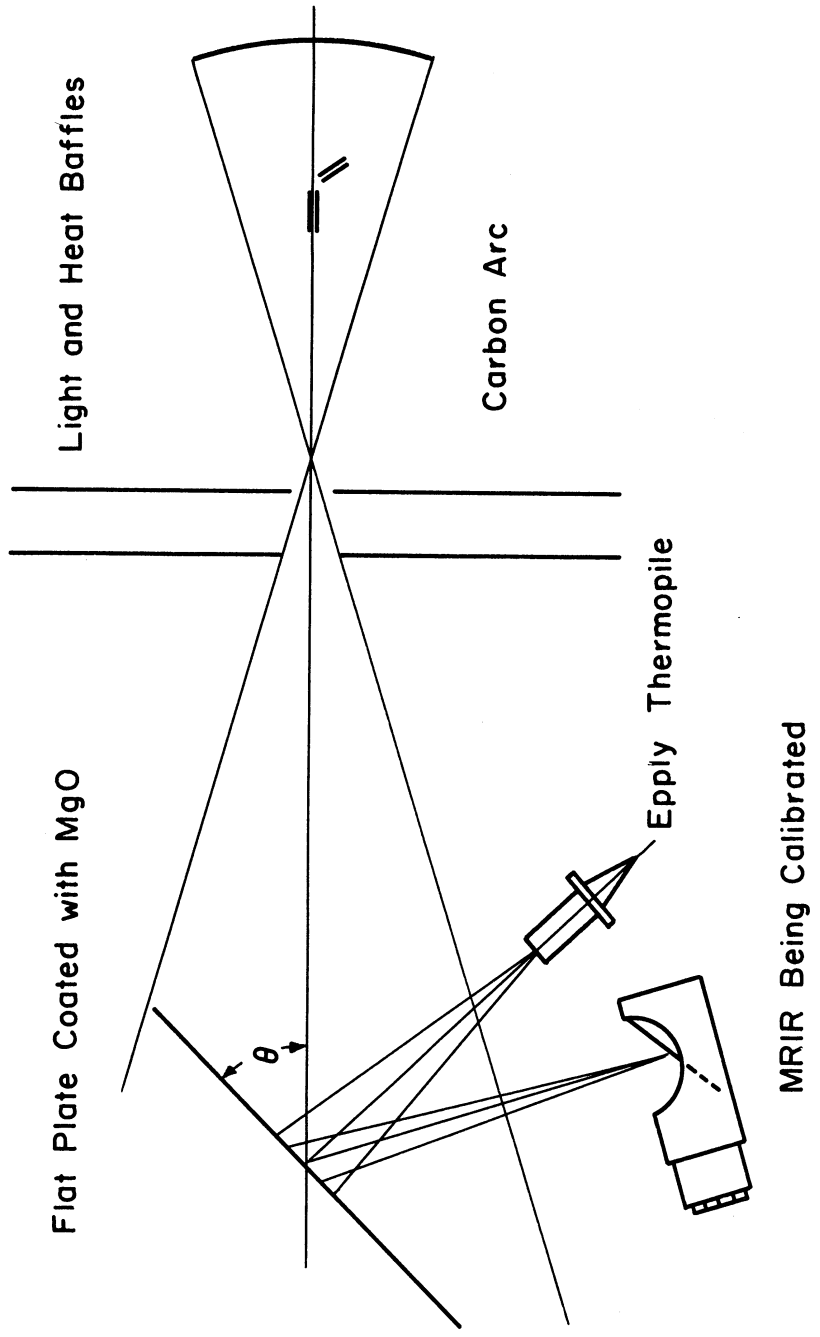

c.) CARBON ARC - MgO REFLECTOR CALIBRATION SOURCE.

Figure 12. Continued.

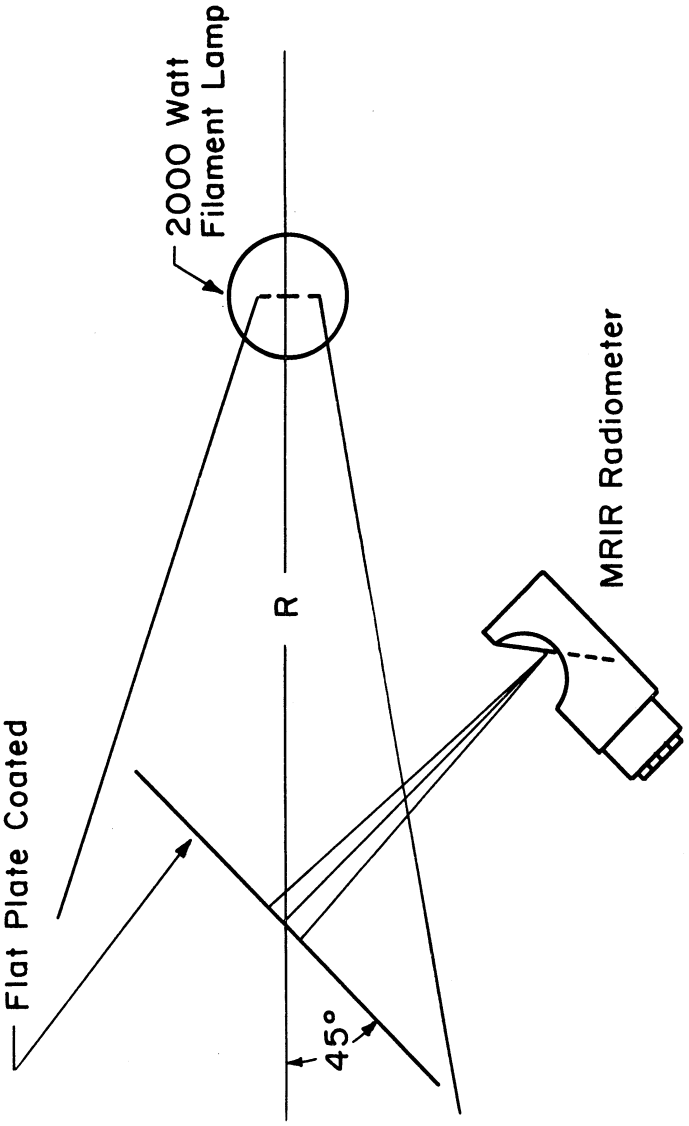

d.) TUNGSTEN FILAMENT LAMP-MgO REFLECTOR CALIBRATION SOURCE.

Figure 12. Continued.

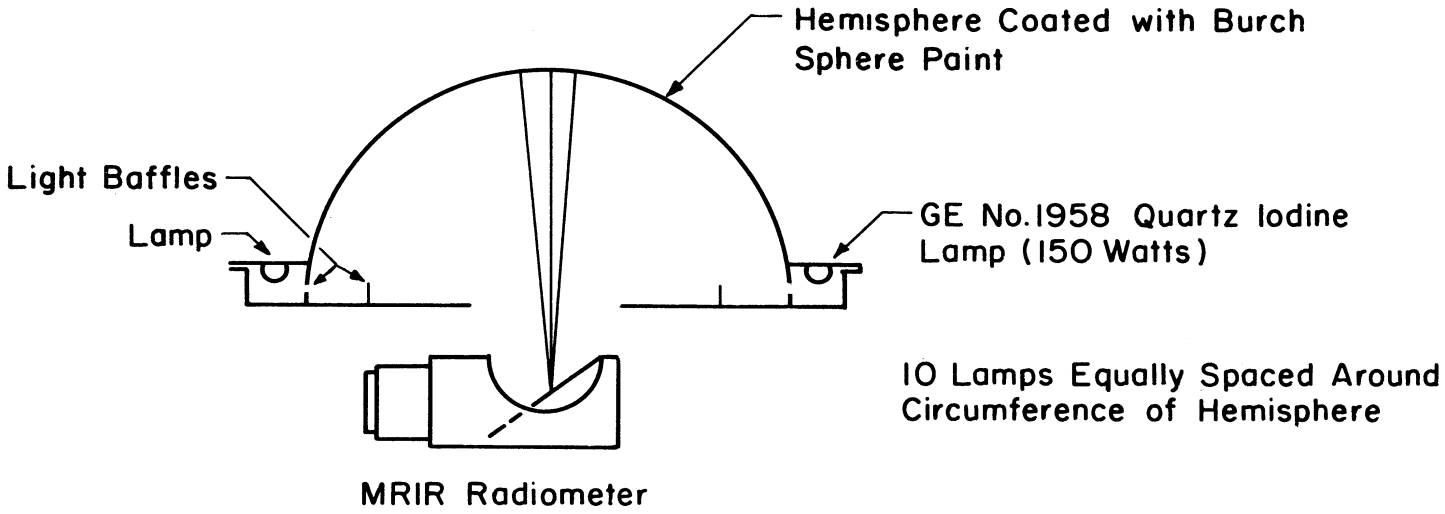

e.) HEMISPHERE SOURCE

Figure 12. Concluded.

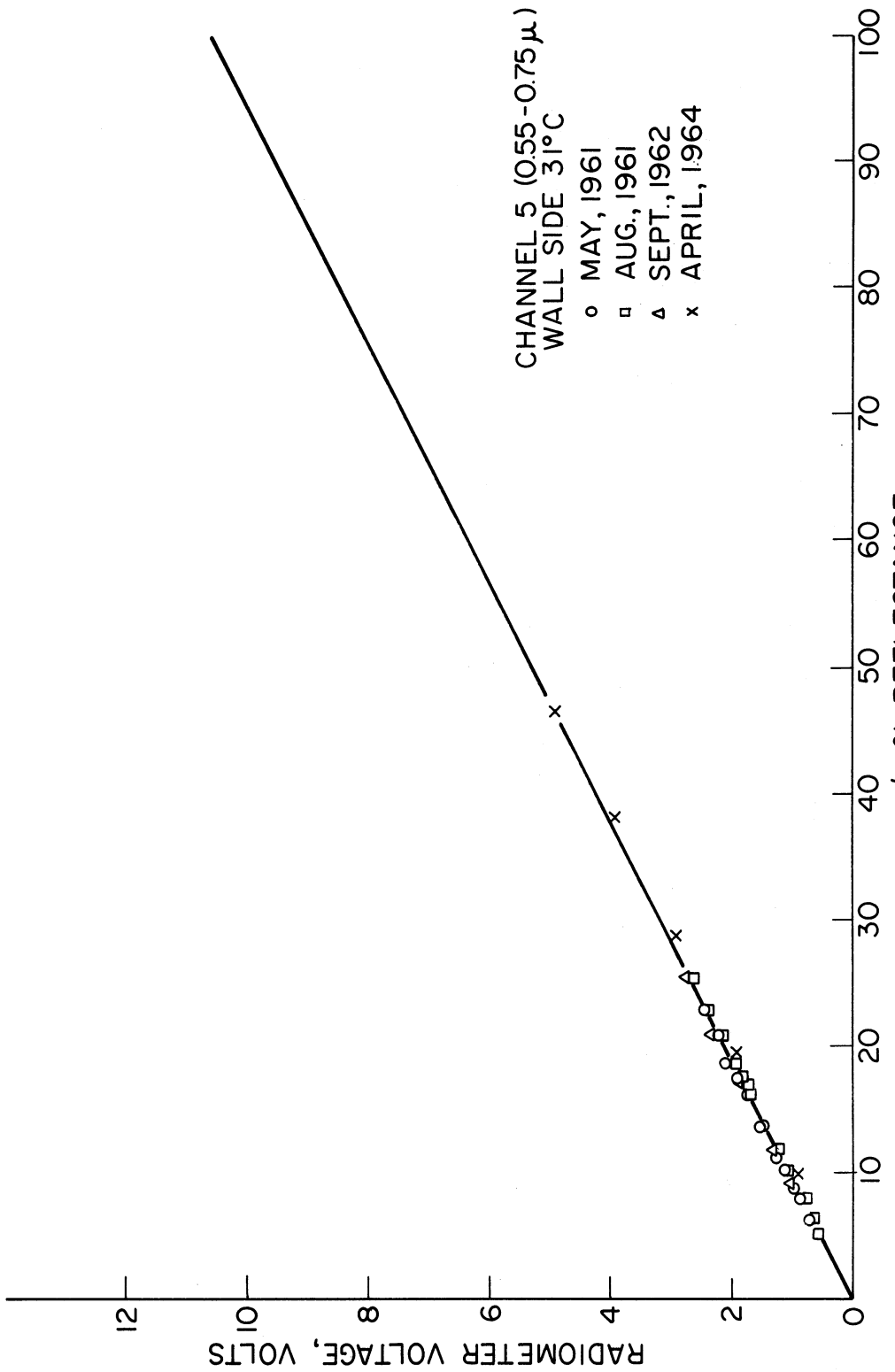

Figure 13. TIROS #103A radiometer channel 5 (0.55-0.75-micron) calibration curves.

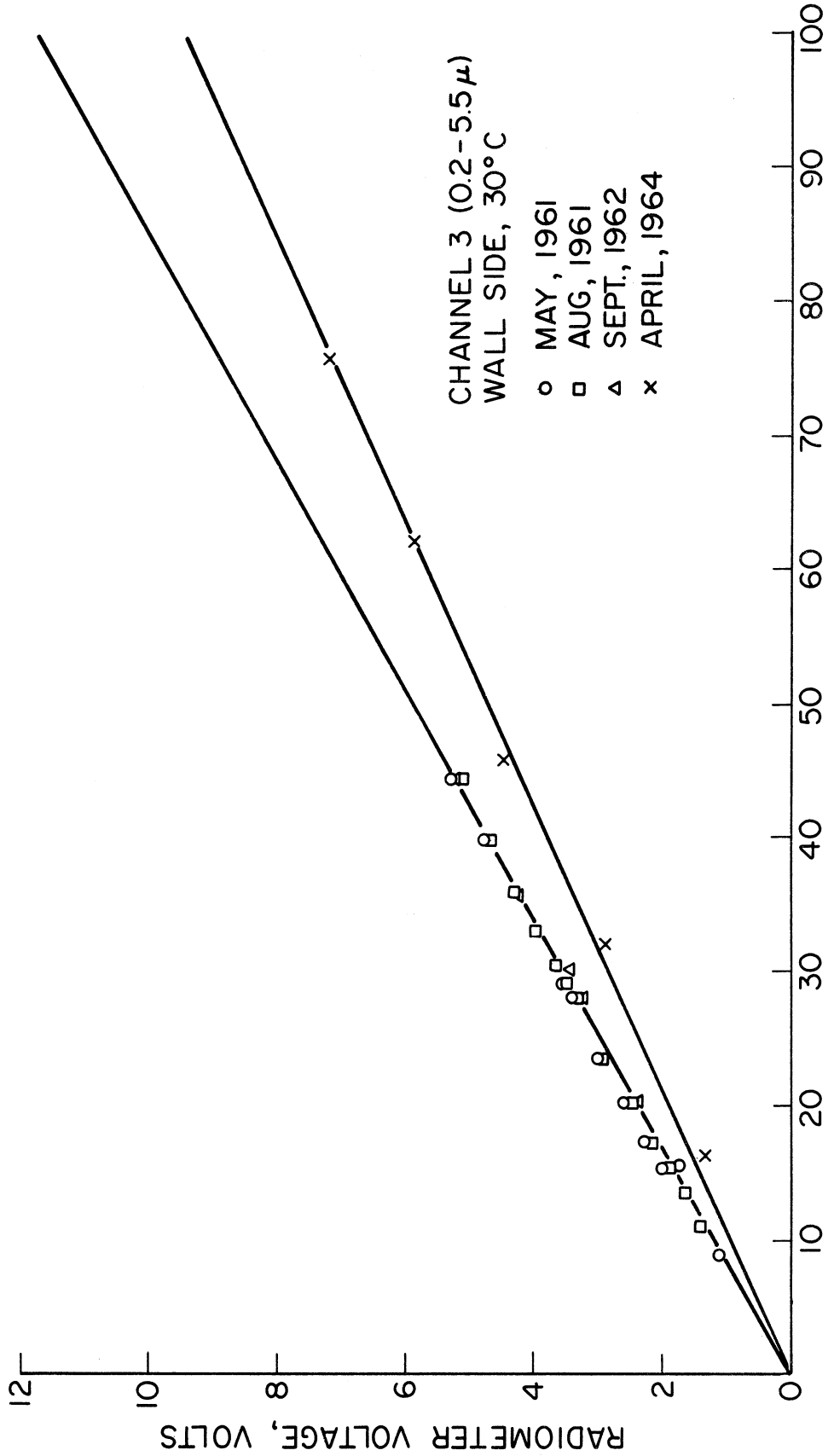

Figure 14. TIROS #103A radiometer channel 3 (0.2-5.5-micron) calibration curves.

All sets of data for the 0.55-0.75-micron channel (Figure 13) agree reasonably well. The calibration curve is extrapolated linearly above 46% reflectance. The 1964 University of Michigan data for the 0.2-5.5-micron channel (Figure 14) disagree with the data taken at GSFC in 1961 and 1962. The University of Michigan 1964 data are thought to be more reliable and have been used as for analyses of the 0.2-5.5-micron data. The reason for the discrepancy in the two sets of calibrations may be due to uncertainties in the reflectance of the Kodak white paper in the GSFC calibration source.[90]

Calibration curves of the F-1 MRIR radiometer are shown in Figures 15 and 16. Calibrations were made over the time between November, 1962 through June, 1964. For the 0.55-0.85-micron channel no two calibrations agree. Inspection of the optics of the radiometer in June, 1964, showed that the filter for this channel had deteriorated badly.[91] The November 1962 calibration data was used for the analyses of data from this channel of this radiometer. It is reasonably close to average of all sets of calibration data. However, it should be kept in mind that the data from this channel of the F-1 radiometer may be in error because of the deterioration of the filter. Calibration curves for the 0.2-4.0-micron channel of this radiometer show excellent agreement. An average calibration curve was used.

Calibration curves for the 0.2-4.0-micron channel of the F-4 MRIR radiometer are shown in Figures 17 and 18. The SBRC data shown in Figure 17 are in agreement within the accuracy expected. The average of the 4 SBRC calibrations cannot be distinguished from the average of the three University of Michigan calibrations.

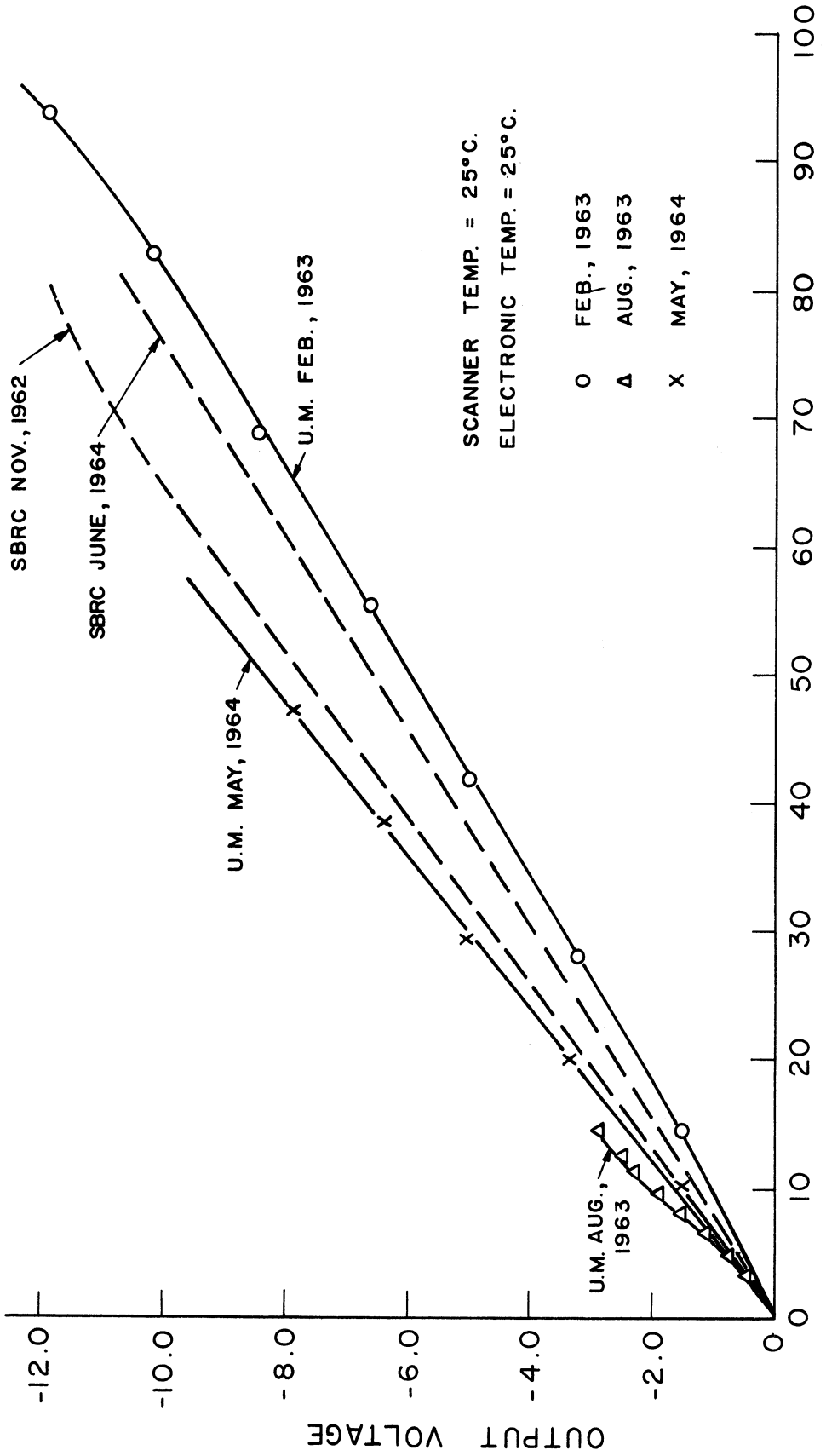

Figure 15. Calibration curves for 0.55-0.85-micron channel of F-1 MRIR radiometer.

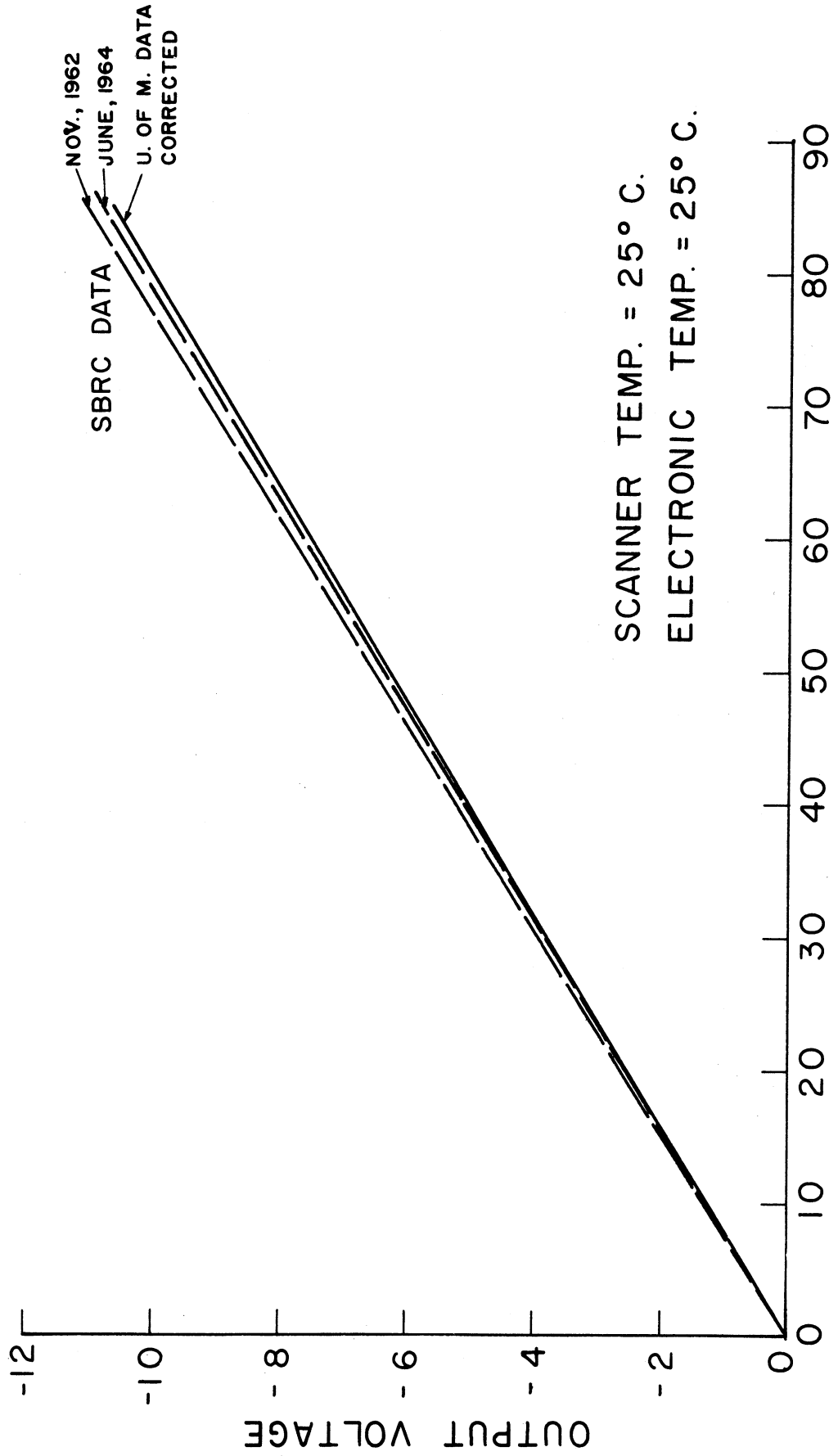

Figure 16. Calibration curves for 0.2-4.0-micron channel of F-1 MRIR radiometer.

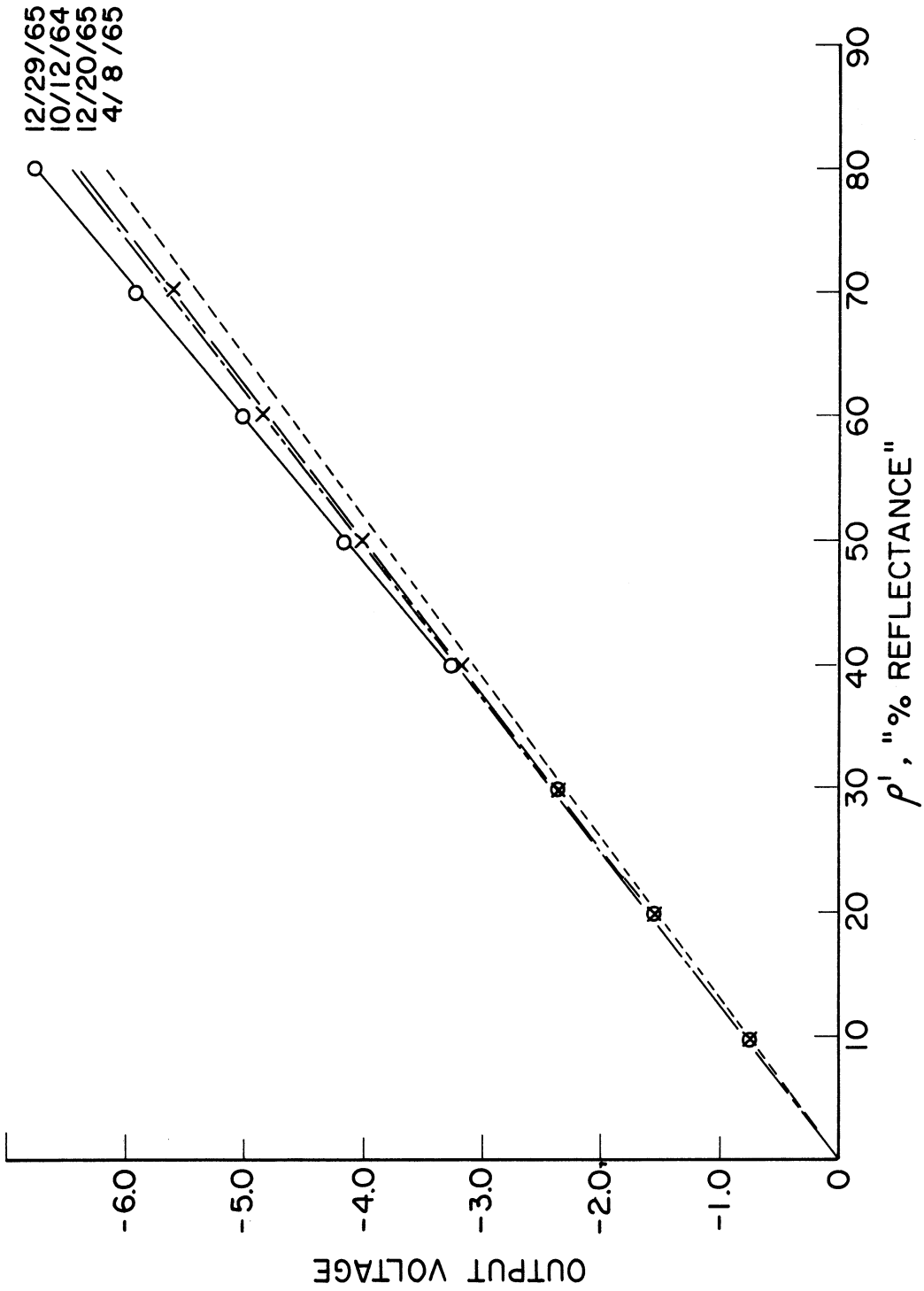

Figure 17. SBRC F-4 MRIR calibration, 0.2-4.0-micron channel.

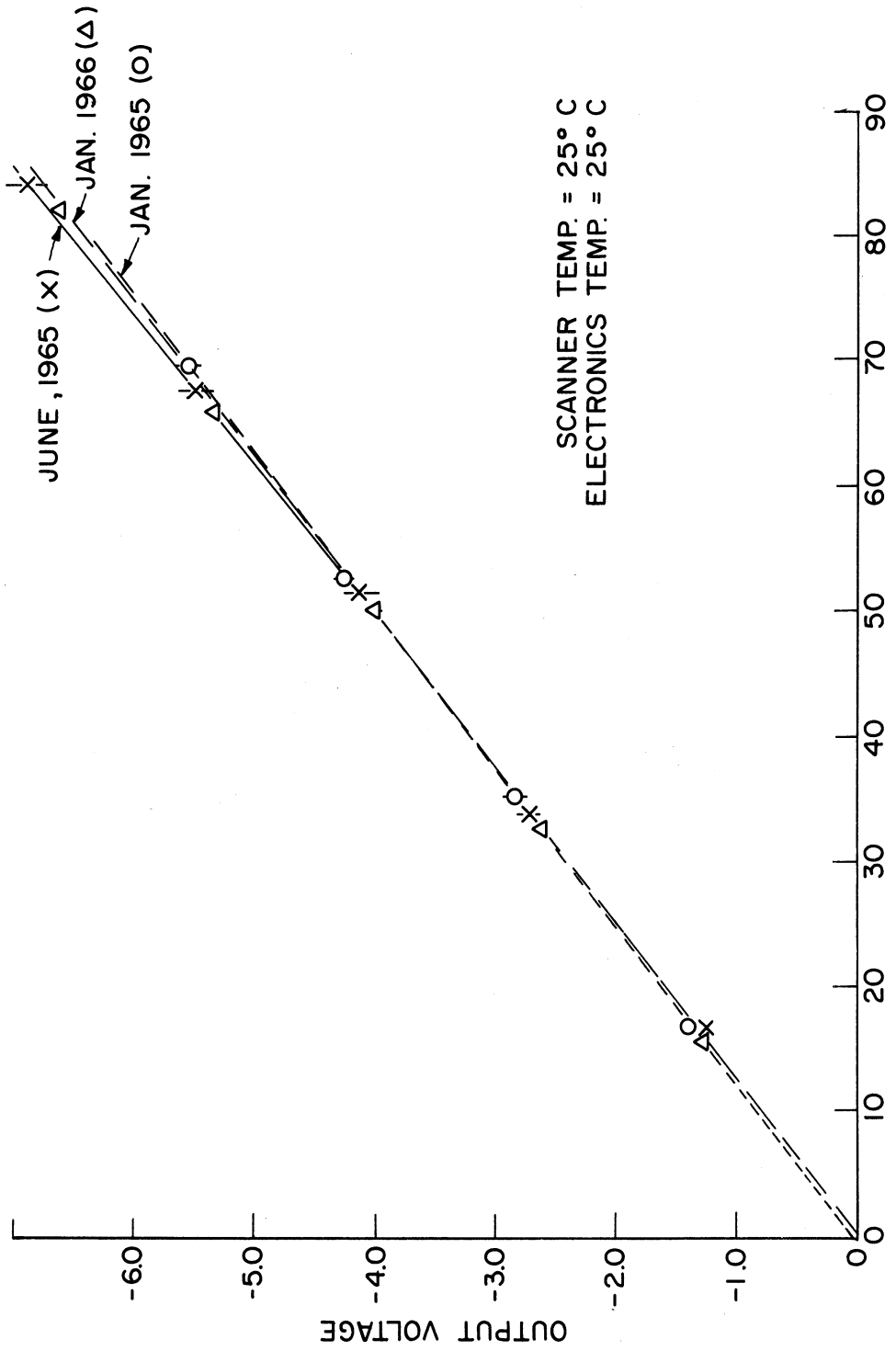

Figure 18. University of Michigan F-4 MRIR calibration data, 0.2-4.0-micron channel.

A discussion of the experimental errors which are possible in making the calibrations is contained in Reference 27. Although the precision should be 2% or better, possible systematic errors as large as 8% may exist because of inaccuracies in the secondary standard thermopiles used in the calibrations. In addition significant errors may arise in the interpretation of the radiometer data. This topic will be discussed next.

2. Interpretation of the Radiometer Data

The values of reflectance measured by the visible channels of the medium resolution radiometers differ from the actual earth reflectances which we desire to measure, as follows. Assuming normal incidence, we want to measure:

$$\rho = \frac{\frac{1}{\pi}\int_0^\infty \rho_\lambda H_{s\lambda}\, d\lambda}{\frac{1}{\pi}\int_0^\infty H_{s\lambda}\, d\lambda} \tag{34}$$

We actually measure:

$$\rho = \frac{\frac{1}{\pi}\int_0^\infty \rho_\lambda H_{s\lambda}\phi_\lambda d\lambda}{\frac{1}{\pi}\int_0^\infty H_{s\lambda}\phi_\lambda d\lambda} = \frac{\int_0^\infty N_{c\lambda}\phi_\lambda\, d\lambda}{\frac{1}{\pi}\int_0^\infty H_{s\lambda}\phi_\lambda d\lambda} \tag{35}$$

In addition to calibration errors, which relate to the substitution of

$$\int_0^\infty N_{c\lambda}\phi_\lambda\, d\lambda$$

for

$$\frac{1}{\pi}\int_0^\infty \rho_\lambda H_{s\lambda}\phi_\lambda\, d\lambda$$

We have the error in interpretation due to the fact that we have measured a weighted average reflectance using the weighting function $H_{s\lambda}\phi_{\lambda}$ instead of $H_{s\lambda}$.

Weighting functions for the visible channels of the TIROS #103A five channel radiometer and the F-1 and F-4 MRIR radiometers are shown in Figures 19 to 22.

The weighting functions of the narrow band channels emphasize the spectral range of 0.55 to 0.75 micron, see Figures 19 and 21, and especially the narrow band channel of the TIROS radiometer which places particularly great emphasis on the 0.58-0.60-micron region. It is apparent that the reflectances measured with these narrow band channels cannot be interpreted as total reflectances (i.e., over the 0.2-4.0-micron range), as was done by Bandeen.[1] Also it is apparent that different results may be obtained with the narrow band channels of the two types of radiometers because of the emphasis of the 0.58-0.60-micron region and the additional spectral region of response (1.2-2.8 microns) of the TIROS #103A radiometer.

The weighting functions for the wide band channels, which are shown in Figures 20 and 22, are similar to the function $H_{s\lambda}$. The weighting function of the NIMBUS F-4 MRIR places relatively greater emphasis on the $\lambda > 3$ micron region.

Finally, in regards to the interpretation of the radiometer data, it is important to keep in mind that the quantity measured is a bidirectional reflectance. The assumption that the surface is a diffuse reflector will often lead to error. It is absolutely necessary to make measurements at all angles of incidence and reflectance to correctly evaluate earth reflectance data.

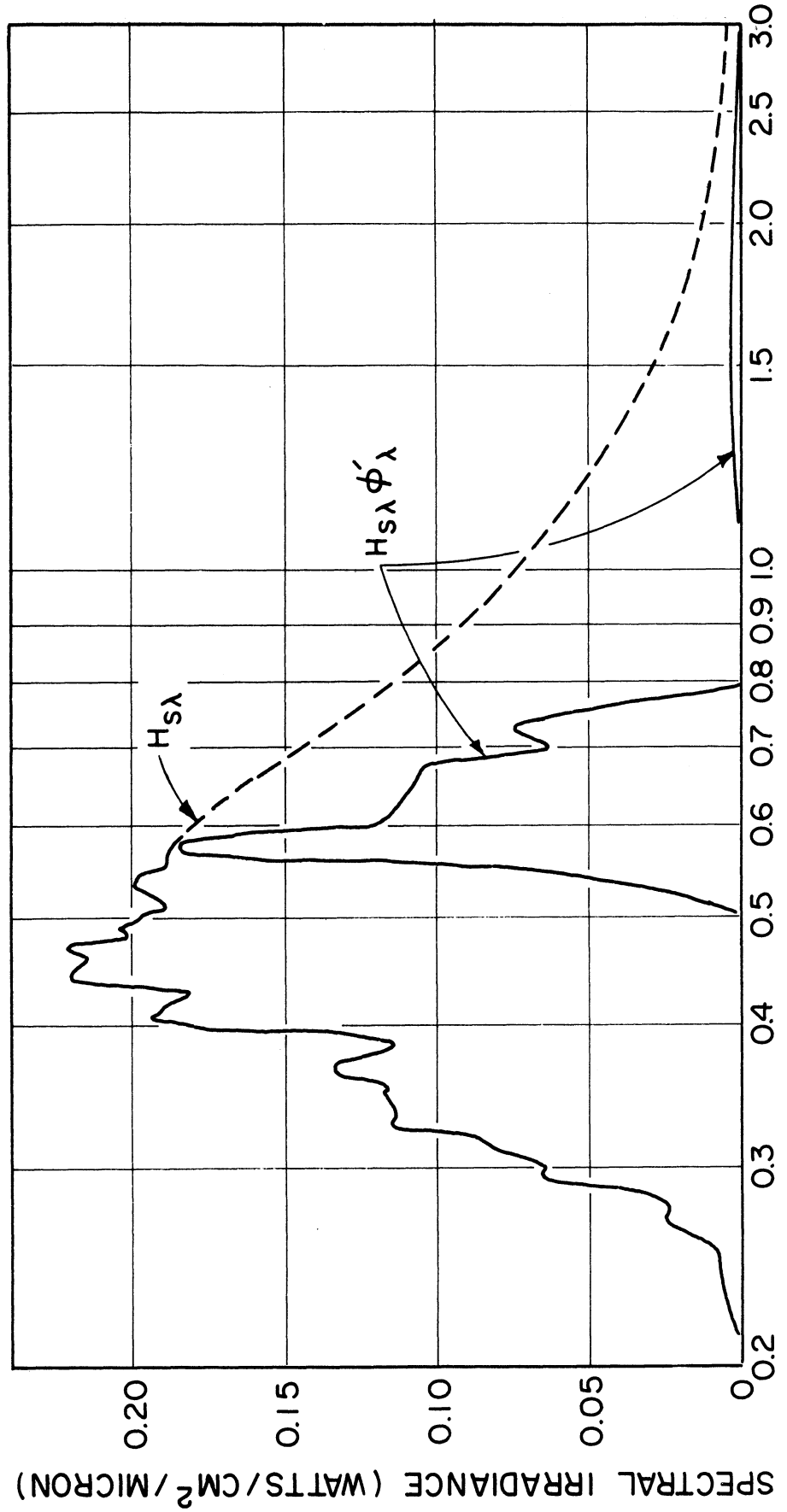

Figure 19. Weighting function, $H_{s\lambda}\phi'_{\lambda}$ for 0.55-0.75-micron channel of TIROS #103A radiometer.

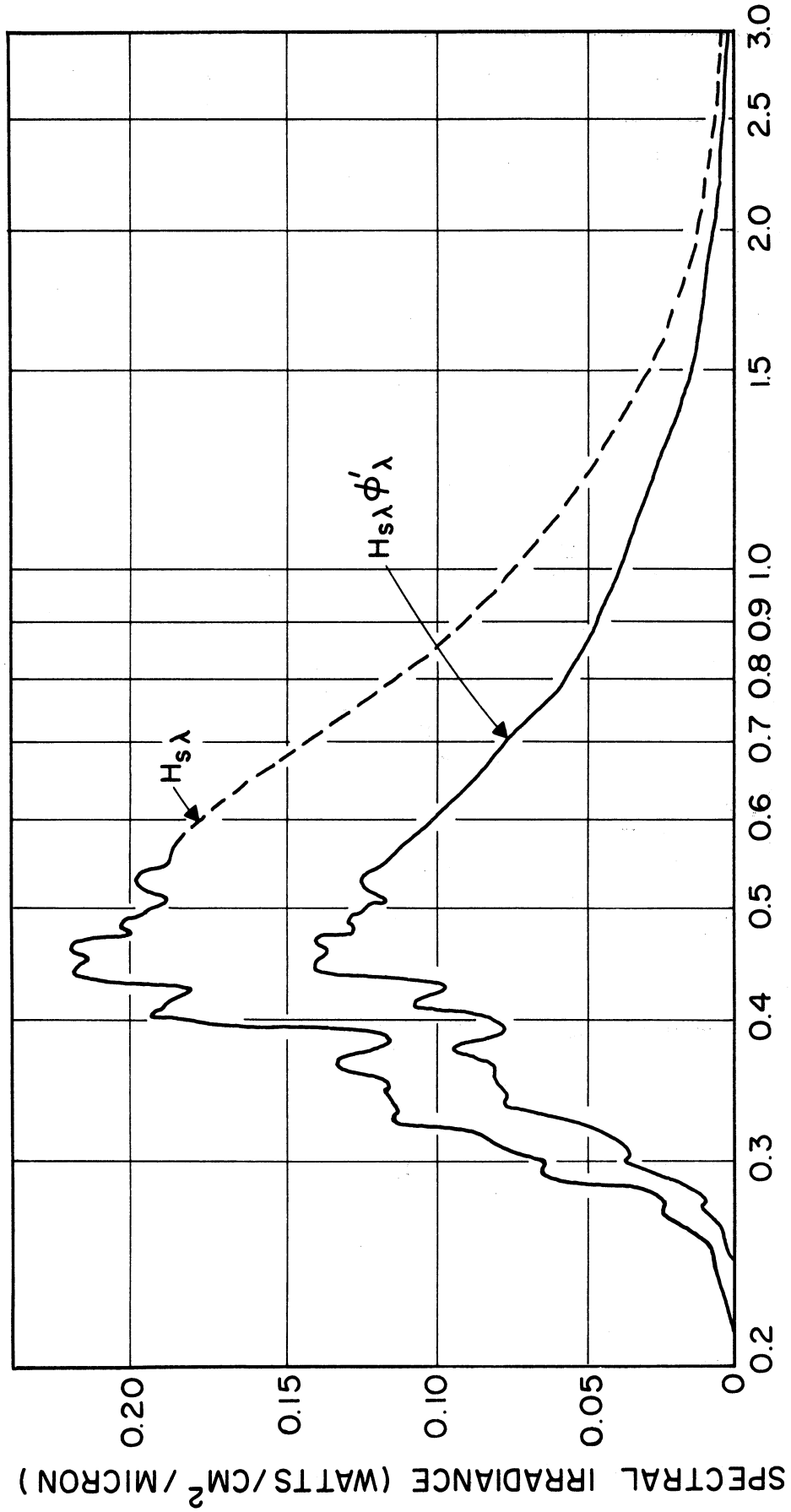

Figure 20. Weighting function, $H_{s\lambda}\phi'_{\lambda}$ for 0.2-6.0-micron channel of TIROS #103A radiometer.

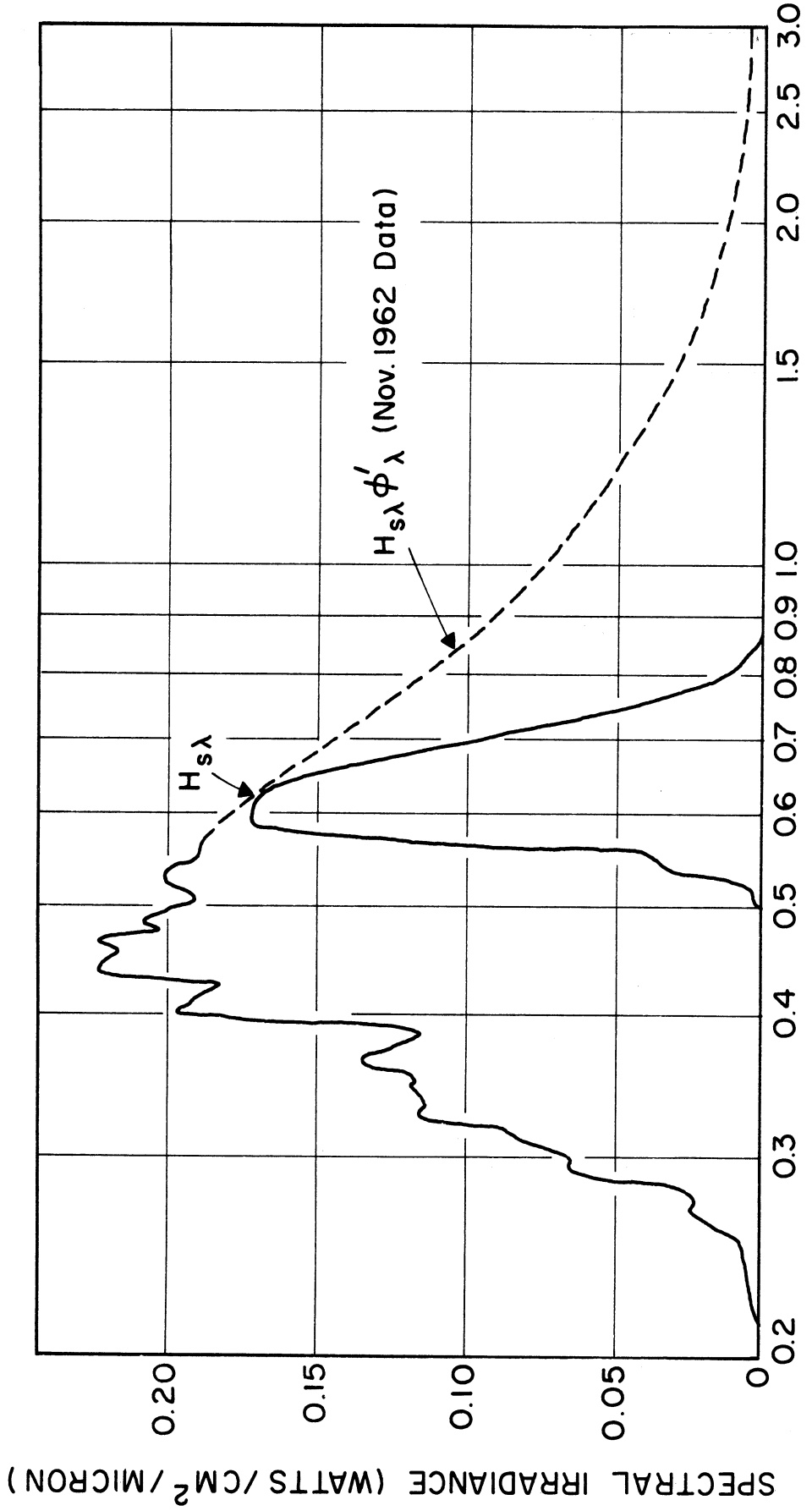

Figure 21. Weighting function, $H_{s\lambda}\phi'_{\lambda}$ for 0.55-0.85-micron channel of F-1 MRIR radiometer.

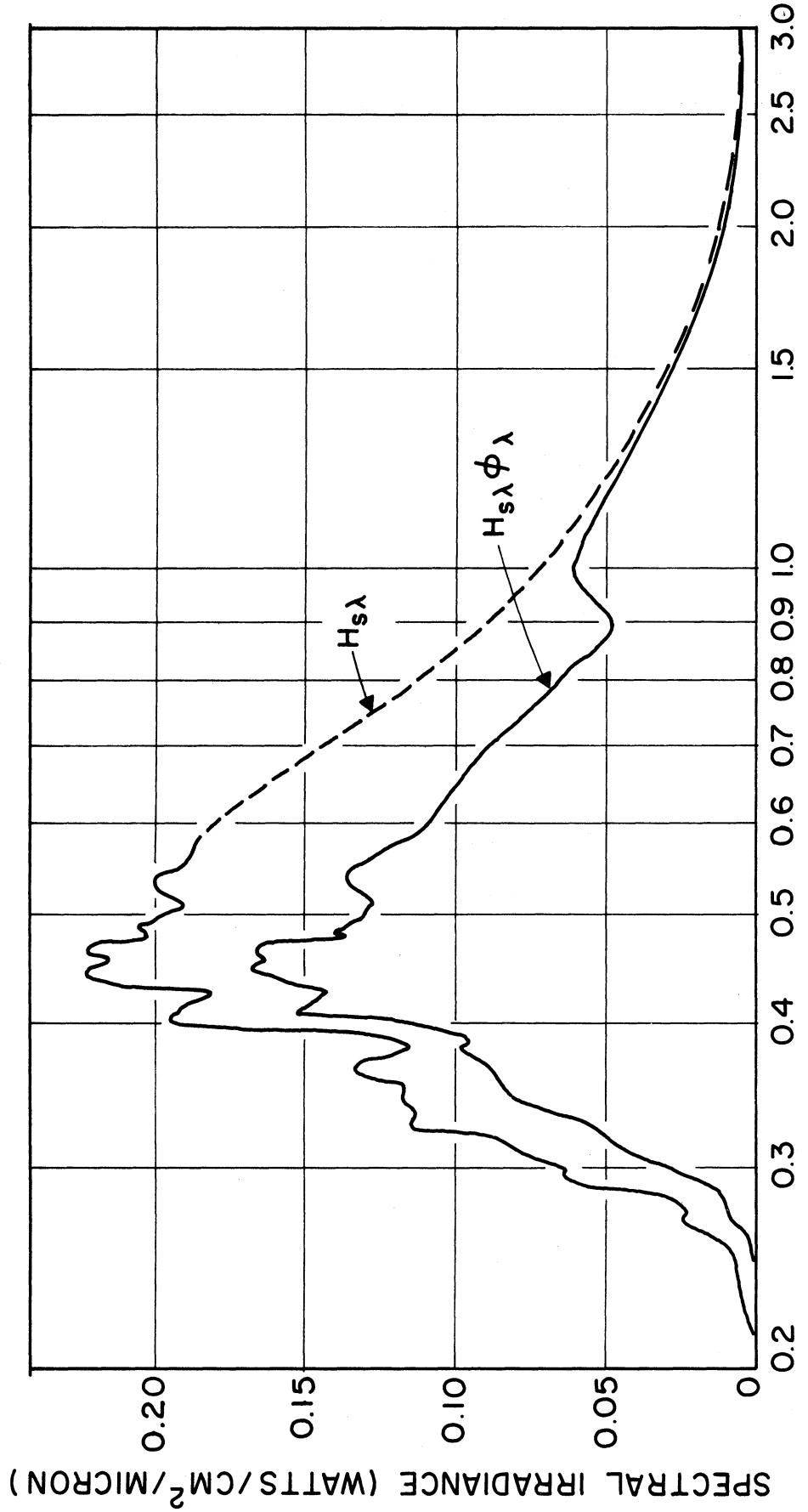

Figure 22. Weighting function, $H_{s\lambda}\phi'_{\lambda}$ for 0.2-4.0-micron channel of F-4 MRIR radiometer.

These two important factors connected with the interpretation of radiometer reflectance data will be discussed more completely in regard to the radiometer data taken on the high altitude balloon flights.

D. DATA OBTAINED ON THREE FLIGHTS

1. The 2 June, 1962 Balloon Flight

The 2 June, 1962 balloon flight was launched through a layer of low altitude clouds at 1034 GMT (0434 CST), from Sioux Falls, S. D. (43.4°N-96.7°W). It floated at an average altitude of 113000 feet (34 km) for about 13 hours above various types of cloud cover. The altitude vs. time curve and a trace of the balloon trajectory are shown in Figures 23 and 24. The flight was terminated at 0120 GMT, 3 June 1966; parachute recovery of the balloon gondola was successful.

The various types of cloud cover viewed by the radiometer on this flight are shown in the four pictures of Figure 25. A summary of the types of clouds viewed by the radiometer is given in Table 7. The reflectance data obtained is difficult to analyse when the clouds viewed are nonhomogeneous as in the last three cases of Table 7. It is only

TABLE 7

CLOUD COVER VIEWED BY RADIOMETER, 2 JUNE, 1962 BALLOON FLIGHT

Time, GMT	Cloud Type	Sun's Elevation Degree
1034-1300	Stratocumulous, 2000 ft thick tops at about 6000 ft	0-22
1300-1745	Cirrus above stratocumulous	22-68
1745-2000	Broken cumulus	68-56
2000-0100	Cirrus above scattered cumulus	56-10

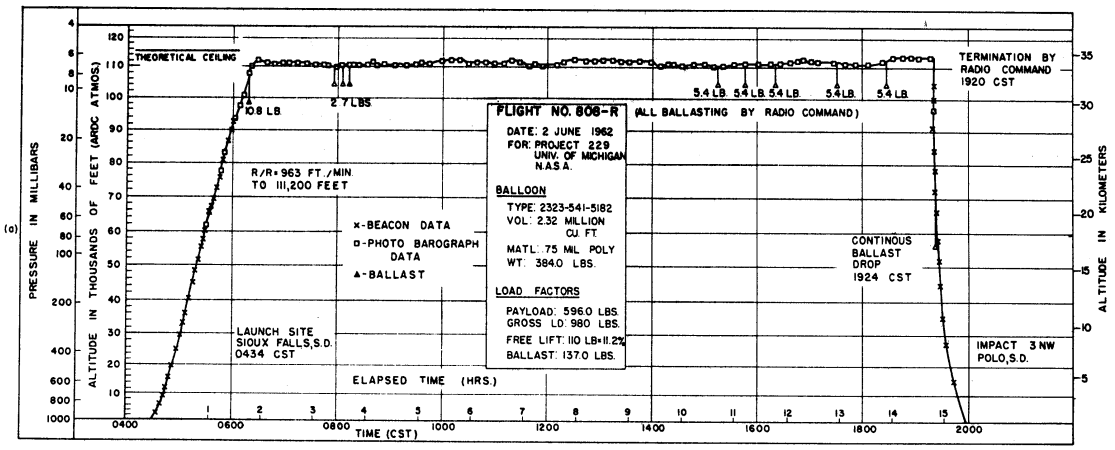

Figure 23. Altitude-time curve for 2 June, 1962 balloon flight.

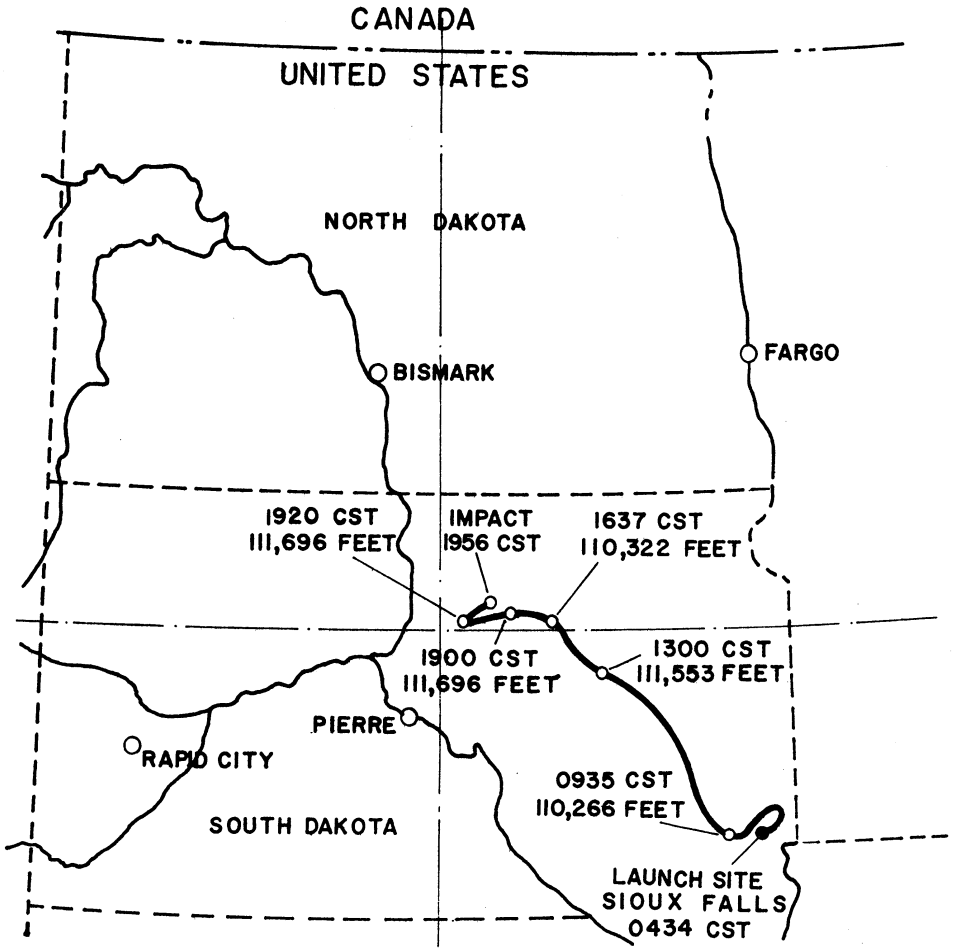

Figure 24. Trajectory for 2 June, 1962 balloon flight.

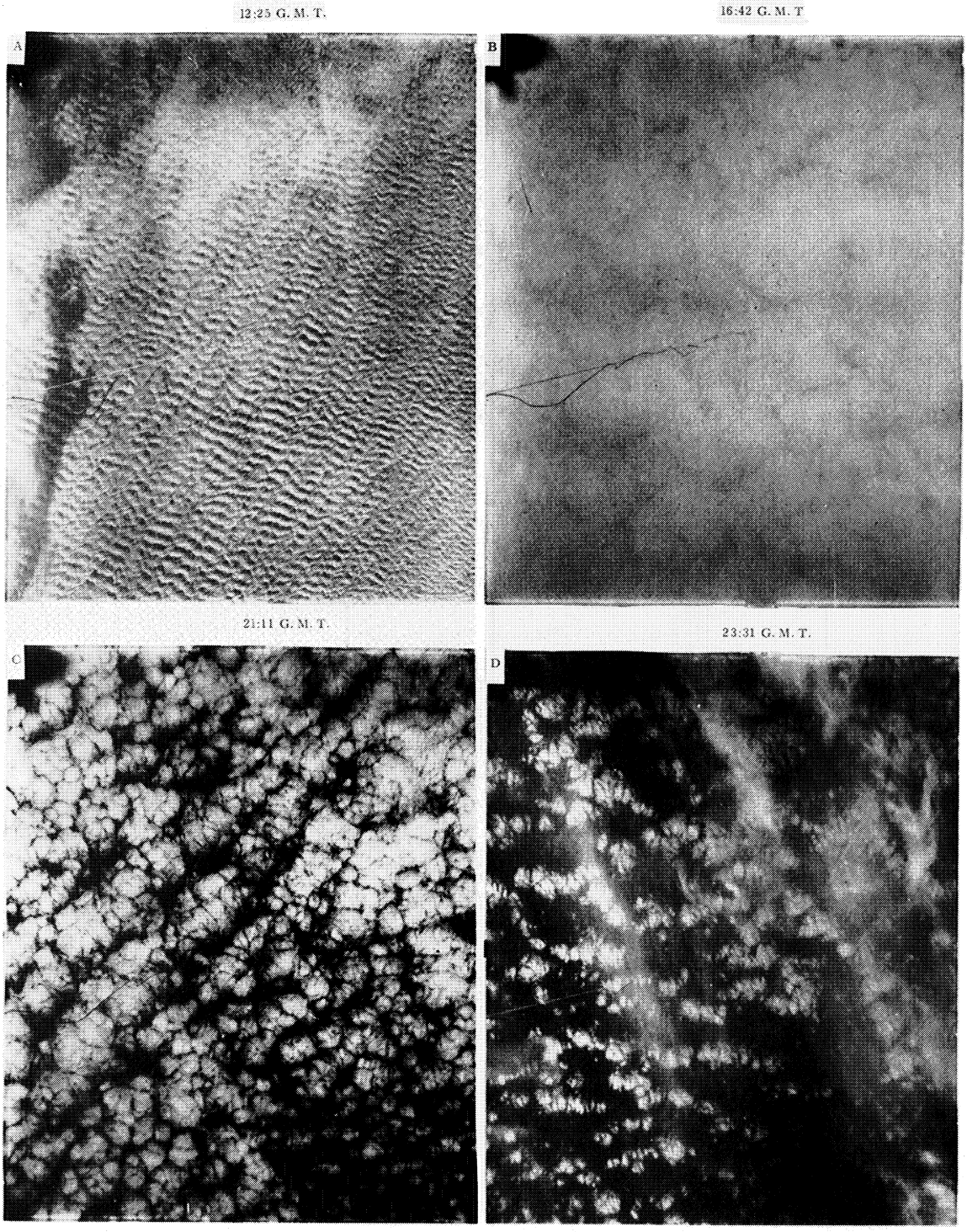

Figure 25. Photographs of cloud cover for 2 June, 1962 balloon flight.

when the cloud surface is quite uniform and homogeneous, as it was up to 1300 GMT; so that the radiometer field of view is completely filled by the same type of cloud surface, that the data is well enough defined to plot a scattering pattern. At the same time, the gondola motion in azimuth combined with the conical scan of the radiometer must be such that data covering a wide range of scattering angles is obtained. Such data was obtained in four 40-sec intervals at 1157, 1215, 1233, and 1251 GMT. Even then, it was necessary to eliminate portions of the data obtained when wispy cirrus or shadows of wispy cirrus came into the field of view. This data, plotted as a function of the scattering angle β, is shown in Figures 26 and 27 for the 0.55-0.75-micron and 0.2-5.5-micron channels of the radiometer, respectively.

Stratocumulus Cloud Reflectance

Data was obtained for scattering angles, β, of 50-145°. The curves are similar in shape to the scattering patterns derived by Deirmendjian for single scattering from a water cloud with realistic size distribution (see Figures 100 and 101, Appendix D). There are maxima of scattering at low scattering angles and at high scattering angles, with a minimum at β equal to 110-120°. There are indications of a fogbow at about 135°. There is a certain amount of scatter in the data, which is probably due to nonuniformities in the cloud structure (i.e., composition and thickness).

There is an indication of a slight increase in forward scattering and a slight decrease in backscattering with increasing time (i.e., increasing sun elevation angle). However, because of insufficient knowledge about the exact cloud thickness and physical characteristics during this time interval, it is premature to say that the increase in forward

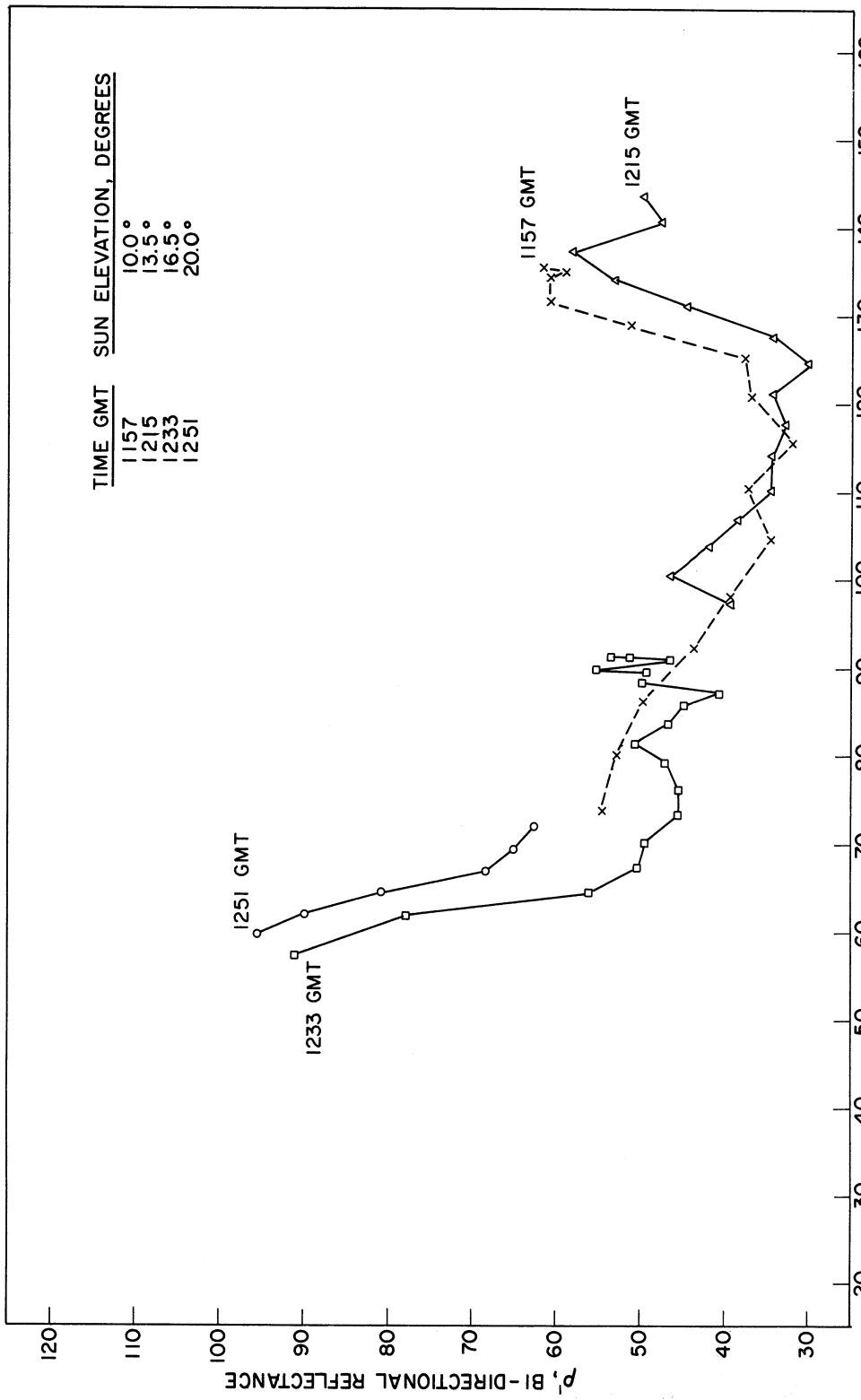

Figure 26. Bidirectional reflectance of stratocumulus clouds, ρ' for 0.55-0.75-micron channel of TIROS #103A radiometer, 2 June, 1962 balloon flight.

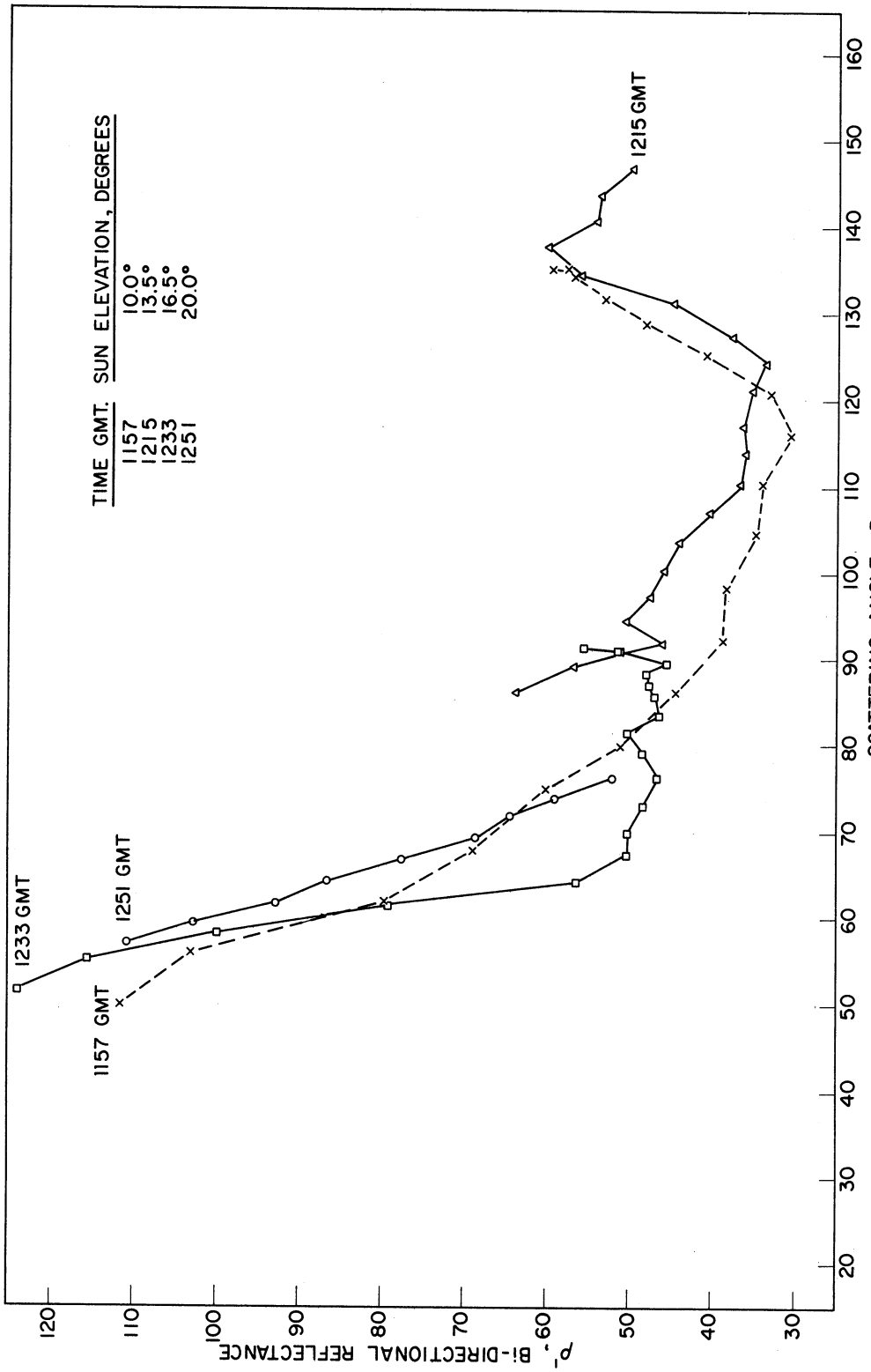

Figure 27. Bidirectional reflectance of stratocumulus clouds, ρ' for 0.2-5.5-micron channel of TIROS #103A radiometer 2 June, 1962 balloon flight.

scattering and decrease in backscattering is caused by the increase in sun elevation angle.

Average curves for each of the channels are shown in Figure 28. They are essentially the same within the accuracy of the radiometer measurements, so that it is reasonable to take an average as representative of the scattering pattern of stratocumulus clouds, over farmland, 1000 to 2000 feet thick with top at about 6000 feet. This average of the radiometer data for stratocumulus clouds is shown in Figure 29, with Deirmendjian's calculation for single scattering in a water cloud model for comparison. While the single scattering model does not produce the intensity of the actual cloud scattering, the qualitative agreement of the functional relationship should be noted, even to the existance of the maximum of the curve at $\beta = 136°$ (i.e., the fogbow). This angle is less than the theoretical angle of 143° for $\lambda = 0.70$.

Since data was obtained only for $50° < \beta < 145°$ the curve has been extrapolated from 50° to 0° and from 145° to 180° using the theoretical curve as a guide. This final curve, also shown in Figure 29 is a final estimate of the scattering pattern of a stratoculumulus could for high solar zenith angles (70-80°). A three-dimensional model of this scattering pattern is shown in Figure 30. In this figure, the flat circular disk represents the top of a flat cloud. Solar radiation is incident from the right at an elevation angle of 20°. The spike in the scattering pattern pointing to the right is backscattering. The fogbow is the next "scallop" in the pattern. The large amount of forward scattering is shown at the left. The truncation of this forward scattering is merely due to the limit in the size of the model. The small bow in the center of the pattern may possibly be due to noise. Deirmendjian's calculations show

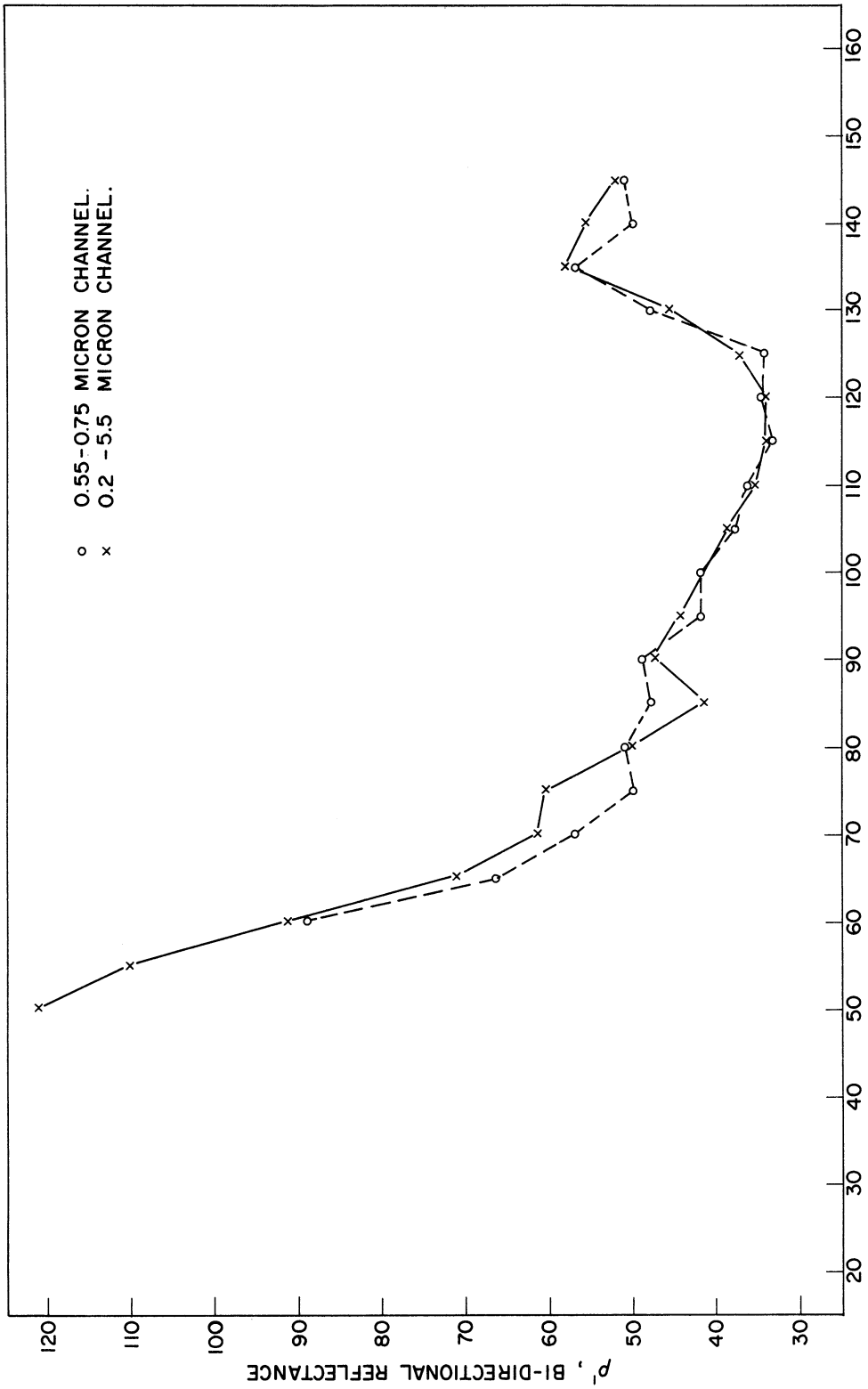

Figure 28. Bidirectional reflectance of stratocumulus clouds as a function of scattering angle, average values.

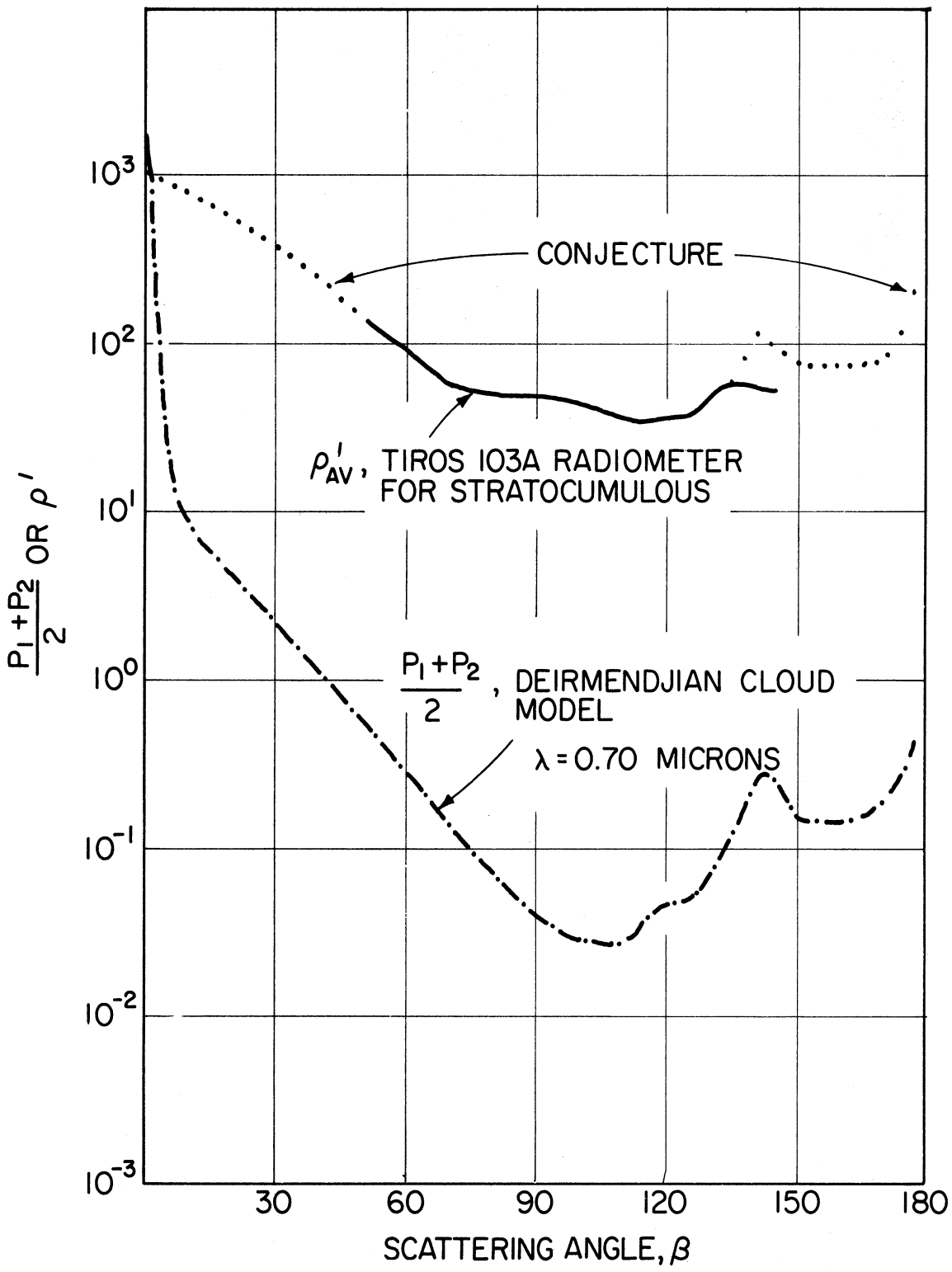

Figure 29. Comparison of experimental measurements of bidirectional reflectance of stratocumulus cloud with theoretical single scattering pattern of water cloud model.

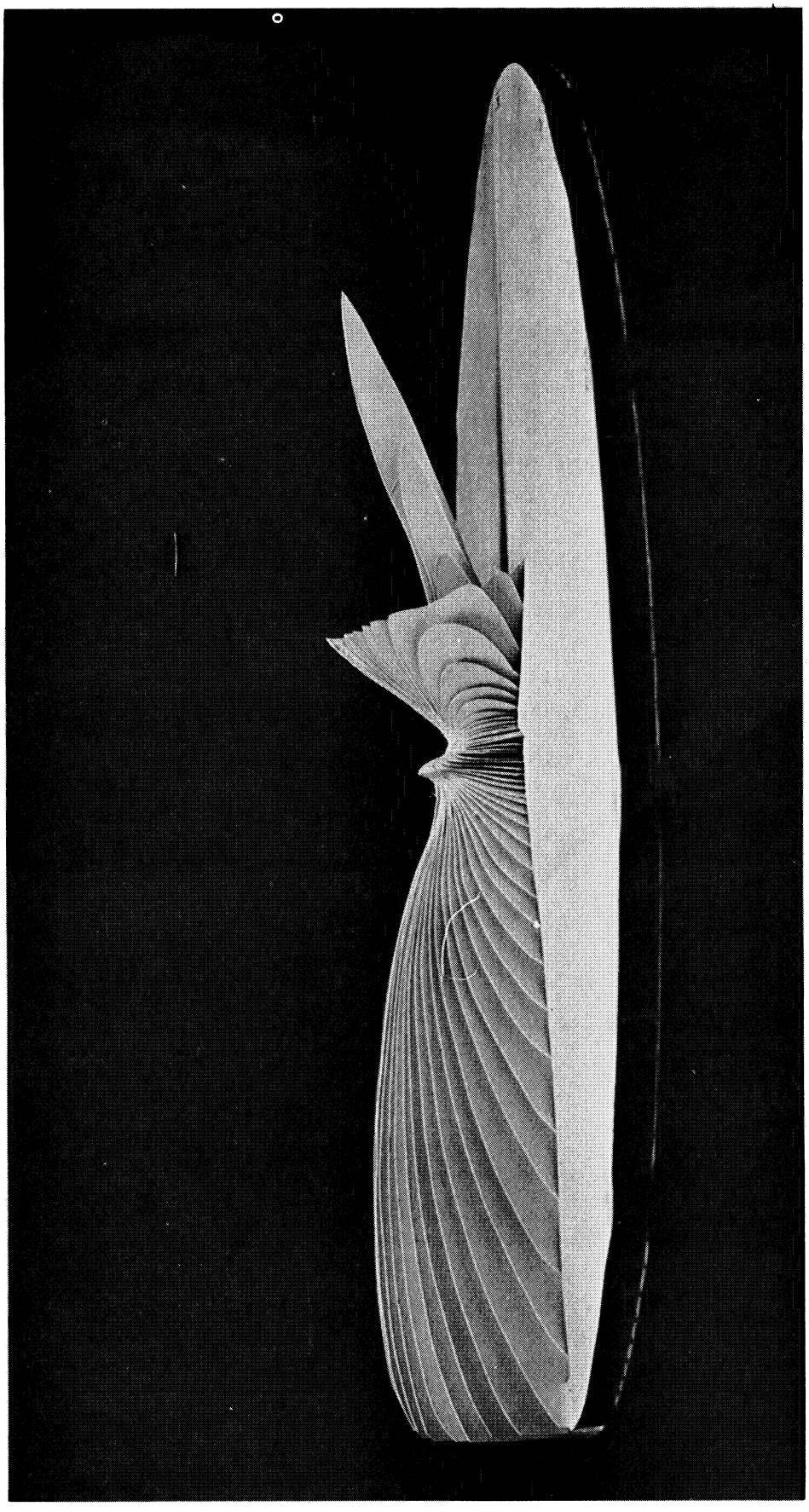

Figure 30. Model of bidirectional reflectance pattern of stratocumulus cloud.

that the bow exists at 5.3 microns but not at lower wavelengths.

Note that the complete scattering pattern is a figure of revolution having the ray of incident solar radiation as axis, and that the bireflectance pattern of the cloud is obtained by merely cutting the scattering pattern with a plane, as in Figure 30, so that the correct angle of incidence is obtained. Thus it is obvious, that the total directional reflectance of such a cloud is a function of the elevation angle of the sun, and can be calculated by integrating over the hemisphere above the plane.

This has been done for the scattering model shown in Figure 30 with the result shown in Figure 31, which shows total directional cloud reflectance as a function of the solar angle of elevation. The total directional reflectance has a minimum value of 58% at a solar elevation angle of 40°, and a maximum of 85% at 0° elevation angle. These results are in good agreement with those of other experimenters (see Section III-D); i.e., Neiburger obtained total reflectances of 70-80% for a 1800 feet thick stratocumulus cloud (solar elevation angle not noted).

Reflectance Scatter Diagrams

Although the data for much of this balloon flight cannot be used to plot bidirectional reflectance or scattering diagrams, it does provide some information about the spectral dependence of reflectances measured. Values of the radiometer measurements taken simultaneously by the two channels of the radiometer are plotted in a modified scatter diagram in Figure 32, i.e., the ratio of the bidirectional reflectance of the wide band channel, ρ'_3, divided by the bidirectional reflectance of the narrow band channel, ρ'_5, is plotted vs. ρ'_5.

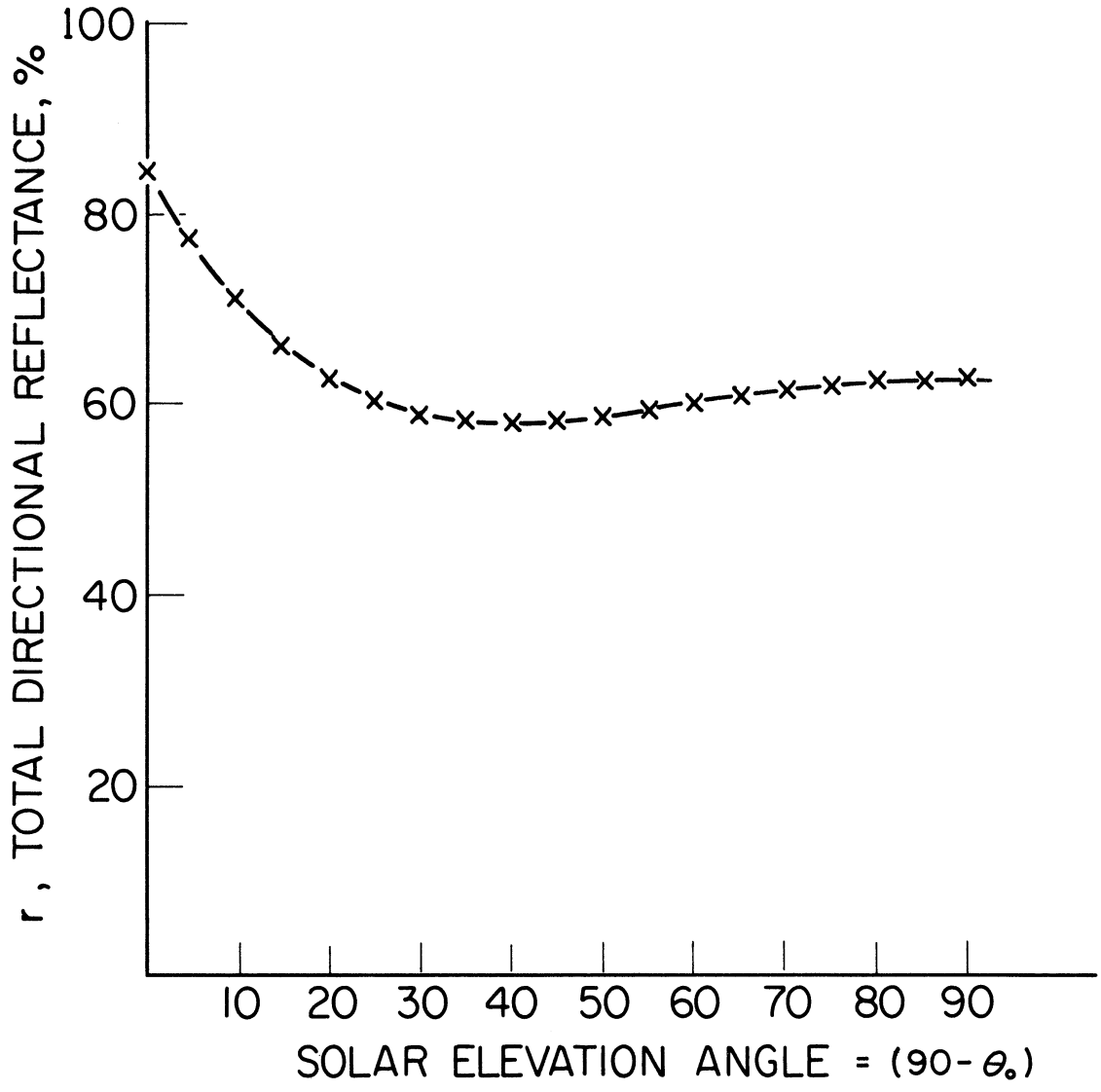

Figure 31. Total directional reflectance of a stratocumulus cloud as a function of solar angle of elevation.

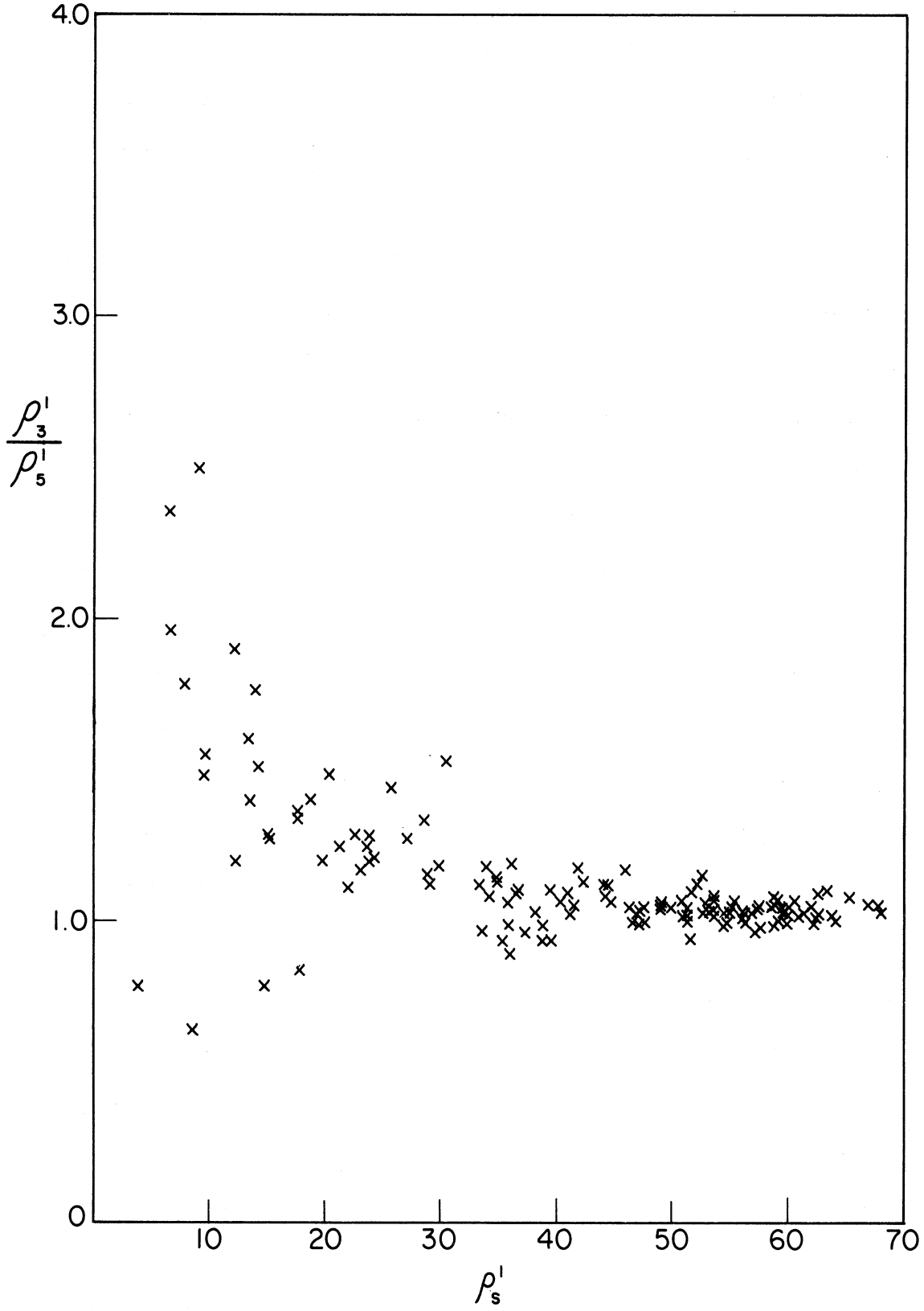

Figure 32. Reflectance diagram, ratio ρ'_3/ρ'_5 vs. ρ'_5 for 2 June, 1962 balloon flight. All data taken above complete overcast or broken to scattered cloud conditions.

The data samples were taken at 4.5-minute intervals throughout the day, so that the diagram shows samples of data taken at different scattering angles and for different cloud conditions. The diagram shows that for the most part channel 3 (0.2-5.5 microns) reflectances are greater than channel 5 (0.55-0.75 micron) reflectances, with the ratio being approximately equal to 1 at high reflectances and as high as 2 for low values of reflectance. This diagram provides additional evidence that the narrow band channel data cannot be used for earth albedo calculations, and that if it is so used a value of earth's albedo which is too small will be obtained (as was obtained by Bandeen[1]). Given Bandeen's data a correction factor for his earth's albedo could be calculated from a curve such as shown in Figure 32.

In Figure 33 the reflectance ratio is plotted as a function of time during the balloon flight. A general description of the scene viewed is given along the bottom of the figure for correlation with the reflectance ratio. When the radiometer views the stratocumulus cloud, the reflectance ratio is very close to 1. However, early in the morning when the sun is at a very low elevation angle ($< 8°$), the ratio is considerably less than 1; and late in the day, when the radiometer is looking through scattered clouds at the earth, the ratio is much greater than 1. This change of the ratio during the day is consistant with a spectral distribution containing primarily short wavelength scattered radiation in the morning, roughly equal intensities at all wavelengths when looking at stratocumulus with the sun above 8°, and increased reflectance at wavelengths above 0.75 micron when looking at the earth through scattered clouds in the afternoon.

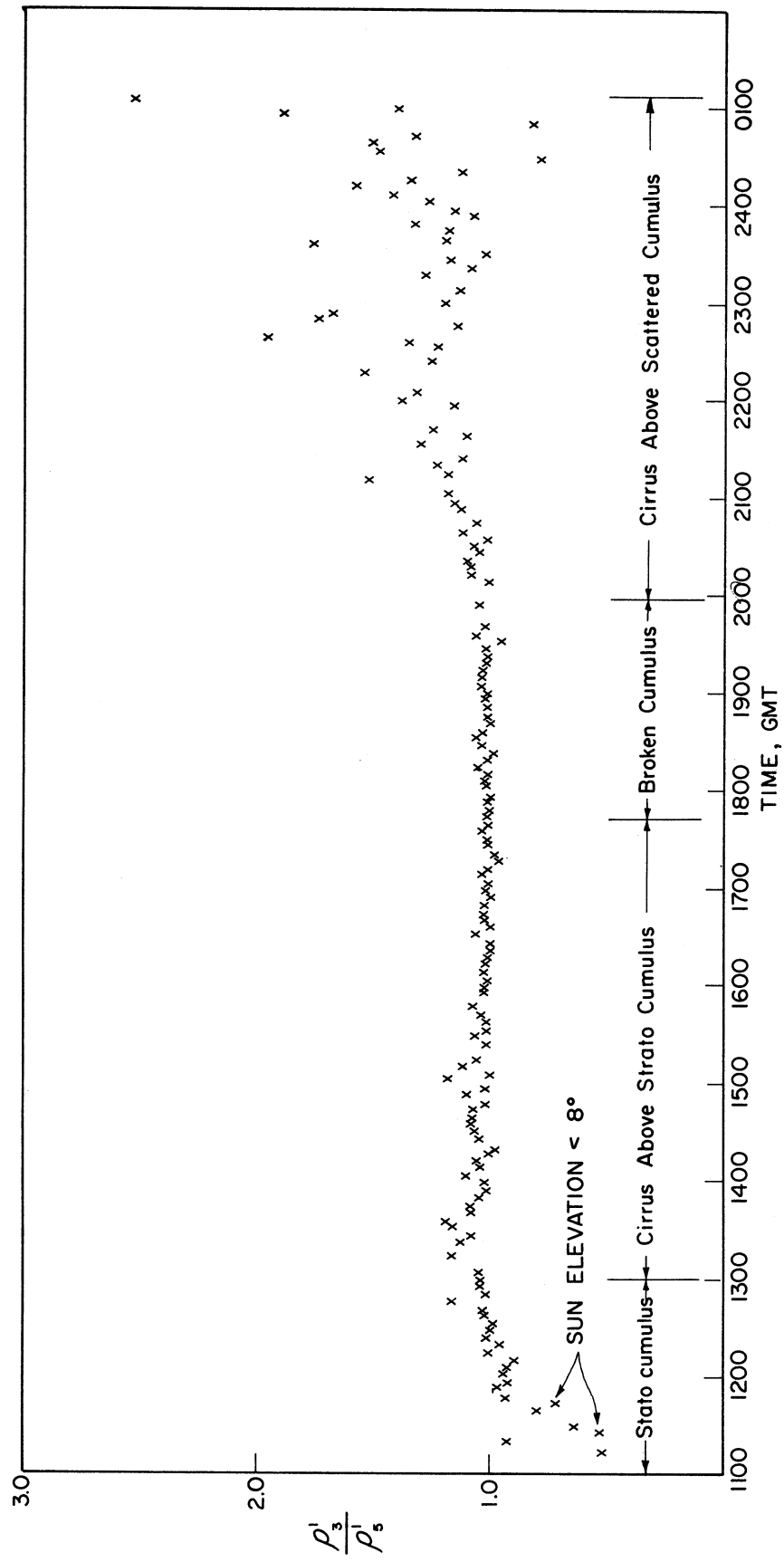

Figure 33. Reflectance ratio vs. time for 2 June, 1962 balloon flight.

2. The 26 June, 1963 Balloon Flight

The 26 June, 1963 balloon flight was launched at 1057 GMT from Sioux Falls, South Dakota. It flew over cloudless skies at a height of 112000 feet until 1730, approximately. The sky then gradually became cloudy and at 1950 GMT the balloon flew over a large storm system with very high clouds. The flight was terminated at 0015 GMT, 27 June; parachute recovery was successful. The altitude vs. time data and a trace of the balloon trajectory are shown in Figure 34. The data has not yet been analyzed for geometrical dependence of reflectance. However, this will be done in the near future. A reflectance ratio study has been made.

Reflectance Scatter Diagrams

Curves of the reflectance ratio ρ_3'/ρ_5' vs. ρ_5' for this balloon flight, were plotted for both the TIROS #103A and MRIR #F-1 radiometers. They are shown in Figures 35 and 36, respectively. They show a functional relationship similar to that shown by the TIROS #103A radiometer on the June 2, 1962 balloon flight, with $\rho_3' > \rho_5'$ for low values of ρ_5' and $\rho_3' \approx \rho_5'$ for high values of ρ_5'. The TIROS radiometer data show $\rho_3'/\rho_5' = 1.0$ at $\rho_5' = 90$, whereas the NIMBUS radiometer data show the ratio = 0.8 at this value of ρ_5'. The difference may be due to calibration errors (recall that the calibration of the narrow band channel of the F-1 radiometer is uncertain because of filter deterioration). At any rate the data bear out the conclusion that the narrow band channel data cannot be used to infer earth albedo values without the use of a correction factor derived from curves such as Figures 35 and 36.

Reflectance ratios have been plotted as a function of time for this balloon flight in Figures 37 and 38. Again the general nature of the terrain viewed is indicated at the bottom of the figure. When the radiom-

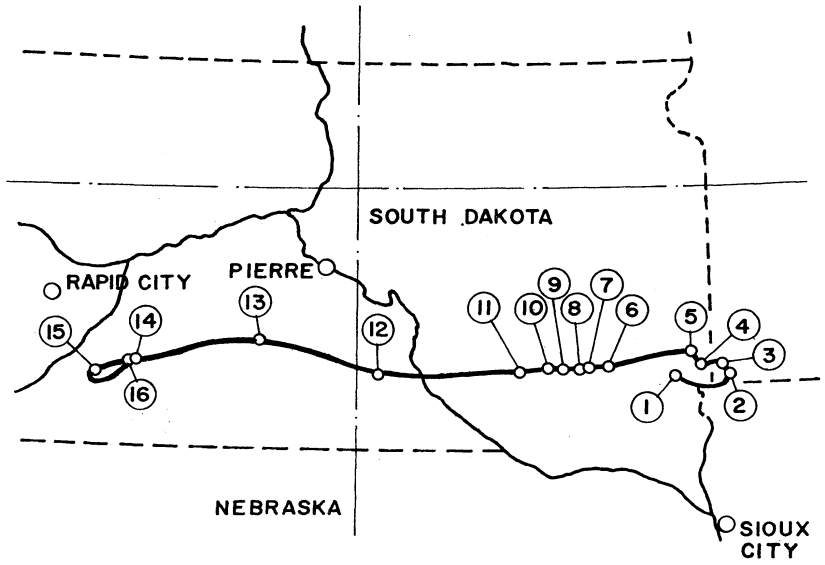

FLIGHT NUMBER 887-R			
SYM.	DATE	TIME (C.S.T.)	ALTITUDE
①	26 JUNE		LAUNCH SITE SIOUX FALLS, S.D.
②	26 JUNE	0605	70,600 FEET
③	26 JUNE	0623	88,000 FEET
④	26 JUNE	0645	111,300 FEET
⑤	26 JUNE	0656	112,400 FEET
⑥	26 JUNE	0800	112,400 FEET
⑦	26 JUNE	0815	112,400 FEET
⑧	26 JUNE	0820	112,400 FEET
⑨	26 JUNE	0839	112,400 FEET
⑩	26 JUNE	0850	112,400 FEET
⑪	26 JUNE	0920	112,400 FEET
⑫	26 JUNE	1130	112,400 FEET
⑬	26 JUNE	1400	111,500 FEET
⑭	26 JUNE	1630	UNKNOWN
⑮	26 JUNE	1740	TERMINATION
⑯	26 JUNE	1810	IMPACT AREA 102°15' W., 43°38' N.

Figure 34. Altitude-time data and trace of balloon trajectory for 26 June, 1963 balloon flight.

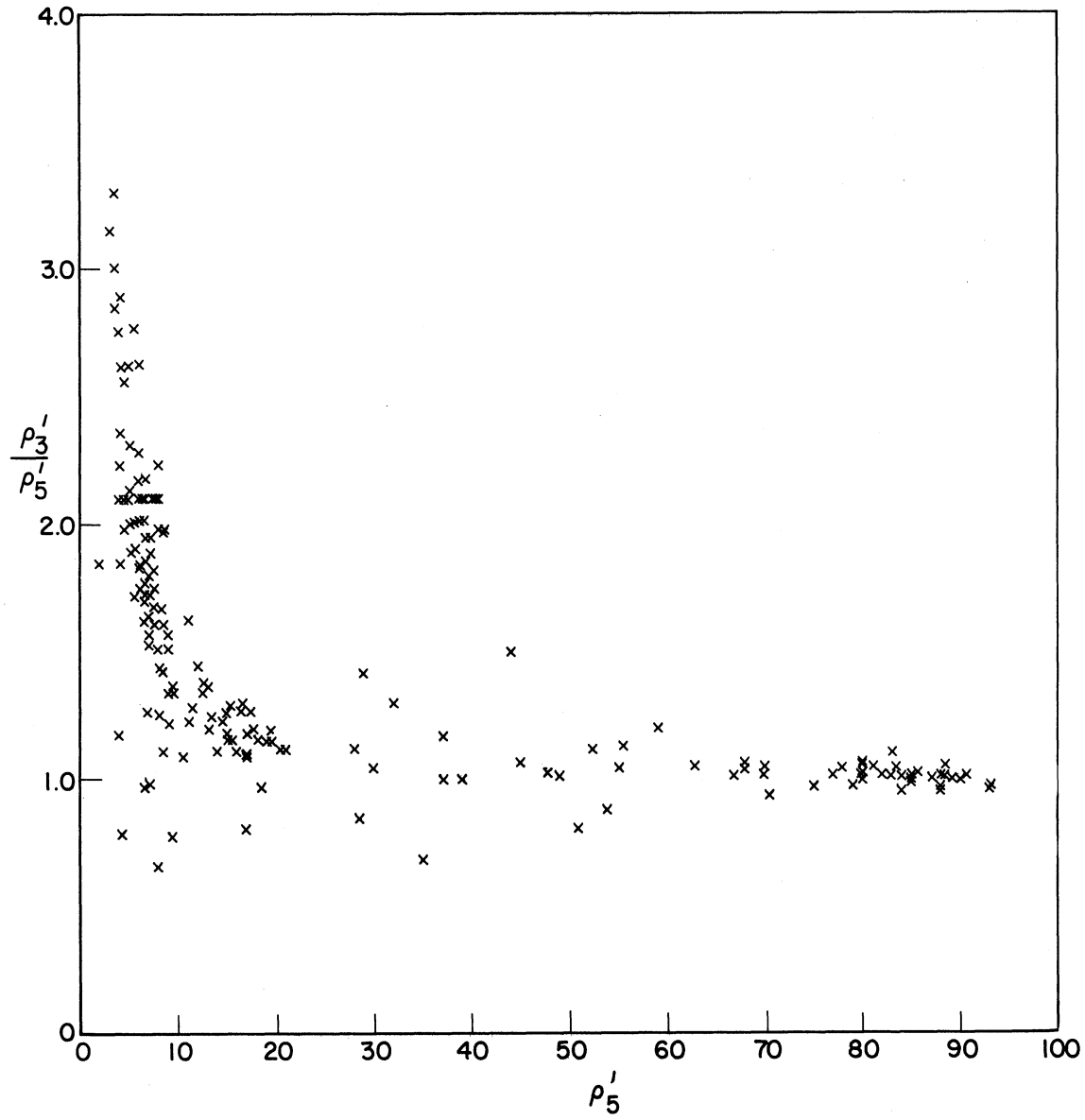

Figure 35. Reflectance diagram, ratio ρ_3'/ρ_5' vs. ρ_5' for 26 June, 1963 balloon flight, TIROS #103A radiometer.

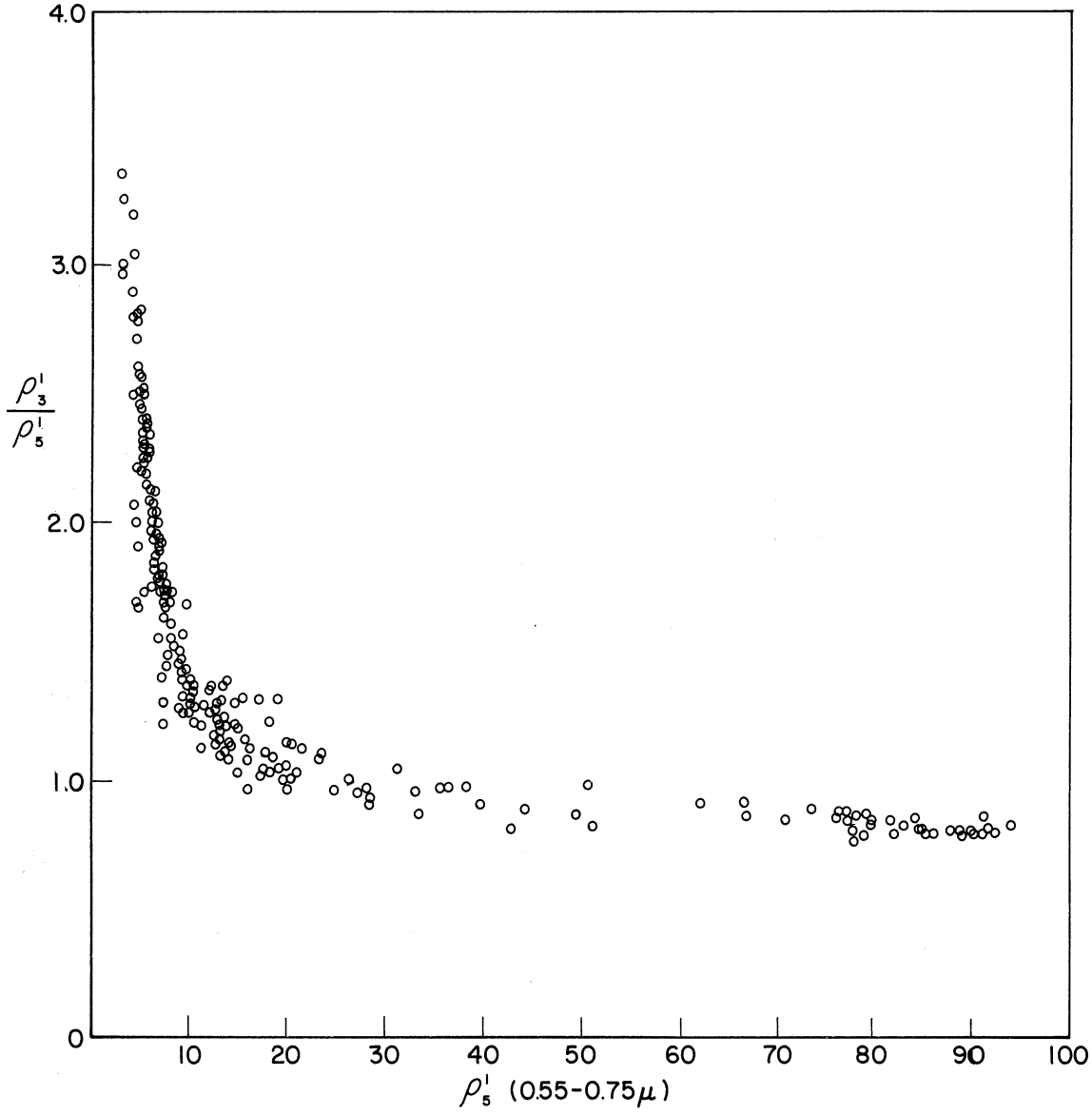

Figure 36. Reflectance diagram ratio ρ'_3/ρ'_5 vs. ρ'_5 for 26 June, 1963 balloon flight, NIMBUS MRIR F-1.

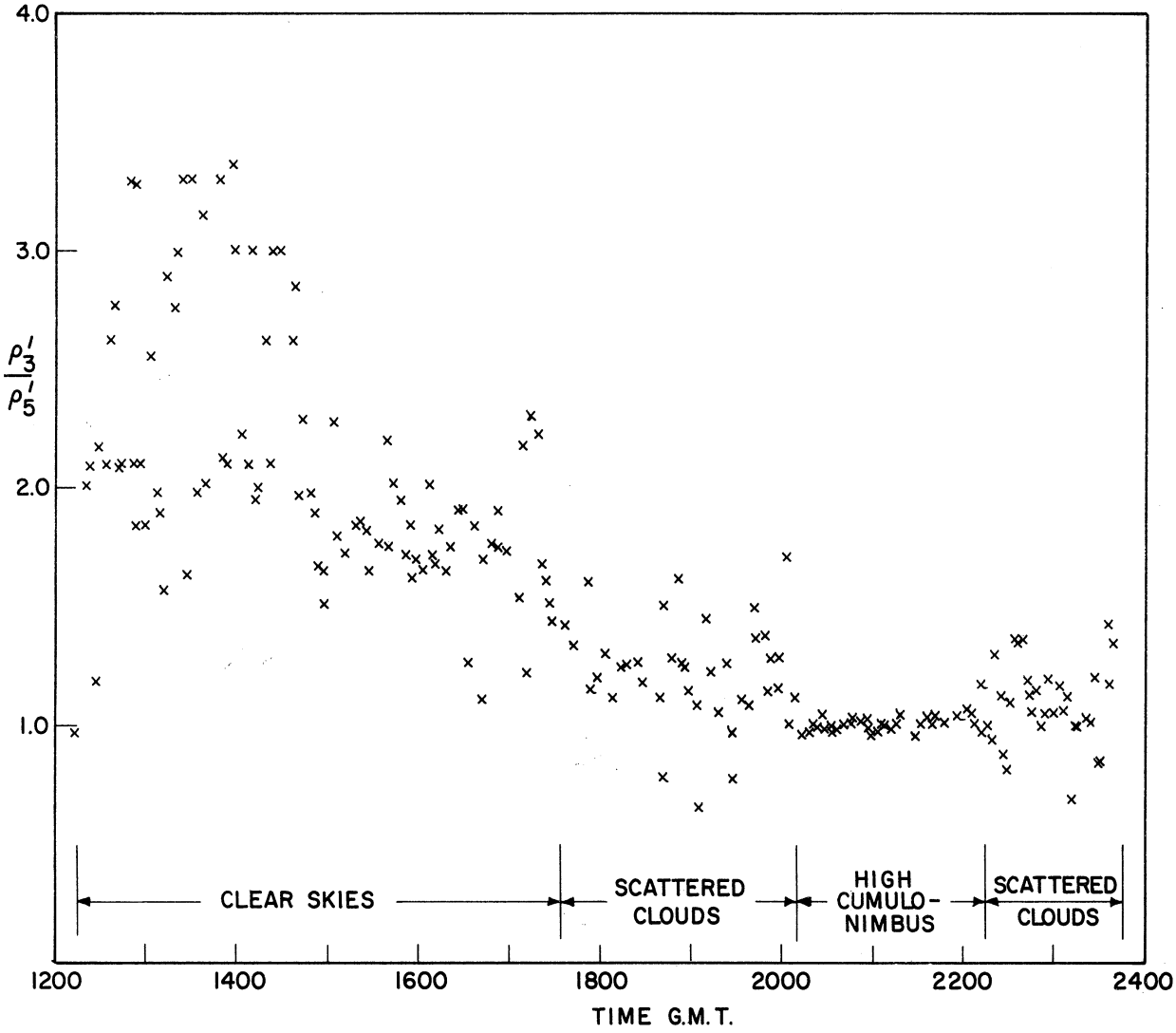

Figure 37. Reflectance ratio vs. time for 26 June 1963 balloon flight, TIROS #103A radiometer.

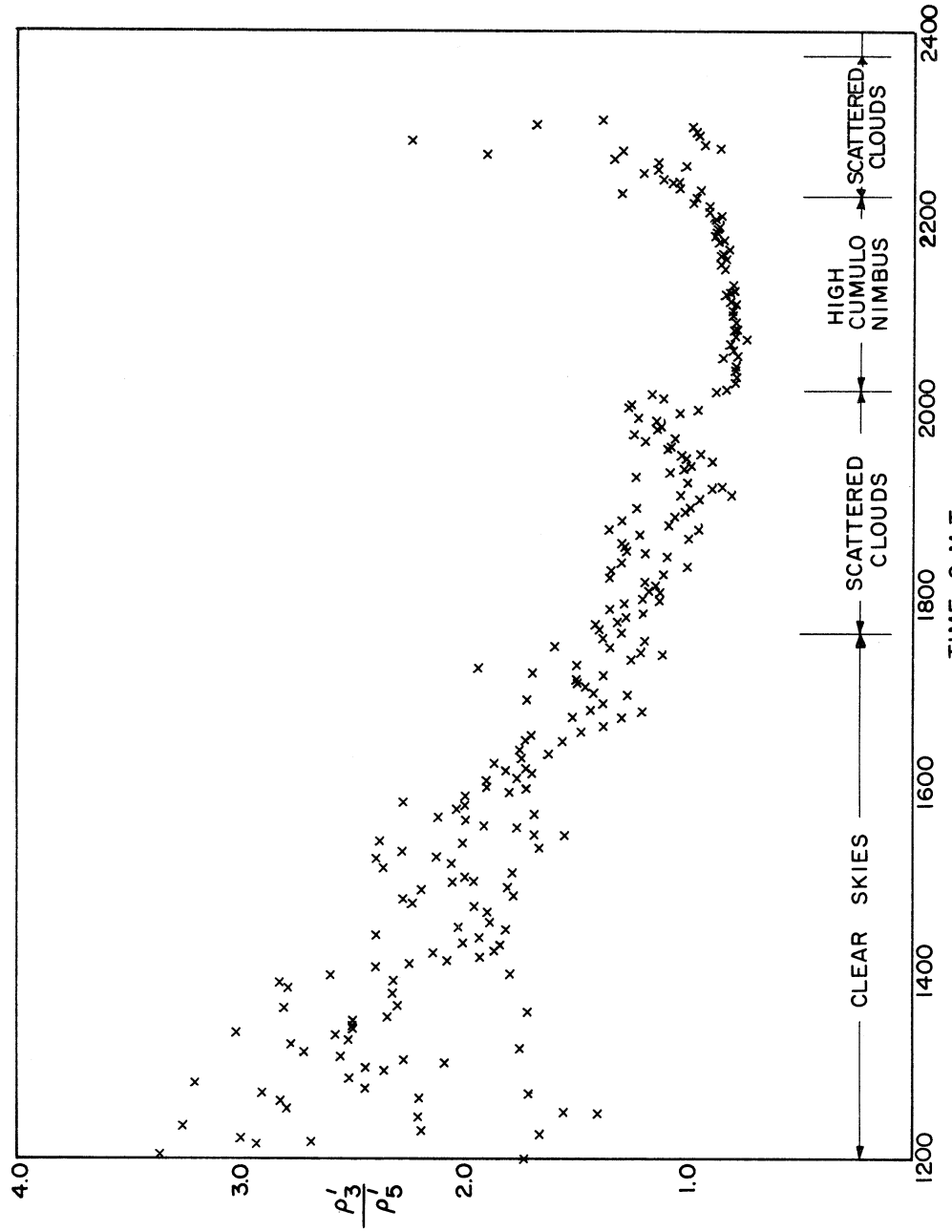

Figure 38. Reflectance ratio vs. time for 26 June, 1963 balloon flight, NIMBUS MRIR F-1.

eters view the high clouds at the end of the flight the reflectance ratio is close to 1. However, for clear sky conditions earlier in the flight, the ratio is as high as 3.5, due to the fact that the reflectance of the earth is greater in the long wavelength region. The ratio for clear skies decreases with increasing sun angle as we should expect, because of a decrease in scattered short wavelength radiation.

3. The 10 March, 1965 Balloon Flight

The 10 March, 1965 balloon flight was launched at 1210 GMT (0610 CST) from Sioux Falls, S. D., and floated at an altitude of 107000 feet for about 7 hours above terrain which was 25-90% covered with wind blown snow. The altitude vs. time curve and a trace of the balloon trajectory are shown in Figures 39 and 40.

The MRIR F-4 radiometer which was flown on this ballon flight had only one channel (0.2-4.0 microns) for measurement of reflected and scattered solar radiation. Thus reflectance ratio was not studied. However, bidirectional reflectance patterns for this type of terrain and atmosphere were obtained at three different sun zenith angles, 72°, 58°, and 50°, at 0834, 0900, and 1110 CST, respectively. When the sun was at zenith angles greater than 72°, the balloon was not yet at altitude and so data was not obtained. During the rest of the flight, except at those times noted, data for reflectance patterns was not obtained because of insufficient gondola rotation or nonhomogeneous fields of view (i.e., scattered clouds in the field of view).

The reflectance patterns obtained show the sum of reflected radiance from the snow covered terrain plus the scattered radiance from the atmosphere. The data is displayed in several ways for better understanding of its characteristics.

Figure 41 shows the coordinate system used for display of the entire bidirectional reflectance pattern in one diagram. The geometry is that of Figure 1, as viewed from the zenith. The angle ψ, measured from the principal plane runs from 0 to 360° counterclockwise around the outside of the polar diagram. The concentric circles are curves of constant zenith angle, running from 0° at the center to 100° at the outside of the diagram. Solar radiation is incident from the azimuth direction ψ = 180°. The orientation of the diagram on the earth's surface will depend on the sun's azimuth, i.e., the time of day; for example sometime in midmorning with the sun shining from the southeast, the direction E would lie at ψ = 225° on the diagram, with N at 315 (i.e., ϕ_o = 45°). Note that the horizon will lie at a zenith angle of 95.9° (i.e., the earth-atmosphere interface as viewed from the balloon at 110000 feet.

The bidirectional reflectance diagram is shown on this coordinate system by a set of contours of constant reflectance.

Figure 42 is a bidirectional reflectance pattern that was obtained at 0832-0836 CST, with the sun at a zenith angle of 72.2-71.5°. The balloon was still rising, and the pressure altitude varied from 20-16.5 mb during the data taking time interval. Note that the sun's position is not shown along the ψ = 180° line. Although calculations were made so that the diagram would have the sun at this value of ψ, the symmetry of the results obtained indicates that the sun's position should be along the ψ = 188° line, inside of the 70% reflectance contour (which represents the peak of the atmospheric backscattering). Large forward scattering is shown by the contours on the right hand side of the diagram. The maximum contour shown is 99%, the maximum value allowed in the data processing. A second pass through the data will yield higher values of

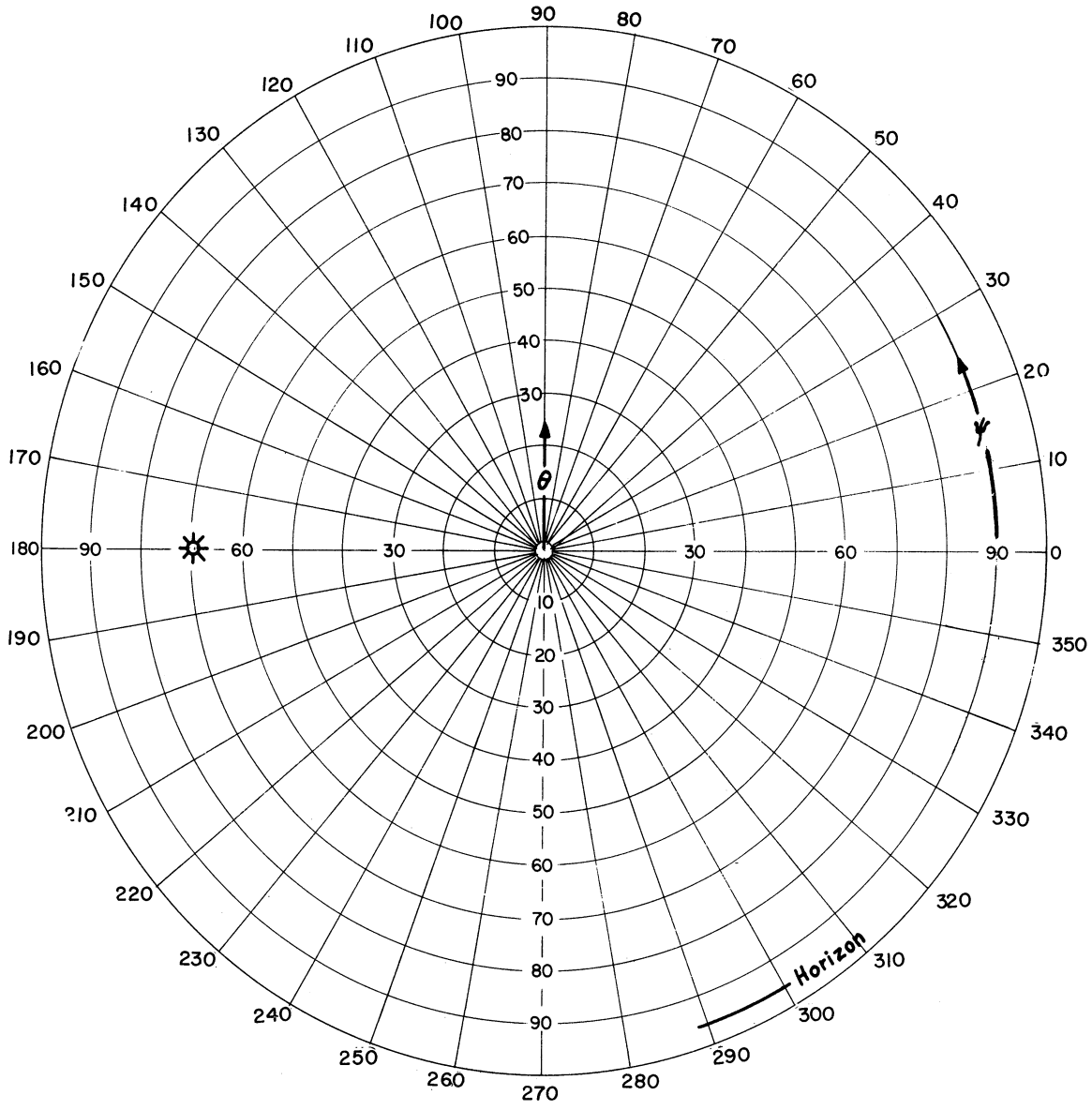

Figure 41. Polar coordinate system for bidirectional reflectance diagrams.

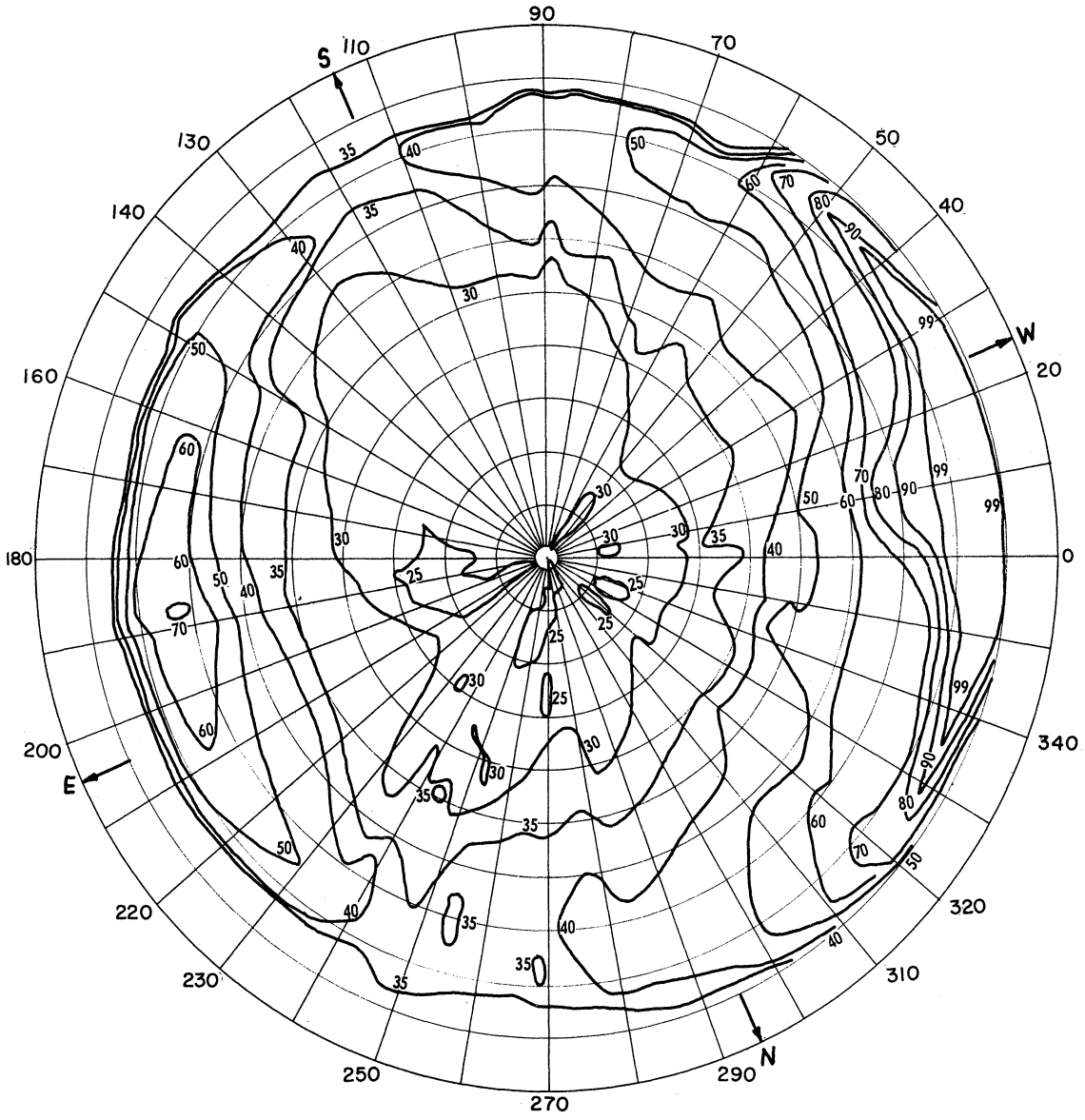

Figure 42. Bidirectional reflectance diagram obtained at 0832-0836 CST on 10 March, 1965 balloon flight. θ_o = 72.2-71.5°, pressure altitude = 20.0-16.5 mb.

reflectance in this region and thus would show more detail on the peak of the forward scattering pattern. The reflectance pattern decreases symmetrically from the forward and backscattering peaks maintaining higher values near the horizon at all azimuths with the minimum value of reflectance of slightly less than 25% at the zenith. For geographical orientation note the E, S, W, and N directions of the figure.

Photographs of a three-dimensional model of this reflectance pattern are shown in Figures 43a and b. In Figure 43a, the view is from N.E., showing the backscattering peak. The arrow indicates the direction of the incident radiation. In Figure 43b the pattern is viewed from the S. W., showing that the forward scattering is a maximum very close to the horizon. The photographs show the generally diffuse but slightly nonhomogeneous nature of the reflectance in directions approaching the zenith.

A third method of data display for the bidirectional reflectance pattern is to select a vertical slice of the pattern at some azimuth and to plot the resulting data as a function of zenith angle. Such a plot of the 0834 CST data in the principal plane is shown in Figure 44, showing the forward and backscattering with a rather uniform diffuse scattering toward the zenith.

The total directional reflectance for this pattern has been calculated by numerical intergration. A value of 35.0% was obtained.

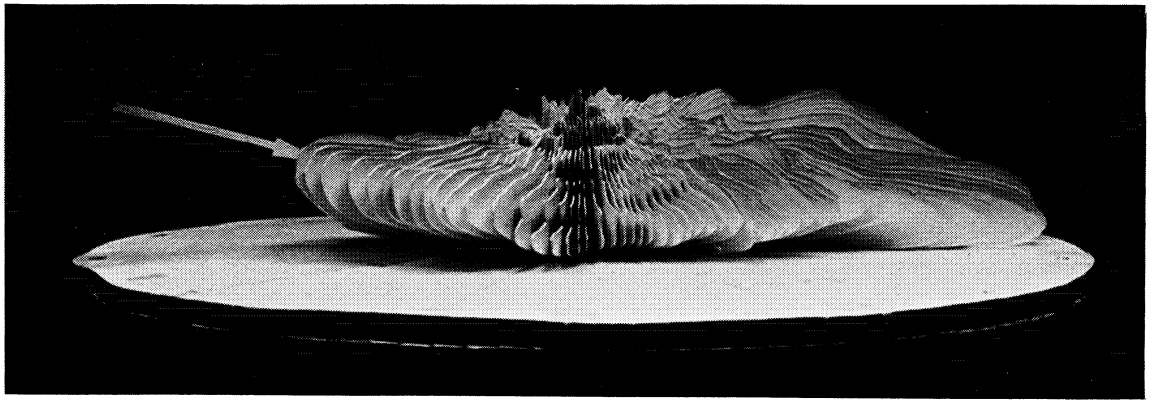

(a) View from N.E.

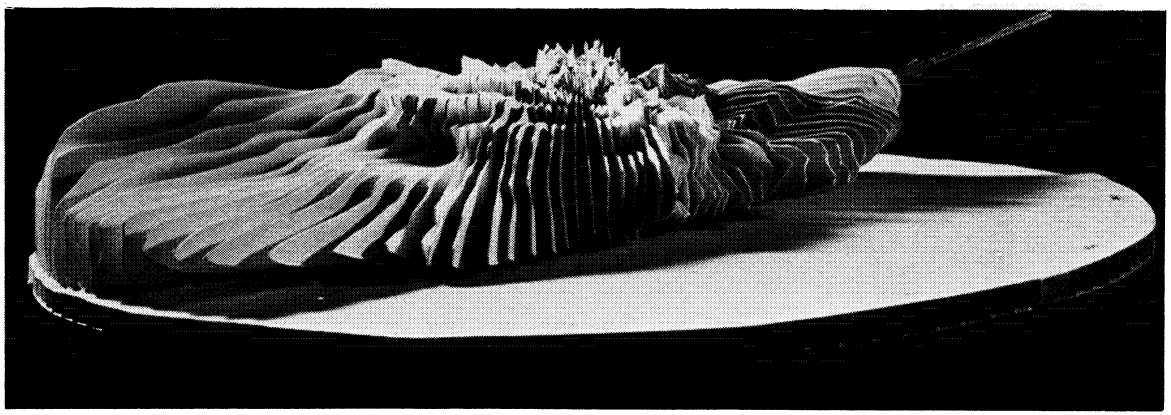

(b) View from S.W.

Figure 43. Photos of model of 0832-0836 CST bidirectional reflectance pattern. θ_o = 72.2-71.5°.

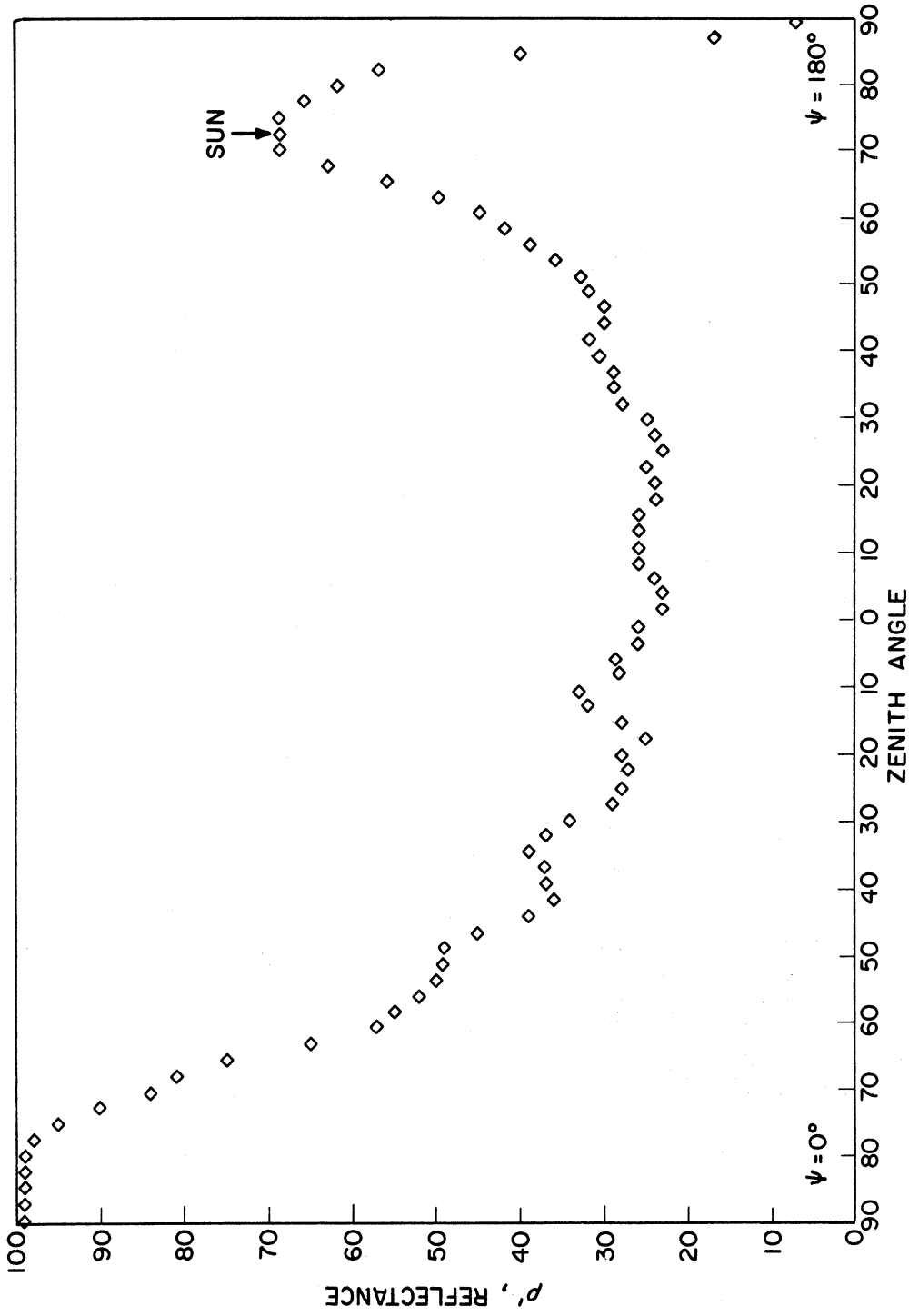

Figure 44. Bidirectional reflectance of snow-covered earth and atmosphere in principal plane, 10 March, 1965 balloon flight. θ_o = 72.2-71.5°.

The three different displays of the bidirectional reflectance pattern obtained at 0855-0909 CST on this balloon flight are shown in Figures 45-47. The sun was approximately 5° higher, i.e., 68.3-66.0° zenith angle. Inspection of the figures shows a pattern similar to that obtained at the earlier time. However, now the backscattering is less intense, but covers a slightly broader range of angles. The forward scattering is less intense and not as broad in angular range. In Figure 47 it can be seen that the forward scattering has dropped to 73% at $\theta = 90°$ whereas at the earlier time, with the sun 5° lower in the sky, the reflectance was still saturated at $\theta = 90°$. The directional reflectance, obtained by numerical integration of this data was 36.2% which is in agreement with the earlier value within the experimental error of measurements.

Figures 48-50 show the bidirectional reflectance pattern with a much higher sun, i.e., a zenith angle of 50°. The pattern is significantly different from that obtained earlier in the day. The high intensity forward and backscattering is not a feature at this high sun angle. There is a small peak at the proper angle for backscattering and a general maximum at almost all azimuths near the horizon. There is another peak at a zenith angle about 8° greater than that for specular reflection. This is consistent with surface measurements of the mirror component of reflection from snow. The directional reflectance, obtained by numerical integration of this reflectance pattern, was found to be 30.1%, about 5% lower than the values obtained earlier in the day.

E. DISCUSSION OF DATA OBTAINED

From the above data, it is apparent that the assumption of isotropic-wavelength independent reflectance usually employed in considerations of the earth's albedo obviously leads to a very poor approximation to

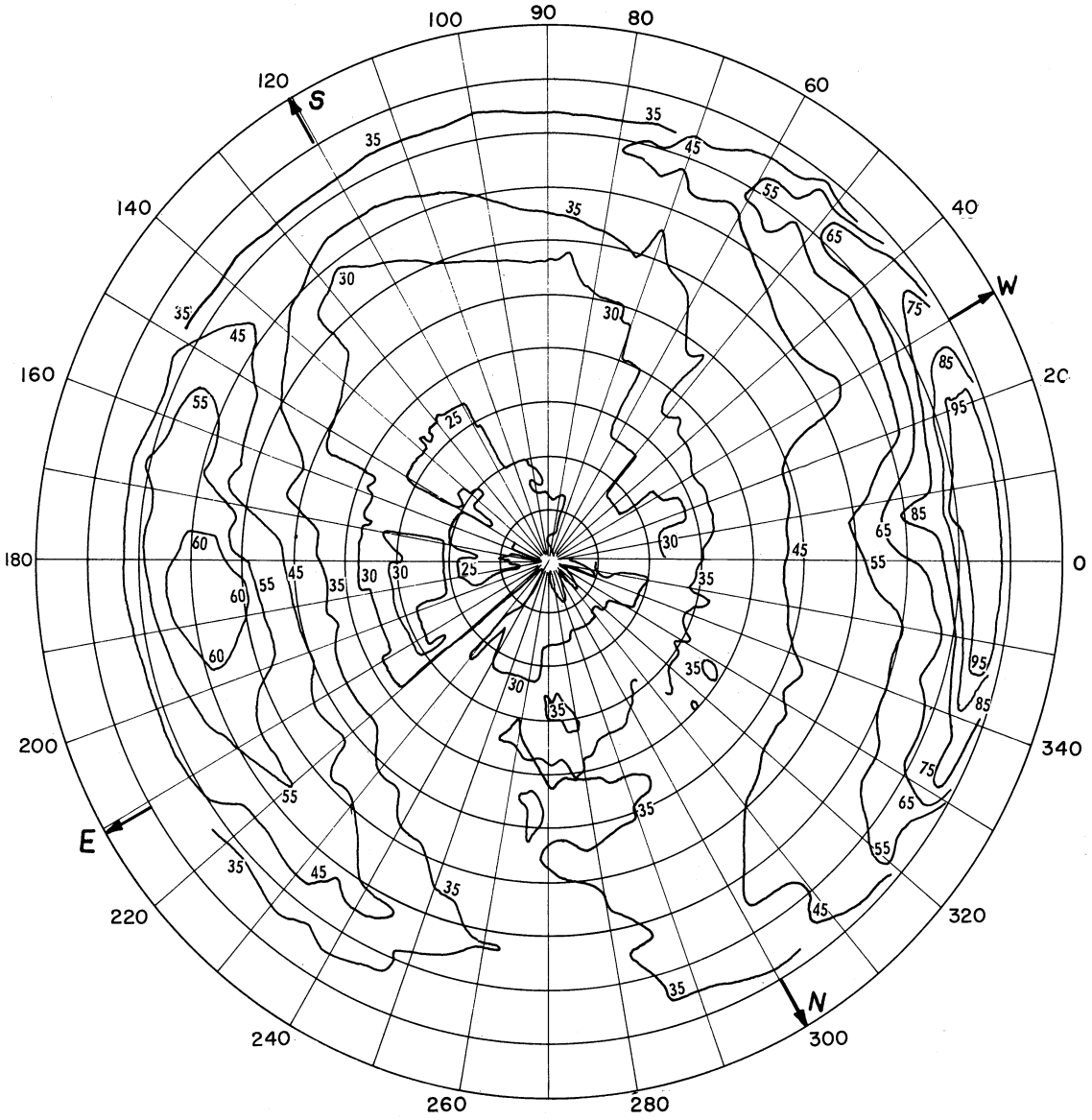

Figure 45. Bidirectional reflectance diagram obtained at 0855-0909 CST on 10 March,1965 balloon flight. θ_o = 68.3-66.0°, pressure altitude = 9.0-8.5 mb.

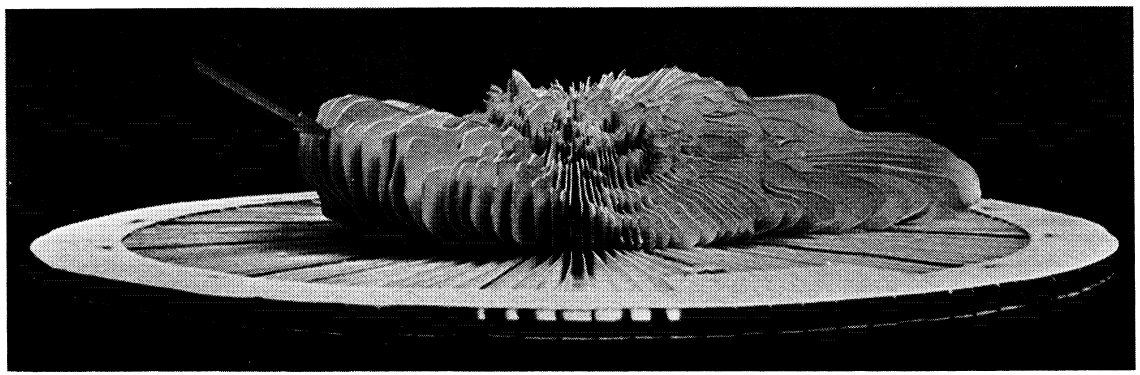

(a) View from E.-N.E.

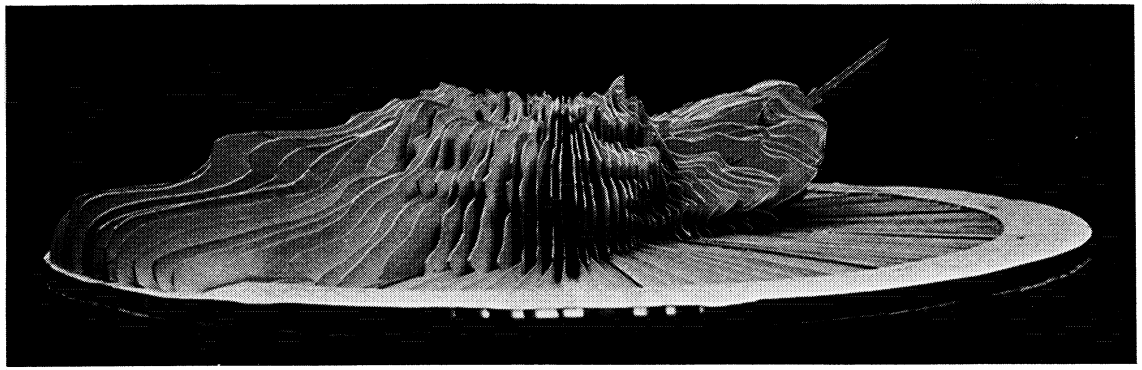

(b) View from S.-S.W.

Figure 46. Photos of model of 0855-0909 CST bidirectional reflectance pattern. θ_o = 68.3-66.0°.

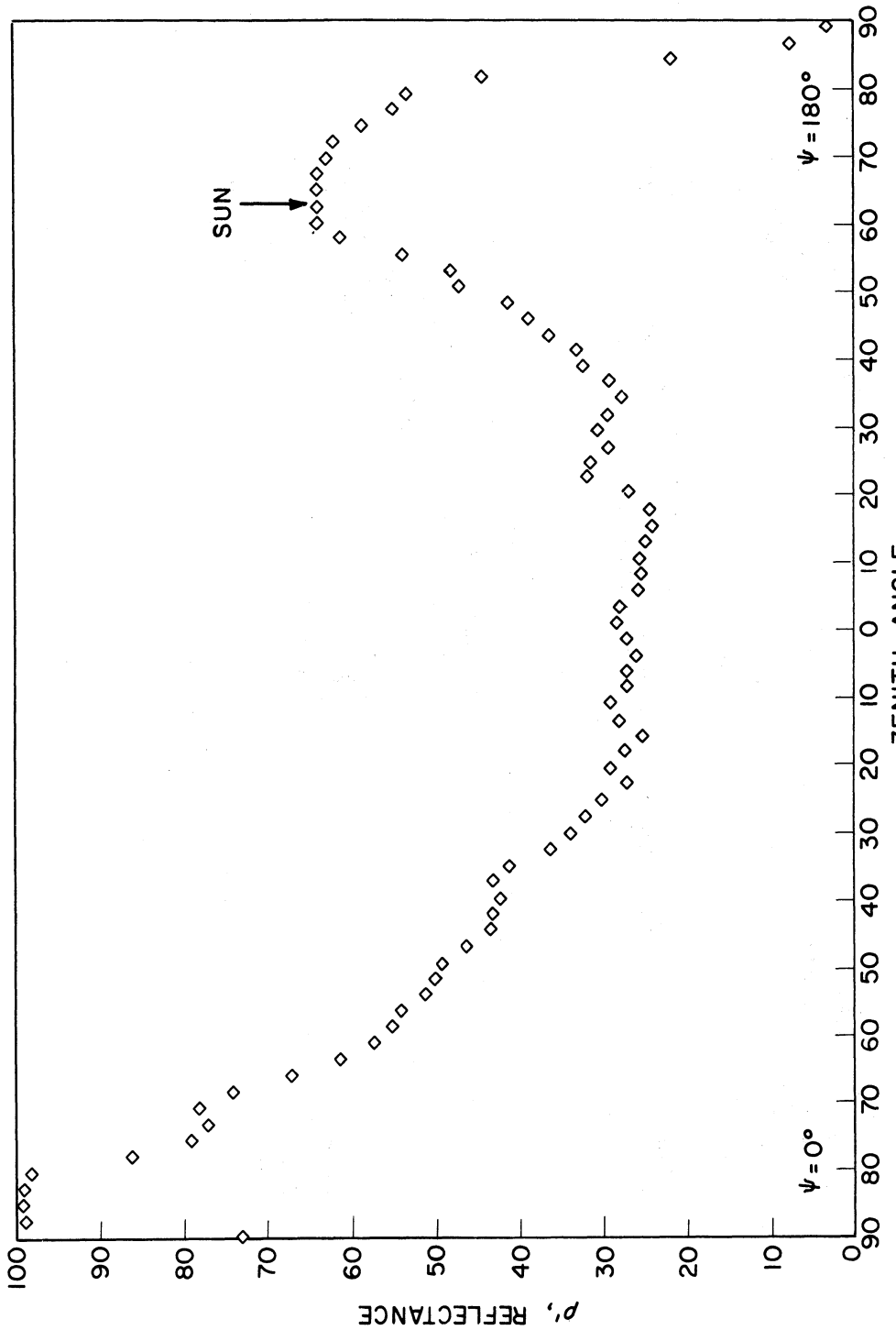

Figure 47. Bidirectional reflectance of snow covered earth and atmosphere in principal plane, 10 March, 1965 balloon flight. θ_o = 68.3-66.0°.

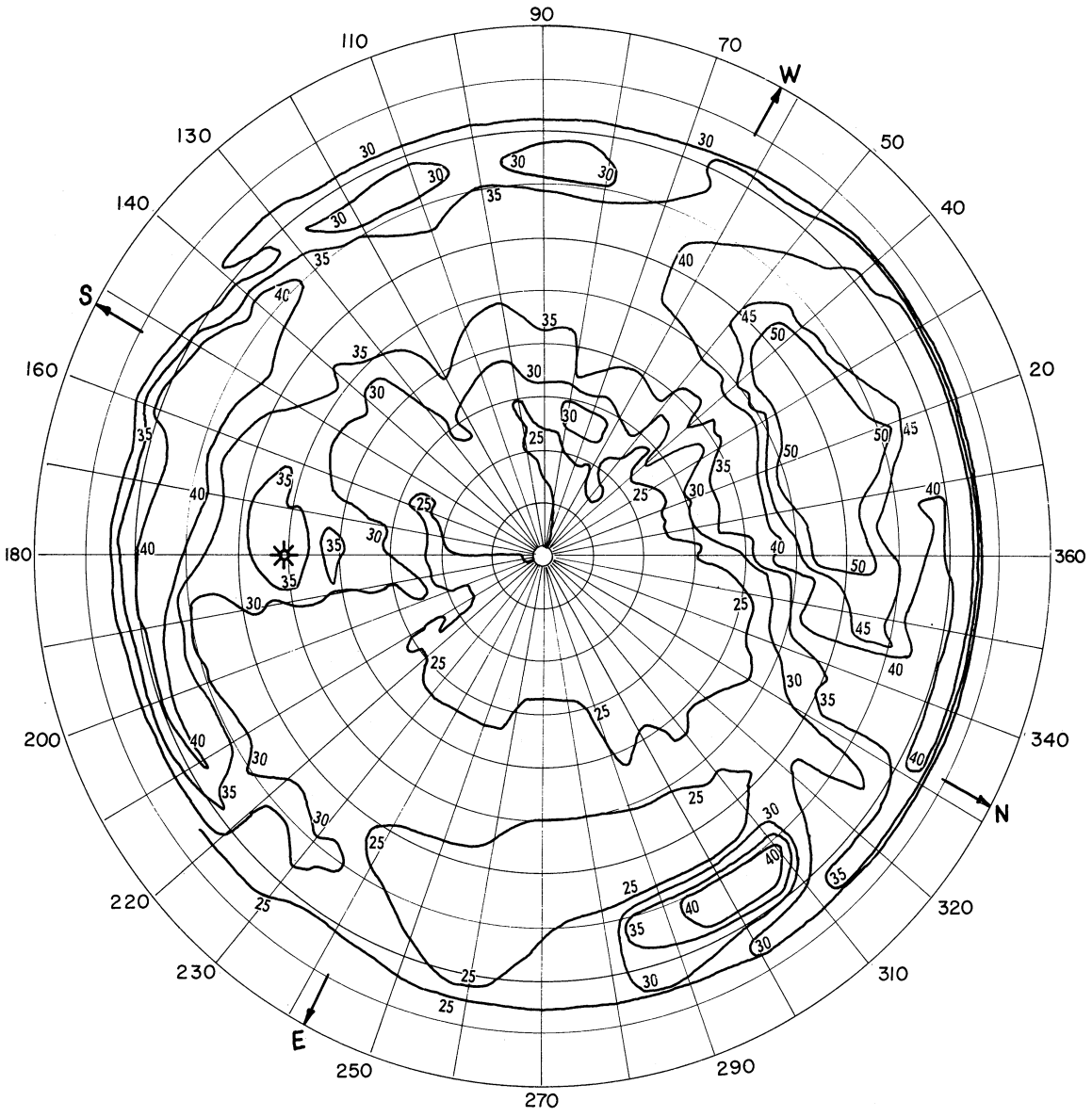

Figure 48. Bidirectional reflectance diagram obtained at 1109-1116 CST on 10 March, 1965 balloon flight. θ_o = 50.5-50.0°, balloon pressure altitude = 8.5-8.3 mb.

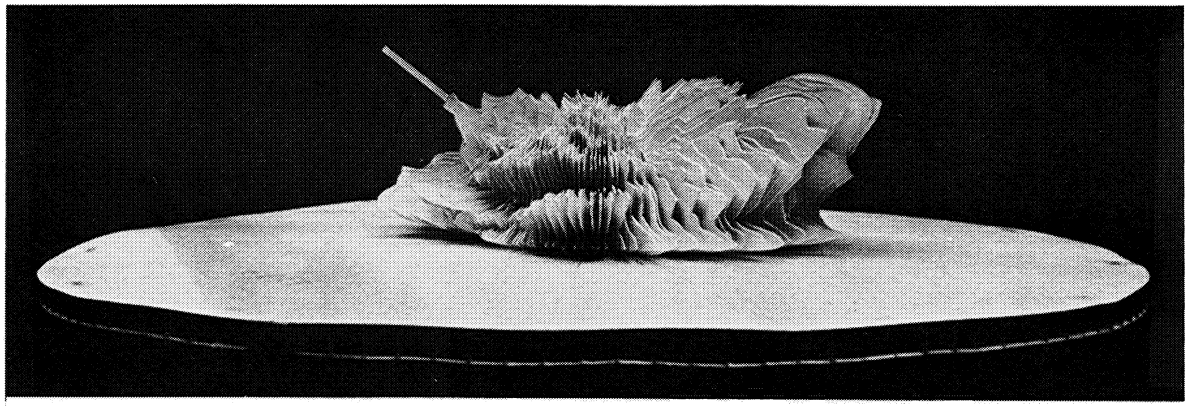

(a) View from N.E.

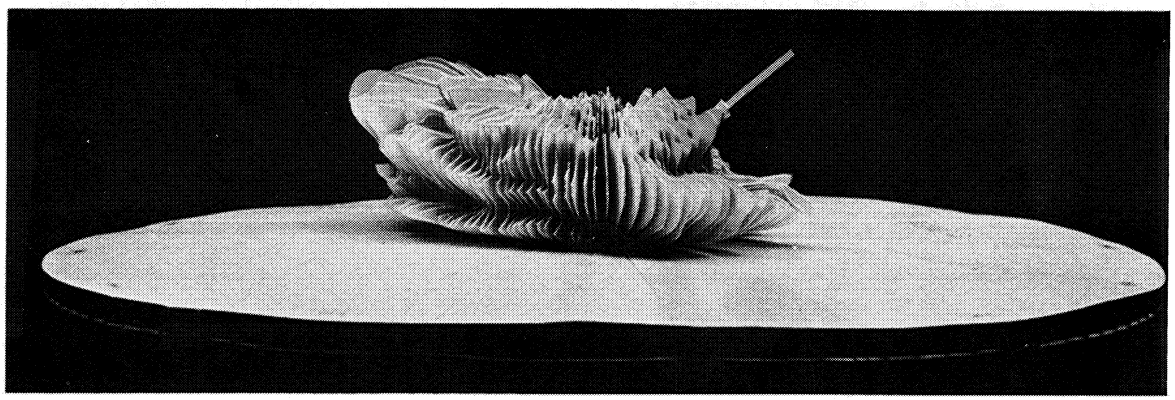

(b) View from South.

Figure 49. Photos of model of 1109-1116 CST bidirectional reflectance pattern. θ_o = 50.5-50.0°.

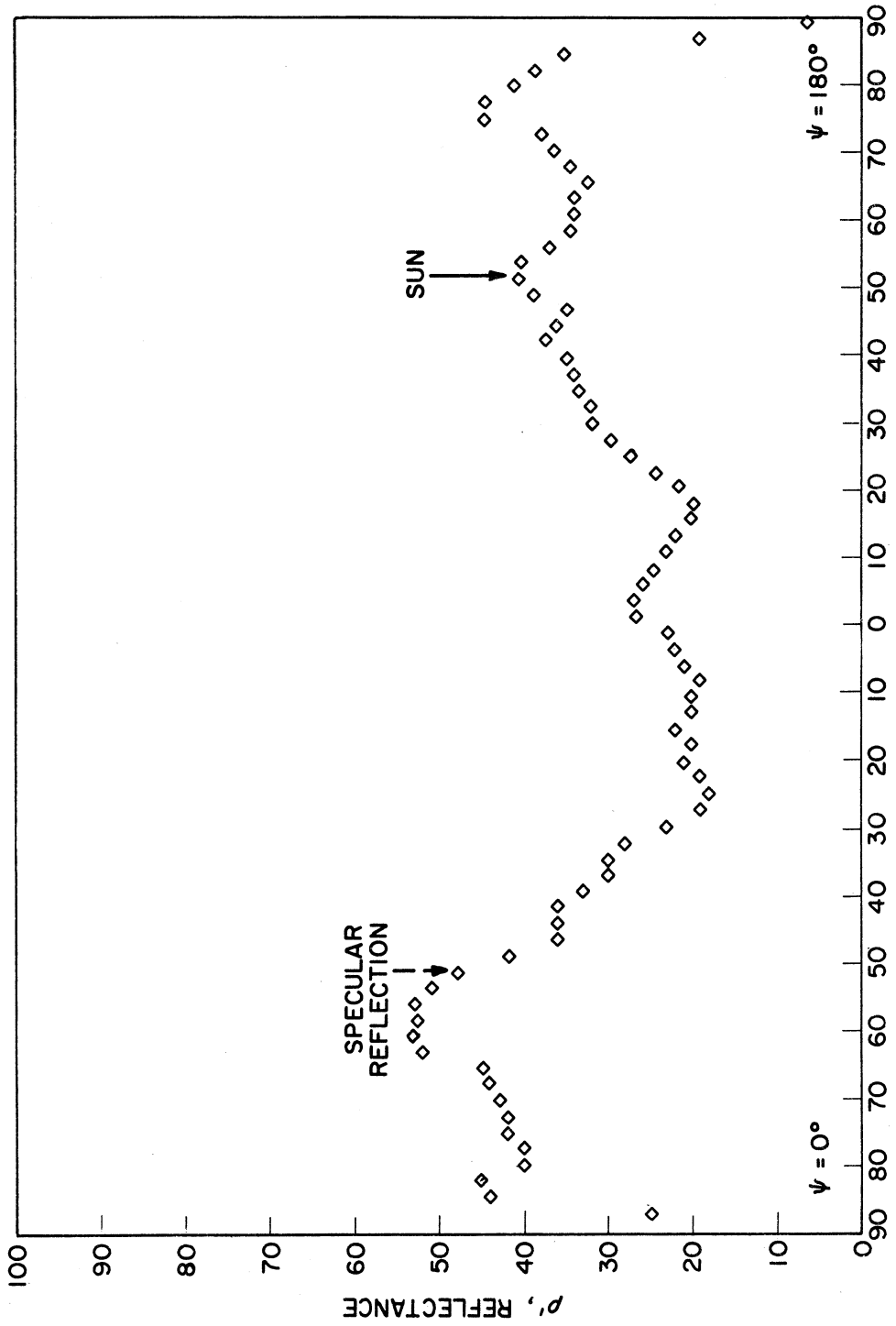

Figure 50. Bidirectional reflectance of snow covered earth and atmosphere in principal plane, 10 March, 1965 balloon flight. θ_o = 50.5-50.0°.

the characteristics of the solar radiation reflected and scattered back out into space by the earth.

1. Nonisotropic Earth Reflectance

The balloon flight measurements of the bidirectional reflectance patterns of the low altitude stratocumulus cloud and the partially snow-covered earth under clear sky conditions are two examples of the extremely nonisotropic nature of the earth's reflectance. The departure from isotropy is greatest at low sun angles, when the very large forward and backscattering peaks put most of the reflected radiation into near-horizontal directions. With increasing sun elevation the departure from isotropy becomes smaller. Although the reflectance patterns for conditions of clear skies and water basins, or clear skies and bare soil or vegetation covered earth have not been measured from balloon flights, the reflectance patterns for these cases should show the same type of nonisotropy because of the large forward scattering of aerosol containing atmosphere and the forward and backscattering of soils and vegetation noted in Section III-D. The reflectance patterns may be nonisotropic to a smaller degree than noted above, but qualitatively they should be the same with greatest nonisotropy for greatest solar zenith angles.

The magnitude of error which might be obtained in the interpretation of satellite radiation measurements can be demonstrated by application of the calculation technique of Bandeen[1] to the balloon flight measured reflectance patterns. Recall that in Bandeen's work the maximum solar zenith angle was 70° and the maximum nadir angle of the radiometer optical axis was 45° for the data used in the study.

If we apply these conditions to the reflectance pattern for stratocumulus clouds, that is assuming that the directional reflectance can be

obtained as the average bidirectional reflectance for nadir angles from 0 to 45°, we will obtain the results indicated in Figure 51. For sun elevation angles > 45°, the apparent directional reflectance r' is greater than r, for sun elevation angles < 45°, r' < r. The average, A', of r' for sun zenith angles of 0-70° is 54.9% whereas the true average A of r over all zenith angles is 61.4%. Thus the assumption of isotropic reflectance combined with Bandeen's limitations for radiometer sampling would produce an earth albedo 89.4% of the true value.

Application of Bandeen's conditions to the three reflectance patterns measured for clear sky, partial snow cover gave the following results.

θ_o	r	r'	r/r'
72.2-71.5°	35.8	29.3	1.22
68.3-66.0°	36.2	30.8	1.17
50.5-50.0°	30.1	26.7	1.13

Thus in this case a lower directional reflectance would be obtained for all three sun zenith angles.

These results are especially significant in the light of the fact that Bandeen's albedo was low by perhaps as much as 60%.

2. The Wavelength Dependence of Earth Reflectance

The balloon flight measurements made with the TIROS and NIMBUS radiometers also demonstrate the wavelength dependence of earth reflectance. Figure 52 shows three smooth curves obtained from Figures 32, 35, and 36 which show plots of the ratio ρ_3'/ρ_5' vs. ρ_5'. These demonstrate that the reflectance in the 0.55-0.75-micron region of the spectrum can be different from the average reflectance over the entire range of the solar

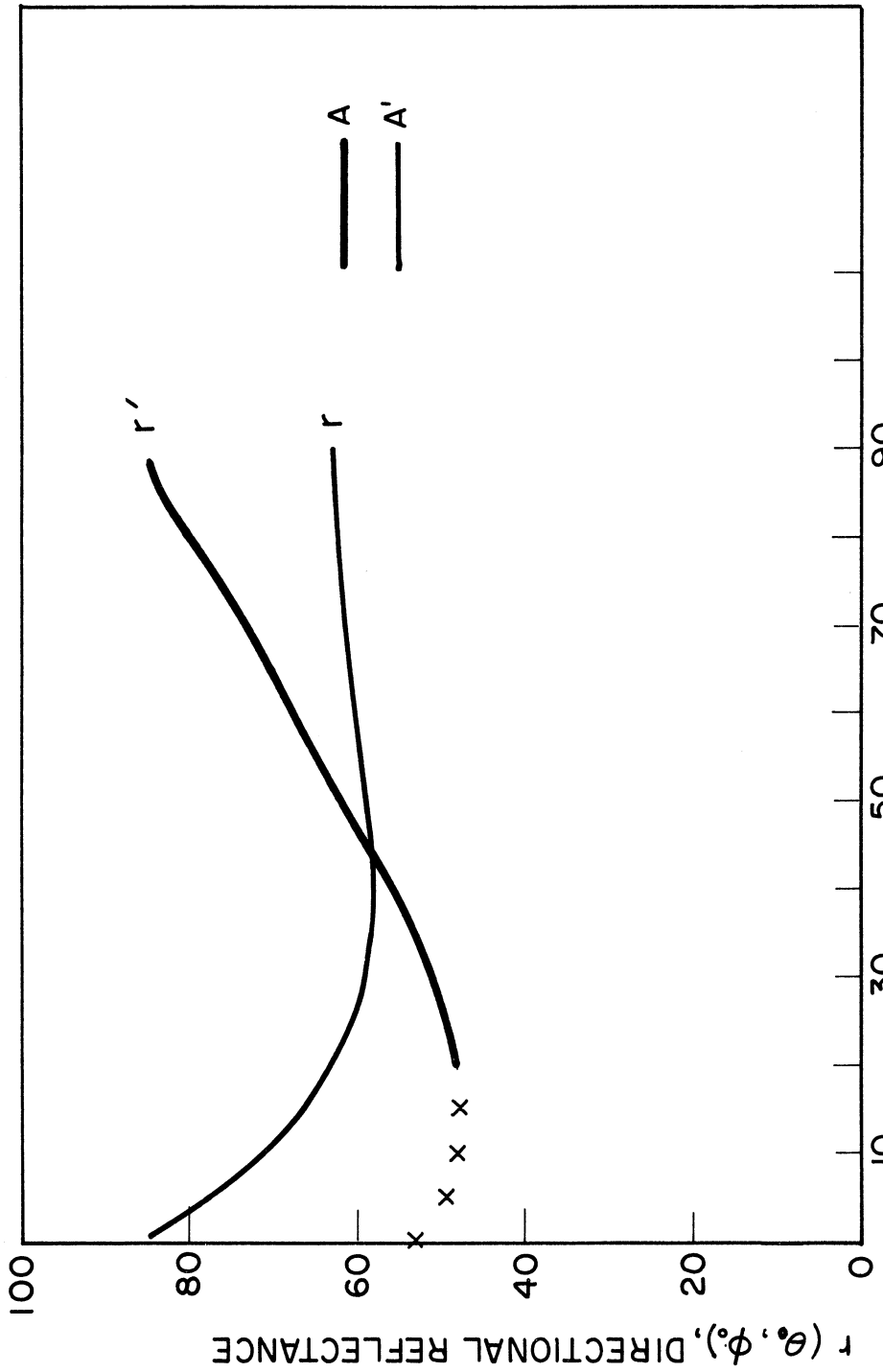

Figure 51 Directional reflectance of stratocumulus cloud as a function of sun elevation angle (r is true directional reflectance, r' is result obtained for average of bidirectional reflectance for radiometer nadir angles of 0-45°).

spectrum 0.2-4.0 microns.

The experimental data has been supplemented with theoretically calculated data points obtained from selected spectral reflectance curves of various types by calculating the true average reflectance and predicted instrument measured reflectances for the spectral response regions of the two channels of the F-1 MRIR radiometers. The results are shown in Table 8, and the ratio of the predicted measured reflectances are plotted in Figure 52. The calculated data are in agreement with the curves measured by the radiometers.

It is quite clear that the spectral dependence of the reflected solar radiation varies considerably with the scene viewed, and that measurements with the radiometer narrow band channel (0.55-0.86 micron) cannot be used for earth albedo without the application of a correction factor. The correction factor however cannot be calculated without a detailed knowledge of the narrow band readings so used.

In addition an inspection of Table 8 shows that for spectral distributions typical of vegetation, the narrow band channel does not measure the true average reflectance over the 0.55-0.75-micron range.

TABLE 8

THEORETICAL F-1 MRIR REFLECTANCE MEASUREMENTS

Spectral Reflectance Curve	0.5-0.86 Micron		0.2-5.0 Microns		ρ'_3/ρ'_5
	ρ_5	ρ'_5	ρ_3	ρ'_3	
Middle layer clouds (Fig. 99)	71.0	71.4	65.9	64.5	.90
Green leaf (Like Fig. 84 curve 4)	26.1	15.6	26.4	27.3	1.75
Dry sand[a] (Like Fig. 82)	13.5	13.4	11.8	12.2	.91
Pinus strobus[a] (Like Fig. 86)	18.0	10.9	18.1	19.6	1.80
Clear sky[a,b] (Fig. 53)	8.6	6.9	14.0	16.0	2.32

[a]Reflectance curves modified by H_2O absorption bands.

[b]Spectral reflectance curve measured over South Dakota on 26 June, 1963 with clear sky.

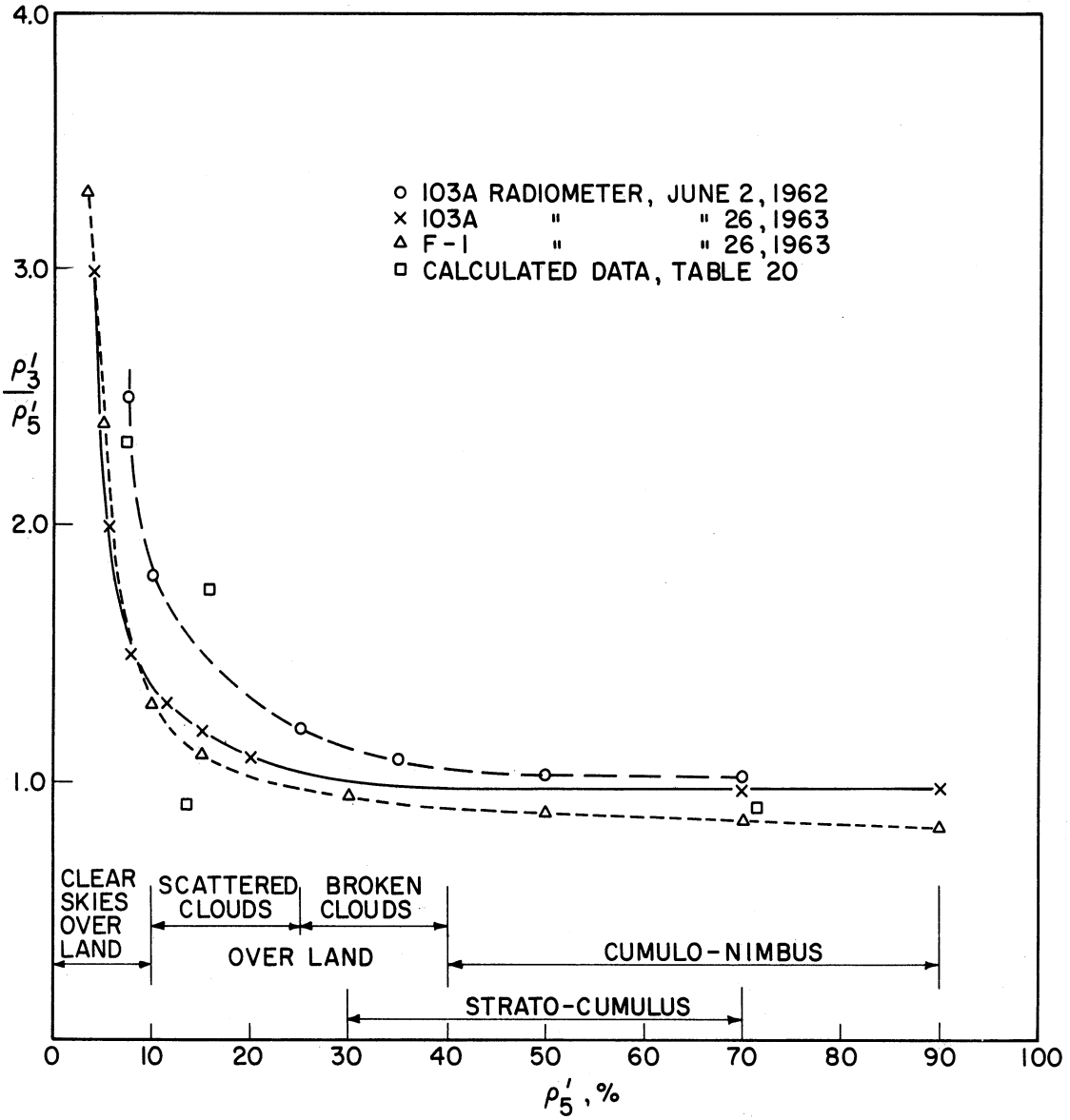

Figure 52. Reflectance diagram demonstrating spectral dependence of earth reflectance.

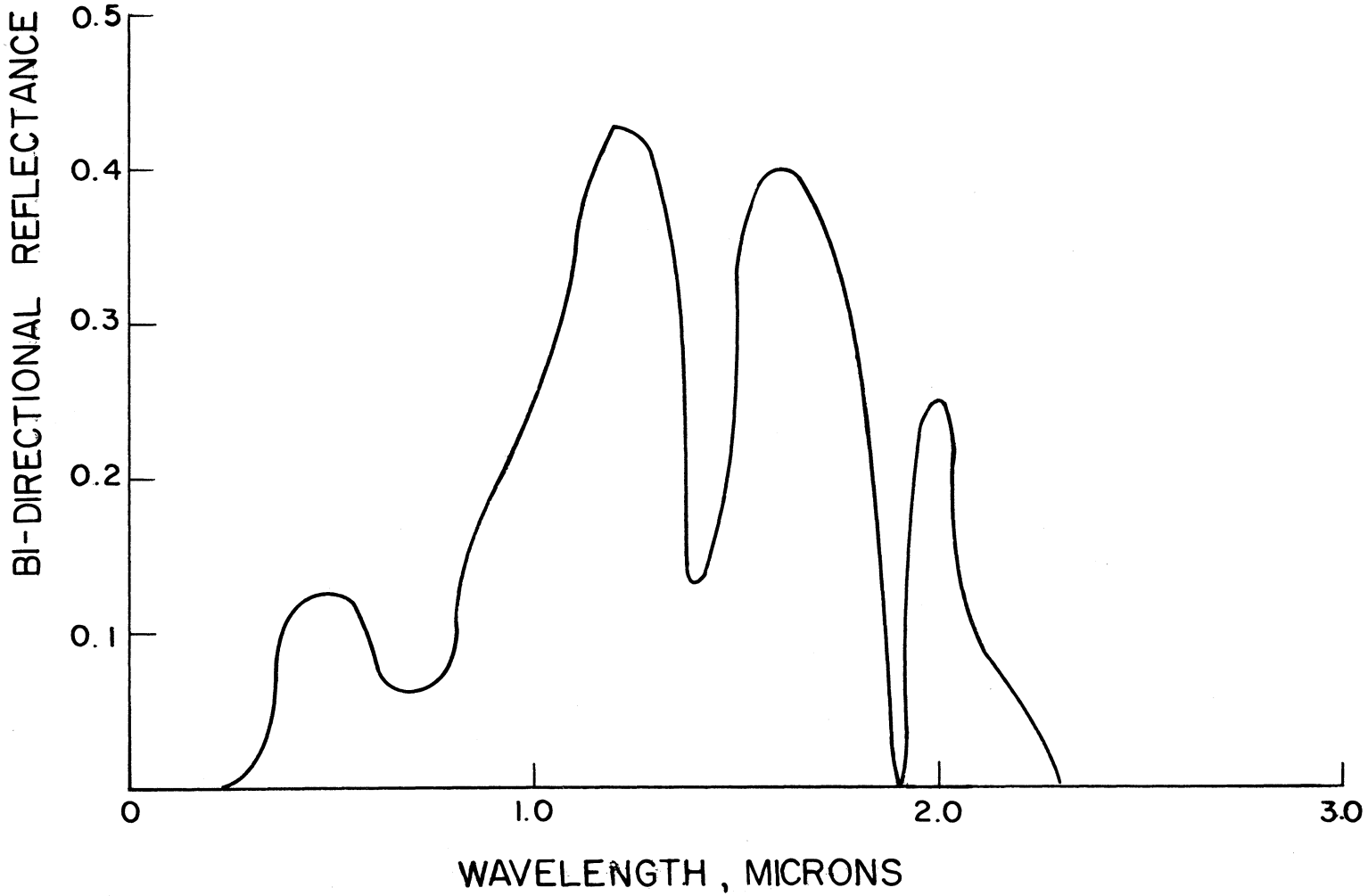

Figure 53. Spectral reflectance curve of earth measured through clear skies from balloon over South Dakota, 26 June, 1963.

V. A MODEL OF THE EARTH FOR ALBEDO PURPOSES

A model of the earth for albedo purposes must be based on the precise definition of earth's albedo which is contained in Equation (19a) i.e.,

$$A(t) = \frac{\int_{\lambda}\int_{\theta_o}\int_{\phi_o'}\int_{\theta}\int_{\psi} \rho_{\lambda}(\theta_o,\phi_o,\theta,\psi,t)H_{s\lambda}(t)\sin\theta_o\cos\theta_o\sin\theta\cos\theta d\psi d\theta d\phi_o' d\theta d\lambda}{\pi^2 \int_{\lambda} H_{s\lambda}(t)d\lambda} \qquad (19a)$$

A. GEOMETRICAL CHARACTERISTICS

The coordinate system (θ_o,ϕ_o') which is used for integration over the earth's surface is that shown in Figure 4a, i.e., one determined by the position of the sun. Now the portion of the earth's surface which lies at any position of this coordinate system continuously changes because of the changing sun's declination and the earth's rotation on its axis. Even though this information is implicitly specified by t, for practical purposes we will indicate that we must know $\rho_{\lambda}(\theta_o,\phi_o,\theta,\psi,\zeta',\eta',t)$ where ζ' is longitude west of the Greenwich meridian and is the angular distance south of the north pole (colatitude).

The relations between t and (ζ',η') can be calculated with the help of Figure 4b. From the law of sines of a spherical triangle, we have

$$\frac{\cos\delta_s}{-\sin\phi_o} = \frac{\sin\theta_o}{\sin h_s} = \frac{\sin\eta'}{-\sin\phi_o'} \qquad (36)$$

From the law of cosines:

$$\cos\eta' = \cos(90-\delta_s)\cos\theta_o + \sin(90-\delta_s)\sin\theta_o\cos\phi_o' \qquad (37)$$

If we specify the bidirectional reflectance $\rho_\lambda(\theta_o,\phi_o,\theta,\psi,\zeta;\eta;t)$ for every point on the earth's surface, we can perform the integration for earth's albedo indicated by Equation (19a) using the following procedure.

1. Specify t (day of year and GMT).
2. Find δ_s and GHA (of sun). (Tables from the Air Almanac are quite suitable.)
3. For a given (θ_o,ϕ_o') calculate η', h_s, ζ', and ϕ_o, in that order from:

$$\cos \eta' = \cos (90-\delta_s) \cos \theta_o + \sin (90-\delta_s) \sin \theta_o \cos \phi_o' \tag{37}$$

$$\sin h_s = \frac{-\sin \theta_o \sin \phi_o'}{\sin \eta'} \tag{38}$$

$$\zeta' = \text{GHA} - h_s \tag{39}$$

$$\sin \phi_o = \frac{\sin h_s \cos \delta_s}{\sin \theta_o} \tag{40}$$

4. Integrate $\rho_\lambda(\theta_o,\phi_o,\theta,\psi,\zeta;\eta;t)$ over θ,ψ.
5. Repeat the process for all θ_o,ϕ_o' to obtain the integral for A(t).

B. PHYSICAL CHARACTERISTICS

The physical characteristics of this model of earth's albedo are specified by $\rho_\lambda(\theta_o,\phi_o,\theta,\psi,\zeta;\eta;t)$. Although it is not possible at the present time to specify ρ_λ in fine detail for all of the earth's surface it appears that an initial rather precise model could be set up as follows.

Divide the wavelength range into four intervals: 0.2-0.4-0.7-2.0-5.0 microns, containing 9, 40, 45, and 6% of the solar energy, respectively. Bidirectional reflectance functions $\rho_{\lambda i}(\theta_o,\phi_o,\theta,\psi)$ would be estimated for each wavelength interval for at least eight basic earth features:

1. Sandy and/or rocky areas - clear sky.
2. Soil and/or vegetation - clear sky.
3. Ocean - clear sky.
4. Snow - clear sky.
5. Low clouds over ocean.
6. Low clouds over land.
7. Low clouds over snow.
8. High clouds.

With the aid of a careful geographical-climatological study a resultant bidirectional reflectance model:

$$\rho_\lambda(\theta_o,\phi_o,\theta,\psi,\zeta';\eta';t) = \sum_i \alpha_i(\zeta';\eta';t)\rho_{\lambda i}(\theta_o,\phi_o,\theta,\psi) \qquad (41)$$

where

$$\sum_i \alpha_i(\zeta';\eta';t) = 1 \qquad \text{for any } (\zeta';\eta';t) \qquad (42)$$

would be set up for each of approximately 100 areas on each hemisphere of the earth. The (ζ',η') areas might be arranged as follows in each hemisphere:

Latitude	$\Delta\eta'$	$\Delta\zeta'$
0	10°	20°
10	10°	20°
20	15°	20°
35	15°	20°
50	17.5°	30°
67.5	22.5°	45°
90		

For a complete study models should be made for one day in each month of the year, although four days, 21 March, 21 June, 20 September, 20 December could be studied first. With each model, diurnal variations of albedo could be revealed by making calculations at 4-8 evenly spaced values of time on each day. The directional characteristics of the reflectance of radiation out into space could be calculated to help in the interpretation of satellite experiments and earth based experiments such as those of Danjon.

C. ILLUSTRATIVE EXAMPLE

The following simplified example is provided to illustrate, in part but not in comprehensive detail, the type of calculation which can be made with the model proposed. Both the model and calculation have been greatly simplified in this example, as follows:

1. The value of albedo, but not the directional characteristics of radiation reflected back out into space, is calculated for 23 December at 0000 GMT and 1200 GMT.
2. Diffuse reflectance is assumed for all earth features except the ocean and clouds. For these two features directional reflectance data is used.
3. The basic reflectance values are assumed to be averages over the entire solar spectrum.

We can write the precise definition of earth's albedo, Equation (19a), as:

$$A(t) = \frac{1}{\pi} \int_{\theta_o} \int_{\phi'_o} r(\theta_o, \phi_o, \zeta; n; t) \sin\theta_o \cos\theta_o \, d\theta_o \, d\phi'_o \qquad (43)$$

where the directional reflectance is given by:

$$r(\theta_o,\phi_o,\zeta;\eta;t) = \frac{\int_\lambda \int_\theta \int_\phi \rho_\lambda(\theta_o,\phi_o,\theta,\psi,\zeta;\eta;t)H_{s\lambda}(t)\sin\theta\cos\theta d\theta d\psi d\lambda}{\pi \int_\lambda H_{s\lambda}(t)d\lambda} \quad (44)$$

substituting from (41), we have:

$$r(\theta_o,\phi_o,\zeta;\eta;t) = \frac{\sum\alpha_i(\zeta,\eta,t) \int_\lambda \int_\theta \int_\psi \rho_{\lambda i}(\theta_o,\phi_o,\theta,\psi)H_{s\lambda}(t)\sin\theta\cos\theta d\theta d\psi d\lambda}{\pi \int_\lambda H_{s\lambda}(t)d\lambda}$$

$$= \sum \alpha_i(\zeta;\eta;t) \cdot r_i(\theta_o,\phi_o) \quad (45)$$

and thus we have

$$A(t) = \frac{1}{\pi} \int_{\theta_o} \int_{\phi_o'} \sum_i \alpha_i(\zeta;\eta;t)r_i(\theta_o,\phi_o)\sin\theta_o \cos\theta_o \, d\theta_o \, d\phi_o' \quad (46)$$

The basic reflectance models used for this simple calculation

1. Sandy and/or rocky area - clear sky, r_1, = 35
2. Soil and/or vegetation - clear sky, r_2 = 15
3. Ocean - clear sky, $r_3(\theta_o)$ (see Figure 96, curve 2)
4. Snow - northern hemisphere, r_4 = 80 (new snow)
5. Snow - antarctic region, r_5 = 83
6. Cloud cover, $r_6(\theta_o)$ (see Figure 51, curve r)
7. Cloud cover over snow, $r_7(\theta_o) = r_6(\theta_o) + 10$

Note that none of these reflectance models are a function of ϕ_o. The integration over θ_o,ϕ_o was obtained by numerical summation over areas with

$$\Delta\phi'_o = 20° = \frac{\pi}{9} \text{ radians}$$

$$\Delta\theta_o = 10° = \frac{\pi}{18} \text{ radians}$$

Thus:

$$A(t) = \frac{1}{\pi} \sum_{j=1}^{18} \sum_{k=1}^{9} \sum_{i} \alpha_i(\zeta'_{jk},\eta'_{jk},t) r_i(\theta_k) \sin\theta_k \cos\theta_k \Delta\theta_k \Delta\theta'_j \qquad (47)$$

This can be written differently to indicate the order in which the summations were carried out:

$$A(t) = \frac{\pi}{18} \sum_{k=1}^{9} \left\{ \frac{1}{18} \left[\sum_{j=1}^{18} \left\{ \sum_{i} \alpha_i(\zeta'_{jk},\eta'_{jk},t) r_i(\theta_k) \right\} \right] \sin 2\theta_k \right\} \qquad (48)$$

The earth was then divided into (1) land, (2) ocean, or (3) snow-covered areas as shown in Figure 54. The global cloud cover assumed was based on a map of mean cloudiness for the month of November[92] and is shown in Figure 55. In Figure 54, where a given (ζ;η) area contains more than one type of earth surface feature (1,2) or (2,3) they were assumed to be equal in area. Values of the α_i for each (ζ;η') area are shown in Figure 56.

Values of $\delta_s = -23.4366°$ and GHA of 180.3° (at 0000 GMT) and 0.23° (at 1200 GMT) were obtained from the Air Almanac.

Then calculations proceeded as follows:

1. For each ϕ'_j,θ_k area, η'_{jk} and ζ'_{jk} were calculated from:

$$\cos\eta'_{jk} = \cos(90-\delta_s)\cos\theta_k + \sin(90-\delta_s)\sin\theta_k \cos\phi'_j \qquad (49)$$

$$\sin h_s(j,k) = \frac{-\sin\theta_k \sin\phi'_j}{\sin \eta'_{jk}} \qquad (50)$$

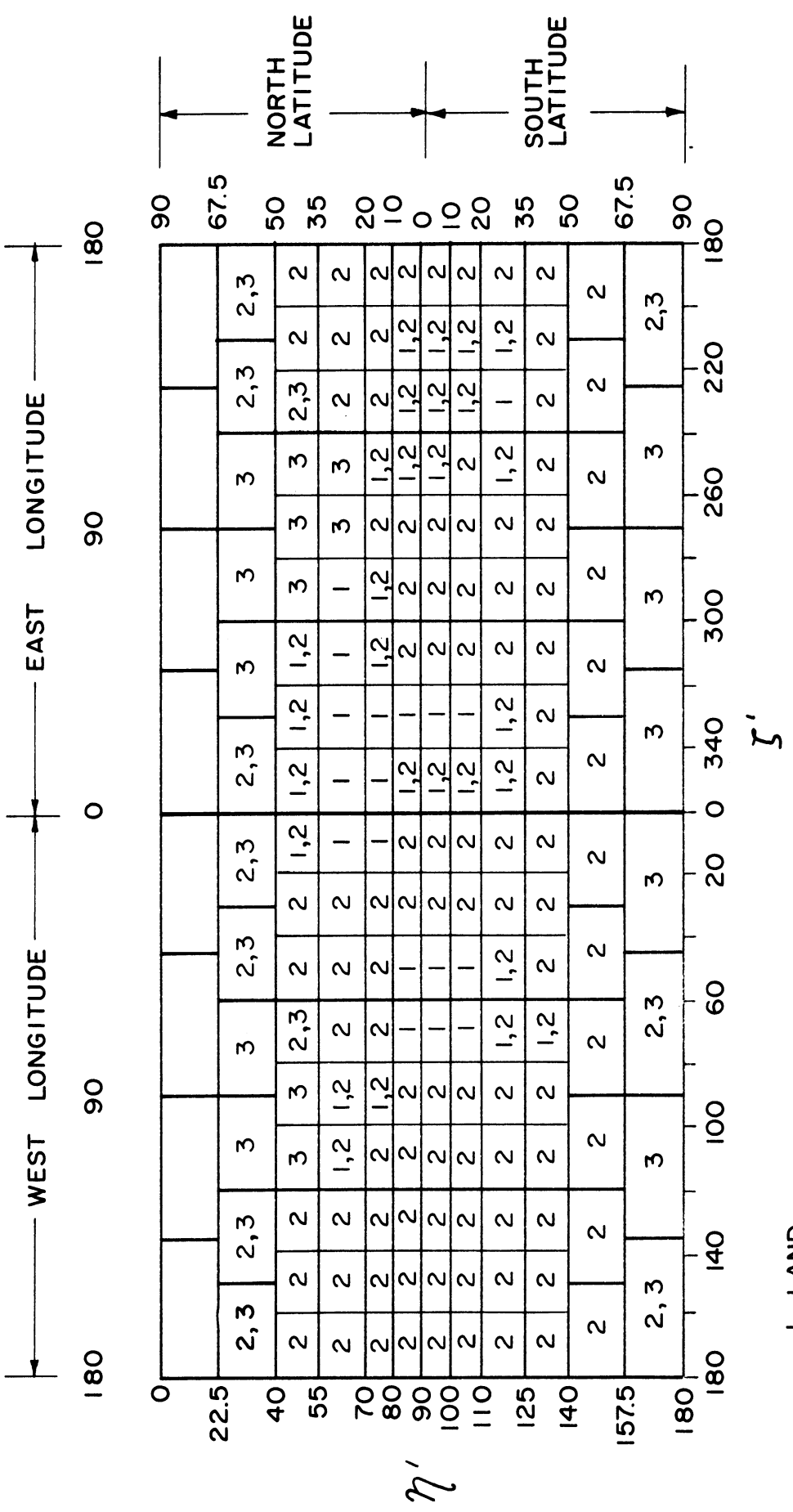

Figure 54. Land, ocean, and snow covered areas of the earth, 23 December.

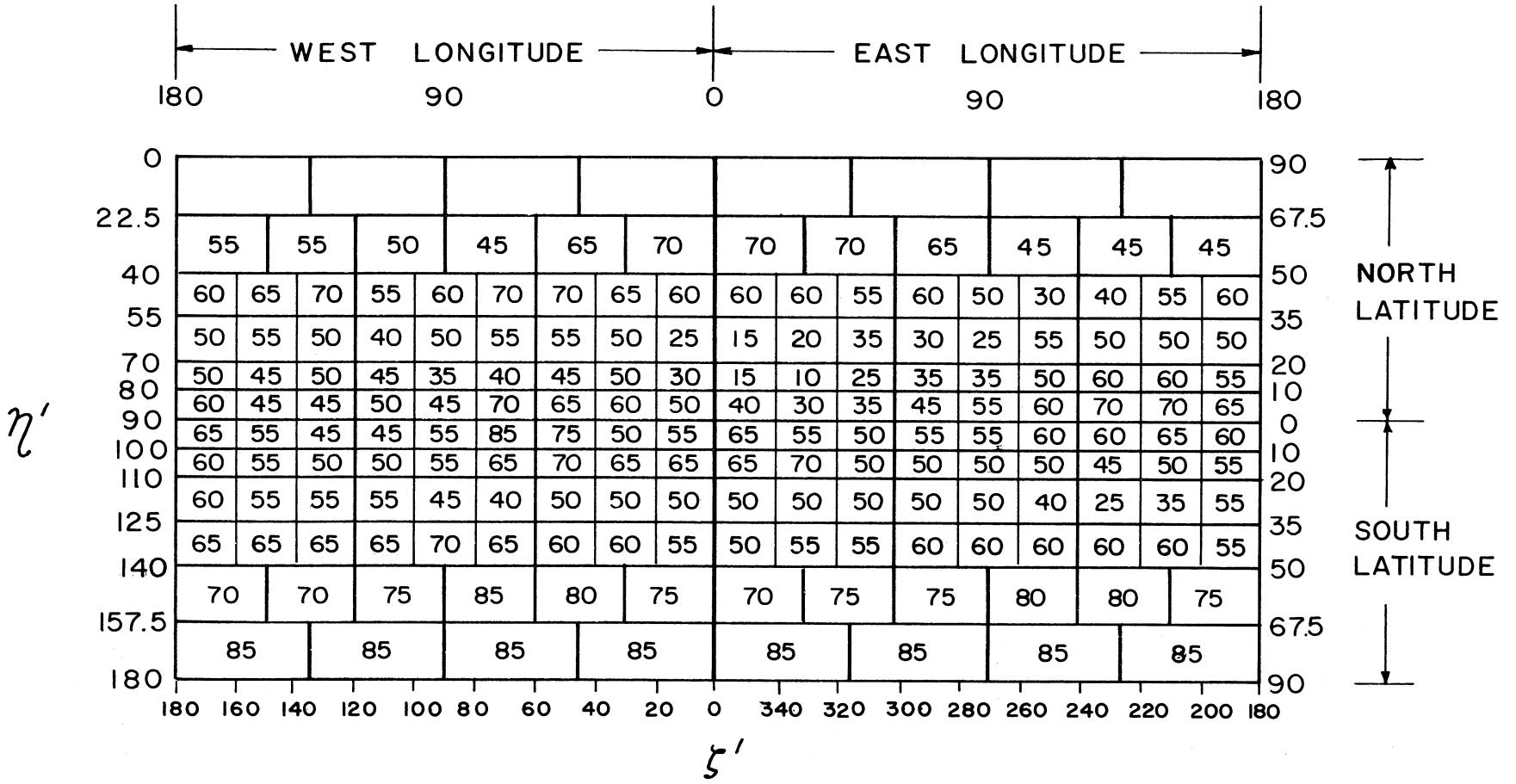

Figure 55. Mean cloudiness of the earth, 23 December.

$$\zeta'_{jk} = GHA - h_s(j,k) \qquad (51)$$

2. The values of ζ'_{jk} and η'_{jk} thus obtained made it possible to calculate the sum over i:

$$\sum_i \alpha_i(\zeta'_{jk},\eta'_{jk},t)r_i(\theta_k)$$

3. and the sum over j:

$$\frac{1}{18} \sum_{j=1}^{18} \left\{ \sum_i \alpha_i(\zeta'_{jk},\eta'_{jk},t)r_i(\theta_k) \right\}$$

4. Finally A(t) was obtained by summing over k.

Values η'_{jk}, ζ'_{jk}, and the sum over i are shown in Tables 9 through 13.

The result obtained showed no diurnal effect, values of A(t) of 41.04 at 0000 GMT and 41.26 at 1200 GMT were obtained. The values of the sum over j are plotted as a function of θ_k in Figure 57. In this figure the increase of reflectance at high solar zenith angles is obvious. Recall that directional effects were included only for ocean and cloud, but since the earth is nearly 80% ocean and average cloud cover is better than 55%, the directional effect is seen in the final results.

Diurnal effects were minimized by the fact that the calculation was made for a day on which the sun was farthest south, thus emphasizing the large ocean areas of the southern hemisphere. It is expected that a diurnal effect would be noticeable when the sun was farther north, and a diurnal change from mainly ocean area to mainly land area would occur.

An additional factor which would serve to minimize diurnal variations, is the smoothing effect contained in the cloud cover distribution

TABLE 9

ILLUSTRATIVE EXAMPLE, VALUES OF η'_{jk}

				K	1	2	3	4	5	6	7	8	9
				θ_k	5	15	25	35	45	55	65	75	85
				$\sin \theta_k$	.0872	.2588	.4226	.5736	.7071	.8192	.9063	.9659	.9962
				$\cos \theta_k$	.9962	.9659	.9063	.8192	.7071	.5736	.4226	.2588	.0872
j	ϕ'_j	$\sin \phi'_j$	$\cos \phi'_j$	$\sin 2\theta_k$	0.1736	0.5000	0.7660	0.9397	1.0000	0.9397	0.7660	0.5000	0.1736
1	10	.1736	.9848		108.5	98.6	88.8	78.9	69.1	59.2	49.4	39.7	30.1
2	30	.5000	.8660		109.1	100.3	91.4	82.6	73.7	65.0	56.5	48.4	40.8
3	50	.7660	.6428		110.2	103.4	96.4	89.3	82.2	75.2	68.5	62.2	56.4
4	70	.9397	.3420		111.7	107.7	103.2	98.4	93.4	88.4	83.3	78.5	73.9
5	90	1.0000	———		113.4	112.6	111.2	109.0	106.4	103.3	97.7	95.9	92.0
6	110	.9397	-.3420		115.1	117.8	119.6	120.4	120.2	119.0	116.9	114.0	113.3
7	130	.7660	-.6428		116.6	122.5	127.6	131.6	134.3	135.4	134.6	132.3	128.5
8	150	.5000	-.8660		117.8	126.2	134.2	141.4	147.5	151.6	152.7	150.5	145.7
9	170	.1736	-.9848		118.4	128.2	138.0	147.6	157.0	165.6	170.7	167.3	159.2
10	190	- .1736	-.9848		118.4	128.2	138.0	147.6	157.0	165.6	170.7	167.3	159.2
11	210	- .5000	-.8660		117.8	126.2	134.2	141.4	147.5	151.6	152.7	150.5	145.7
12	230	- .7660	-.6428		116.6	122.5	127.6	131.6	134.3	135.4	134.6	132.3	128.5
13	250	- .9397	-.3420		115.1	117.8	119.6	120.4	120.2	119.0	116.9	114.0	113.3
14	270	-1.0000	———		113.4	112.6	111.2	109.0	106.4	103.3	97.7	95.9	92.0
15	290	- .9397	.3420		111.7	107.7	103.2	98.4	93.4	88.4	83.3	78.5	73.9
16	310	- .7660	.6428		110.2	103.4	96.4	89.3	82.2	75.2	68.5	62.2	56.4
17	330	- .5000	.8660		109.1	100.3	91.4	82.6	73.7	65.0	56.5	48.4	40.8
18	350	- .1736	.9848		108.5	98.6	88.8	78.9	69.1	59.2	49.4	39.7	30.1

TABLE 10

ILLUSTRATIVE EXAMPLE, VALUES OF ζ'_{jk} FOR GHA = 180.3° (0000 GMT)

				K	1	2	3	4	5	6	7	8	9
				θ_k	5	15	25	35	45	55	65	75	85
				sin θ_k	.0872	.2588	.4226	.5736	.7071	.8192	.9063	.9659	.9962
				cos θ_k	.9962	.9659	.9063	.8192	.7071	.5736	.4226	.2588	.0872
j	ϕ'_j	sin ϕ'_j	cos ϕ'_j	sin $2\theta_k$	0.1736	0.5000	0.7660	0.9397	1.0000	0.9397	0.7660	0.5000	0.1736
1	10	.1736	.9848		181.2	182.9	184.5	186.1	187.8	189.8	192.3	195.5	200.5
2	30	.5000	.8660		182.9	187.9	192.5	197.1	201.9	207.2	213.2	220.5	230.0
3	50	.7660	.6428		184.4	192.1	199.3	206.4	213.4	220.8	228.6	237.2	246.7
4	70	.9397	.3420		185.4	195.1	204.4	213.3	222.0	230.7	239.3	248.2	257.3
5	90	1.0000	———		185.8	196.6	207.3	217.6	227.8	237.7	246.4	256.5	265.7
6	110	.9397	- .3420		185.5	196.3	207.5	219.0	230.5	242.0	253.0	263.8	270.3
7	130	.7660	- .6428		184.6	193.9	204.4	216.3	229.6	243.6	257.5	270.3	283.1
8	150	.5000	- .8660		183.1	189.5	197.4	207.7	221.4	239.8	261.5	281.4	298.2
9	170	.1736	- .9848		181.3	183.6	186.6	191.0	198.6	215.2	257.1	310.6	331.2
10	190	- .1736	- .9848		179.3	177.0	174.0	169.6	162.0	145.4	103.5	50.0	29.4
11	210	- .5000	- .8660		177.5	171.1	163.2	152.9	139.2	120.8	99.1	79.2	62.4
12	230	- .7660	- .6428		176.0	166.7	156.2	144.3	131.0	117.0	103.1	90.3	77.5
13	250	- .9397	- .3420		175.1	164.3	153.1	141.6	130.1	118.6	107.6	96.8	90.3
14	270	-1.0000	———		174.8	164.0	153.3	143.0	132.8	122.9	114.2	104.1	94.9
15	290	- .9397	.3420		175.2	165.5	156.2	147.3	138.6	129.9	121.3	112.4	103.3
16	310	- .7660	.6428		176.2	168.5	161.3	154.2	147.2	139.8	132.0	123.4	113.9
17	330	- .5000	.8660		177.7	172.7	168.1	163.5	158.7	153.4	147.4	140.1	130.6
18	350	- .1736	.9848		179.4	177.7	176.1	174.5	172.8	170.8	168.3	165.1	160.1

TABLE 11

ILLUSTRATIVE EXAMPLE, VALUES OF ζ'_{jk} FOR GHA = 0.23° (1200 GMT)

				K	1	2	3	4	5	6	7	8	9
				k	5	15	25	35	45	55	65	75	85
				$\sin \theta_k$	.0872	.2588	.4226	.5736	.7071	.8192	.9063	.9659	.9962
				$\cos \theta_k$	.9962	.9659	.9063	.8192	.7071	.5736	.4226	.2588	.0872
j	ϕ'_j	$\sin \phi'_j$	$\cos \phi'_j$	$\sin 2\theta_k$	0.1736	0.5000	0.7660	0.9397	1.0000	0.9397	0.7660	0.5000	0.1736
1	10	.1736	.9848		1.1	2.8	4.4	6.0	7.7	9.7	12.2	15.4	20.4
2	30	.5000	.8660		2.8	7.8	12.4	17.0	21.8	27.1	33.1	40.4	49.9
3	50	.7660	.6428		3.3	12.0	18.2	26.3	33.3	40.7	48.5	57.1	66.6
4	70	.9397	.3420		5.3	15.0	24.3	33.2	41.9	50.6	59.2	68.1	77.2
5	90	1.0000	———		5.7	16.5	27.2	37.5	47.7	57.6	66.3	76.4	85.6
6	110	.9397	-.3420		5.4	16.2	27.4	38.9	50.4	61.9	72.9	83.7	90.2
7	130	.7660	-.6428		4.5	13.8	24.3	36.2	49.5	63.5	77.4	90.2	103.0
8	150	.5000	-.8660		3.0	9.4	17.3	27.6	41.3	59.7	81.4	101.3	118.1
9	170	.1736	-.9848		1.2	2.5	6.5	10.9	18.5	35.1	77.0	130.5	151.1
10	190	- .1736	-.9848		-0.8	- 3.1	- 6.1	-10.5	-18.1	-34.7	-76.6	-130.1	-150.7
11	210	- .5000	-.8660		-2.6	- 9.0	-16.9	-27.2	-40.9	-59.3	-81.0	-100.9	-117.7
12	230	- .7660	-.6428		-4.1	-13.4	-23.9	-35.8	-49.1	-63.1	-77.0	-89.8	-102.6
13	250	- .9397	-.3420		-5.0	-15.8	-27.0	-38.5	-50.0	-61.5	-72.5	-83.3	- 89.8
14	270	-1.0000	———		-5.3	-16.1	-26.8	-37.1	-47.3	-57.2	-65.9	-76.0	- 85.2
15	290	- .9397	.3420		-4.9	-14.6	-23.9	-32.8	-41.5	-50.2	-58.8	-67.7	- 76.8
16	310	- .7660	.6428		-3.9	-11.6	-18.8	-25.9	-32.9	-40.3	-48.1	-56.7	- 66.2
17	330	- .5000	.8660		-2.4	- 7.4	-12.0	-16.6	-21.4	-26.7	-32.7	-40.0	- 49.5
18	350	- .1736	.9848		-0.7	- 2.4	- 4.0	- 5.6	- 7.3	- 9.3	-11.8	-15.0	- 20.0

TABLE 12

ILLUSTRATIVE EXAMPLE, VALUES OF $\sum_i$ FOR GHA = 180.3°, (0000GMT)

				K	1	2	3	4	5	6	7	8	9
				θ_k	5	15	25	33	45	55	65	75	85
				$\sin \theta_k$	.0872	.2588	.4226	.5736	.7071	.8192	.9063	.9659	.9962
				$\cos \theta_k$	.9962	.9659	.9063	.8192	.7071	.5763	.4226	.2588	.0872
j	ϕ'_j	$\sin \phi'_j$	$\cos \phi'_j$	$\sin 2\theta_k$	0.1736	0.5000	0.7660	0.9397	1.0000	0.9397	0.7660	0.5000	0.1736
1	10	.1736	.9848		35.9	38.8	4.07	34.4	31.5	33.1	41.9	60.5	73.3
2	30	.5000	.8660		35.9	35.9	37.8	40.0	36.8	33.1	37.3	58.6	71.7
3	50	.7660	.6428		35.9	35.9	37.8	42.7	41.1	38.1	31.3	46.6	84.4
4	70	.9397	.3420		35.9	35.9	35.0	41.9	38.8	42.9	46.6	43.6	56.5
5	90	1.0000	———		35.9	35.9	27.3	34.4	35.1	37.9	42.1	48.1	67.7
6	110	.9397	-.3420		35.9	35.9	27.3	26.9	40.7	36.2	38.9	46.6	66.5
7	130	.7660	-.6428		35.9	35.9	37.8	37.2	36.8	38.1	41.9	50.5	68.8
8	150	.5000	-.8660		35.9	35.9	35.0	45.5	47.4	48.2	51.2	55.0	72.3
9	170	.1736	-.9848		35.9	35.9	35.0	45.5	44.8	56.3	72.4	77.3	87.3
10	190	- .1736	-.9848		38.8	40.3	40.7	42.7	41.1	56.3	72.4	77.3	87.3
11	210	- .5000	-.8660		38.8	40.3	40.7	42.7	41.1	42.9	48.9	60.4	74.6
12	230	- .7660	-.6428		38.8	38.8	40.7	40.0	39.5	40.6	44.2	54.4	63.0
13	250	- .9397	-.3420		38.8	38.8	35.0	34.4	34.2	35.6	39.6	44.7	65.4
14	270	-1.0000	———		38.8	38.8	35.0	34.4	31.5	33.1	34.9	44.7	67.7
15	290	- .9397	.3420		38.8	38.8	35.0	34.4	26.9	30.6	34.9	44.7	65.4
16	310	- .7660	.6428		38.8	38.8	40.7	28.9	26.9	33.1	37.3	46.6	58.2
17	330	- .5000	.8660		38.8	38.8	40.7	37.2	26.9	35.6	39.6	52.5	71.1
18	350	- .1736	.9848		38.8	40.3	37.8	31.7	31.5	33.1	41.9	60.5	73.3
				$\frac{1}{18} \sum_j$	37.35	37.76	36.67	37.49	36.26	39.16	44.63	54.03	70.81
				$\frac{1}{18} [\sum_j] \sin 2\theta_k$	6.48	18.88	28.09	35.23	36.26	36.80	34.19	27.02	12.18

TABLE 13

ILLSUTRATIVE EXAMPLE, VALUES OF $\sum_i$ FOR GHA = 0.23° (1200 GMT)

				K	1	2	3	4	5	6	7	8	9
				θ_k	5	15	25	35	45	55	65	75	85
				$\sin \theta_k$	.0872	.2588	.4226	.5736	.7071	.8192	.9063	.9659	.9962
				$\cos \theta_k$	.9962	.9659	.9063	.8192	.7071	.5736	.4226	.2588	.0872
j	ϕ'_j	$\sin \phi'_j$	$\cos \phi'_j$	$\sin 2\theta_k$	0.1736	0.5000	0.7660	0.9397	1.0000	0.9397	0.7660	0.5000	0.1736
1	10	.1736	.9848		41.7	35.9	35.0	20.6	40.8	39.5	47.1	62.4	74.9
2	30	.5000	.8660		41.7	41.7	35.0	34.5	31.5	33.1	37.3	54.4	71.1
3	50	.7660	.6428		33.0	41.7	35.0	37.2	36.8	30.6	39.6	48.6	67.7
4	70	.9397	.3420		33.0	41.7	40.7	31.7	47.3	41.8	44.4	42.7	64.2
5	90	1.0000	———		33.0	33.0	32.2	40.0	45.1	45.0	46.9	50.8	67.7
6	110	.9397	-.3420		33.0	33.0	32.2	31.7	34.0	30.2	32.9	44.7	65.4
7	130	.7660	-.6428		33.0	33.0	32.2	37.2	36.8	41.8	44.4	54.4	70.0
8	150	.5000	-.8660		33.0	35.9	35.0	45.7	47.4	48.2	53.5	56.5	72.3
9	170	.1736	-.9848		33.0	35.9	35.0	45.5	44.8	70.5	38.7	77.3	76.7
10	190	-.1736	-.9848		35.8	33.0	32.2	42.7	42.1	70.5	72.4	77.3	76.7
11	210	-.5000	-.8660		35.8	33.0	32.2	42.7	44.8	45.7	48.9	58.4	73.4
12	230	-.7660	-.6428		35.8	35.8	35.0	34.4	34.2	38.1	41.9	50.5	68.8
13	250	-.9397	-.3420		35.8	35.8	35.0	34.5	31.5	33.1	37.3	46.6	66.5
14	270	-1.0000	———		35.8	35.8	35.0	45.9	31.5	33.1	37.3	48.6	67.7
15	290	-.9397	.3420		35.8	43.6	46.8	39.4	31.5	34.4	37.1	36.4	50.1
16	310	-.7660	.6428		35.8	43.6	42.2	28.3	27.9	30.7	44.0	46.0	47.9
17	330	-.5000	.8660		43.6	43.6	42.6	29.4	37.3	39.6	40.1	45.9	58.7
18	350	-.1736	.9848		43.6	43.6	29.9	38.2	38.5	38.5	42.1	62.4	74.9
				$\frac{1}{18} \sum_j$	36.23	37.76	35.73	36.63	37.99	41.36	44.49	53.53	67.48
				$\frac{1}{18} [\sum_j] \sin 2\theta_k$	6.29	18.88	27.37	34.42	37.99	38.87	34.08	26.78	11.71

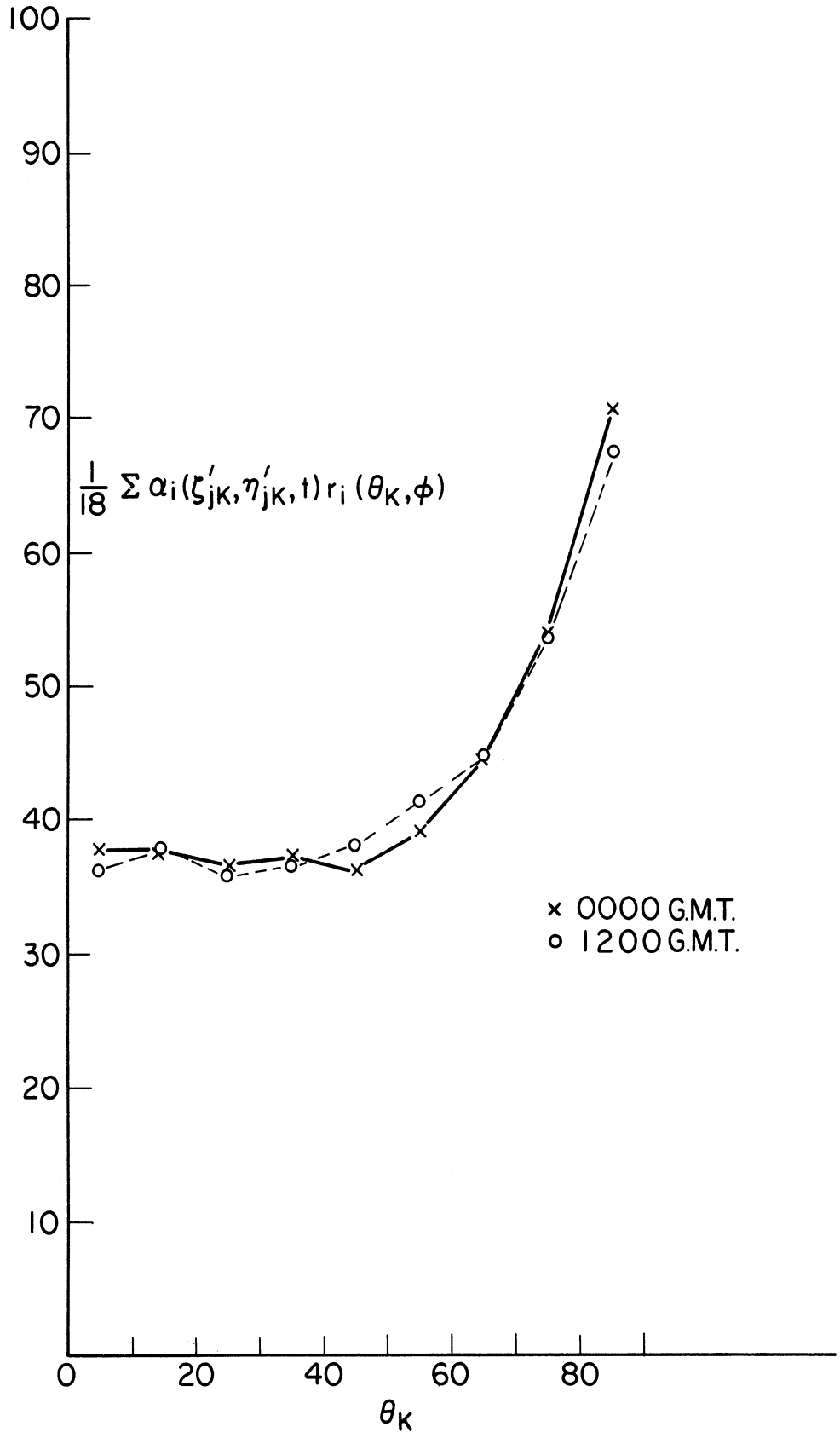

Figure 57. Average albedo in integration ring k vs. θ_k.

chosen, i.e., an average over a month. Thus most (ζ,η') areas contained about 50% cloud cover, with a few showing as low as 15% and a few as high as 85%. Actually on a given day some areas would have 0% and others 100% cloud cover and diurnal variations would be much more noticeable.

VI. CONCLUSIONS AND SUGGESTIONS FOR FURTHER RESEARCH

A. CONCLUSIONS

The above study has been carried out with the ultimate objective of creating a precise model of the earth for albedo purposes, to replace, on a practical basis the isotropic, wavelength independent homogeneous earth model which is usually employed in the analysis of satellite measured relectance data. To this end the following results have been obtained.

1. A precise definition of earth's albedo has been formulated in terms of the distribution of bidirectional reflectance over the surface of the earth (including clouds and the atmosphere).
2. This definition was compared with the Bond definition of planetary albedo which has been employed by astronomers in the interpretation of measurements of photometric earth albedo. The Bond definition was shown to represent earth's albedo only if the earth is homogeneous with perfectly diffuse reflectance.
3. A review of research related to earth's albedo was used to demonstrate that, insofar as albedo is concerned, the earth is obviously nonhomogeneous with wavelength dependent, nonisotropic reflectance. However, in the application of Bond's definition, in the analysis of satellite radiation data, and in general heat balance considerations, these characteristics are usually ignored.

4. New data obtained from outside the earth's atmosphere on three high altitude balloon flights was shown to confirm both the spectral dependence and nonisotropic nature of earth reflectance as follows.

   a. Curves of the ratio of wide band (0.2-4.0 microns) reflectance to narrow band (0.55-0.75 micron) reflectance were shown to be a function of narrow band reflectance. Thus the narrow band channel data cannot be used for earth albedo data over the 0.2-5.0-micron range, as it was by Bandeen, et al., without the application of an appropriate correction factor. Correction factors, obtained from the balloon flight data, were verified by theoretical calculations.

   b. Bidirectional reflectance data for a stratocumulus cloud was shown to verify that cloud reflectance is a scattering process, consistent with theoretical results of Deirmendjian for an approximate cloud model. Using this data the total directional reflectance was calculated for all solar zenith angles and the results were shown to be consistent with measurements by Neiburger. These results were then used to demonstrate the kind of error which could result in the analysis of satellite radiation data based on the assumption of isotropic earth reflectance combined with satellite radiometer data sampling for a limited range of solar zenith angles and radiometer nadir angles.

   c. Bidirectional reflectance data for partially snow covered earth at several solar zenith angles showed pronounced forward scattering for low sun angles and less forward

scattering with a specular reflectance component for a higher sun angle. The reflectance patterns obtained agree qualitatively with surface measurements of snow reflectance.

5. The characteristics of a more precise model of the earth for albedo purposes were discussed. The model would have nonisotropic wavelength dependent reflectance and a nonhomogeneous earth; and would be based on the exact definition of earth albedo formulated in Section II of this paper. The procedure for setting up a first approximation to this model and for calculating earth's albedo from this model was outlined.
6. An illustrative example was carried out with a simplified model of earth reflectance. The example did not have the characteristics of the precise model of the earth. It served only to illustrate the calculation procedure and not the comprehensive detail that can be obtained from the precise model.

B. FURTHER RESEARCH

The precise model of the earth for albedo purposes should be studied more completely.

A geographical climatological study of the earth should be made to determine the number of characteristics of basic bidirectional reflectance patterns $\rho_{\lambda i}$ and the coefficients $\alpha_i(\zeta,\eta,t)$ that are needed for the model.

Additional measurements of bidirectional reflectance patterns should be made of various earth surface features from outside of the earth, and these measurements should be supported by theoretical calculations

of scattering in a real atmosphere including the effects due to multiple-scattering processes, absorption and nonisotropic reflectance at the earth's surface.

The results of the study of the more precise model of the earth should be applied to the planning and analysis of satellite measurements of earth's albedo, to all other albedo experiments, and to theoretical calculations of earth's albedo.

APPENDIX A

EARTH'S ALBEDO FROM MEASUREMENTS OF EARTHLIGHT ON THE MOON

1. THE WORK OF DANJON[9]

The measurements of Danjon[9] were made with a double image photometer. Using this photometer, two images of moon are observed as shown in Figure 58. The two images are arranged so that region B of the sunlit crescent of one image is adjacent to region A of the earthlight of the other image.

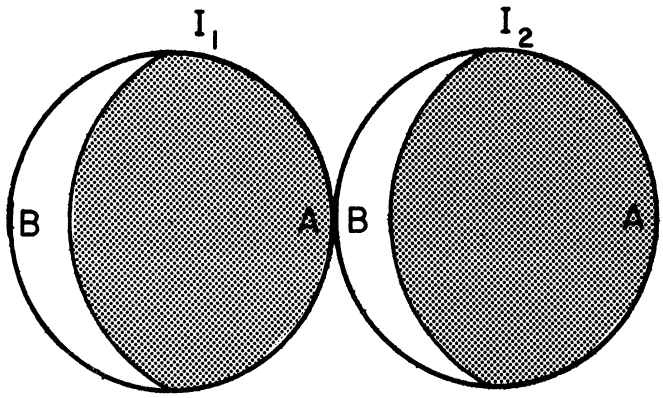

Figure 58. Images in cat-eye photometer.

Image I_1 passes directly through the photometer, but image I_2 passes through the photometer after two reflections from prisms between which is located and adjustable diaphragm. The intensity of B is reduced to that of A by the diaphragm which is calibrated to give the ratio of intensity of the two images. In this fashion, many measurements of the ratio E/C of earthlight to the sunlit crescent were made for phase angles of the moon (η) from about 40 to 165°. This ratio is usually expressed

in stellar magnitudes, i.e., $M_E - M_C = 2.5 \log \frac{C}{E}$. The brightness of the sunlit crescent is also measured relative to the brightness of the sun, i.e., the ratio C/S is measured. The ratio E/S is then calculated from the data and expressed in stellar magnitudes $M_E - M_S = 2.5 \log \frac{S}{E}$. The data $M_E - M_S$ are plotted vs. α, the phase angle of the earth, where:

$$\alpha = 180 - \eta$$

Danjon found that the function:

$$M_E - M_S = 9.99 + 1.30 \left(\frac{\alpha}{100}\right) + 0.19 \left(\frac{\alpha}{100}\right)^2 + 0.48 \left(\frac{\alpha}{100}\right)^3 \qquad (52)$$

was a good fit for data obtained in the photometric region of the spectrum (λ = 0.554 micron) during the years 1926-1935. The constant term is $M_{o\lambda} = 9.99$, equal to the magnitude difference of the apparent brightness of earth at full phase as viewed from the moon and the brightness of the sun at 1 AU (astronomical unit).

If we change the constant term to $R_{o\lambda}$, the magnitude difference of the apparent brightness of earth at 1 AU and the brightness of the sun at 1 AU we have $R_{o\lambda} = 22.94$ (magnitude).

The Bond albedo is then given by:

$$A_\lambda = \frac{R_{o\lambda}}{\sigma^2} \cdot 2 \int_0^{180} \phi_\lambda(\alpha) \sin \alpha \, d\alpha = p_\lambda \cdot q_\lambda \qquad (53)$$

where $\sigma = a/R$ = radius of earth/distance of earth from sun.

Thus we have:

$$\frac{R_{o\lambda}}{\sigma^2} = 22.94 - 21.85 = 1.09 \text{ (magnitude)}$$

and

$$p_\lambda = \frac{R_{o\lambda}}{\sigma^2} = (2.512)^{-1.09} = 0.366$$

$$q_\lambda = 2\int_0^{180} 2.512^{-[1.30(\alpha/100) + 0.19(\alpha/100)^2 + 0.48(\alpha/100)^3]} \sin \alpha d\alpha \qquad (54)$$

$$= 1.095$$

$$A_\lambda = p_\lambda \cdot q_\lambda = 0.366 \cdot 1.095 = 0.40$$

Note that A_λ = 40% is the mean albedo, 1926-1935, in the visible region of the spectrum (i.e., λ = 0.554 micron, approximately).

The accuracy of the method is limited by several factors. Some of the light from the sunlit crescent is scattered by the atmosphere and therefore interferes with the measurement of the ratio C/E. This scattering has greatest effect just before or after full moon, when the earthlight results from a very narrow earth crescent, while the scattered and reflected light is very strong. Danjon states that the double image photometer measurement, with regions A and B on the same diameter, eliminates the effect of scattered light. However, Bakos[11] notes (after Whipple) that the sky background still affects the measurement, because although the background is the same for both regions A and B, it adds the same amount to both numerator and denominator of the ratio and therefor changes the ratio.

Neither ratio C/E or C/S can be measured for all of the necessary phase angles. In the work of Danjon, C/E was measured for $40° < \eta < 165°$, and C/S for $11° < \eta < 156°$. The data is extrapolated to 0° and 180°, respectively.

Fritz[12] notes that, since the measurements of Danjon and Dubois were made from western Europe, they do not necessarily apply to the earth as a whole.

Danjon notes that his measurements and those of Dubois are not sufficient to establish variations of the phase function (i.e., diurnal, seasonal, etc.). If the phase function is assumed to be constant then each observation yields a value of magnitude at full phase. With this assumption, the observations show seasonal variations from the mean value 9.99, with albedo maximum in spring and fall and minimum in summer and winter.

Angstrom[13] has derived values of photometric albedo from Danjon's data for the years 1926-34, as follows:

Year	1926	1927	1928	1929	1930	1931	1932	1933	1934
Photometric Albedo	0.41	0.44	0.40	0.39	0.39	0.40	0.38	0.37	0.38

2. THE WORK OF BAKOS[11]

During the International Geophysical Year an attempt was made to correlate fluctuations in the earthshine with cloud conditions on the surface of the earth. Six Danjon-type photometers were installed at the satellite tracking stations of the Smithsonian Astrophysical Society (see

Table 14). Measurements were made from 1957 until 1960 and have been reported on by Bakos.[11]

TABLE 14

EARTHSINE PHOTOMETER STATIONS

Station	Longitude	Latitude
Arequipa, Peru	$4^h\ 46.1^m$	-16.4°
Yerkes Observatory Williams Bay, Wis.	$5^h\ 54.2^m$	+42.6°
Organ Pass, N.M.	$7^h\ 06.2^m$	+32.4°
Haleakala, Hawaii	$10^h\ 25.1^m$	+20.7°
Woomera, Australia	$14^h\ 12.8^m$	-31.1°
Shiraz, Iran	$20^h\ 29.8^m$	+29.6°

Measurements of the ratio C/E, as described above, were made with red, green, and blue filters, as well as without any filter. Systematic differences between data taken at each station were found by plotting the earthshine observations as a function of phase angle. When these plots were compared to that for Yerkes (Williams Bay, Wis.) a vertical shift was found. These vertical shifts were eliminated, thus making all observations consistant with those of Yerkes. Also morning observations were found to be brighter than those made in the evening, because of different reflectivities of the two parts of the lunar surface. Observations made with the green and blue filter were reduced to clear observations by the same technique of eliminating systematic differences. The

"red" observations were excluded.

Statistical errors were evaluated by comparison of "filter" and "no filter" observations after they were reduced to a common base, i.e., to Yerkes magnitudes. Also comparison of readings made by different observers on the same instrument checked the consistancy of the data. It was concluded that the mean error of a single observation was ±0.20 magnitude.

The data obtained was prepared for analysis as follows:

a. A curve of mean values (uncorrected for systematic or other errors) vs. phase angle was prepared.

b. A curve of best values (the mean of observations reduced to "no filter" and Yerkes magnitudes) vs. phase angle was prepared.

c. The difference between best and mean values was computed. This is called the O-C reading and contains errors as well as fluctuations of earthshine due to varying conditions on earth.

d. Cloud cover information for a time close to the time of an observation was plotted on a globe and the area of the earth which would reflect light to the moon was photographed. Of 196 such weather maps, only 17 contained cloud cover distribution for more than 70% of the area of interest.

e. Estimates of snow cover were added to each of the maps.

Following are some results obtained from analysis of the data:

a. O-C readings showed no obvious correlation with cloud cover.

b. The earthshine shows a slow and continuous fluctuation with a period of one day, resulting from the earth's rotation. The author attributes this fluctuation to a "bright spot" on the earth in the Asian hemisphere. Average mean cloud cover for five longitudinal areas of the earth are compared with mean values of O-C in Table 15. For Asia the cloud cover is about 10% higher than for the other longitudes and the earthshine brighter by about 0.5 magnitude.

c. Changes of the earthshine during the year are shown by the monthly means of the O-C data taken in 1957, 1958, and 1959 (see Table 16). These data show that the earthshine is the brightest in March through June. Bakos reasons that because, statistically, the cloud cover does not change substantially during the course of a year, this phenomenom must be due to the difference in reflectance of continents and oceans. During March through June, the earthshine is primarily from the northern hemisphere and thus reflectance of the continents would be dominant. The reflectivity of continents must therefore, in general be greater than the reflectivity of the oceans.

d. Finally the data was used to calculate the average albedo of the earth for 1958 and 1959. The equation used for earth's albedo was that due to Kazachevsky:

$$A = \frac{\Delta^2}{a^2} \cdot 2 \int_0^{180} Q(\alpha) \sin \alpha \, d\alpha \qquad (55)$$

TABLE 15

LONGITUDINAL VARIATION OF CLOUD COVER
(After Bakos[11])

Longitude	Area	O-C	Cloud Cover
0°W	Africa	0.14 mag.	30%
90°	America	0.04	---
150°	E. Pacific	0.10	29%
180°	W. Pacific	0.09	31%
240°	Asia	-0.32	41%

TABLE 16

MONTHLY VARIATIONS OF THE BRIGHTNESS OF THE EARTHSHINE
(After Bakos[11])

Month	O-C		
	1957	1958	1959
January			-0.03
February			-0.10
March		-0.16	+0.14
April		+0.02	-0.36
May		+0.03	+0.07
June		-0.13	-0.49
July		+0.01	-0.01
August		+0.12	+0.05
September		+0.11	+0.21
October		+0.10	+0.08
November	+0.30	+0.17	+0.16
December		-0.02	+0.09

where:

A = earth's albedo

Δ = the mean distance of the moon from the earth

a = the radius of the earth

The function $Q(\alpha)$ is of the form:

$$Q(\alpha) = \frac{I_1}{I_2}\frac{\eta_2}{\eta_1}F(\eta) = K \cdot f(\alpha) \qquad (56)$$

where

$$I_1/I_2 = \frac{\text{intensity of earthshine}}{\text{intensity of sunlit portion of moon}}$$

$$\eta_2/\eta_1 = \frac{\text{reflectance of sunlit area}}{\text{reflectance of earthshine area}}$$

$F(\eta)$ = lunar phase function

$\eta = 180 - \alpha$

$f(\alpha)$ = proportional to the earth's phase function

Using Danjon's phase function, Bakos found:

$$A = 0.368K = 0.368\,\frac{Q(\alpha)}{f(\alpha)}$$

Next, Bakos applied the idea of a "normal" brightness of the earthshine. This is the value of earthshine at $\alpha = 115°$ or $245°$, used because other writers have found, that for different phase functions considered all had essentially the same value at these values of α. At $\alpha = 115°$ and $245°$, $F(\eta) = 0.192$, and $f(\alpha) = 0.345$. Therefore, the albedo is given by:

$$A = 0.368 \frac{I_1}{I_2} \frac{\eta_2}{\eta_1} \frac{F(\eta)}{f(\alpha)} \qquad (57)$$

$$= 0.205 \frac{I_1}{I_2} \frac{\eta_2}{\eta_1}$$

where $\frac{I_1}{I_2} \frac{\eta_2}{\eta_1}$ is the normal brightness of earthshine, i.e., at $\alpha = 115°$ or 245°.

Each value of earthshine measured by Bakos, et al., was converted to a normal brightness using a correction factor obtained from a plot of all observations vs. phase angle. A mean value was then obtained after adjustments for systematic errors were made. The yearly mean values of earth's albedo obtained in this way are:

Year	Albedo	No. of Observations
1958	0.41	219
1959	0.42	158

These values agree nicely with Danjon's average albedo of 0.4 for 1926-1935.

3. THE WORK OF DUBOIS[10]

Dubois has made measurements similar to those of Danjon, using blue, green, yellow, and red filters. He notes that the brightness of the earthshine varies with phase, color, and also the hour of the observation, because a diurnal variation is caused by the dissimilarity of the albedos of oceans and continents. He has reported on data taken between 1940 and March, 1945.

He has studied the seasonal variation of the earthlight, using the green-filter observations near 0.53 micron, for phase angle $\alpha = 115°$, taken around 1900 GMT. These brightness curves are shown in Figures 59a and 59b for the years 1946-1948 and 1949-1954, respectively. Maxima of brightness (minima of Δm) occur in April-May-June, and October-November-December.

In addition, the yearly variations were studied. Relative luminances for 30 June of each year 1940-1954 are shown in Figure 59c. The figure shows that the earthshine approaches a maximum as the minimum activity of the solar cycle approaches and then decreases rapidly right after the minimum of the solar activity.

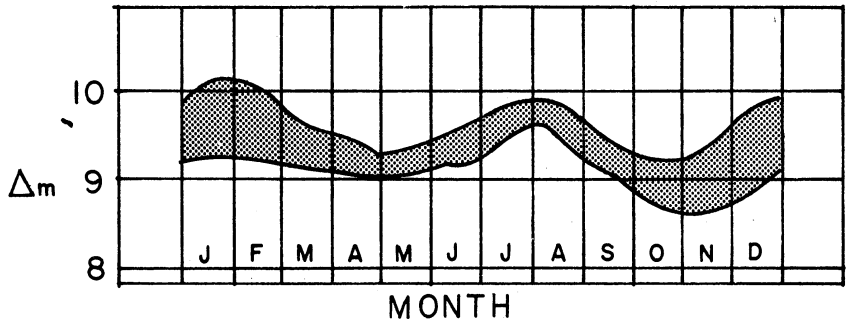

a.) 1946-1948 MONTHLY VARIATIONS

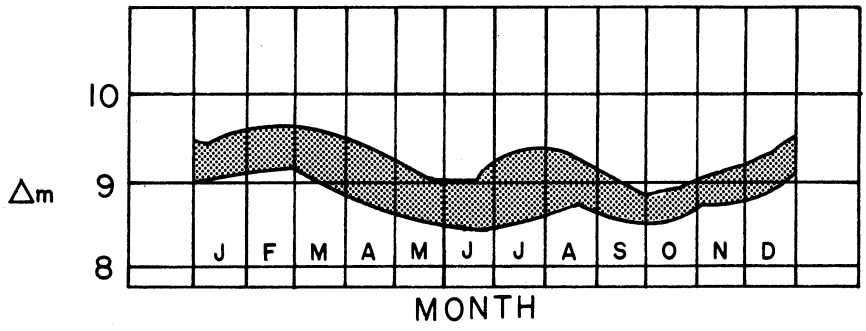

b.) 1949-1954 MONTHLY VARIATIONS

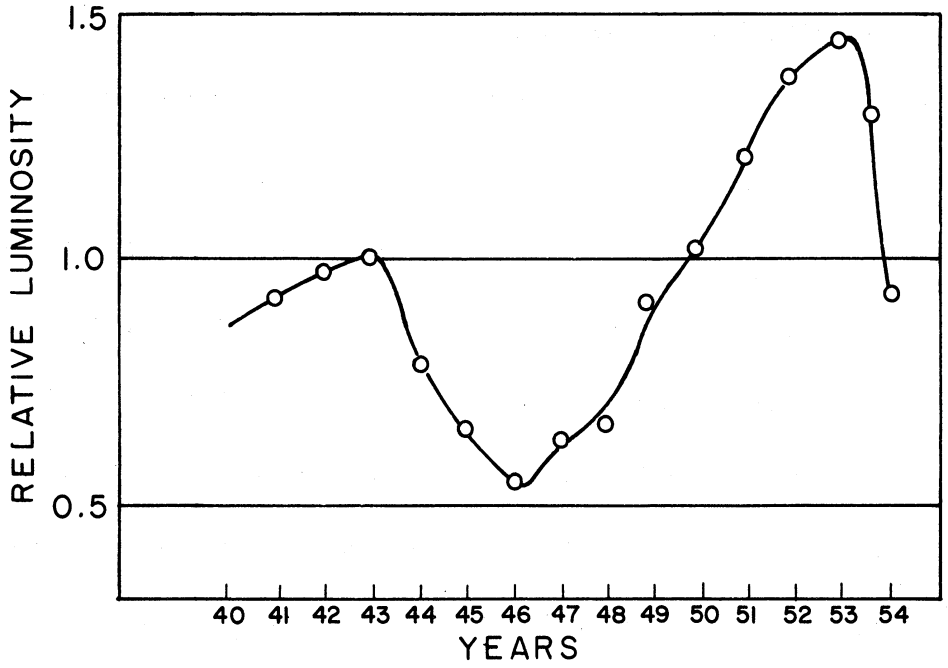

c.) YEARLY VARIATIONS

Figure 59. Variation of the brightness of the earthshine (after Dubois[10]).

APPENDIX B

EARTH'S ALBEDO MEASUREMENTS FROM SATELLITES AND SPACECRAFT

The instruments used for these measurements are of two basic types; the low resolution instrument with broad field of view and wide spectral response and the medium resolution instrument with a narrower field of view and wide (sometimes not wide enough) spectral response. The measurements with the low resolution instruments will be discussed first, those with the medium resolution instrument next. The Mariner 2 measurements which are different from the satellite measurements in that they were made from a deep space probe (and, indeed, are most like the measurements made by Danjon) will be discussed last.

1. THE LOW RESOLUTION MEASUREMENTS

The low resolution measurements are made with instruments which are an extension of the design of the Suomi-Kuhn "economical" net radiometer. In the idealized instrument, a small spherical shell sensor of low heat capacity, exposed to radiation from the earth and the sun, shielded from satellite radiated energy and isolated from the satellite by insulators of very low heat conductivity, will assume a temperature determined by its radiative heat balance. For the ideal experiment, the radiative heat balance equation is usually written in a form similar to:

$$\alpha_s \cdot \pi \cdot R_s + \alpha_s \cdot \beta \cdot R_r + \alpha_\ell \beta \cdot R_\ell = 4\pi \epsilon_\ell \cdot \sigma \cdot T^4 \qquad (58)$$

where:

R_s = Direct radiation from the sun, watts/cm^2.

R_r = Radiation reflected from the surface of the earth, watts/cm^2.

R_ℓ = Thermal radiation emitted by the earth and its atmosphere, watts/cm^2.

α_s = The absorptivity of the shell for solar radiation.

α_ℓ = The absorptivity of the shell for thermal radiation.

ϵ_ℓ = The emissivity of the shell for thermal radiation.

β = The solid angle subtended by the earth as viewed from the satellite.

σ = The Stefan-Boltzmann constant.

T = The sensor's temperature, °K.

Different forms of the experiment have been discussed, by:

a. V. Suomi, R. J. Parent, and co-workers at the University of Wisconsin.[14]

b. R. A. Hanel, F. Bartko, and co-workers at Goddard Space Flight Center.[17,18]

c. F. B. House at the University of Wisconsin.[2]

Two excellent papers which discuss theoretical and practical aspects of the experiment are those by K. J. Bignell[19] and M. S. Malkevich, et al.[20]

In the form of the experiment originally proposed by Suomi, several sensors with different coatings, providing wavelength discrimination, were used and some were shielded from the direct radiation of the sun. In this case each of the sources of radiation can be determined from the temperatures of the several sensors. For example, if the values of absorptivity were as given in Table 17, we could write the following

equations.

TABLE 17

VALUES OF ABSORPTIVITY FOR VARIOUS COATINGS

Coating	α_s	α_ℓ
Black paint	0.95	0.95
White paint	0.05	0.95
Tabor coating	0.90	0.10

For the dark side of the earth (for any sensor):

$$\alpha_\ell \beta R_\ell = 4\pi \epsilon_\ell \sigma \cdot T^4$$

$$R_\ell = \frac{4\pi}{\beta} \frac{\epsilon_\ell}{\alpha_\ell} \sigma T^4$$

If β, ϵ_ℓ, and α_ℓ are known R_ℓ can be calculated from measured values of T.

On the sunlit side of the earth:

Black Sphere:

$$0.95\ \pi R_S + 0.95\ \beta R_r + 0.95\ \beta R_\ell = 4\pi \cdot 0.95 \cdot \sigma T_B^4$$

White Sphere:

$$0.05\ \pi R_S + 0.05\ \beta R_r + 0.95\ \beta R_\ell = 4\pi \cdot 0.95 \cdot \sigma T_W^4$$

Tabor Sphere:

$$0.90\ \pi R_S + 0.90\ \beta R_r + 0.10\ \beta R_\ell = 4\pi \cdot 0.10 \cdot \sigma T_T^4$$

Shielded Tabor Sphere:

$$0.90\ \beta R_r + 0.10\ \beta R_\ell = 4\pi \cdot 0.10 \cdot \sigma T_S^4$$

Combining the equations for the Tabor and shielded spheres:

$$R_S = \frac{4\sigma}{9}(T_T^4 - T_s^4) \tag{59}$$

From the equations for the black and white spheres:

$$\pi R_S + \beta R_r = \frac{38\sigma}{9}(T_B^4 - T_W^4)$$

thus

$$R_r = \frac{38}{9}\frac{\sigma}{\beta}(T_B^4 - T_W^4) - \frac{4}{9}\frac{\sigma\pi}{\beta}(T_T^4 - T_s^4) \tag{60}$$

also

$$R_\ell = \frac{2}{9}\frac{\sigma\pi}{\beta}(19T_W^4 - T_B^4) \tag{61}$$

Now R_S is the solar constant. It is probable that its value is known more accurately than can be obtained from Equation (59). The accepted value can be used instead of the data obtained from the Tabor and shielded sensors. In this case

$$R_r = \frac{38}{9}\frac{\sigma}{\beta}(T_B^4 - T_W^4) - \frac{\pi}{\beta}R_S \tag{62}$$

Sensors of this type were constructed by the University of Wisconsin group under Suomi for one of the Vanguard satellites which was not orbited successfully. Other sensors of a different design were flown on Explorer VII, TIROS III, TIROS IV, and TIROS VII. In the new design hemispherical sensors were used. They were thermally isolated from the satellite by being mounted on insulating rods above a highly reflective mirror surface. Thermal isolation was not complete, however, and so it was necessary to add terms to the radiation balance equation to account

for heat conducted from the satellite to the hemisphere along the insulating rod. Data analysis also required consideration of the heat capacity of the sensor. Thus the heat balance equation for a sensor is changed to:

$$\alpha_s \pi R_s + \alpha_s \beta R_r + \alpha_\ell \beta R_\ell = 4\pi \epsilon_\ell \sigma T^4 - H \frac{\partial T}{\partial t} - K(T_m - T) \qquad (63)$$

where the factors involved are:

H = Heat capacity of the sensor.

$\frac{\partial T}{\partial t}$ = Time derivative of the sensor's temperature.

K = Conductivity of the hemisphere support rod.

T_m = The mirror temperature.

Papers written by Suomi indicate that it is not possible to calculate daily heat balance from the satellite because of restrictions imposed on data sampling by the satellite orbit. Results from Explorer VII data were a series of long-wave radiation loss maps derived from data taken by the white hemispherical sensor at night. Daytime measurements of earth reflectance were not obtained (not published).

R. Hanel and F. Bartko have discussed low-resolution sensors of a different design, i.e., thermister detectors mounted on an insulating base at the bottom of a highly reflecting truncated cone. The detectors were assembled in pairs with one white thermister and one black thermister for wavelength discrimination. This design was flown on TIROS II, TIROS III, and TIROS IV. Some data have been published, however, Bartko, et

al.,[18] indicate that the value of this instrument for heat balance and earth albedo measurements is limited because of the data acquisition limitations of TIROS.

The only study of albedo and long-wave radiation based on measurements with the low resolution instrument is that of F. B. House, using data from TIROS IV. This study is unique in that data from only the black sensor was used, and that constants in the equation were determined from in-flight data, i.e., in part, in-flight calibrations were made.

The sensors on TIROS IV were hemispheres mounted above mirrors which prevent the hemisphere from "seeing" the satellite. Two systems of sensors and mirrors were mounted on opposite sides of the satellite, each system having one black and one anodized sensor. When the satellite, rotates on its axis, at some point of the rotation a part or all of one sensor may be eclipsed from direct view of the earth. However, at this time, the matched sensor on the opposite side of the satellite starts viewing the earth. The sensors are connected in series, so that the average temperature of the two sensors is measured. When the satellite spin period is short compared to the sensor's time constant, the measured average temperature can be taken as the temperature of a severed sphere which views the earth.

The radiation balance of this spinning sensor is written as:

$$\frac{\alpha_s}{\alpha_\ell}\,\pi R_s + \frac{\alpha_s}{\alpha_\ell}\,\beta R_r + \beta R_\ell = 4\pi\,\frac{\epsilon_\ell}{\alpha_\ell}\,\sigma T^4 - C_m\cdot\sigma T_m^4 + C_c\cdot(T-T_m) + C_t\cdot d(\sigma T^4) \tag{64}$$

where the terms on the right hand side of the equation represent:

a. The energy emitted by the sensor to the mirror and to space.

b. The energy radiated to the sensor by the mirror.

c. The energy conducted to the sensor along the mounting post.

d. A thermal lag term involving the heat capacity of the sensor.

Sensor temperature measurements were taken on the satellite every 29.16 seconds. If T_1 and T_2 are two consecutive sensor temperature observations and $\bar{T}$ and $\bar{T}_m$ are average sensor and mirror temperatures, then the radiation balance for the sensor can be written as:

$$\frac{\alpha_s}{\alpha_\ell}\pi R_s + \frac{\alpha_s}{\alpha_\ell}\beta R_r + \beta R_\ell = 4\pi\frac{\epsilon_\ell}{\alpha_\ell}\sigma\bar{T}^4 - C_m\sigma\bar{T}_m^4 + C_c(\bar{T}-\bar{T}_m) + C_t(\sigma T_2^4-\sigma T_1^4) \tag{65}$$

The constants C_m, C_c, and C_t were evaluated from in-flight data and laboratory tests, as follows. Laboratory measurements by Sparkman on instruments similar to the ones flown on the TIROS IV satellite yielded the relation:

$$C_m = 30C_c$$

A study of sensor and mirror temperature changes (350 cases) in the 3-min. period after the satellite entered the earth's shadow (see Figures 60 and 61) with the assumption of constant thermal radiation βR_ℓ during this time gave the result:

$$C_t = K_2C_c + K_3$$

Finally a study of sensor and mirror temperature changes over a 25-min interval while the satellite was in the earth's shadow, for many orbits over a precessional period of the satellite, resulted in a value of C_c. The radiation balance equation could be written as:

$$\beta R_\ell = 4\pi \frac{\epsilon_\ell}{\alpha_\ell} \sigma\bar{T}^4 + C_c[(\bar{T}-\bar{T}_m) - K_1\sigma\bar{T}^4 + K_2(\sigma T_2^4-\sigma T_1^4)] + K_3(\sigma T_2^4-\sigma T_1^4) \tag{66}$$

i.e.,

$$\beta R_\ell = A + C_c \cdot B + C$$

In each orbit the equation is evaluated at position a at the beginning of the 25-min. interval and position b near the end of the interval (see Figure 61). Summing over all orbits considered we have:

$$\sum(\beta R_\ell)_a = \sum(A)_a + C_c\sum(B)_a + \sum(C)_a$$

$$\sum(\beta R_\ell)_b = \sum(A)_b + C_c\sum(B)_b + \sum(C)_b$$

assuming

$$\sum(\beta R_\ell)_a = \sum(\beta R_\ell)_b$$

we find

$$C_c = \frac{\sum(A)_a - \sum(A)_b + \sum(C)_a - \sum(C)_b}{\sum(B)_b - \sum(B)_a} \tag{67}$$

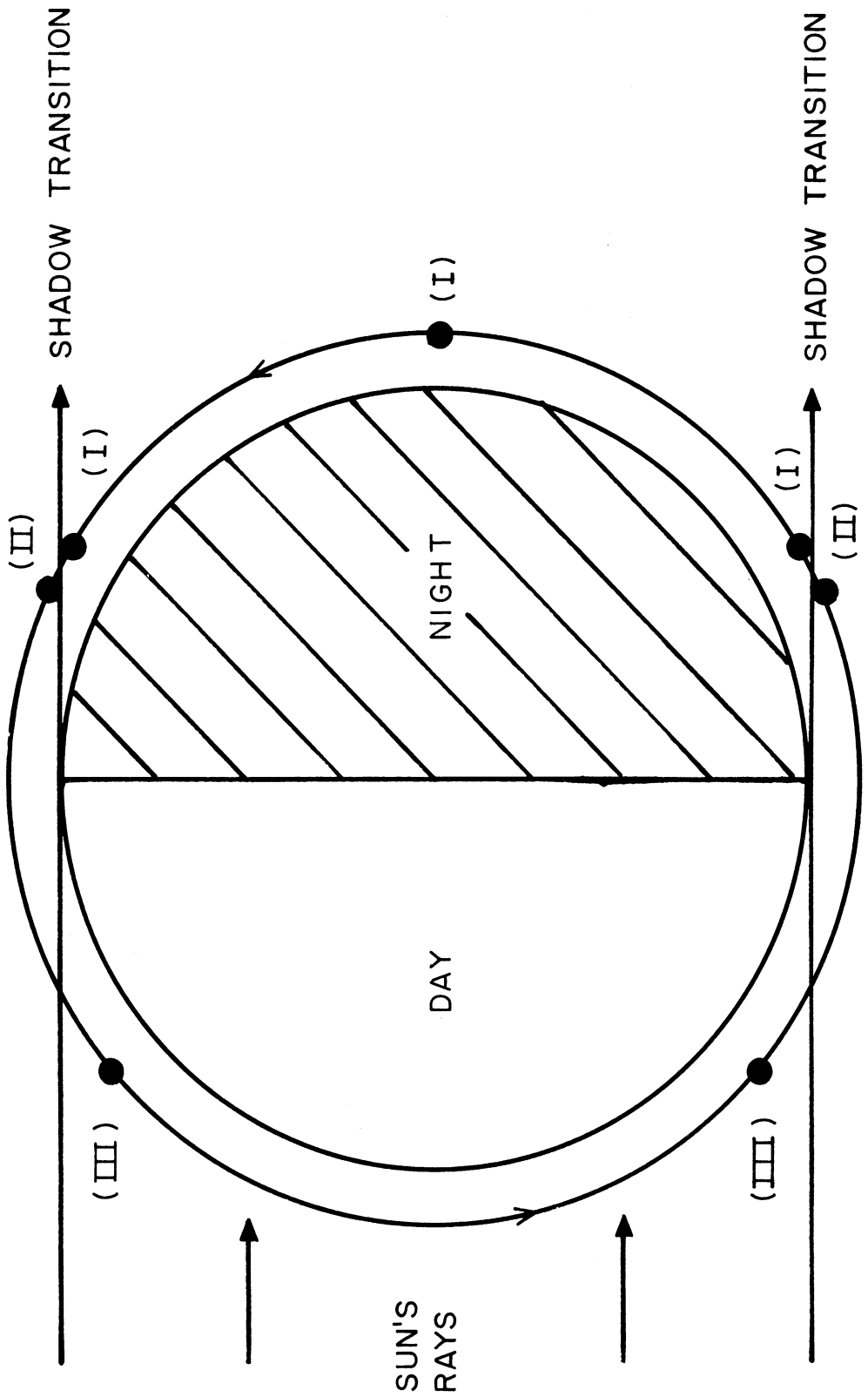

Figure 60. Schematic diagram of satellite orbiting the earth (after House[2]).

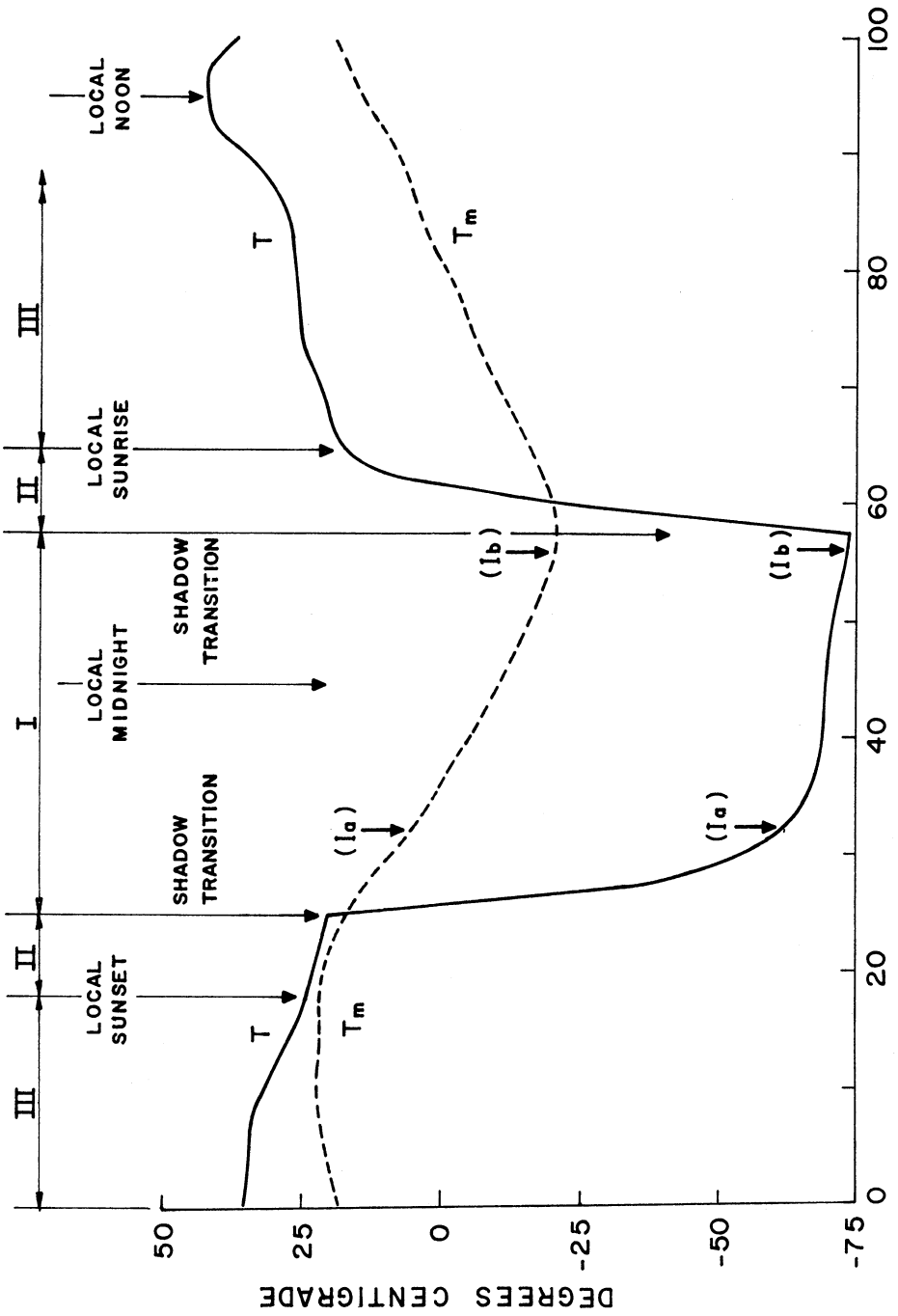

Figure 61. Typical black sensor and mirror temperature observations during a TIROS IV orbit (after House[2]).

Values of the constants obtained were:

$$C_c = 0.010 \pm 0.0005$$

$$C_m = 0.300 \pm 0.015$$

$$C_t = 43 \pm 2.15$$

Thus, the radiation balance equation becomes

$$\frac{\alpha_s}{\alpha_\ell}\pi R_\ell + \frac{\alpha_s}{\alpha_\ell}\beta R_r + \beta R_\ell = 4\pi\frac{\epsilon_\ell}{\alpha_\ell}\sigma\bar{T}^4 - 0.15\sigma\bar{T}_m^4 + 0.010(\bar{T}-\bar{T}_m)+43.0(\sigma T_2^4-\sigma T_1^4) \tag{68}$$

The data from the black sensor was then analyzed as follows. At night, we have

$$(\beta R_\ell)_I = \left[4\pi\frac{\epsilon_\ell}{\alpha_\ell}\sigma\bar{T}^4 + \text{corrections}\right]_I \tag{69}$$

At the time of transition to earth shadow,

$$\left(\frac{\alpha_s}{\alpha_\ell}\pi R_s + \beta R_\ell\right)_{II} = \left[4\pi\frac{\epsilon_\ell}{\alpha_\ell}\sigma\bar{T}^4 + \text{corrections}\right]_{II} \tag{70}$$

On the sunlit side of the earth,

$$\left(\frac{\alpha_s}{\alpha_\ell}\pi R_s + \frac{\alpha_s}{\alpha_\ell}\pi R_r + \beta R_\ell\right)_{III} = \left[4\pi\frac{\epsilon_\ell}{\alpha_\ell}\sigma\bar{T}^4 + \text{corrections}\right]_{III} \tag{71}$$

Then also, assuming

$$(\beta R_\ell)_I = (\beta R_\ell)_{II}$$

$$\left(\frac{\alpha_s}{\alpha_\ell}\pi R_s\right)_{II} = \left(\frac{\alpha_s}{\alpha_\ell}\pi R_s + \beta R_\ell\right)_{II} - (\beta R_\ell)_I \tag{72}$$

Assuming

$$\left(\frac{\alpha_s}{\alpha_\ell}\,\pi R_s\right)_{II} = \left(\frac{\alpha_s}{\alpha_\ell}\,\pi R_s\right)_{III}$$

$$\left(\frac{\alpha_s}{\alpha_\ell}\,\beta R_r + \beta R_\ell\right)_{III} = \left(\frac{\alpha_s}{\alpha_\ell}\,\pi R_s + \frac{\alpha_s}{\alpha_\ell}\,\beta R_r + \beta R_\ell\right)_{III} - \left(\frac{\alpha_s}{\alpha_\ell}\,\pi R_s\right)_{II} \tag{73}$$

The mean thermal radiation loss at a latitude over a precessional period is:

$$\overline{(\beta R_\ell)_I} = \frac{\sum_I^n (\beta R_\ell)_I}{n} \tag{74}$$

The mean daytime radiation loss (reflected solar plus emitted thermal radiation) at a given latitude over a precessional period is:

$$\overline{\left(\frac{\alpha_s}{\alpha_\ell}\,\beta R_r + \beta R_\ell\right)_{III}} = \frac{\sum_I^n \left(\frac{\alpha_s}{\alpha_\ell}\,\beta R_r + \beta R_\ell\right)_{III}}{n} \tag{75}$$

The mean of the reflected solar radiation is taken to be:

$$\overline{\left(\frac{\alpha_s}{\alpha_\ell}\,\beta R_r\right)_{III}} = \overline{\left(\frac{\alpha_s}{\alpha_\ell}\,\beta R_r + \beta R_\ell\right)_{III}} - \overline{(\beta R_\ell)_I} \tag{76}$$

The incident solar radiation is $R_s \cos^*\phi$, where $\cos^*\phi$ geometrically weights the solar radiation which is incident to the area viewed by the satellite. Assuming perfectly diffuse reflection, the mean albedo at a given latitude over a precessional cycle is:

$$\overline{A} = \frac{100 \cdot \left(\frac{\alpha_s}{\alpha_\ell}\,\beta R_r\right)_{III}}{\left(\frac{\alpha_s}{\alpha_\ell}\,\frac{\beta}{\pi}\,R_s \cos^*\phi\right)} \tag{77}$$

where $\frac{\alpha_s}{\alpha_\ell}\frac{\beta}{\pi}\cdot R_s \cos^*\phi$ is a term which represents the mean reflected solar radiation which would be received by the sensor if the earth's reflectance were 100% and perfectly diffuse. This term can be calculated from:

$$\overline{\frac{\alpha_s}{\alpha_\ell}\frac{\beta}{\pi} R_s \cos^*\phi} = \frac{\sum_{I}^{n} \frac{\beta}{\pi^2}\left(\frac{\alpha_s}{\alpha_\ell}\pi R_s\right)_{III} \cos^*\phi}{n} \qquad (78)$$

Results were obtained by House for four months of TIROS IV data, 8 February, 1962 to 11 June, 1962. The method of sampling over the earth's surface, and limitations in coverage in time and geographical area should be noted. Factors which result in sampling limitations are: the inclination of the satellite orbit and the precession of the orbit with respect to the sun, data storage capability, and the location of data readout ground stations. House has discussed the problem briefly, more complete discussions of the problem are those of Widger and Wood,[21] and in the TIROS IV Radiation Data Catalogue and Users Manual.[22] These discussions can be summarized as follows:

The geographical area of sampling by TIROS IV was limited by the inclination of the orbit to the earth's surface area between 48°N and 48°S. Further limitation in the latitude of data coverage is imposed by the need for solar illumination of the earth's surface. The TIROS IV orbital plane had a precessional motion of -4.43°/day. As a result of this precession of the orbital plane and the movement of the earth in its orbit, a complete cycle of the precession of the plane of the satellite orbit occurred in about 66 days. The TIROS IV launch was made on 8 February,

with the northern part of the orbit over the sunlit portion of the earth (see Figure 62). On 23 February, the orbital plane was located in such position that TIROS IV viewed sunlit earth in both northern and southern hemispheres, with sampling at the equator at about high noon. On 11 March, the southern hemisphere portion of the orbit was sunlit with noon sampling corresponding to the southernmost portion of the orbit. Since the albedo varies as a function of solar elevation angle; it is necessary that samples be obtained at all solar elevation angles if a proper albedo value is to be obtained. For any geographical area it is necessary to sample over the entire precessional cycle to obtain samples at all times of the day.

It is obvious that the weather (and even the season) is different for days early in the cycle when morning samples are being obtained in the northern hemisphere, as compared to days later in the cycle when the afternoon hours are being sampled. The distribution of samples obtained should be studied carefully to see that a bias is not introduced into the data. House did not consider this problem except to say that it could be expected that samples are obtained with equal frequency in clear and cloudy situations and therefore weighting of the result due to storm systems would not occur.

Averaging periods were selected for two almost complete precessional cycles, 8 February to 10 April, and 11 April to 10 June. Meridional profiles of outgoing thermal radiation, albedo, and net radiation were pre-

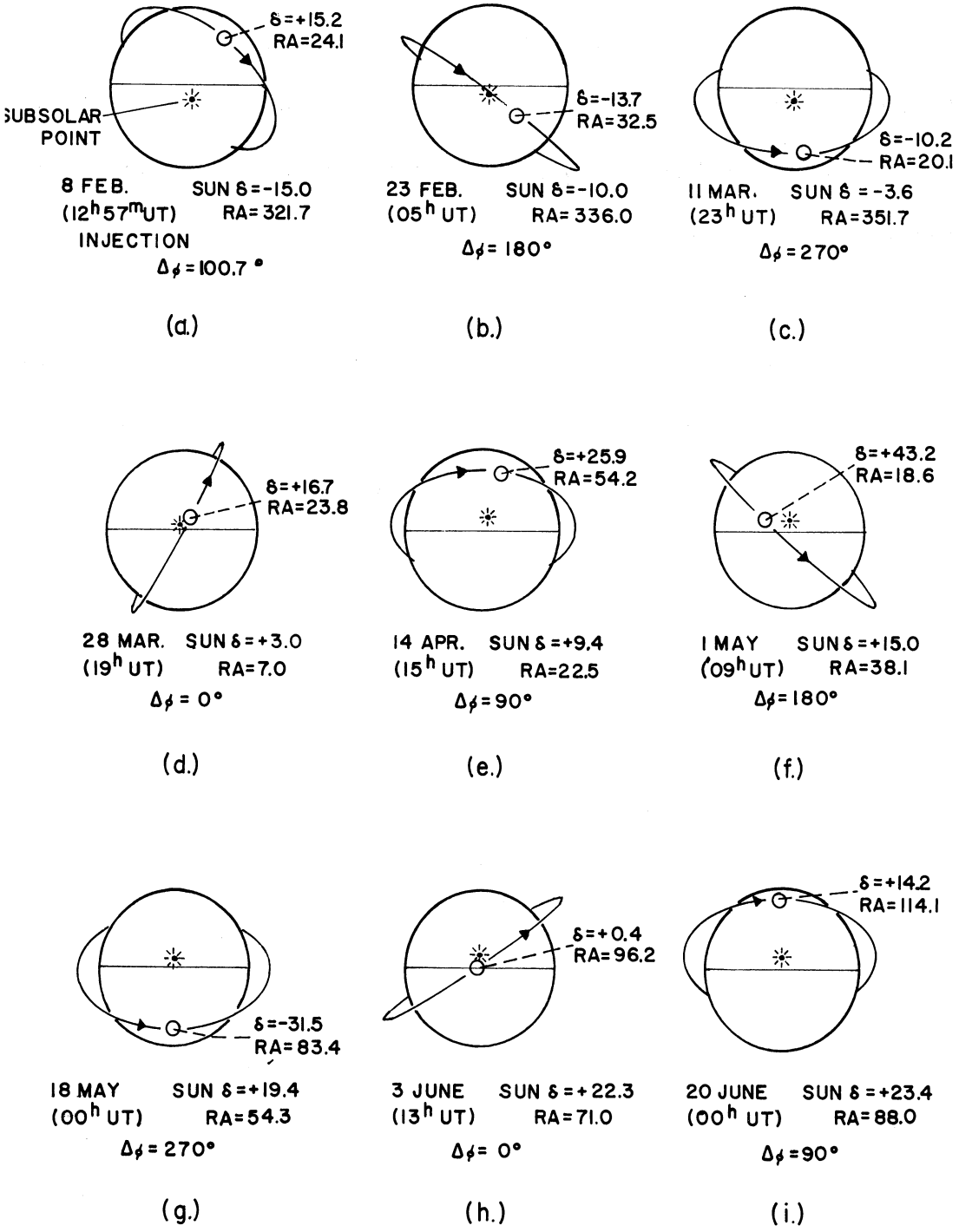

Figure 62. View of the earth and the precessing TIROS IV orbital plane (after Staff Members[22]).

sented. Limitations in the data due to sampling techniques were not further discussed.

The meridional profiles of albedo obtained by House are shown in Figures 63 and 64. In Figure 63 the results for the two precessional periods are compared. Both periods show slight maxima in the tropical regions, minima in the subtropics, and increasing values towards the poles. The albedos in the subtropical regions are 1-3% higher for the second period. In Figure 64, the data for March, April, and May are compared with estimates, by London[23] (see Appendix F), of albedo for spring and fall seasons. House's data indicate a lower albedo in tropical latitudes of 4-6% and higher values of 3-5% in middle latitudes. A global albedo of 35% was obtained after extrapolating the profile linearly to 61% at the pole.

In summary, the only albedo measurements obtained with the low resolution instrument are those of House. Assumptions made in the analysis were:

a. The earth's reflectance is assumed to be isotropic.

b. The term which represents thermal radiation received by the sensor is the same in the transition region as it is on the dark side of the earth, i.e.,

$$(\beta R_\ell)_I = (\beta R_\ell)_{II}$$

c. The term which represents the direct solar radiation received by the sensor is the same in the transition region as it is on the sunlit side of the earth, i.e.,

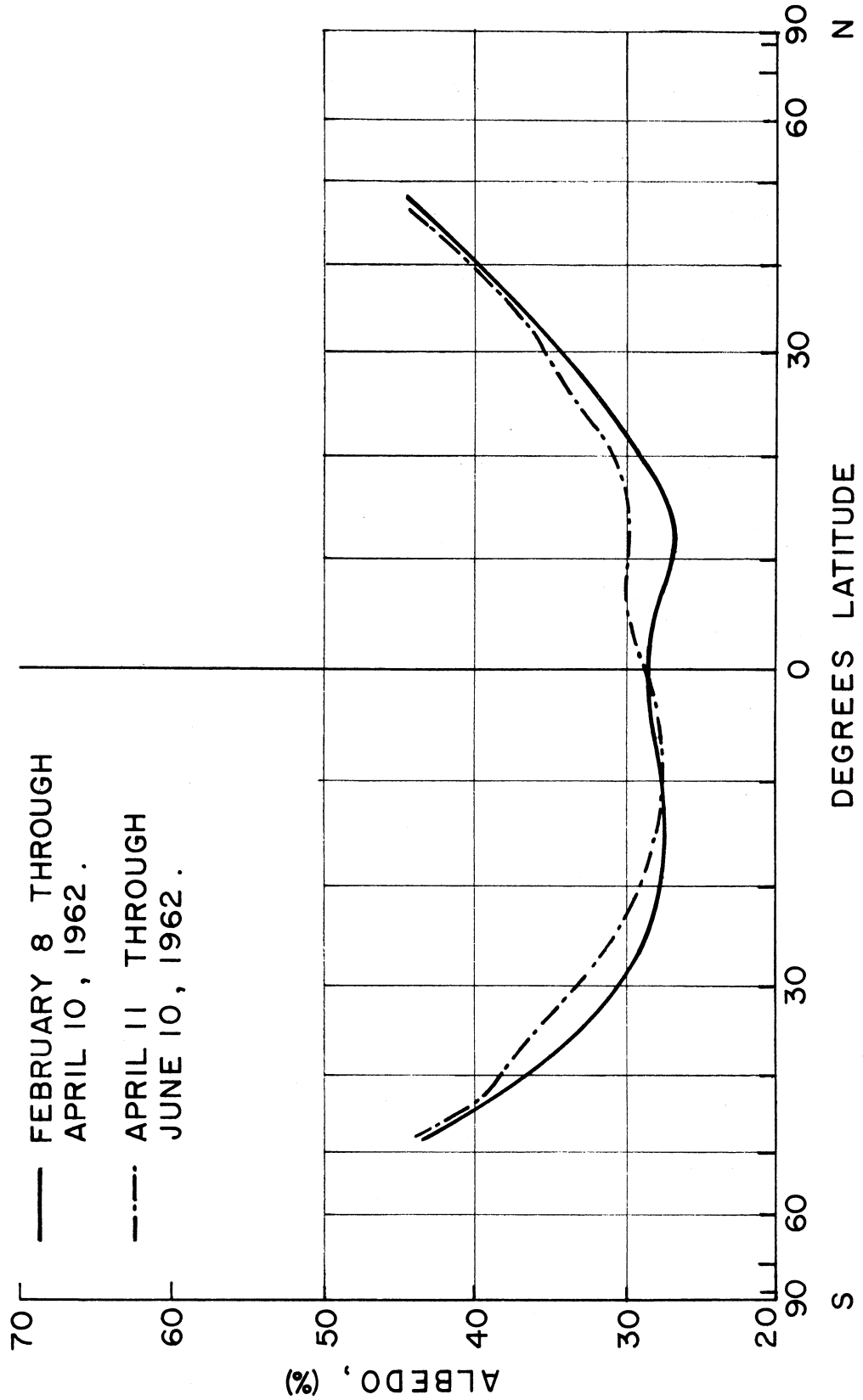

Figure 63. Comparison of the meridional variation of albedo for two precessional cycles (after House[2]).

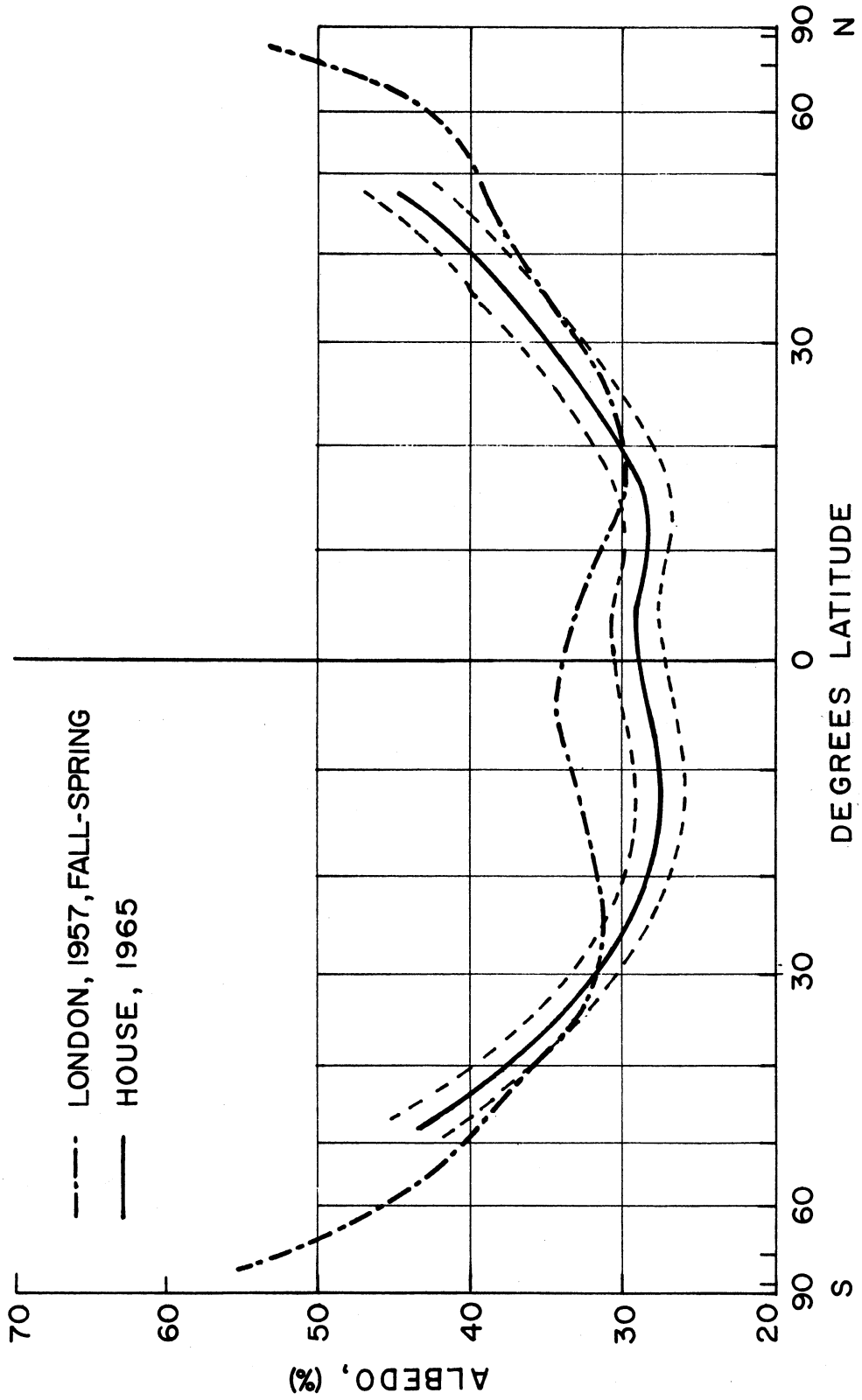

Figure 64. Comparison of the meridional variation of albedo for March, April, and May with data of London (after House[2]).

$$\left(\frac{\alpha_s}{\alpha_\ell}\,\pi R_s\right)_{II} = \left(\frac{\alpha_s}{\alpha_\ell}\,\pi R_s\right)_{III}$$

d. The mean value of the thermal radiation on the dark side of the earth is equal to the mean value of the thermal radiation on the sunlit side of the earth, i.e.,

$$\overline{(\beta R_\ell)_I} = \overline{(\beta R_\ell)_{III}}$$

e. Averaging the samples at a meridian which are available over a precessional cycle produces the average daily meridional value of albedo, i.e., there is no sampling error.

2. THE MEDIUM RESOLUTION MEASUREMENTS

Two types of medium resolution instrument have been used for satellite measurement of earth reflectance or albedo to date. The TIROS 5-channel radiometer[24] was flown on TIROS II, III, IV, and VII. The NIMBUS Medium Resolution Infrared Radiometer (MRIR),[25] also a 5-channel instrument but of a different design, has been flown on the NIMBUS II satellite.

The principle of the TIROS 5-channel radiometer is illustrated schematically in Figure 65, showing the basic components of a single channel of the radiometer. The field of view of each channel is about 5° wide at the half power-point (the field of view down to 5% of maximum response is 8 to 9°). The chopper disk-prism arrangement causes the radiometer to look alternately in opposite directions. During flight and

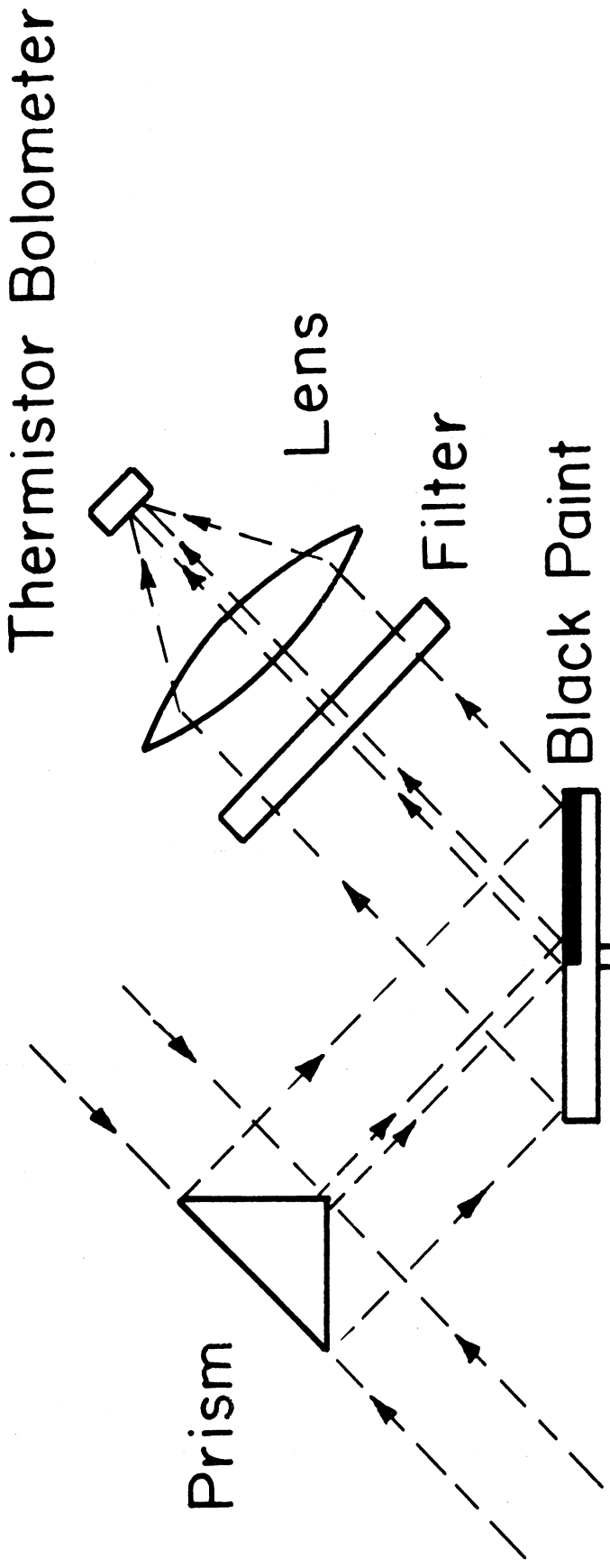

Figure 65. Diagram indicating principle of operation of a channel of the TIROS five channel radiometer (after Staff Members[22]).

during calibration, a reference target is viewed in one direction, and the earth or calibration target in the opposite direction. The reference target for the visible channels is outer space during flight and is a dark cavity during calibration. As the half mirror-half black shopper disk rotates, the radiation reaches the detector alternately from opposite directions. The resulting chopped signal is amplified and rectified to produce a d-c signal, which in the ideal instrument is proportional to the difference in energy flux received from the two directions. The two viewing directions are called "wall" and "floor" side of the radiometer according to their location in the TIROS satellite, i.e., one view is through the wall side, the other through the floor side of the satellite.

The nominal characteristics of the two visible channels, channels 3 and 5, with which we are concerned, are given in Table 18. The effective spectral response of each of the channels is given in Figure 66.

TABLE 18

NOMINAL CHARACTERISTICS OF TIROS RADIOMETER CHANNELS 3 AND 5

Channel number:	3	5
Purpose of measurement:	"Reflected" solar radiation	Comparison with TV photos
Wavelength (nominal):	2-6 micron	.55-.75 micron
Optics (lenses):	Al_2O_3 BoF_2	Al_2O_3 SiO_2
Filters:		Interference and chance glass

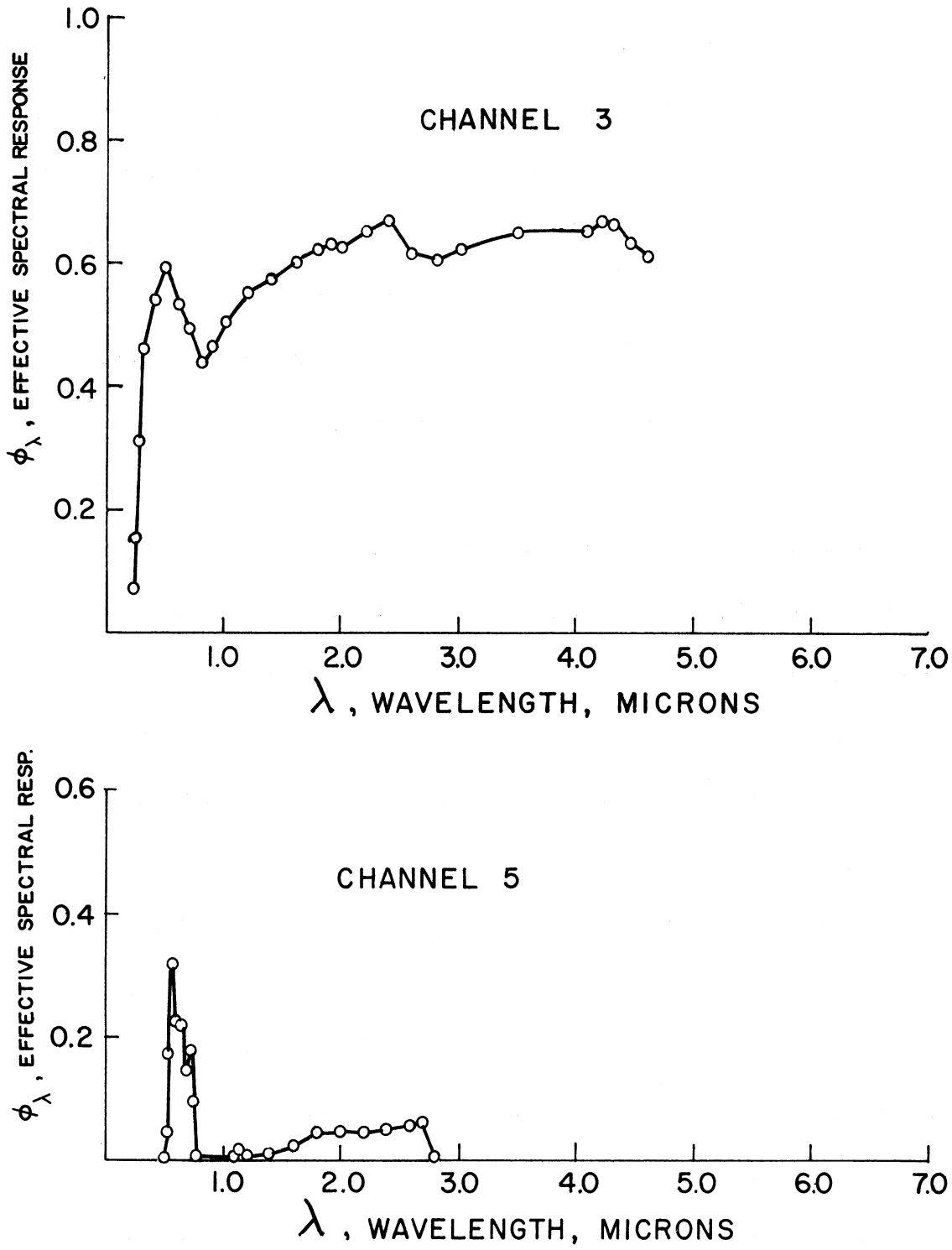

Figure 66. Effective spectral response of channels 3 and 5 of TIROS five-channel radiometer.

The radiometer is mounted in the satellite with its optical axis at 45° from the satellite spin axis. It revolves around the spin axis in a double cone with 45° half angle. The scan over the earth varies from a circle to two alternating quasi-hyperbolic branches, as shown in Figure 67.

The NIMBUS MRIR is a five-channel scanning radiometer designed to measure the flux of thermal radiation and the reflected and scattered solar radiation from the earth and its atmosphere.

The optical design of the radiometer is illustrated schematically in Figure 68. Incoming radiation is reflected by the scanning mirror into the five Cassegranian telescopes and then passes through the chopper into the collecting optics, filter, and bolometer detector.

The associated electronics consists of preamplifiers, mixer circuits, power amplifiers, synchonous detectors, output filters, and power supply.

The relative characteristic response ϕ'_λ of the two visible channels of the F-1 (flight model 1) radiometer are shown in Figures 69 and 70. The response of the one visible channel of the F-4 MRIR is also shown in Figure 70. This data was supplied with the radiometers by the Santa Barbara Research Center.

Other characteristics of the visible channels are illustrated by those of the F-4 MRIR visible channel, given in Table 19.[26] The field of view contours of the 0.2-4.0 micron channel of the F-4 MRIR are shown in Figure 71.

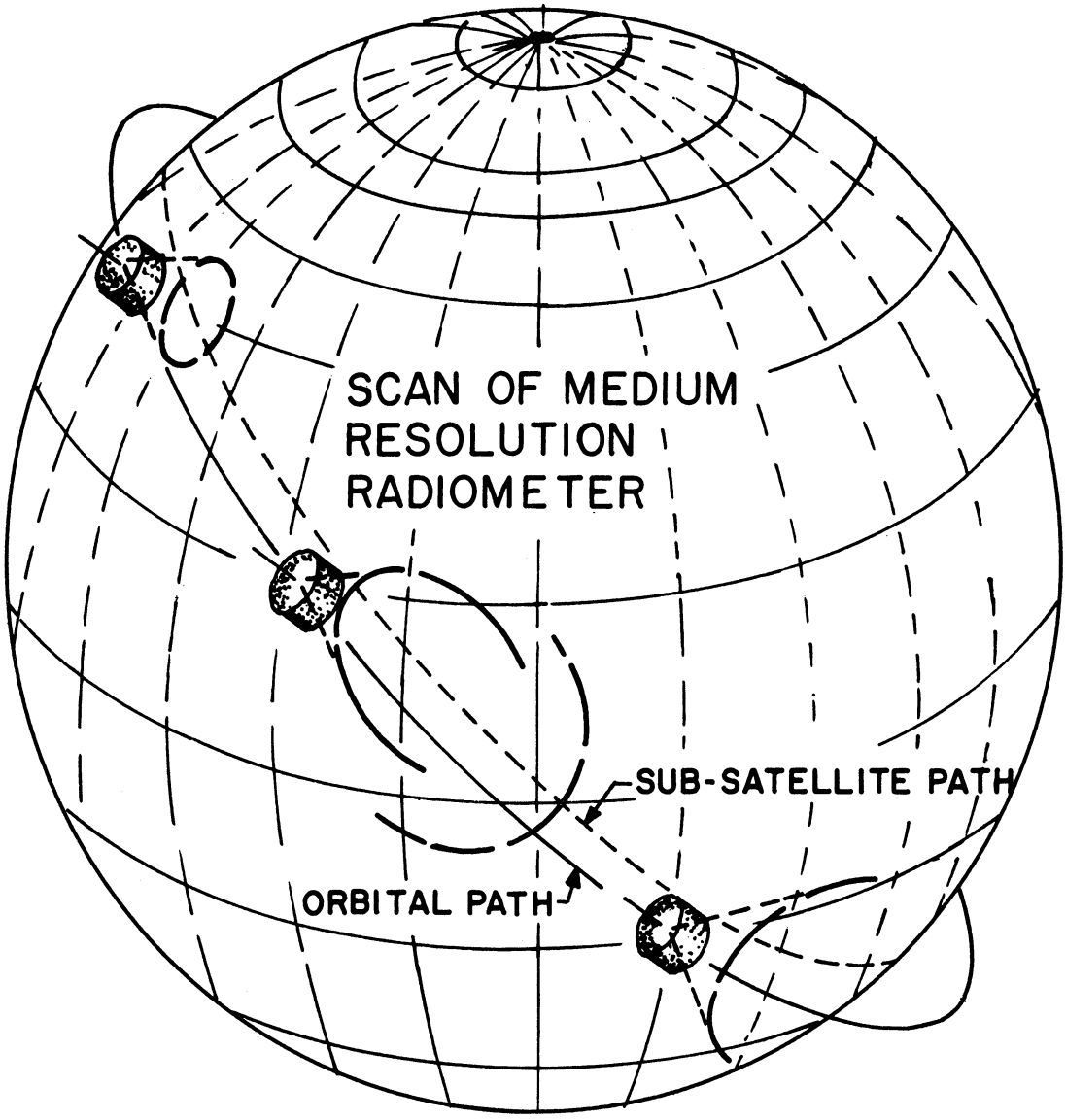

Figure 67. The scan patterns of the TIROS medium resolution radiometer (after Staff Members[22]).

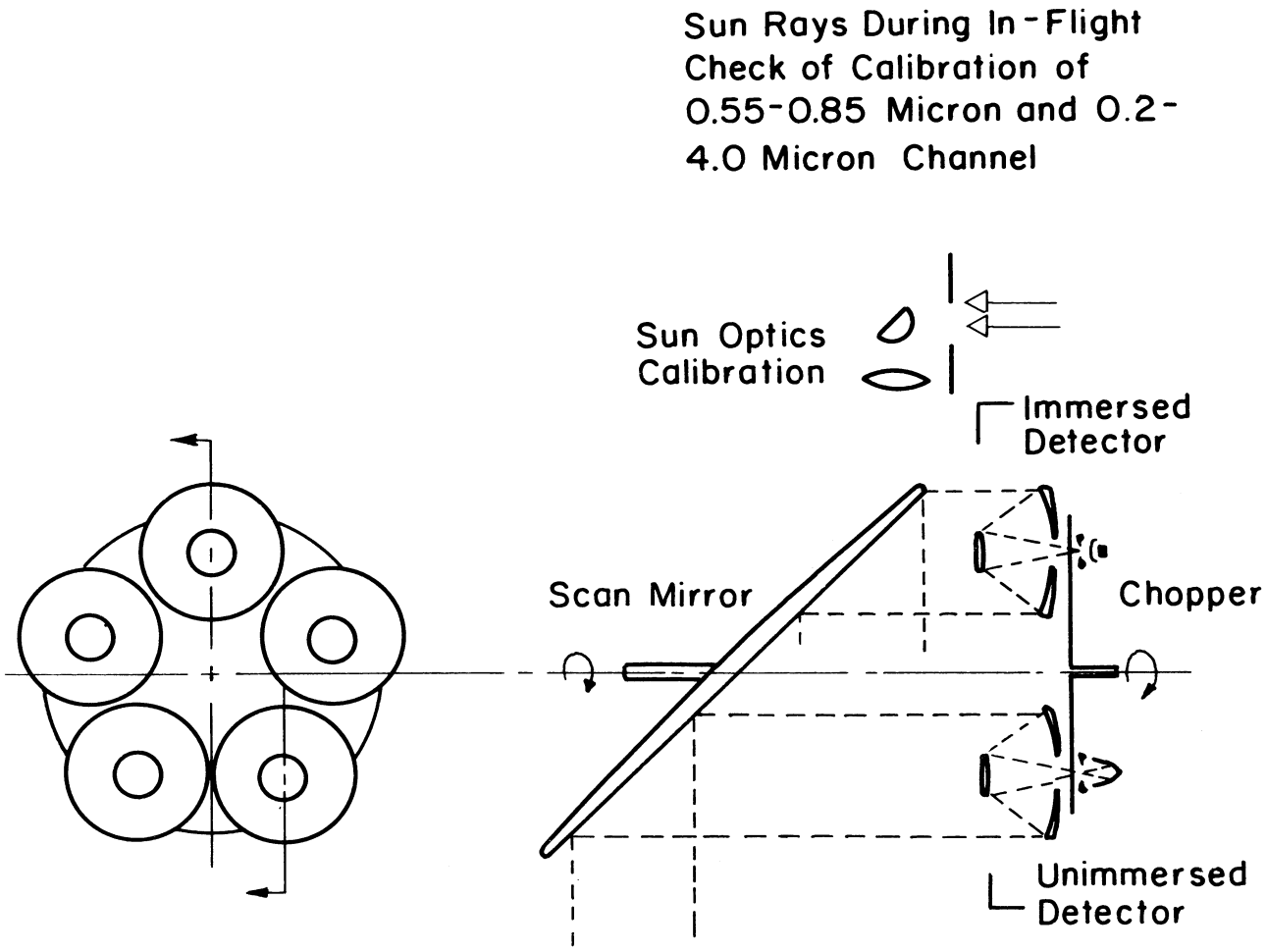

Figure 68. Optical arrangement of NIMBUS five-channel radiometer (MRIR).

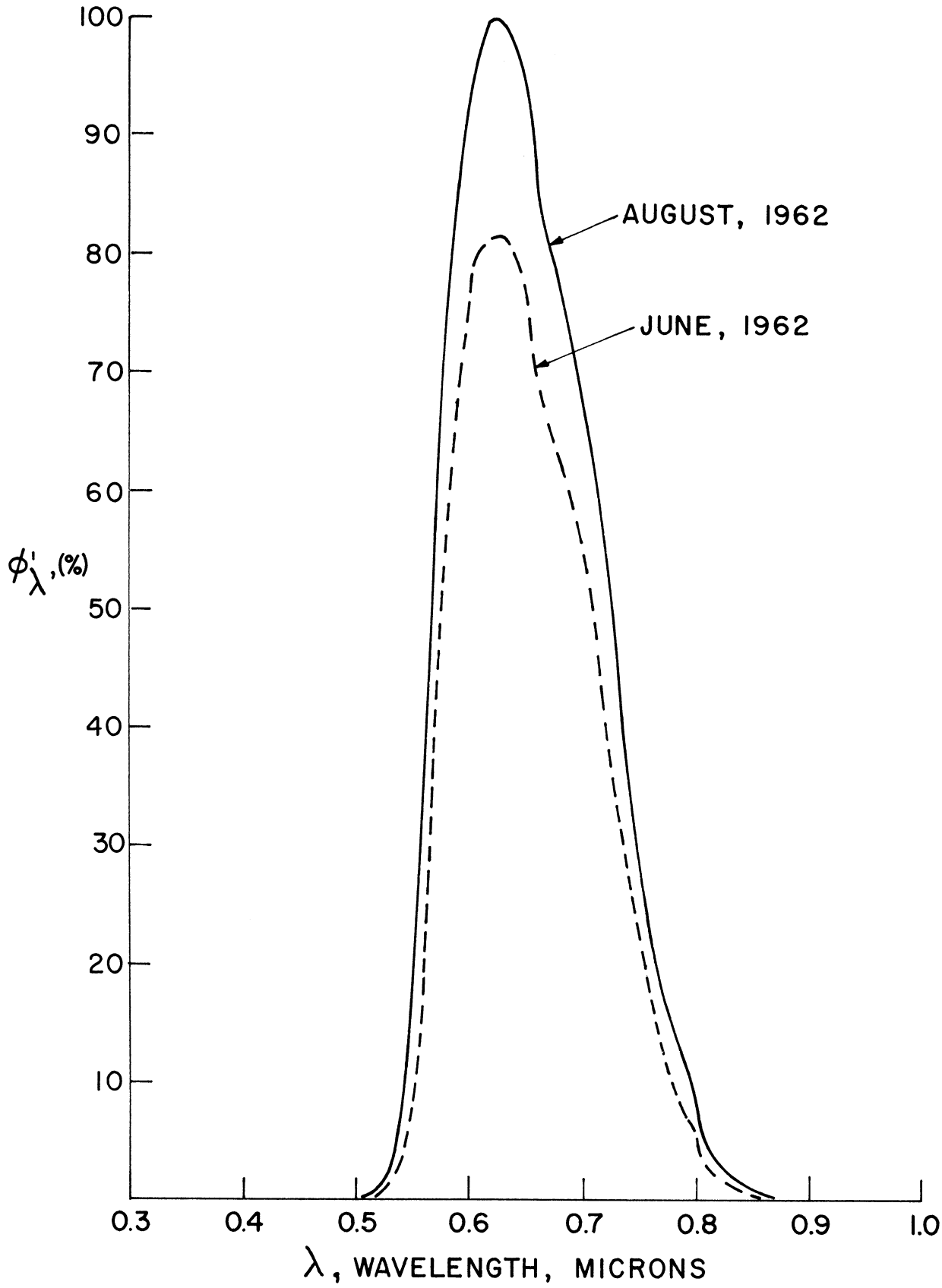

Figure 69. Relative characteristic response, ϕ', of 0.55-0.85-micron channel of F-1 MRIR.

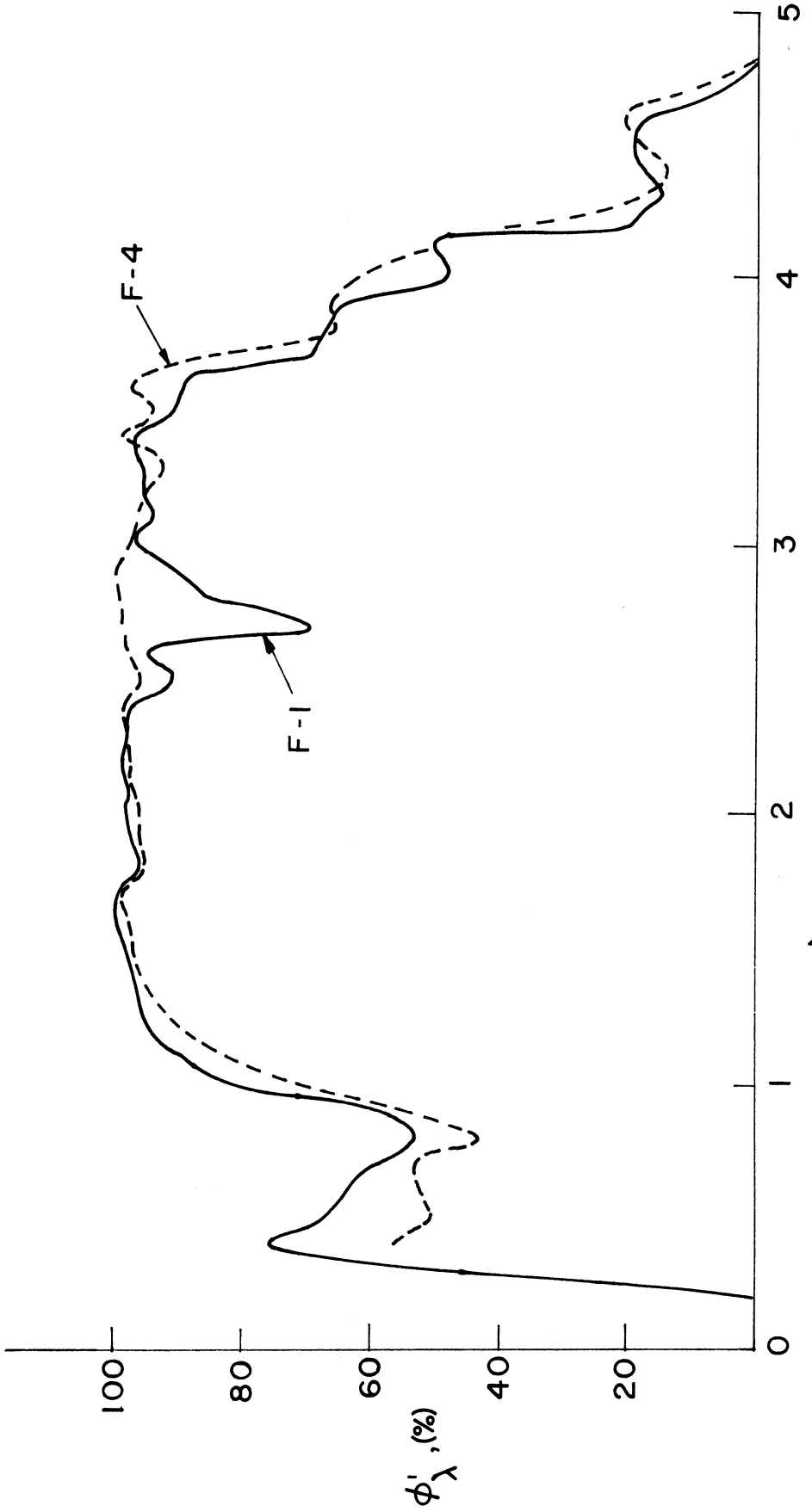

Figure 70. Relative characteristic response, ϕ', of 0.2-4.0-micron channel of F-1 and F-4 MRIR instruments.

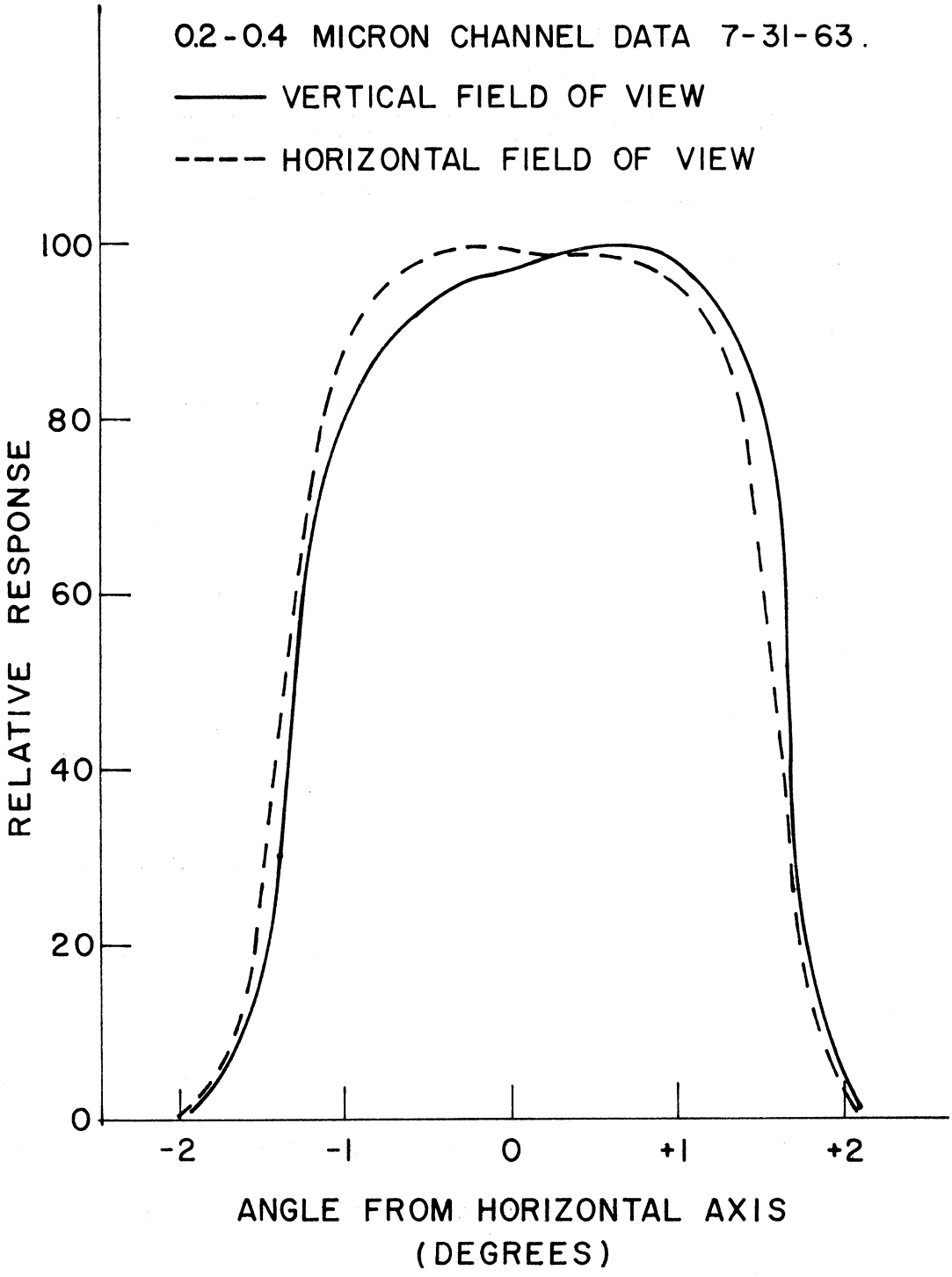

Figure 71. Field of view contours of the 0.2-4.0-micron channel of the F-4 MRIR.

TABLE 19

NOMINAL CHARACTERISTICS OF F-4 MRIR
(0.2-4.0-Micron Channel)

Spectral region (5% points)	0.2-4.8 microns
Field of view (-6 db points)	2.8°
Optical entrance aperture	1.72 in. dia
Effective system f/no.	0.93
System input noise	0.59 μvolts rms
System gain	$3.9 \cdot 10^3$ (rms to dc)
Responsivity	$1.6 \cdot 10^5$ volts/watt/cm^2
NEPD	$1.52 \cdot 10^{-8}$ watts/cm^2
Time constant	0.02 sec
Target range	0-80% albedo
Output impedance	5.8°K
Output voltage range	0 to -6.4 volts

The MRIR is installed on the NIMBUS satellite so that its rotation mirror scans at right angles to the plane of the satellite orbit. The field of view gives each channel a resolution of about 25 miles on the earth's surface. When the orbit is at the proper altitude, slightly overlapping scans of the earth, extending to the horizon on each side of the orbital path, are obtained.

The visible channels of the medium resolution radiometers are designed to obtain a measurement of the fraction of incident solar radiation which is reflected or scattered back out into space from the sur-

face of the earth, the clouds and the atmosphere. Thus the attempt is made to interpret the radiometer readings in terms of an equivalent average "reflectivity" or "albedo" of that portion of the earth and its atmosphere lying within the radiometer field of view.

The interpretation is made as follows.[27] Recall that the solar constant is defined to be the amount of solar radiation received at normal incidence (i.e., on a plane surface normal to the sun's rays) outside of the atmosphere at the mean earth-sun distance. The value used is 2.0 langleys min^{-1} (2 cal cm^{-2} min^{-1} or 0.1395 watt cm^{-2}). Recall that the solar constant can be expressed as:

$$H_S = \int_0^\infty H_{S\lambda} d\lambda \qquad (9)$$

where

H_S is the solar constant (irradiance).

$H_{S\lambda}$ is the solar spectral irradiance in watts cm^{-2} $micron^{-1}$.

If one solar constant of radiation at normal incidence is reflected from a perfectly diffuse reflecting surface with spectral bidirectional reflectance ρ_λ, the radiance of the reflecting surface will be:

$$N_S = \frac{1}{\pi} \int_0^\infty \rho_\lambda H_{S\lambda} d\lambda$$

and the bidirectional reflectance of the surface, averaged over all wavelengths will be:

$$\rho = \frac{\frac{1}{\pi}\int_0^\infty \rho_\lambda H_{s\lambda} d\lambda}{\frac{1}{\pi}\int_0^\infty H_{s\lambda} d\lambda} \tag{79}$$

This average bidirectional reflectance is a weighted average with weighting function taken to be the spectral distribution of the solar radiation.

When the surface is viewed by the visible channel of the radiometer, the radiometer voltage will be:[28]

$$V_s = R' A_r \Omega N'_s \tag{80}$$

where

R' is the responsity of the detector

A_r is the area of the radiometer aperture

Ω is the solid angle viewed by the radiometer

N'_s is the effective radiance of the reflected solar constant, i.e.,

$$N'_s = \frac{1}{\pi}\int_0^\infty \rho_\lambda H_{s\lambda} \not{\rho}_\lambda d\lambda \tag{81}$$

For $\rho_\lambda = 1$ (i.e., 100% reflectance), we would have:

$$N'_s(100\%) = \frac{1}{\pi}\int_0^\infty H_{s\lambda} \not{\rho}_\lambda d\lambda \tag{82}$$

For $\rho_\lambda \neq 1$, we may calculate an "effective" average bidirectional reflectance of the surface

$$\rho' = \frac{\frac{1}{\pi}\int_0^\infty \rho_\lambda H_{s\lambda}\phi_\lambda d\lambda}{\frac{1}{\pi}\int_0^\infty H_{s\lambda}\phi_\lambda d\lambda} \tag{83}$$

The average reflectance ρ' thus obtained is a weighted average with weighting function taken to be the product of spectral distribution of the solar radiation multiplied by the instrument response function.

The instrument readings cannot actually be interpreted at all unless suitable calibrations have been made. Problems typically encountered in making such calibrations are discussed in detail in Reference 27. Briefly, the method used for the calibration is referred to in the literature[28] as the "near extended source method." A diffuse source larger than the radiometer aperture, which will completely fill the radiometer, so that the transmissivity of the medium between the source and the instrument is essentially unity. The calibration procedure consists of the following four steps:

a. Vary N_c, the radiance of the diffuse calibration source for which the distribution of spectral radiance $N_{c\lambda}$ is known, over the desired range of amplitudes.

b. Record corresponding values of radiometer output voltage V_c and source radiance N_c.

c. For each value of N_c, calculate the corresponding value of N'_c by the equation

$$N'_c = \int_0^\infty N_{c\lambda}\phi_\lambda d\lambda$$

d. Plot the calibration curves of V_c vs. N'_c.

This calibration procedure must be carried out for all instrument temperatures at which the instrument will be operated.

The calibration curve of the visible channel of the radiometer may be given in terms of percent reflectance by taking that value of N'_c equal to N'_s (100%) as representing 100% reflectance, for radiation normally incident upon the surface viewed. Further a radiometer voltage reading V_c corresponding to a value of $N'_c = 0.5\ N'_s$ (100%) represents a reflectance of 50% for normally incident radiation. Similarly, in general, we define the percent reflectance of solar radiation, as measured by the visible channel of the radiometer by:

$$\rho' = \frac{N'_c}{N'_s(100\%)} = \frac{\int_0^\infty N_{c\lambda}\phi_\lambda d\lambda}{\frac{1}{\pi}\int_0^\infty H_{s\lambda}\phi_\lambda d\lambda} \tag{84}$$

Finally, to correct for angles of incidence other than 90°, it is necessary to divide the value of reflectance obtained by cos Θ, where Θ is the zenith angle of the incident radiation.

To summarize then, the interpretation of radiometer readings as percent reflectance is made by changing the radiometer calibration curves to the form of N'_c/N'_s (100%) vs. V_c. For normal incidence, a given radiometer reading corresponds to a reflectance equal to the value of N'_c/N'_s (100%) obtained from this curve. For other angles of incidence of the solar rays it is necessary to divide by cos Θ, where Z is the solar

zenith angle. Thus:

$$\rho' = \frac{N'_c}{N'_s(100\%)\cdot\cos\Theta}$$

$$= \frac{\int_0^\infty N_{c\lambda}\phi_\lambda d\lambda}{\cos\Theta\cdot\frac{1}{\pi}\int_0^\infty H_{s\lambda}o_\lambda d\lambda} \qquad (85)$$

One final correction to be made is a correction for variation in values of $H_{s\lambda}$. Values of $H_{s\lambda}$ used in drawing calibration curves are values for the sun at its mean distance from the earth. Variations of values of $H_{s\lambda}$ during a year are as great as ±3.3% and should be corrected for.

The only study of earth's albedo based on medium resolution measurements from a satellite is that of Bandeen, et al.,[1] using data obtained with the TIROS VII 5-channel radiometer. The albedo study was only a part of a general radiation balance study using the TIROS VII data. Results have been obtained for a two-year interval, June 1963 through May 1965. The first years results were published in Reference 1 and the second year's data were included in a paper presented at the 47th Annual Meeting of the American Geophysical Union.[29] Only the first year's results are discussed herein.

Although ideally a study of heat balance and albedo would be made with data obtained by the "total" thermal and solar radiation channels, 8-30 microns and 0.2-6 microns, these channels were not used by Bandeen, et al., because of engineering problems. Instead data from the 8-12-

micron and 0.55-0.75-micron channels were used.

The albedo results were obtained as follows. Values of reflectance calculated by Equation (65) were used, assuming isotropic, i.e., perfectly diffuse reflection. The reflectance was also assumed to be independent of wavelength. The maximum allowable solar zenith angle allowed was 70° and the maximum nadir angle of the radiometer optical axis was 45° for the data used in the study. With the satellite orbital inclination of 58.2°, this resulted in coverage between 63.5°N and S. This area was called the "quasi-globe." A square mesh grid having 2376 elements was superimposed on a Mercator map of the "quasi-globe," and averages were made of measurements accumulated in each grid square over a period of about seven days. Averages of all individual measurements for the week were also calculated. Seventeen of these averages were plotted vs. time for the first years data (see Figure 72). A least squares linear curve fitted to these data were taken to represent an apparent degradation of the instrumental response as a function of time. The individual reflectance readings were then corrected for the degradation by the factor h(t), i.e., a corrected reflectance value becomes,

$$\rho'' = h(t)\cdot\rho' \tag{86}$$

The weekly grid averages were then recomputed using the correction factor for degradation. Grid averages of four weekly maps, each separated by approximately 19 days, were averaged to give a grid average for a season.

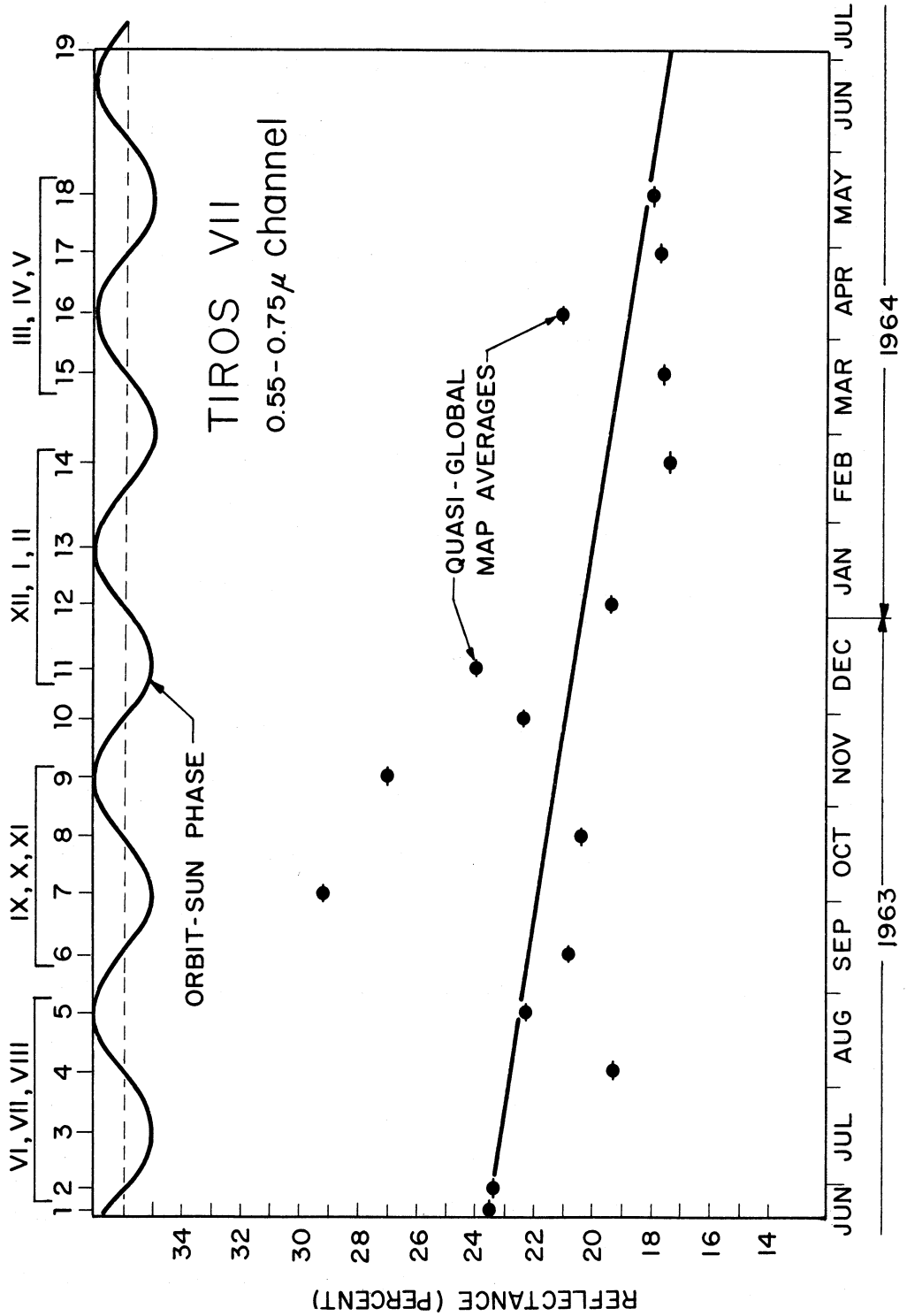

Figure 72. TIROS VII: 0.55-0.75-micron channel quasi-global map averages (after Bandeen[1]).

Meridional averages were then computed for each season, as shown in Figures 73 through 76. The meridional averages for the season were extended beyond 63.5°, up to 90° by reference to the work of London,[23] i.e., the curve was extended in a direction parallel to the data of London.

Meridional integrations were then made using a planimeter to integrate over the curve, thus weighting the albedo contributions according to land area of the various latitude zones. The annual albedo of the earth was then found by averaging the results for the four seasons.

When this was done, it was found that the annual planetary albedo required to balance the annual long wave flux determined from the 8-12 micron channel was 32.2%, whereas the value obtained from the calculation was 20.1%. Assuming that radiation balance exists on the average over the year, there is a glaring inconsistancy between the two types of data. Since it was felt that the long wave measurements were more precise than the solar radiation reflectances, all reflectances were multiplied by a factor of $\frac{32.2}{20.1} = 1.6$. Thus finally we have for TIROS VII reflectances:

$$\rho_c''' = 1.6 \cdot h(t) \cdot \rho' \qquad (87)$$

The final values obtained are given in Table 20. The annual meridional values of albedo are shown in Figure 77. Data from London are shown for comparison.

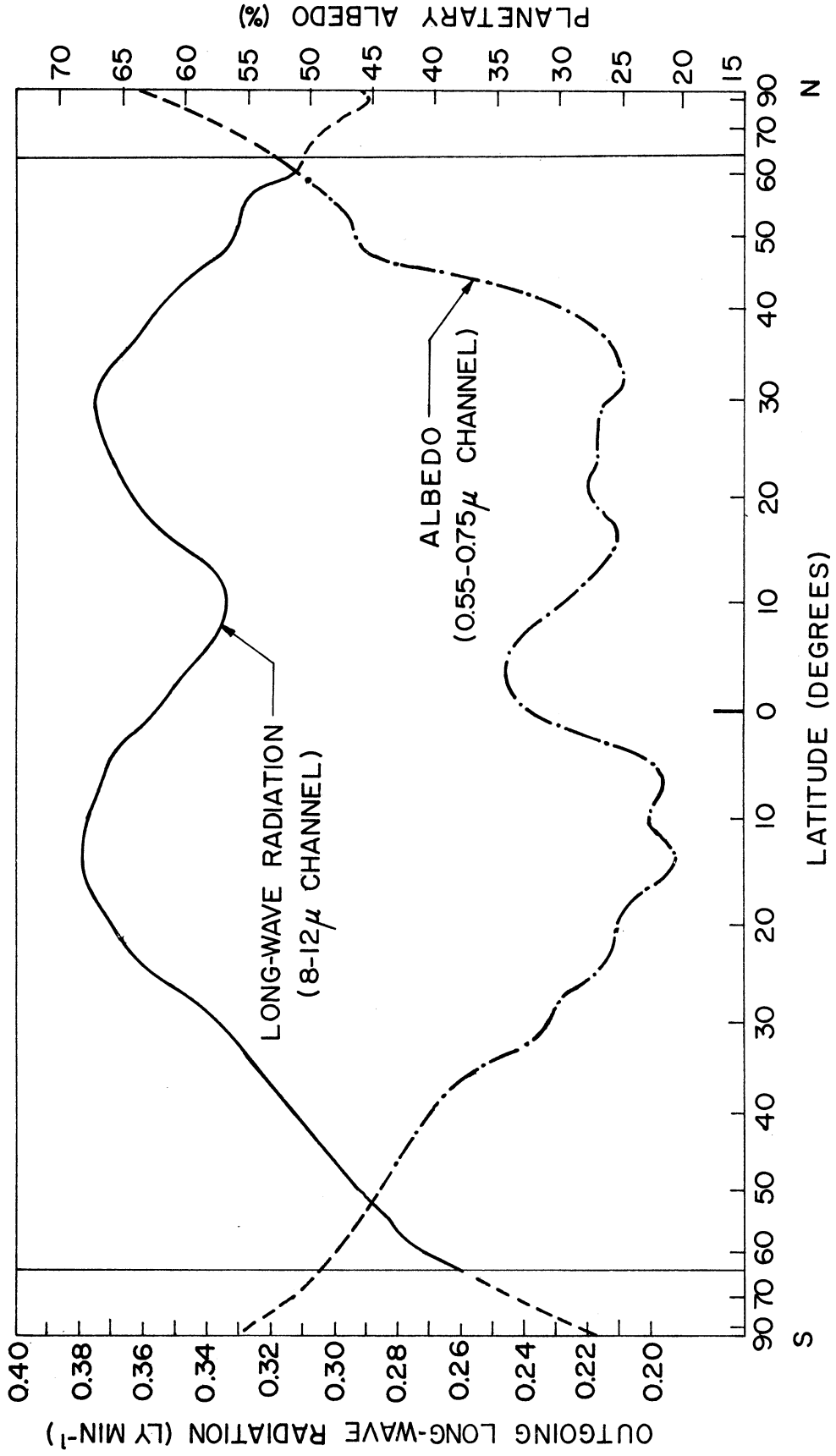

Figure 73. TIROS VII: 0.55-0.75-micron channel albedo, June-July-August 1963 (after Bandeen[1]).

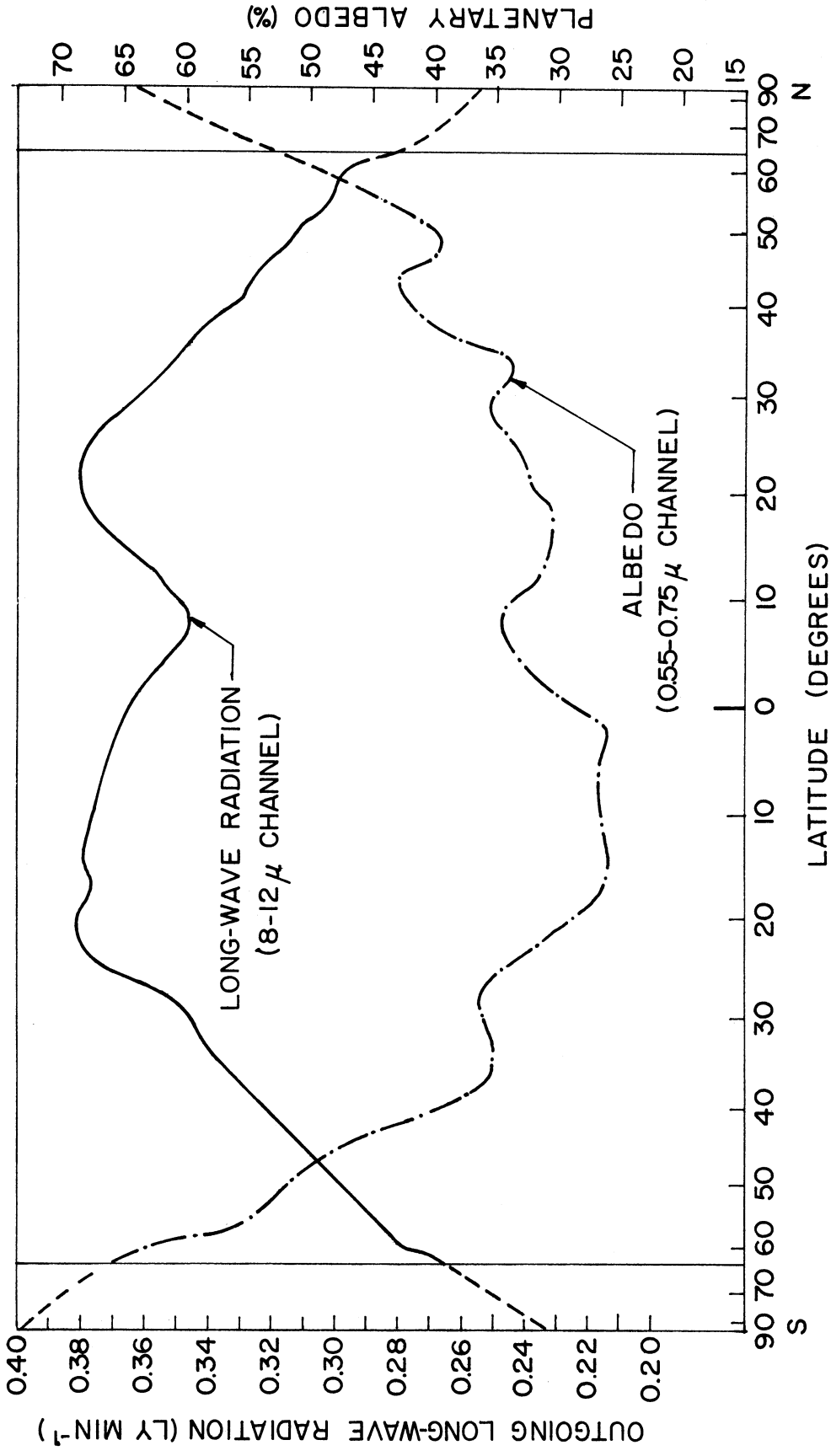

Figure 74. TIROS VII: 0.55-0.75-micron channel albedo, September-October-November 1963 (after Bandeen[1]).

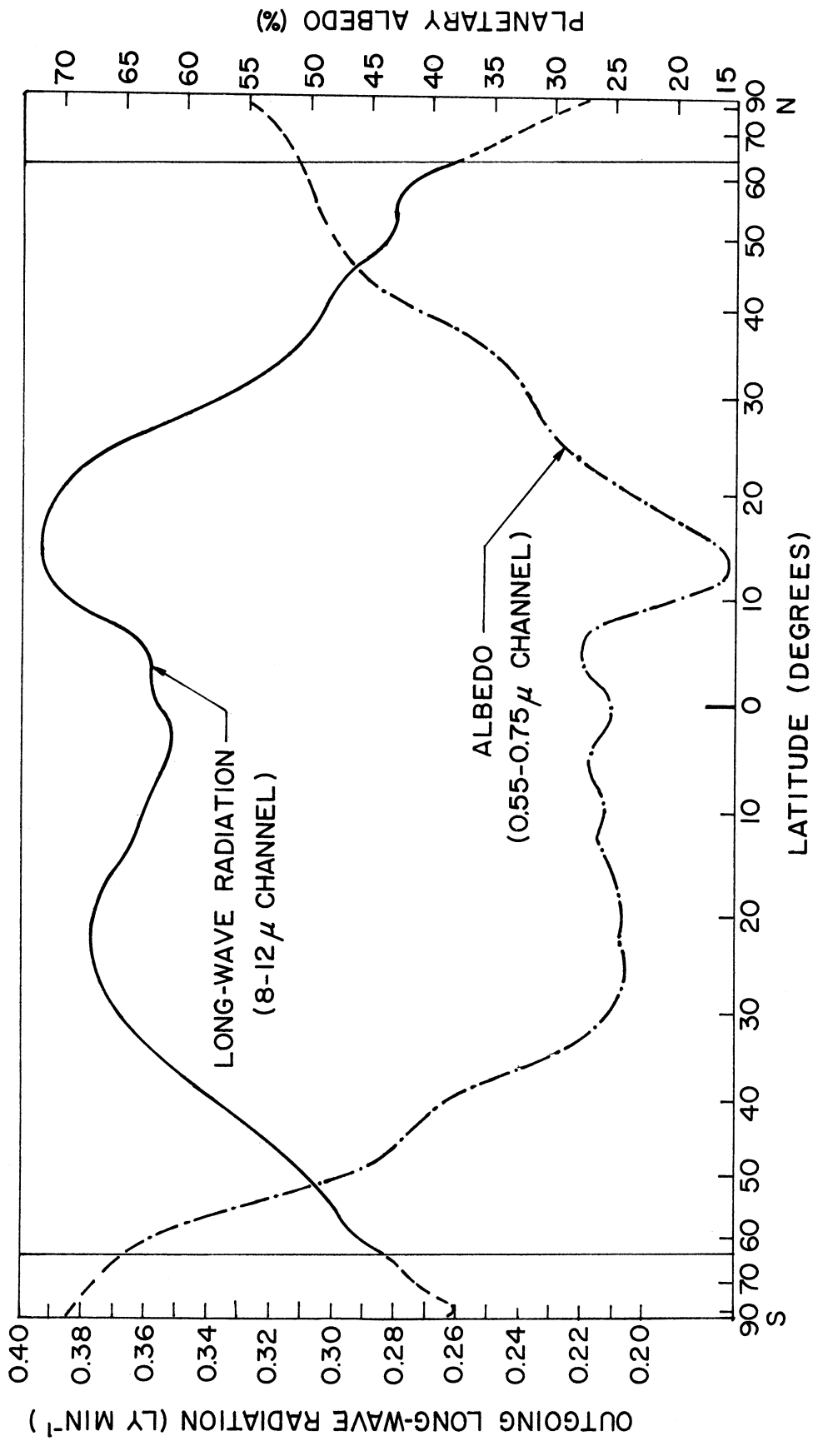

Figure 75. TIROS VII: 0.55-0.75-micron channel albedo, December 1963-January-February 1964 (after Bandeen[1])

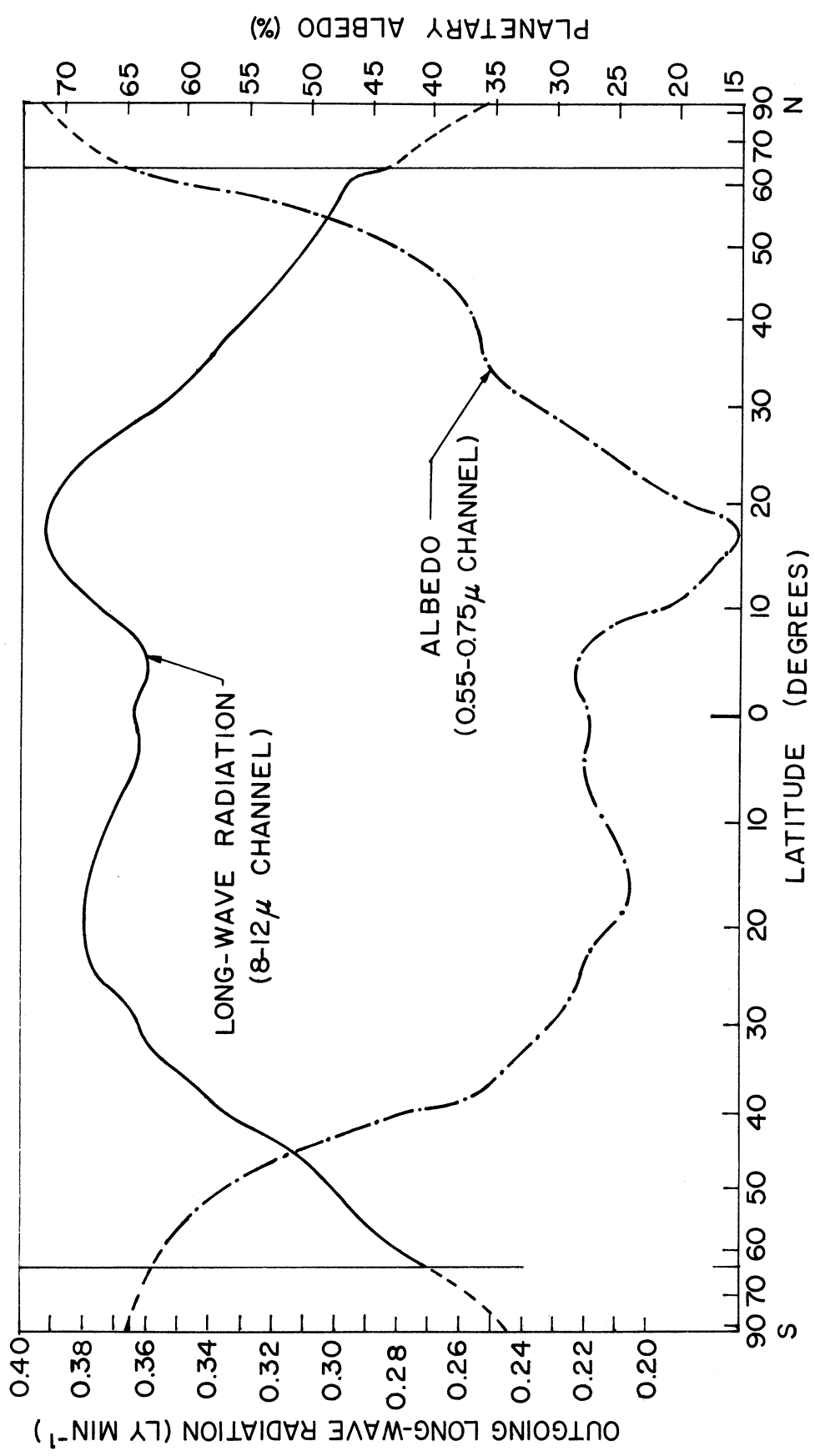

Figure 76. TIROS VII: 0.55-0.75-micron channel albedo, March-April-May 1964 (after Bandeen[1]).

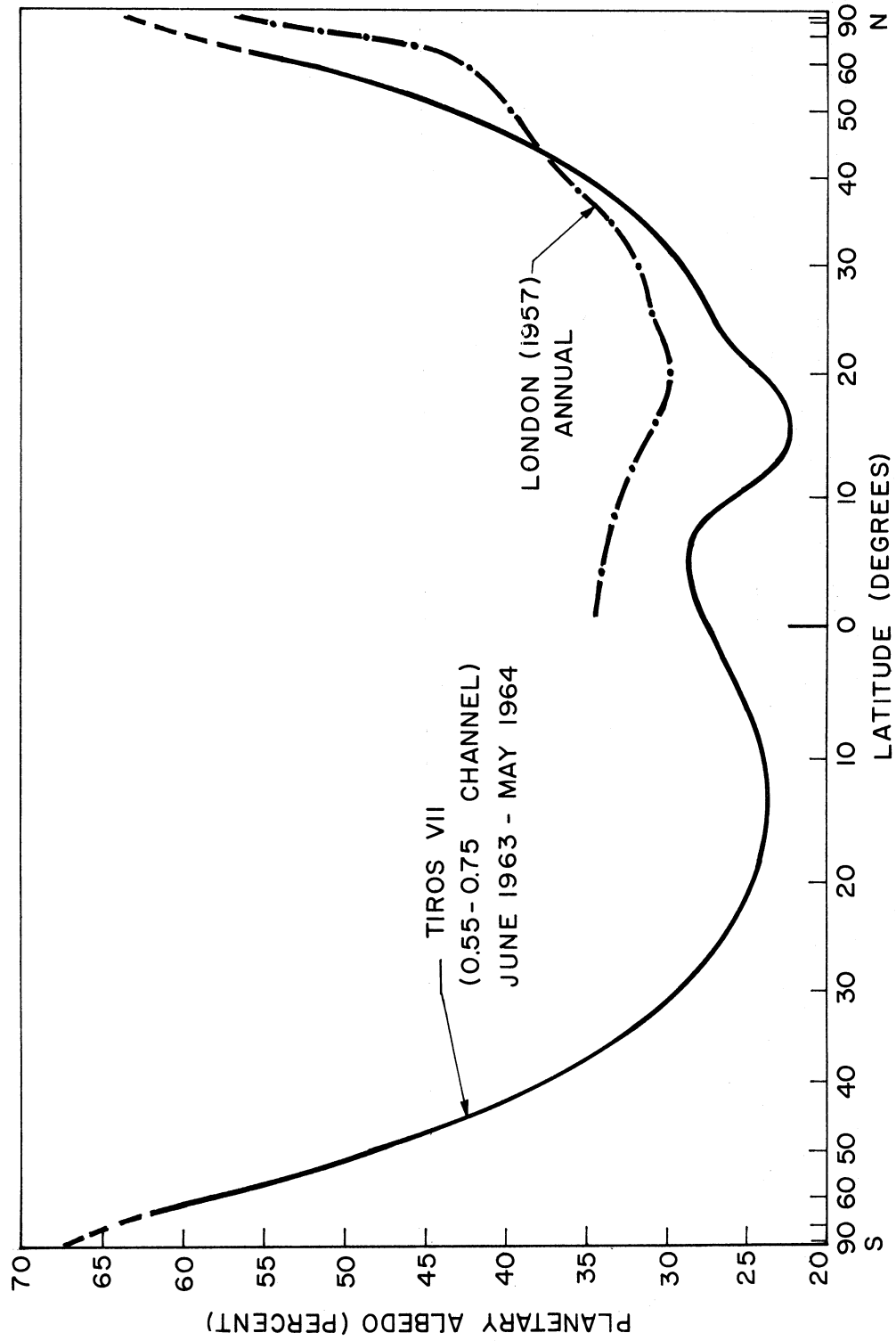

Figure 77. TIROS VII: 0.55-0.75-micron channel albedo, June 1963-May 1964 (after Bandeen[1]).

TABLE 20

FINAL SEASONAL AND ANNUAL VALUES OF LONG- AND SHORT-WAVE RADIATION
(After Bandeen[1])

Season (Months)	Planetary Long-Wave Radiant Power (10^{15} cal min^{-1})	Solar Radiation		Planetary Albedo (%)
		Reflected (10^{15} cal min^{-1})	Incident on Planet (10^{15} cal min^{-1})	
J-J-A	1725.2	699.0	2457.8	28.4
S-O-N	1725.2	922.2	2574.8	35.8
D-J-F	1712.2	859.7	2609.8	32.9
M-A-M	1746.5	796.0	2544.2	31.3
Annual	1727.3	819.4	2546.7	32.2

The author assumes that the additional unexplained factor of 1.6 for reflectances, which is necessary to provide radiation balance over the year, may be explained by some combination of the following factors.

a. Error in the original calibration.

b. Error due to the assumption of isotropic reflectance. (In this regard, recall that reflectance samples used were restricted to solar zenith angles of less than 70° and radiometer nadir angles of less than 45°.)

c. Error due to unobserved deterioration before the first orbit on 19 June, 1963.

d. Error due to the assumption of reflectance independent of wavelength. (Related to this is use of the 0.55-0.75-micron channel reflectances for total solar albedo.)

Examination of the method of data analysis indicates two other possible sources of error.

a. A bias due to the geographical sampling technique.

b. Error in the method used to obtain planetary albedo from the meridional albedo curves.

3. THE MARINER 2 MEASUREMENTS

Some information on brightness variations of the earth as viewed from relatively large distances was obtained from measurements made with the earth tracking system on board the Mariner 2 spacecraft on its flight to the planet Venus.[16]

The measurements were obtained by the photometer which was one part of the Long Range Earth Sensor (LRES) on this spacecraft. In addition to signals which provided information for altitude correction of the spacecraft, the instrument output included a signal which indicated the amount of light being sensed. This signal was calibrated photometrically before the flight, however no in-flight calibration was made.

The brightness of the earth as seen from the spacecraft was computed from the photometer signals by means of the following equation:

$$S_{\oplus} = \frac{\int_0^{\infty} f_{\oplus}(\lambda)\cdot\phi_v(\lambda)\cdot d\lambda \cdot \int_0^{\infty} f_o(\lambda)\phi_{sII}(\lambda)d\lambda}{\int_0^{\infty} f_{\oplus}(\lambda)\cdot\phi_{sII}(\lambda)d\lambda \cdot \int_0^{\infty} f_o(\lambda)\cdot\phi_v(\lambda)d\lambda} \cdot S_o\cdot R(T,70)\,\frac{I_{\oplus}}{I_o} \qquad (88)$$

where

ϕ_v = the response function of the eye.

ϕ_{sII} = the response function of the SII photo emissive surface multiplied by the transmission function of the objective lens.

$f_o(\lambda)$ = spectral energy distribution of the standard source.

$f_{\oplus}(\lambda)$ = spectral distribution of the earth radiation.

I_o = photoelectric current produced by the standard source.

$I_{\oplus}$ = photoelectric current produced by the earth radiation.

$R(T,70)$ = $\frac{\text{response at } 70^\circ F}{\text{response at } T^\circ F}$.

S_o = footcandle output of the standard source.

$S_{\oplus}$ = the earth brightness in footcandles.

The spectral distribution of earth radiation was assumed to be constant and equal to

$$f_{\oplus}(\lambda) = f_1(\lambda) \cdot f_2(\lambda) \cdot f_3(\lambda) \qquad (89)$$

where

$f_1(\lambda)$ = the empirical solar continuum according to Minnaert.

$f_2(\lambda)$ = 1-F.

F = the Fraunhofer line blanketing coefficient according to Michard.

$f_3(\lambda)$ = an assumed wavelength dependence of the overall reflectivity of the earth, based on three color observations of Danjon. The assumed curve is linear with a value of 1.47 at 4330Å and 1 at 5540Å.

Data were obtained for a 52-day period, from 29 September to 22 November, 1962. The space probe distance from the earth varied from $8.6 \cdot 10^6$ km to $33.4 \cdot 10^6$ km during this time. During this time, the earth's phase angle as viewed from the space probe varied from 45° down to 11.3° and then back to 24.4°. After this time, the temperature, which had been rising rapidly, was too high for temperature corrections.

It was found that the data obtained did not agree with absolute values obtained by Danjon. The following conclusions were drawn:

a. The part of the data obtained for increasing phase did not agree with the data for decreasing phase angles. It was assumed that the temperature corrections were incorrect for high temperatures.

b. Danjon's phase curve, normalized to fit the Mariner 2 data at minimum phase angle, was found to agree well with data taken for decreasing phase angle.

c. Diurnal brightness variations and a semi periodic variation of 5-6 days was observed.

d. Since the latitude variation of the Mariner 2 suborbital point did not very greatly, being approximately at the earth's equator, variation with latitude was not measured.

e. The diurnal variations indicated most pronounced relative maxima corresponding to a point in the Atlantic above the eastern extreme of South America, and most pronounced relative minima corresponding to the center of the Pacific Ocean. A calculation, considering the percent land/ocean area in each case, indicated a reflectance of land forms 1.41 times as great as that of ocean area.

f. A possible explanation of the greater reflectivity of land relative to ocean is that clouds may tend to concentrate over land rather than water.

APPENDIX C

REFLECTANCE OF THE EARTH'S SURFACE

1. SPECTRAL REFLECTANCE

a. Soils and Rocks

The spectral reflectance of soils and rocks is illustrated by Figures 78 to 83, taken from References 31 to 36. Although all of these figures yield information concerning the spectral dependence of reflectance, care must be taken in using the data, because different quantities have been measured.

In Figures 78, the quantity measured is the bidirectional reflectance: $\rho_\lambda(45°, 0, 0, 0)$, i.e., the incident radiation has zenith angle 45° and the reflected radiation is measured normal to the reflecting surface (at zero degrees zenith angle).

Figures 80, 81, and 82 are measurements of the directional reflectance:

$$r_\lambda(\theta_o,\phi_o) = \frac{1}{\pi} \int_{\phi=0}^{2\pi} \int_{\theta=0}^{\frac{\pi}{2}} \rho_\lambda(\theta_o,\phi_o,\theta,\phi)\cos\theta \sin\theta \, d\theta d\phi \qquad (90)$$

The zenith angle of incidence θ_o will not necessarily be the same for all three cases, since it has not been noted in the papers, however, it is probably close to zero degrees.

The quantity indicated in Figure 79 was measured under conditions of natural illumination, so that the source is direct sunlight plus the diffuse skylight. We can indicate this measurement by the following definition:

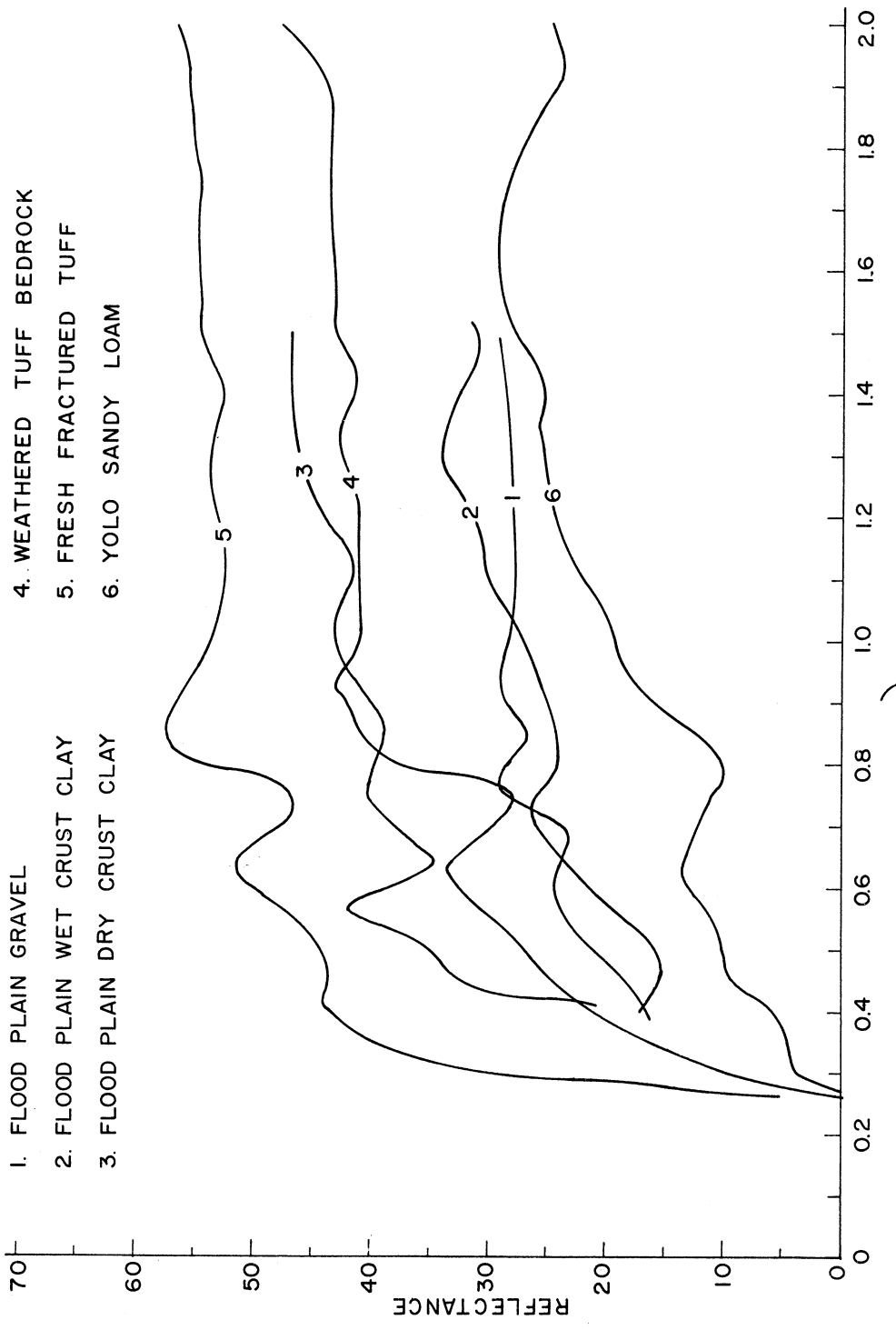

Figure 78. Reflectance curves for soils and rocks (after Orr, et al.[31]).

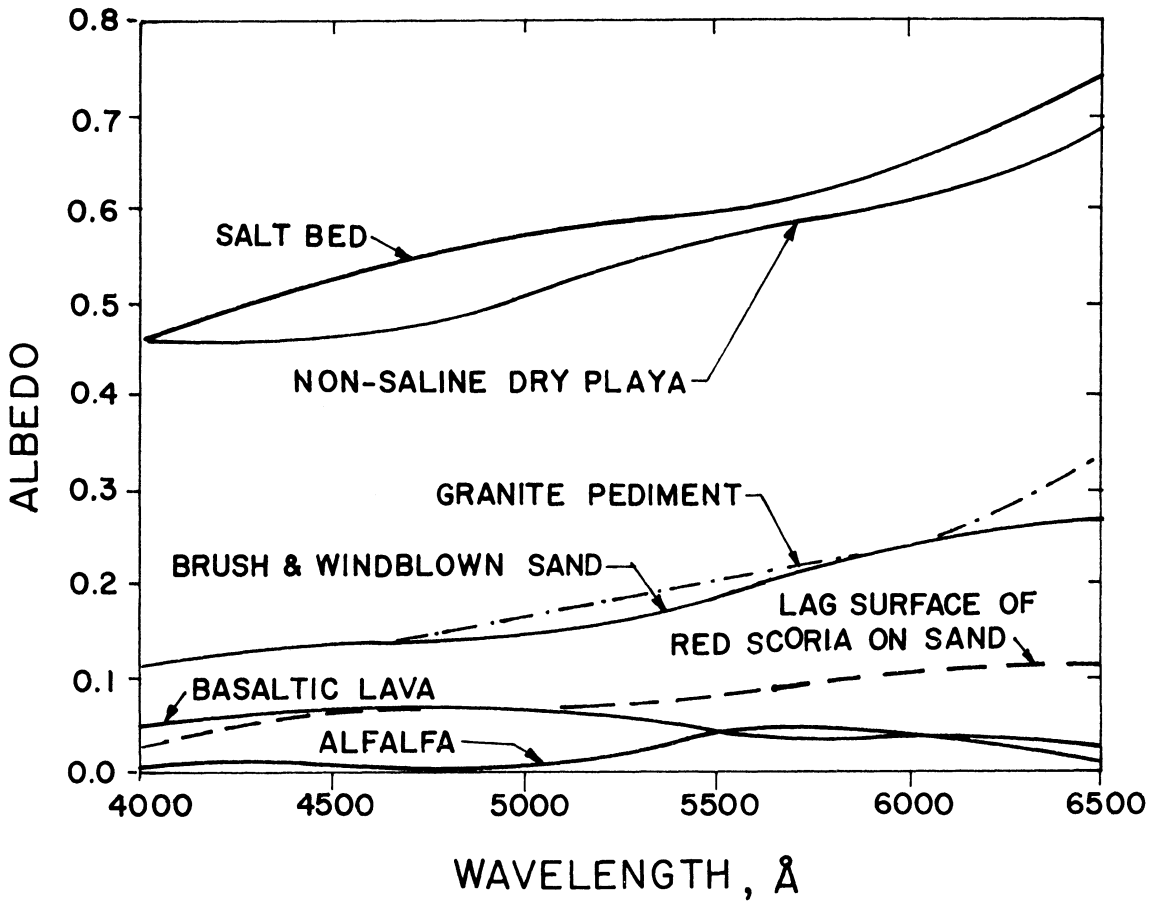

Figure 79. Diffuse reflectance of representative types of desert surfaces (after Ashburn, et al.[32]).

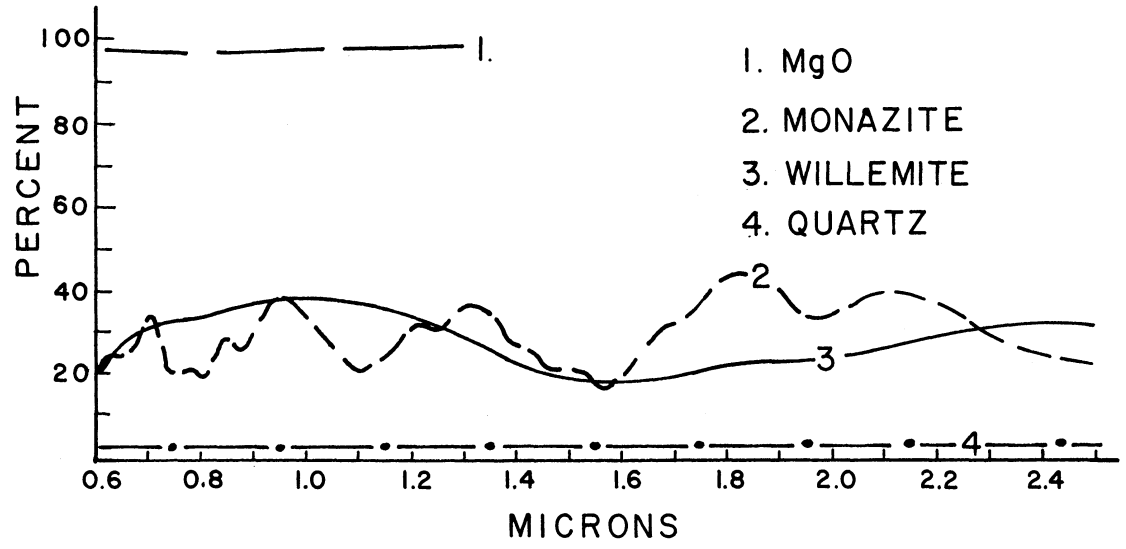

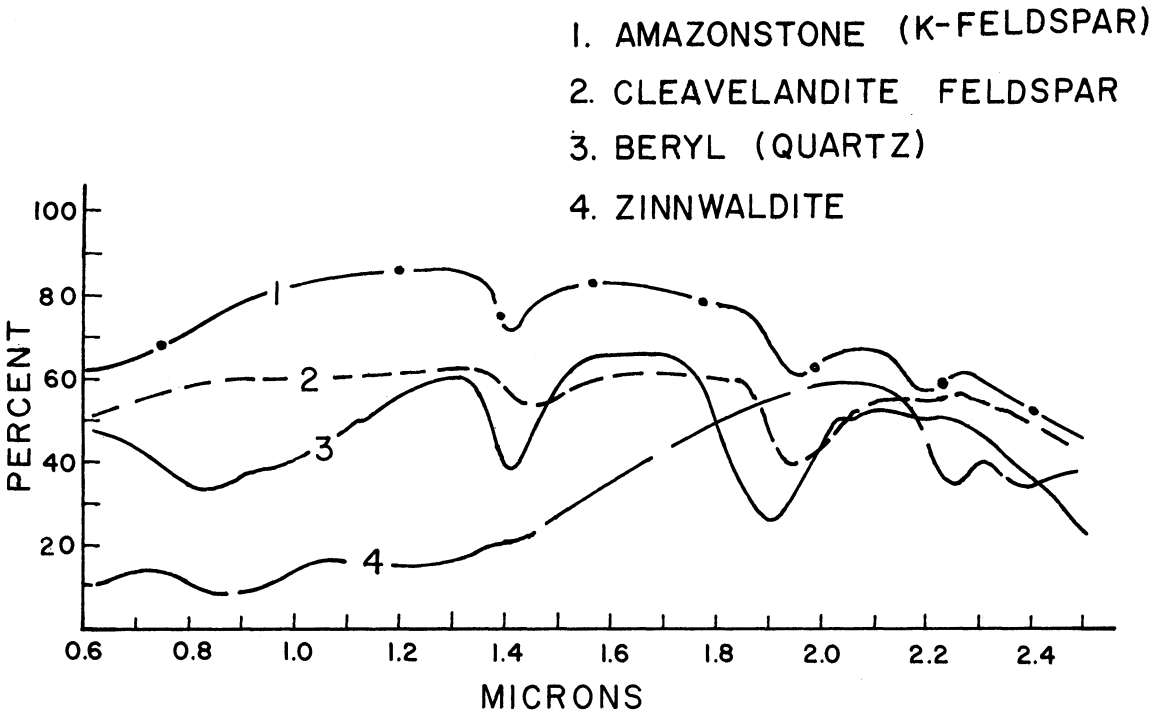

Figure 80. Spectral distribution of reflected energy for minerals and rocks (after Gerharz, et al.[33]).

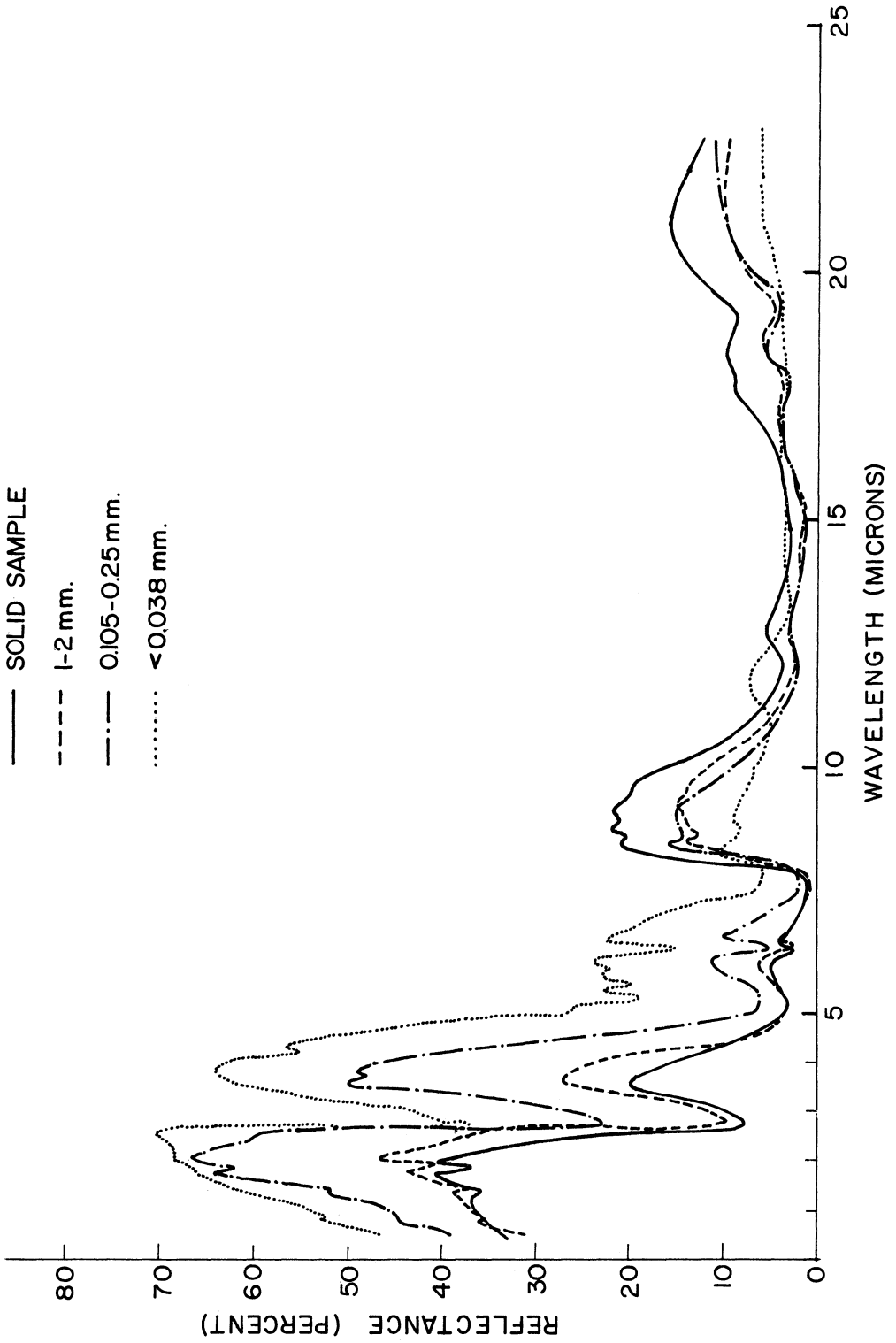

Figure 81. Reflectance of NAA standard granite (after Hovis, et al.[34]).

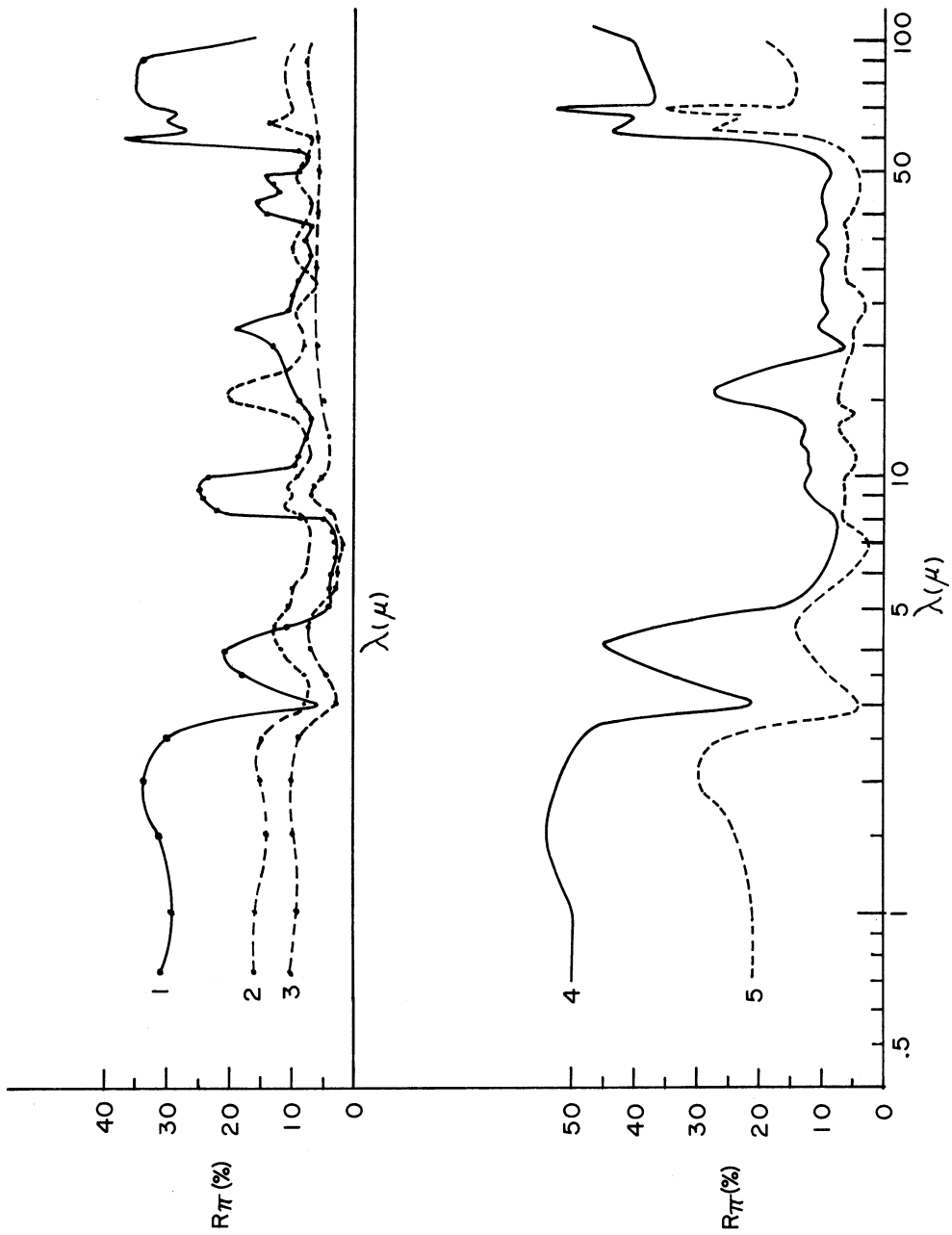

Figure 82. Spectral reflectance coefficients. (1) sand; (2) soil; (3) asphalt; (4) brick; (5) concrete (after Kropotkin, et al.[35]).

$$\overline{r_\lambda(\theta_o,\phi_o)} = \frac{\int_{\phi=0}^{2\pi}\int_{\theta=0}^{\frac{\pi}{2}}\int_{\phi_o=0}^{2\pi}\int_{\theta_o=0}^{\frac{\pi}{2}} \rho_\lambda(\theta_o,\phi_o,\theta,\phi)\cdot H_\lambda(\theta_o,\phi_o)\cos\theta\sin\theta\cos\theta_o\ \sin\theta_o d\theta d\phi d\theta_o d\phi_o}{\int_{\phi_o=0}^{2\pi}\int_{\theta_o=0}^{\frac{\pi}{2}} H_\lambda(\theta_o,\phi_o)\cos\theta_o\cdot\sin\theta_o d\theta_o d\phi_o} \qquad (91)$$

It is a weighted average directional reflectance, with the weighted average taken over all directions of incidence. The zenith angle of the sun was not specified for this figure and so the amount of diffuse incident radiation is not known (for low sun angles, it may be as much as 10% of the direct sunlight). This quantity is called the albedo of the surface element by the author.

The data of Figures 83a and 83b, show the bidirectional reflectances $\rho_\lambda(53°, 0, \theta,\phi)$ for desert sand and $\rho_\lambda(78.5°, 0,\theta,\phi)$ for black loam soil. The measurements are taken in the principal plane so that ϕ has the values o, 180° as shown.

All of the above measurements show an increase of reflectance with increasing wavelength up to at least 1 micron, and a decrease of reflectance with increasing wavelength beyond 2 microns.

The data of Figure 78 indicate that wetting a crust clay surface decreases its reflectivity, and Figure 81 indicates that powdering a rock material may increase its reflectivity.

b. Vegetation

The spectral reflectance of various types of vegetation is illustrated by Figures 84 to 86 taken from References 31, 37, and 38. Again the figures represent different quantities. Figure 84 shows the bidirectional reflectance $\rho_\lambda(45°, 0, 0, 0)$, Figure 85 represents measurements made under conditions of natural illumination, i.e., the

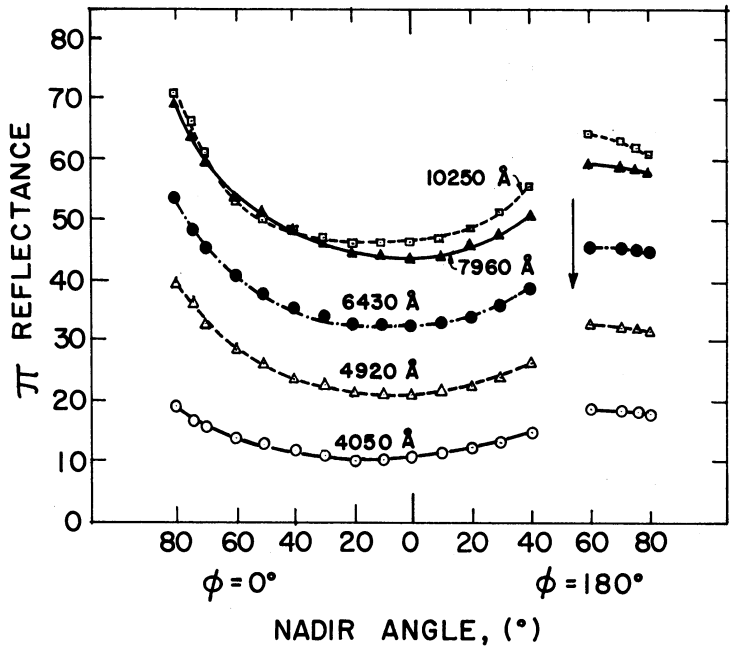

a.) DESERT SAND.

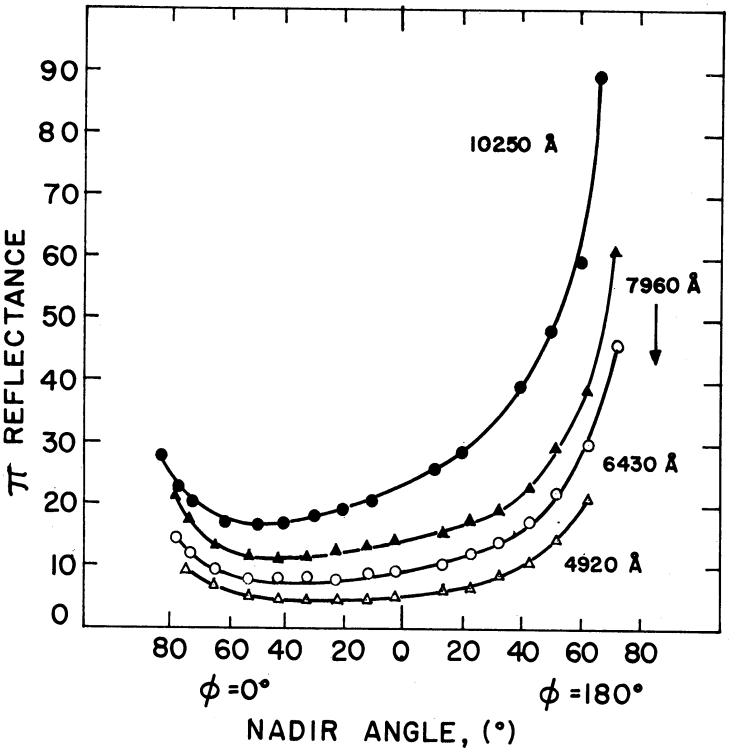

b.) BLACK LOAM SOIL.

Figure 83. Bidirectional reflectance of sand (θ_o = 53°) and black loam soil (θ_o = 78.5°) at different wavelengths (after Coulson[36]).

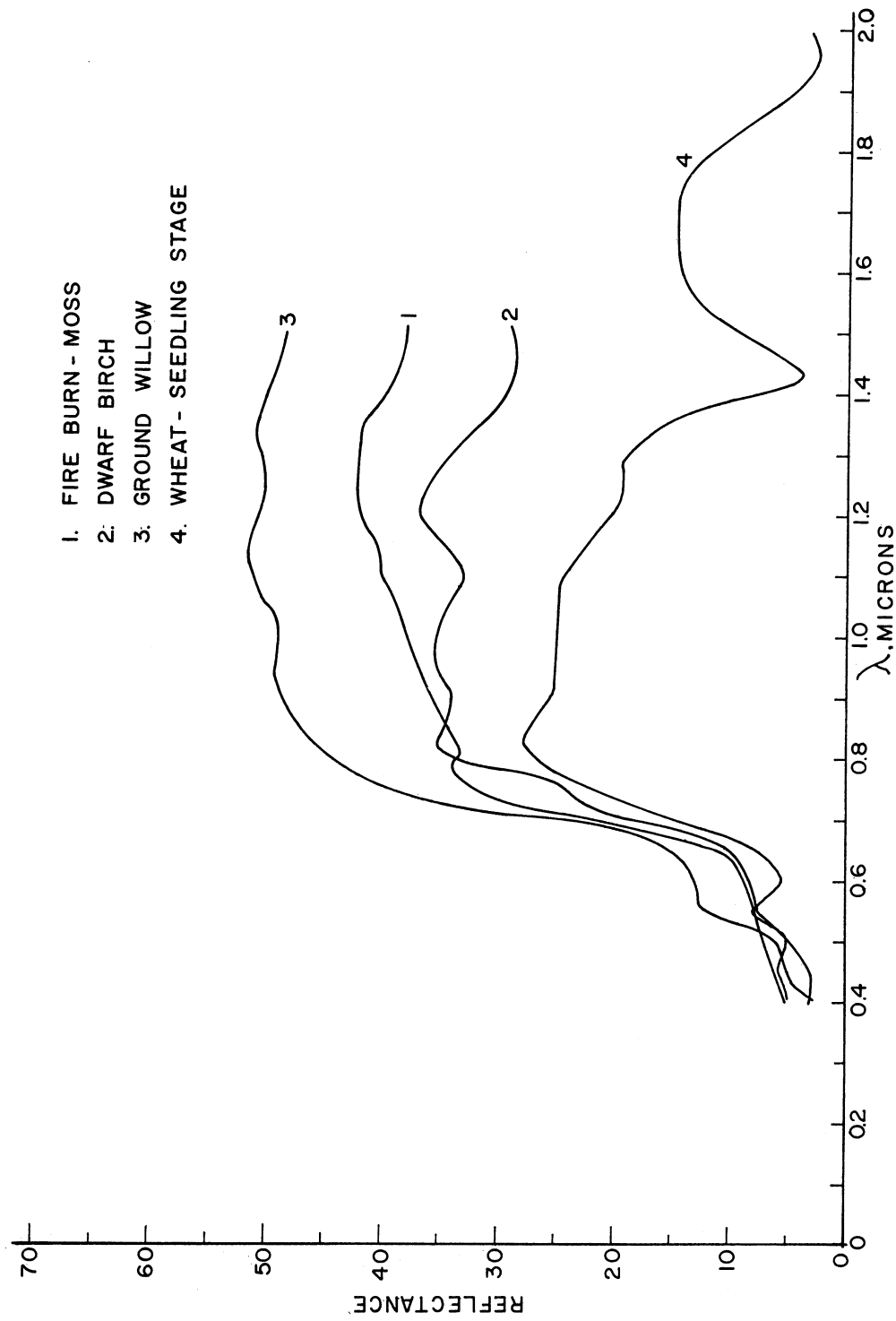

Figure 84. Spectral reflectance curves for vegetation (after Orr, et al.[31]).

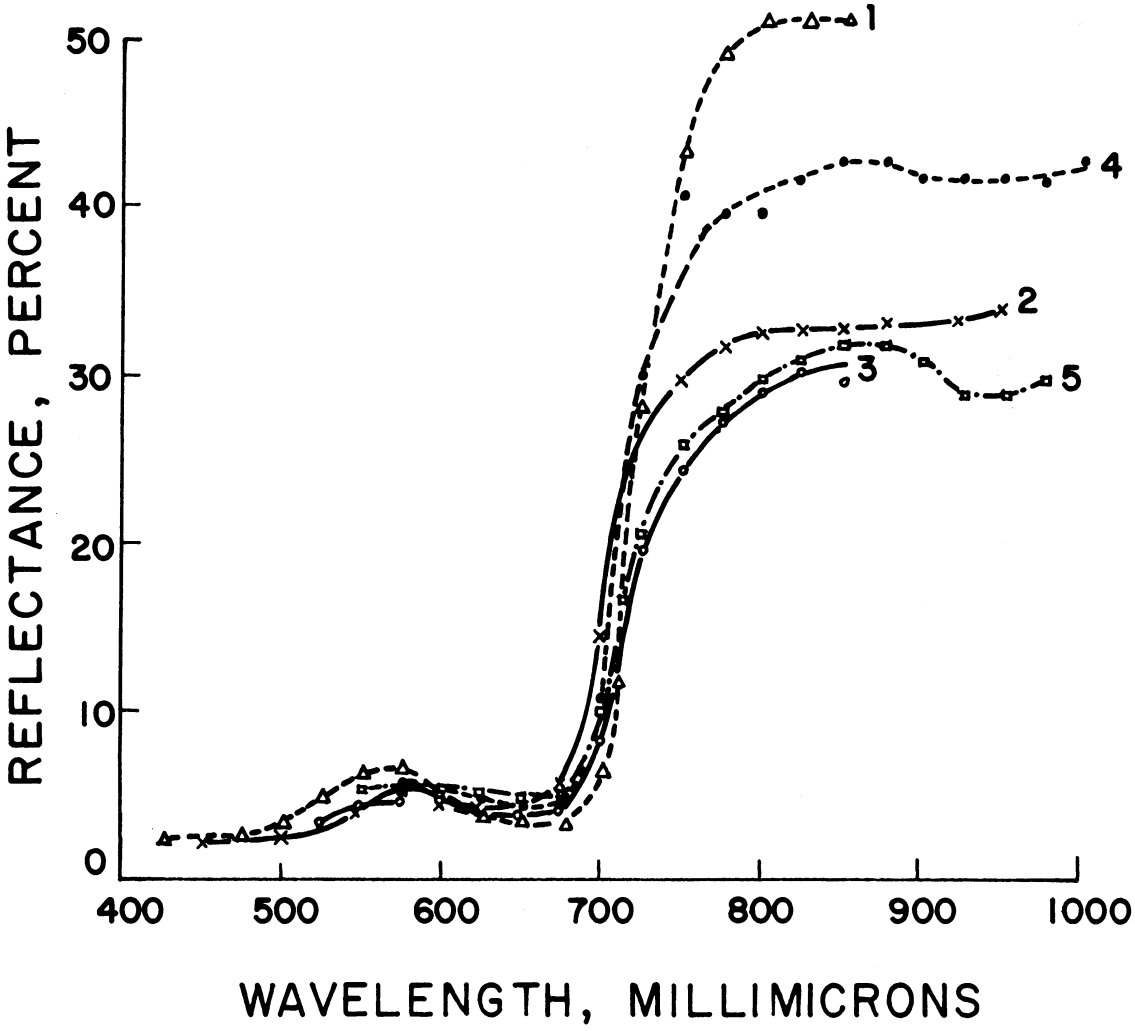

Figure 85. Spectral albedo of different vegetation: (1) sudan grass; (2) maize; (3) clover; (4) lucerne grass (June), (5) lucerne grass (July) (after Kondratier, et al.[37]).

quantity $\overline{r_\lambda(\theta_o,\phi_o)}$ defined above (sun's zenith angle not given), and Figure 86 shows measurements of directional reflectance $r_\lambda(6°,0)$.

The data show low reflectance starting at 0.4 micron with a small maximum in the region 0.5-0.55 micron, followed by a minimum in the chlorophyll absorption band at 0.68 micron. There is a sudden increase in reflectance at 0.7 micron to a higher value which is maintained up to a wavelength greater than 1 micron; the reflectance then decreases in the infrared.

The change in reflectance with growing season is shown by curves 4 and 5 in Figure 85 and by Figure 86; the chloryphyll absorption at 0.68 micron is most noticeable when the leaf is green, the reflection above 1 micron is a maximum for young plants, decreases as the plant matures, and increases again as the plant looses its green color.

c. Water Basins

The spectral reflectance of a smooth water surface is illustrated by Figure 87 (from Reference 37), which shows the quantity $\overline{r_\lambda(\theta_o,\phi_o)}$ measured under natural illumination (sun's zenith angle not given). These measurements agree quantitatively with calculations based on the Fresnel formula for spectral reflection from a smooth surface, i.e., a decrease of reflectance of water depends on the backscattering of radiation in the water as well as by reflection at the surface, and thus depends on the water turbidity. In addition the surface reflectance depends on the surface roughness and conditions of illumination. Details of the spectral reflectance of water for various turbidities and surface conditions are not presently available in the literature.

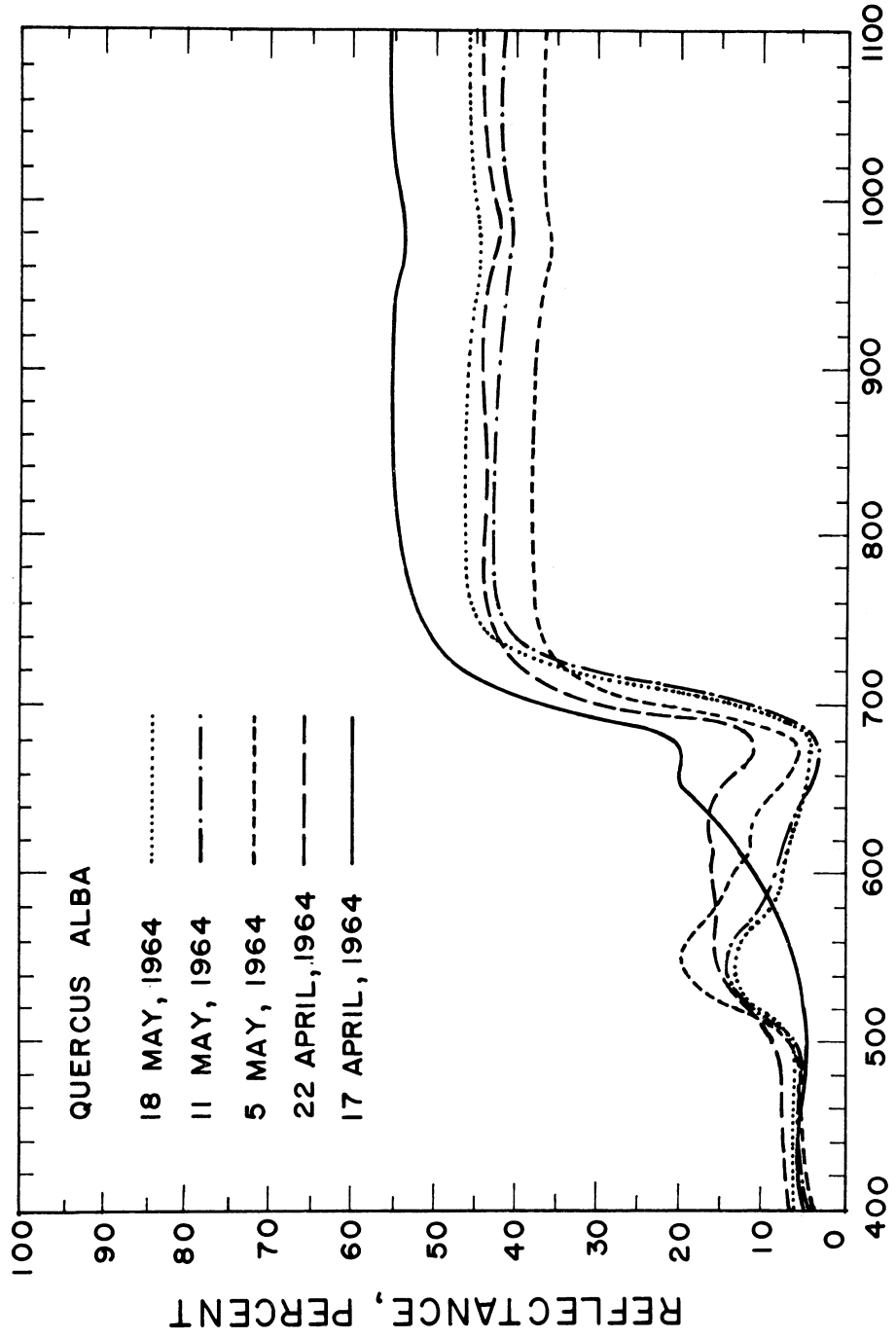

Figure 86. Evolution of Spectral reflection of a leaf during the growing season (after Gates, et al.,[38]).

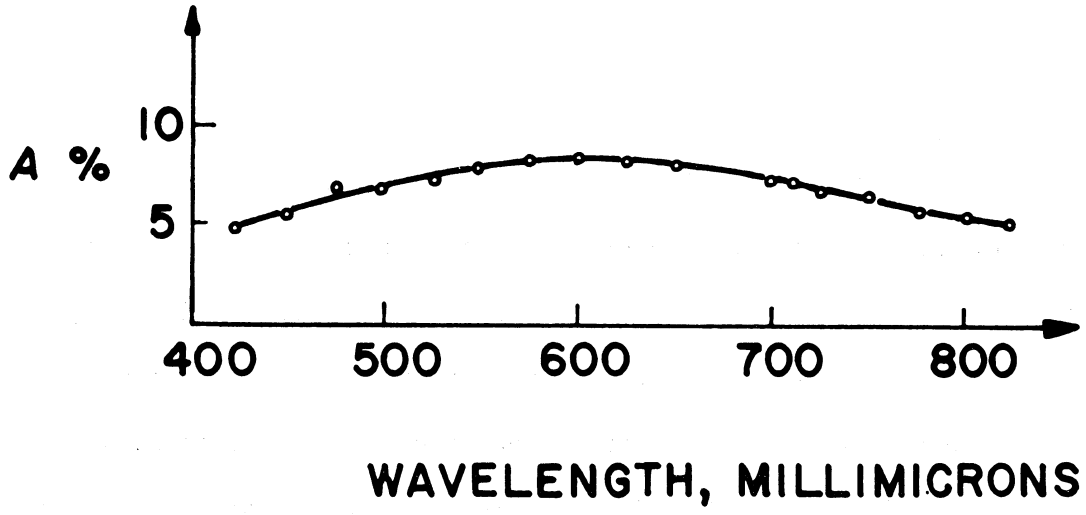

Figure 87. Spectral albedo of a water surface (measured over a lake with depth of 60 to 70 cm) (after Kondratiev, et al.[37]).

d. Snow and Ice

The spectral reflectance of snow is illustrated by the data of Figure 88. The quantity measured is $\overline{r_\lambda(\theta_o,\phi_o)}$, under conditions of natural illumination. Data have been taken at different times during the day. The spectral reflectance is a maximum in the 0.7 to 0.8 micron region and slightly less at lower and higher wavelengths. The reflectance of snow shows great variability, dependence on dryness, purity, surface roughness and conditions of illumination.

2. ANGULAR DISTRIBUTION OF REFLECTANCE

a. Soil and Rocks

The angular distribution of spectral reflectance for various soils is illustrated by the curves of Figure 89, taken from references 36 and 39. As the data shows, the reflectance is not perfectly diffuse, although for small zenith angles it approximates this ideal case. Each set of data shows backscattering of an amount which increases with increasing zenith angle of incidence. In addition, as the zenith angle of incidence increases, forward scattering develops. For large zenith angles of incidence the forward scattering becomes greater than the backscattering for both types of sand, whereas for red clay and black loam the backscattering is greater than the forward scattering. For black loam the forward scattering is almost nonexistant. The back-scattering property is referred to as "black gloss" by those interested in visibility problems.

Additional data on bidirectional reflectance characteristics are contained in Table 21, taken from Reference 40. The data in this table, taken under conditions of natural illumination, show forward and back-scattering for both hard packed dirt and sand dunes, the data for podsol,

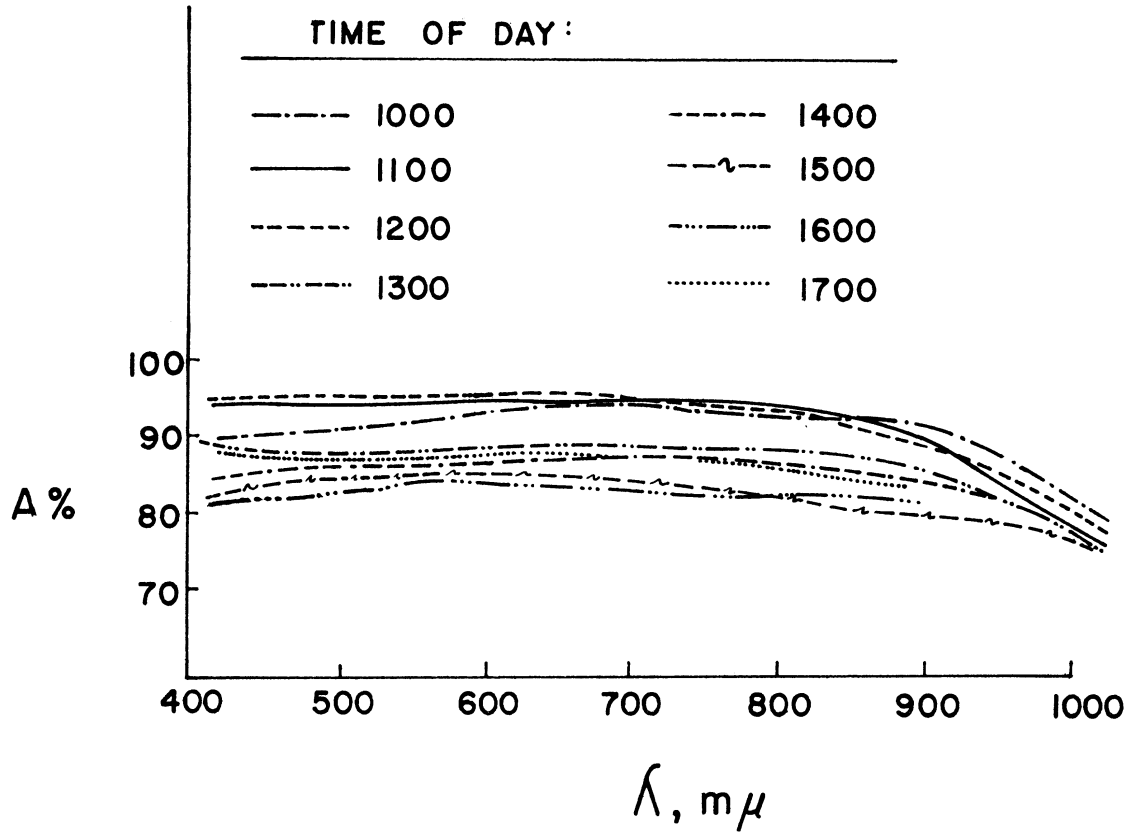

Figure 88. Spectral albedo of the snow cover in clear weather, 28 March, 1963. The Leningrad Region. Dry snow (after Kondratiev, et al.[37]).

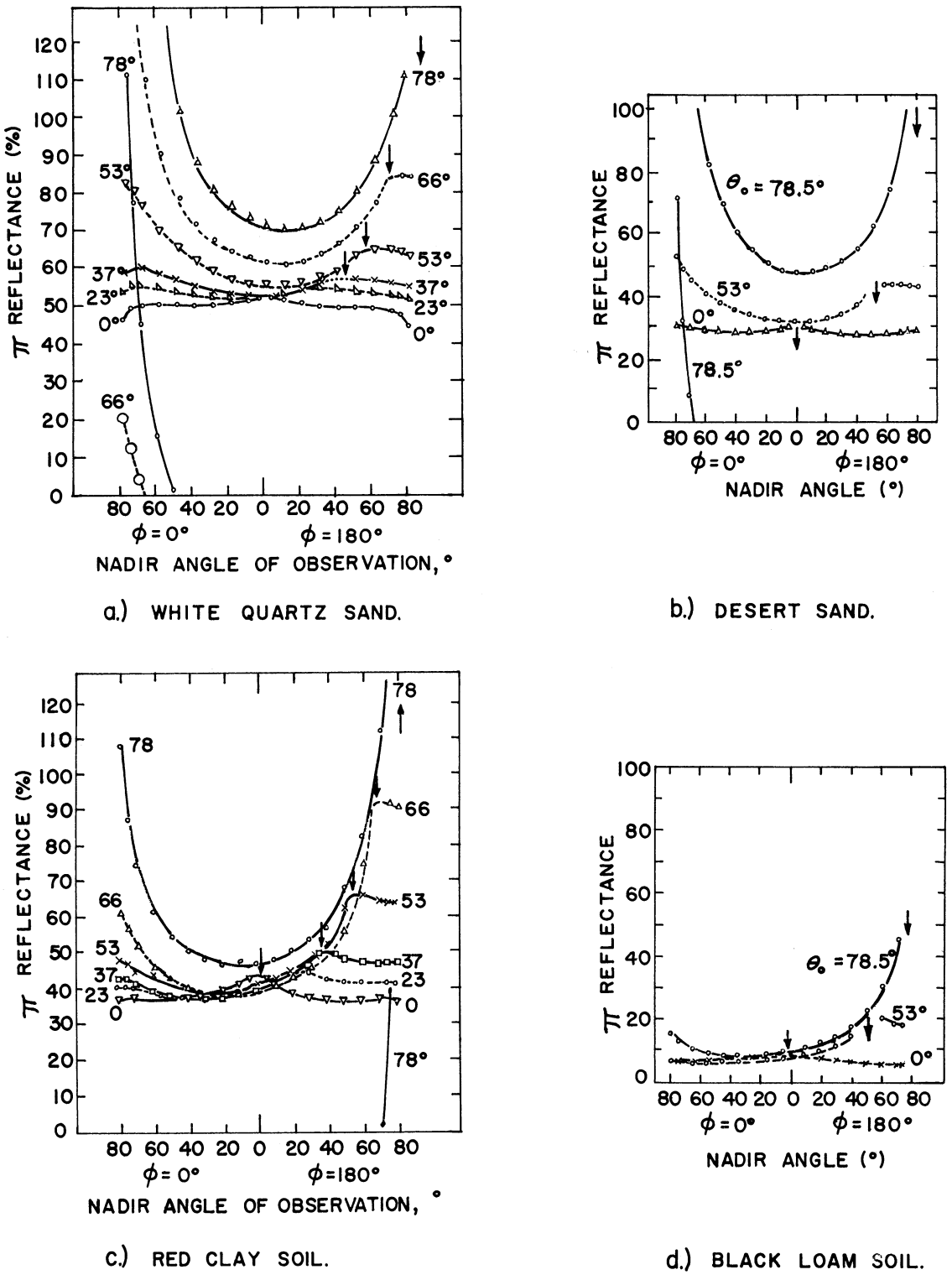

Figure 89. Bidirectional reflectance of various types of soil at different angles of incidence. λ = 0.643 micron (after Coulson[36]).

TABLE 21

BIDIRECTIONAL LUMINOUS REFLECTANCE OF TERRAIN BACKGROUNDS FOR MODERATELY HIGH SUN

(After Duntley, et al.[40])

Description	Sun zenith angle	Azimuth of the path of sight relative to the sun	Zenith angle of path of sight							
			180	165	150	135	120	105	100	95
1. Pine trees, small, uniformly spaced. Data are for unresolved terrain over which atmospheric data given in Sec. VI were collected.	41.5	0	0.0333	0.0241	0.0214	0.0214	0.0261	0.0379	0.0463	0.0859
		45		0.0222	0.0202	0.0194	0.0210	0.0303	0.0387	0.0549
		90		0.0315	0.0311	0.0317	0.0317	0.0337	0.0387	0.0463
		135		0.0335	0.0382	0.0392	0.0387	0.0438	0.0463	0.0572
		180		0.0402	0.0444	0.0578	0.0640	0.0711	0.0758	0.0825
2. Grass, thick, rather long, pale green, dormant, dryish, little ground showing.[a]	41.5	0	0.088	0.081	0.076	0.077	0.088	0.094	0.096	0.094
		180		0.098	0.119	0.146	0.150	0.153	0.153	0.160
3. Asphalt, oily, with dust film blown onto oil.[a]	42.0	0	0.061	0.057	0.058	0.060	0.068	0.090	0.104	0.127
		180		0.067	0.080	0.101	0.090	0.086	0.086	0.088
4. "White" concrete, aged.[a]	42.2	0	0.266	0.263	0.254	0.254	0.266	0.298	0.320	0.374
		180		0.289	0.313	0.343	0.367	0.350	0.343	0.320
5. Calm water, infinite optical depth.[b]	41.5	0	0.0222	0.0234	0.0297		0.0569	0.139	0.267	0.461
		45		0.0230	0.0240	0.0272	0.0357	0.107	0.199	0.325
		90		0.0221	0.0222	0.0234	0.0293	0.0711	0.121	0.214
		135		0.0213	0.0212	0.0220	0.0270	0.0665	0.113	0.203
		180		0.0214	0.0212	0.0216	0.0267	0.0718	0.125	0.254
6. Grass, lush green, closely mowed thick lawn.[c]	40.4	0	0.100	0.096	0.098	0.108	0.120	0.149	0.168	
	39.6	90		0.103	0.110	0.121	0.138	0.159	0.168	
	39.6	135		0.107	0.125	0.148	0.166	0.178	0.178	
	39.9	180		0.109	0.109	0.119	0.122	0.125	0.125	
7. Macadam, washed off and scrubbed.[c]	48.5	0	0.113	0.115	0.119	0.128	0.148	0.194	0.229	
	60.1	90		0.110	0.109	0.116	0.122	0.139	0.147	
	46.0	180		0.126	0.141	0.156	0.166	0.172	0.176	
8. Dirt, hard packed, yellowish.[c]	53.2	0	0.243	0.230	0.229	0.239	0.252	0.300	0.330	
	56.5	90		0.243	0.258	0.260	0.276	0.300	0.304	
	51.1	180		0.272	0.313	0.370	0.422	0.432	0.434	
9. Mixed green forest, deciduous (oak) and evergreen (pine).[d]	39.0	0	0.0360	0.0325	0.0291	0.0205	0.0205	0.0342		
	37.0	180		0.0410	0.0493	0.0493	0.0820	0.263		
10. Pine forest.[d]	33.5	0	0.0385	0.0385	0.0308	0.0246	0.0246	0.0200		
11. Grass, dry meadow, dense, mid-summer.[e]	45	0	0.0955	0.0897	0.0960	0.0952	0.108	0.129		
	45	90		0.0778	0.0890	0.101	0.111	0.130		
	45	180		0.116	0.131	0.143	0.153	0.170		
	45	270		0.107	0.121	0.134	0.137	0.132		
12. Ilyas, sparse and dry, yellowish grass on sand at end of summer.[e]	40	0	0.231		0.320		0.342	0.356		
	40	90			0.163		0.176	0.198		
	40	180			0.295		0.353	0.359		
	40	270			0.262		0.237	0.229		
13. Sand dunes, sharply expressed micro-relief, dry.[e]	40	0	0.288		0.183		0.337	0.353		
	40	90			0.284		0.329	0.306		
	40	180			0.246		0.259	0.276		
	40	270			0.278		0.410	0.281		
14. Podsol, ploughed, moist.[e]	50	0	0.0600	0.0680	0.0646		0.0555			
	50	90		0.0662	0.0953	0.0715	0.0614	0.0761		
	50	270		0.149	(0.180)[f]	0.168	0.168	(0.189)		

[a] These terrains were measured on the ground by means of a goniophotometer, beneath and during the collection of the data in Sec. VI.

[b] Computed from equations by Duntley (1952) for the lighting condition prevailing for items 1 and 2 in this table.

[c] Data taken with a goniophotometer, 10 October 1956.

[d] Data taken with a photoelectric telephotometer from a helicopter at 300 ft (91.4-m) altitude, mountain forested area near Julian, California, 23 September 1959.

[e] Luminous directional reflectance for terrains 11 through 14 were computed from spectrophotometric data by Krinov (1947) using C.I.E. Illuminant B. Disparity between data for azimuths 90° and 270° "is explained apparently by the direction of shallow furrows in relation to the sun", (Krinov–Belkov, 1953, p. 75).

[f] Parentheses indicate estimates based on incomplete spectral data.

ploughed, moist, shows only backscattering.

b. Vegetation

The angular distribution of reflectance of vegetaion of various types is illustrated by the curves in Figure 90 for green grass turf and in Table 21 for several kinds of grassy and forested areas. The data all show pronounced backscattering (black gloss) and a small amount of forward scattering for very high angles of incidence.

c. Water Basins

Table 21 has angular reflectance data for calm water calculated according to Duntley, for a moderately high sun angle. Similar calculated data for calm water and low sun angle, and measured data for ocean water, under wind speed of 5 m/sec and high sun angle, are given in Table 22 (Reference 41). Calculated data for calm water and overcast conditions are given in Table 23 (Reference 42). The data for these four cases have been plotted for the principal plane in Figure 91. The sun's angle is shown for each figure. The calculations in-

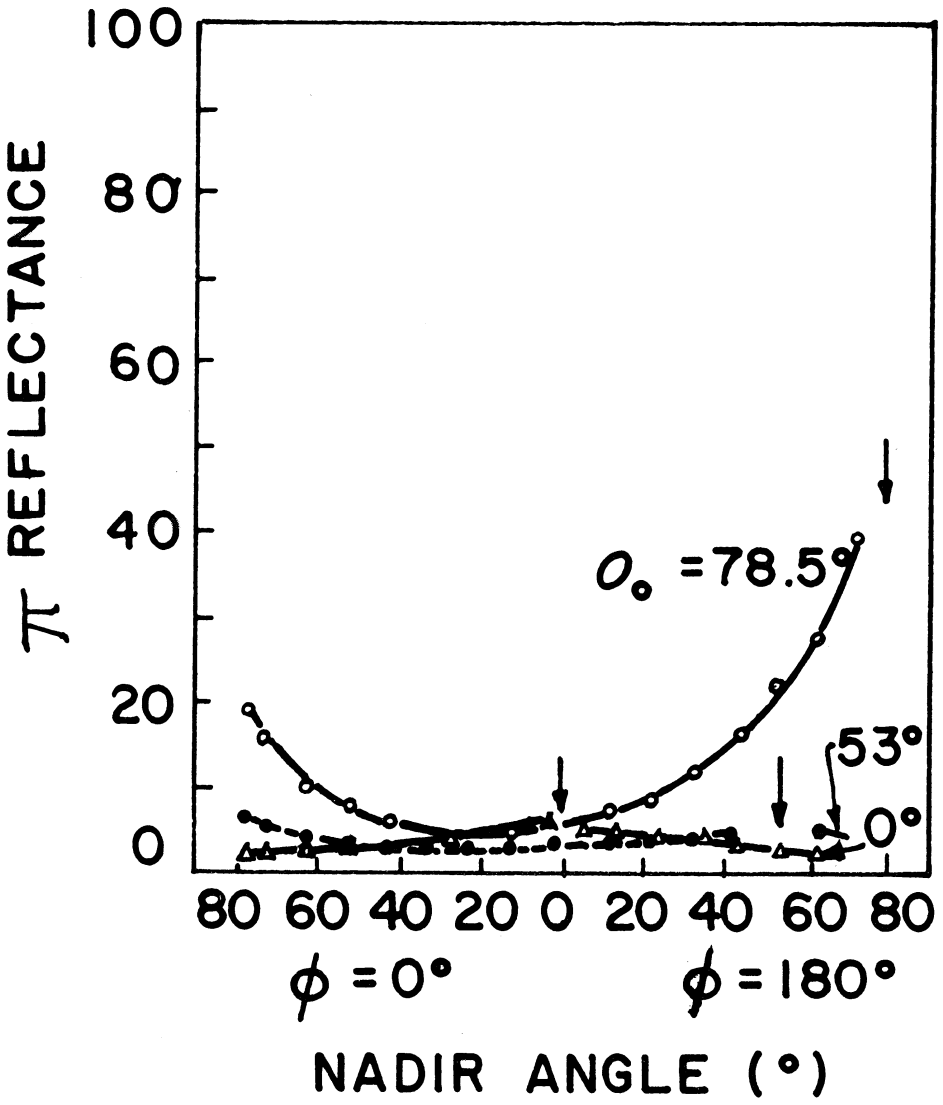

Figure 90. Bidirectional reflectance of green grass turf at different angles of incidence. λ = 0.643 micron (after Coulson[36]).

TABLE 22

BIDIRECTIONAL LUMINOUS REFLECTANCE OF TERRAIN FOR LOW SUN ANGLES

(After Boileau and Gordon[41])

Description	Sun zenith angle	Azimuth φ of path of sight relative to sun	Directional reflectance for zenith angle θ							
			$\theta = 180$	165	150	135	120	105	100	95
1. Ocean water, infinite optical depth, wind speed 5m/sec[a]	77.3	0	0.0230	0.0288	0.0390	0.055	0.132	[b]	0.384	0.358
		45		0.0246	0.0329	0.0417	0.065	0.087	0.104	0.158
		90		0.0242	0.0266	0.0297	0.0373	0.061	0.076	0.093
		135		0.0264	0.0280	0.0309	0.0384	0.072	0.096	0.116
		180		0.0266	0.0288	0.0325	0.0449	0.072	0.099	0.125
2. Calm ocean water, infinite optical depth[c]	77.3	0	0.0152	0.0177	0.0219	0.0408	0.140	[d]	1.03	1.03
		45		0.0188	0.0200	0.0181	0.0371	0.107	0.190	0.345
		90		0.0139	0.0139	0.0156	0.0388	0.132	0.154	0.243
		135		0.0133	0.0141	0.0160	0.0267	0.0823	0.149	0.345
		180		0.0158	0.0206	0.0425	0.108	0.508	0.823	1.03
3. Snow, with surface hoar[e]	74.0	0	0.69	0.69	0.73[f]	0.78[f]	0.89	1.20	1.39	1.73
		90		0.64	0.65	0.69	0.72	0.73	0.73	
4. Snow, with rain crust (a crust formed by falling rain which does not freeze upon falling)[e]	74.0	0	0.73	0.73	0.74[f]	0.79[f]	0.91	1.47	1.81	2.44
		45		0.71	0.71	0.69	0.67	0.62	0.60	0.58
		90		0.73	0.73	0.71	0.72	0.71	0.69	
		135		0.71	0.74	0.77	0.82	0.89	0.90	
5. Snow, with glazed rain crust (rain crust completely covered by a slightly undulating sheet of ice formed by freezing rainfall followed by warm rain, subsequent freezing temperatures but no further precipitation)[e]	74.0	0	0.80	0.80	0.88[f]	1.13[f]	1.90	5.6	8.4	10.9
		45		0.75	0.77	0.72	0.68	0.65	0.61	0.56
		90		0.75	0.75	0.75	0.74	0.72	0.70	0.65
		135		0.76	0.77	0.80	0.81	0.85	0.84	
6. Dirt, flat desert road, freshly bulldozed to remove encroaching sage[g]	77.8	90	0.230	0.243	0.264	0.275	0.314	0.380	0.426	0.458

[a] Data are from Flight 105.

[b] Value not available, near to direct reflectance from sun.

[c] Computed from equations by Duntley[3] for the lighting condition prevailing for Item 1 in this table.

[d] Value not computed since sky luminances near sun are poorly defined.

[e] Data taken with a telephotometer April 1960 of simulated snow having reflectance characteristics reported by Middleton and Mungall.[4] The photometry was done in the natural lighting simulator, using the sky luminance distribution from Flight 105.

[f] Data interpolated graphically.

[g] Data taken with a goniophotometer at Naval Ordnance Test Station, China Lake, California, in July and August 1962. The spectral reflectance of a sample of the dirt was measured with a Hardy spectrophotometer. Using CIE illuminant B, chromaticity coordinates were $x = 0.370$, $y = 0.361$, $z = 0.269$; dominant wavelength = 580 mμ; excitation purity = 10%.

TABLE 23

BIDIRECTIONAL LUMINOUS REFLECTANCE OF TERRAIN BACKGROUNDS UNDER OVERCAST

(After Gordon and Church[42])

1 . . 10 Omitted (see Gordon and Church[42])

Description	Sun zenith angle	Azimuth of path of sight relative to sun	Zenith angle of path of sight: 180	165	150	135	120	105	100	95
11. Calm water, infinite optical depth[a]	51	0	0.0296	0.0314	0.0336	0.0287	0.053	0.197	0.356	0.57
	51	45	—	0.0302	0.0313	0.0287	0.058	0.229	0.376	0.55
	51	90	—	0.0306	0.0272	0.0294	0.064	0.229	0.340	0.51
	51	135	—	0.0273	0.0239	0.0264	0.057	0.182	0.260	0.425
	51	180	—	0.0273	0.0254	0.0238	0.0421	0.145	0.234	0.459
12. Snow, with surface hoar[d]	51	0	0.69	0.68	0.66	0.66	0.67	0.67	0.70	—
	51	45	—	0.66	0.65	0.65	0.66	0.67	0.68	—
	51	90	—	0.66	0.65	0.66	0.67	0.68	0.69	—
	51	135	—	0.67	0.65	0.66	0.67	0.69	—	—
	51	180	—	0.68	0.64	0.65	0.66	0.68	0.69	—
13. Snow, with rain crust (a crust formed by falling rain which does not freeze upon falling)[d]	51	0	0.67	0.67	0.67	0.67	0.67	0.67	0.67	0.67
	51	45	—	0.67	0.66	0.66	0.67	0.67	0.67	0.68
	51	90	—	0.66	0.67	0.67	0.68	0.68	0.68	—
	51	135	—	0.65	0.66	0.67	0.68	0.68	0.67	0.69
	51	180	—	0.67	0.64	0.65	0.67	0.68	0.68	0.69
14. Snow, with glazed rain crust (rain crust completely covered by a slightly undulating sheet of ice formed by freezing rain, subsequent freezing temperatures but no further precipitation)[d]	51	0	0.74	0.76	0.76	0.76	0.77	0.77	0.77	—
	51	45	—	0.76	0.76	0.76	0.76	0.77	0.78	—
	51	90	—	0.74	0.76	0.76	0.76	0.78	0.77	—
	51	135	—	0.74	0.76	0.77	0.77	0.79	0.78	—
	51	180	—	0.74	0.74	0.75	0.75	0.76	0.77	—
15. Calm water, infinite optical depth[e]	52	0	0.0236	0.0278	0.0359	0.0393	0.095	0.287	0.438	0.69
	52	45	—	0.0249	0.0249	0.0262	0.069	0.247	0.405	0.66
	52	90	—	0.0239	0.0229	0.0239	0.061	0.212	0.343	0.58
	52	135	—	0.0216	0.0210	0.0218	0.054	0.194	0.314	0.462
	52	180	—	0.0216	0.0214	0.0223	0.057	0.201	0.331	0.414
16. Snow, with surface hoar[f]	52	0	0.65	0.62	0.63	0.67	0.66	0.70	0.71	—
	52	45	—	0.65	0.65	0.67	0.68	0.70	0.70	—
	52	90	—	0.65	0.65	0.65	0.65	0.68	0.68	—
	52	135	—	0.64	0.63	0.64	0.67	0.68	—	—
	52	180	—	0.65	0.64	0.63	0.65	0.66	0.66	—
17. Snow, with rain crust (a crust formed by falling rain which does not freeze upon falling[f]	52	0	0.65	0.62	0.63	0.63	0.66	0.67	0.67	0.68
	52	45	—	0.66	0.66	0.67	0.68	0.66	0.68	0.68
	52	90	—	0.66	0.66	0.66	0.67	0.67	0.66	0.67
	52	135	—	0.66	0.66	0.67	0.69	0.70	0.70	0.73
	52	180	—	0.65	0.65	0.67	0.67	0.68	0.67	0.69
18. Snow, with glazed rain crust (rain crust completely covered by a slightly undulating sheet of ice formed by freezing rain, subsequent freezing temperatures but no further precipitation)[f]	52	0	0.75	0.72	0.72	0.74	0.77	0.81	0.81	—
	52	45	—	0.75	0.76	0.77	0.79	0.79	0.80	—
	52	90	—	0.75	0.75	0.75	0.75	0.76	0.76	—
	52	135	—	0.74	0.73	0.74	0.77	0.78	0.78	—
	52	180	—	0.74	0.74	0.73	0.74	0.76	0.76	—

[a] Directional luminous reflectances of terrains 1 through 10 were computed from spectrophotometric data taken by Krinov using C.I.E. Illuminant B.

[b] The zenith angle of the path of sight is 115°.

[c] Computed from equations by Duntley for the luminance distribution measured by Hood on 21 May 197.

[d] Data taken with a telephotometer (April 1960) of simulated snow having reflectance characteristics reported by Middleton and Mungall. The photometry was done in the natural lighting simulator, using the sky luminance distribution measured by Hood on 21 May 1957.

[e] Computed from equations by Duntley for the luminance distribution measured by Hood on 24 May 1957.

[f] Data taken with a telephotometer (April 1960) of simulated snow having reflectance characteristics reported by Middleton and Mungall. The photometry was done in the natural lighting simulator, using the sky luminance distribution measured by Hood on 24 May 1957.

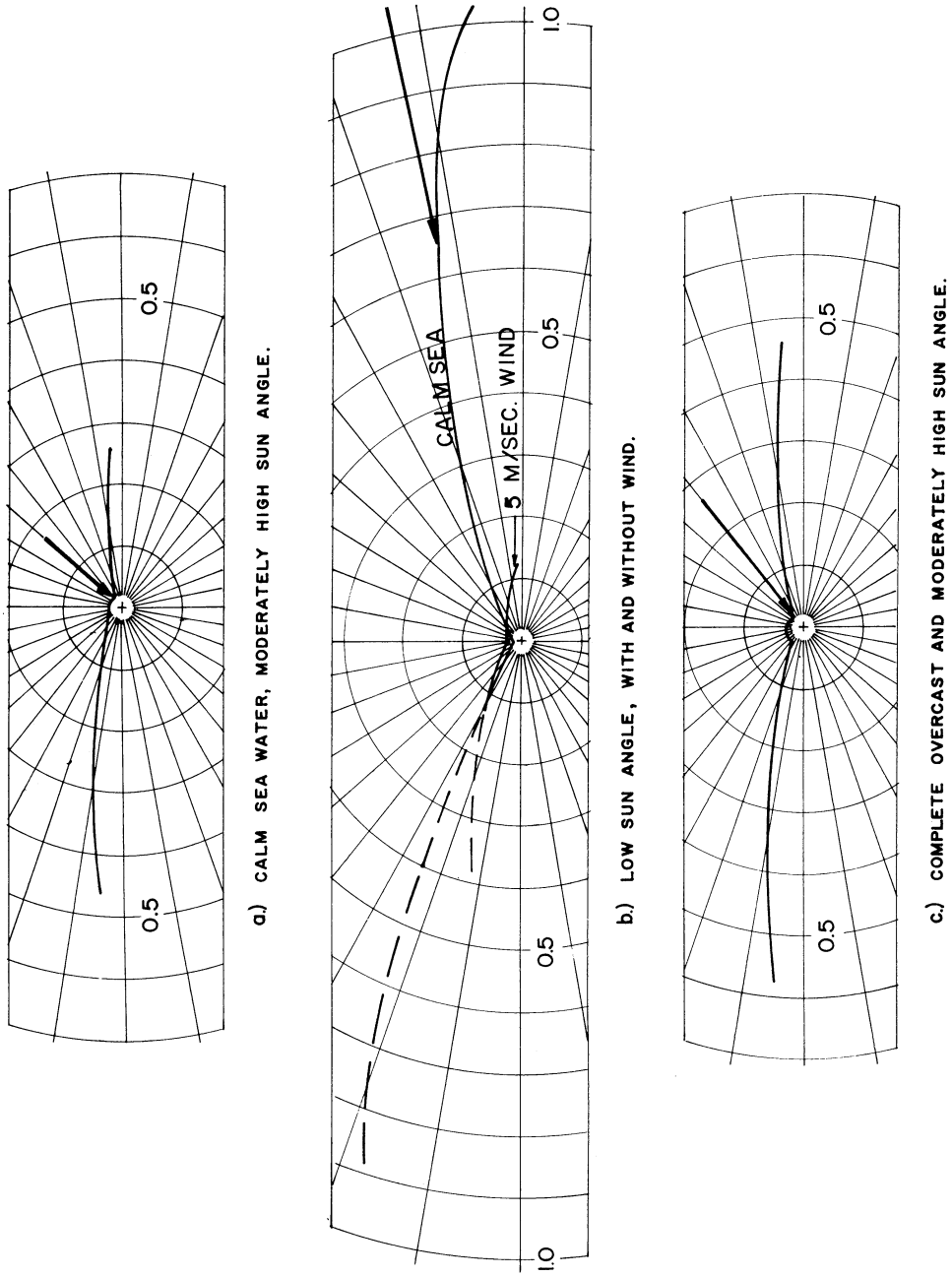

Figure 91. Bidirectional luminous reflectance in the principal plane for water of infinite depth.

clude scattering in the turbid sea as well as reflection at the surface. All of these data show a very large amount of scattering at low angles, in both forward and backward directions. The experimental data for low sun angles also shows a large amount of scattering in the forward direction with a rather small amount of backscatter. The possibility of a mirror component of reflection is also indicated by the experimental data.

d. Snow and Ice

The measured luminance of snow cover indicated in Figure 92 (Reference 43) shows a diffuse reflectance component plus a specular component which becomes larger for large angles of incidence. The five types of snow may be listed in order of increasingly large specular component as follows, surface hoar, settling snow, new snow, rain crust, wind packed snow, and glazed rain crust. These results have been confirmed for low sun angles by the results of Kondratyev and Manolova.[44]

3. TOTAL DIRECTIONAL REFLECTANCE

a. Soils and Rocks

The total reflectance of various types of soil, shown in Figure 93 (Reference 30), range from 5-43%. From this data we see that the total reflectance of soil is decreased by 5-20% by the addition of moisture. The dependence of surface conditions is illustrated by the data of Figure 94. In general, the smoother the surface, the higher the total reflectance.

If we refer back to Figure 89, we note the increase in bidirectional reflectance for large angles of incidence. This effect appears for all

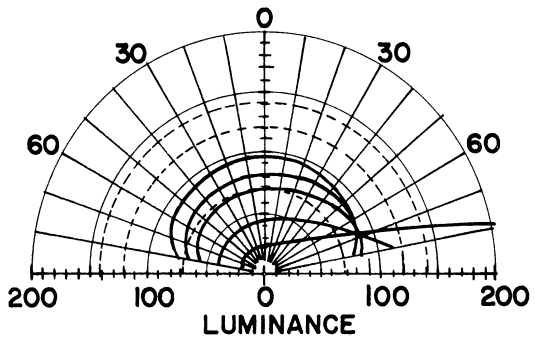

a.) WIND PACKED SNOW.

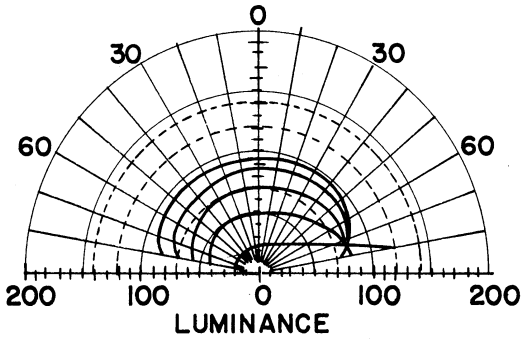

d.) SETTLING SNOW.

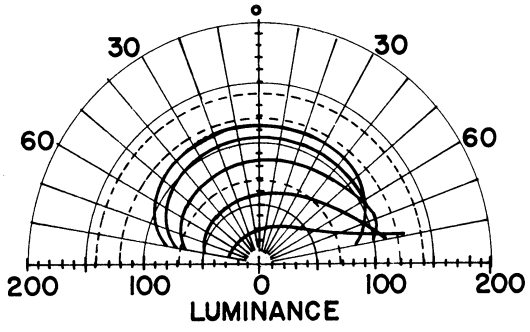

b.) NEW FALLEN SNOW IN CALM.

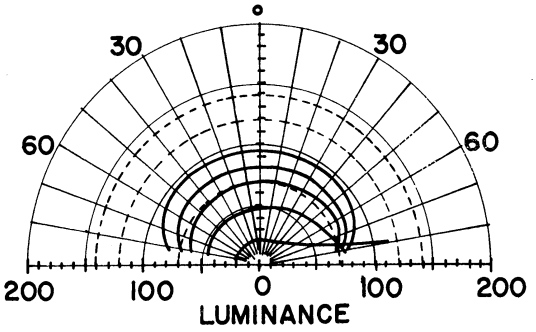

e.) SURFACE HOAR.

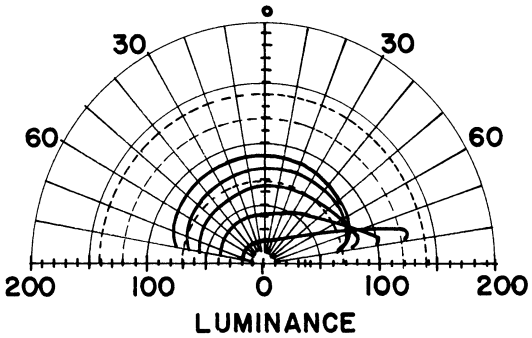

c.) RAIN CRUST.

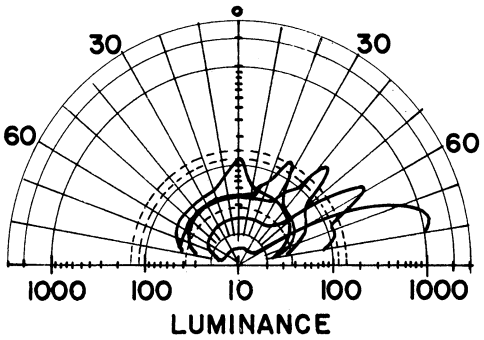

f.) GLAZED RAIN CRUST.

Figure 92. Measured luminance of a snow surface (after Middleton, et al.[43]).

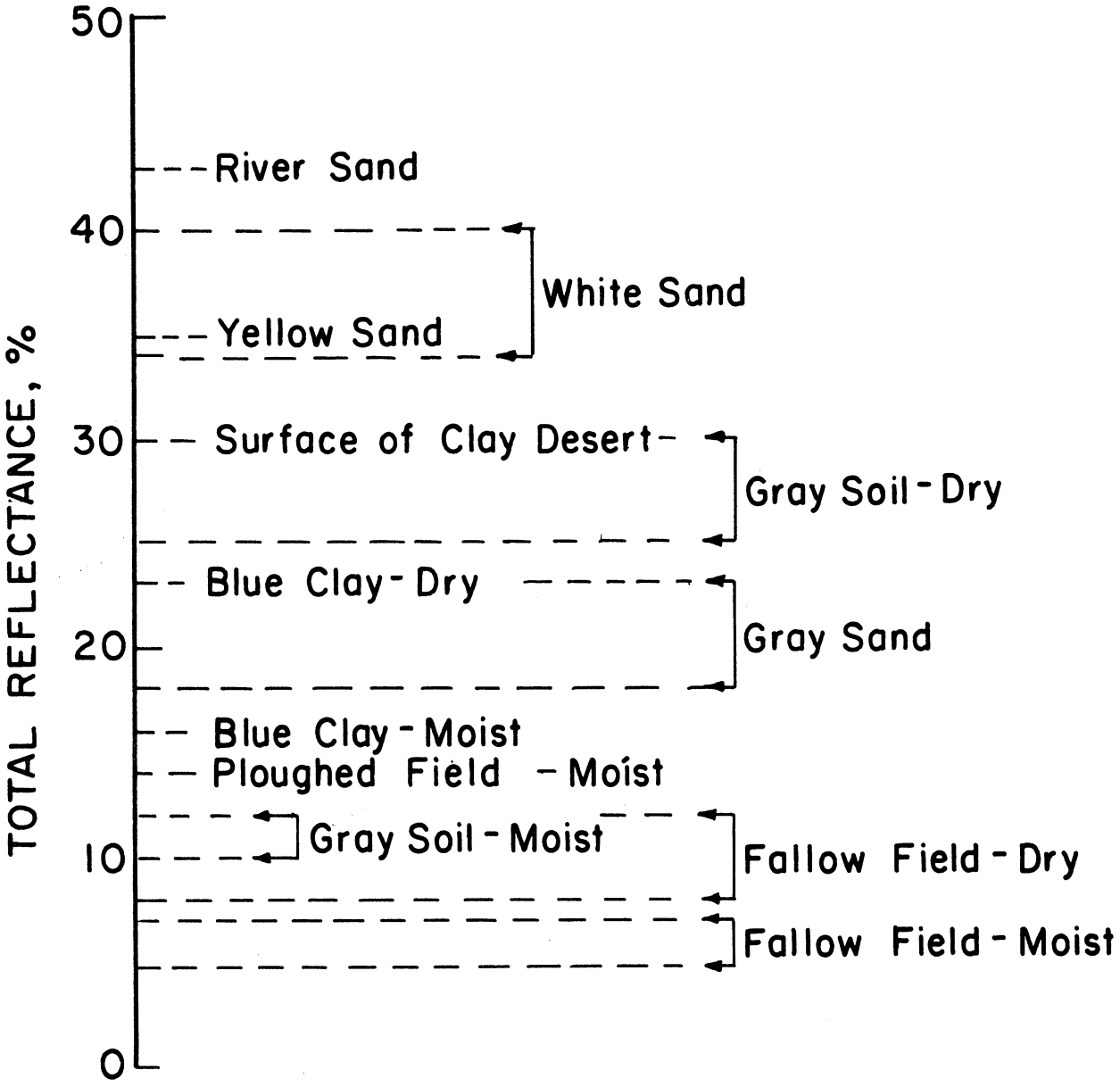

Figure 93. Total reflectance of various types of soil.

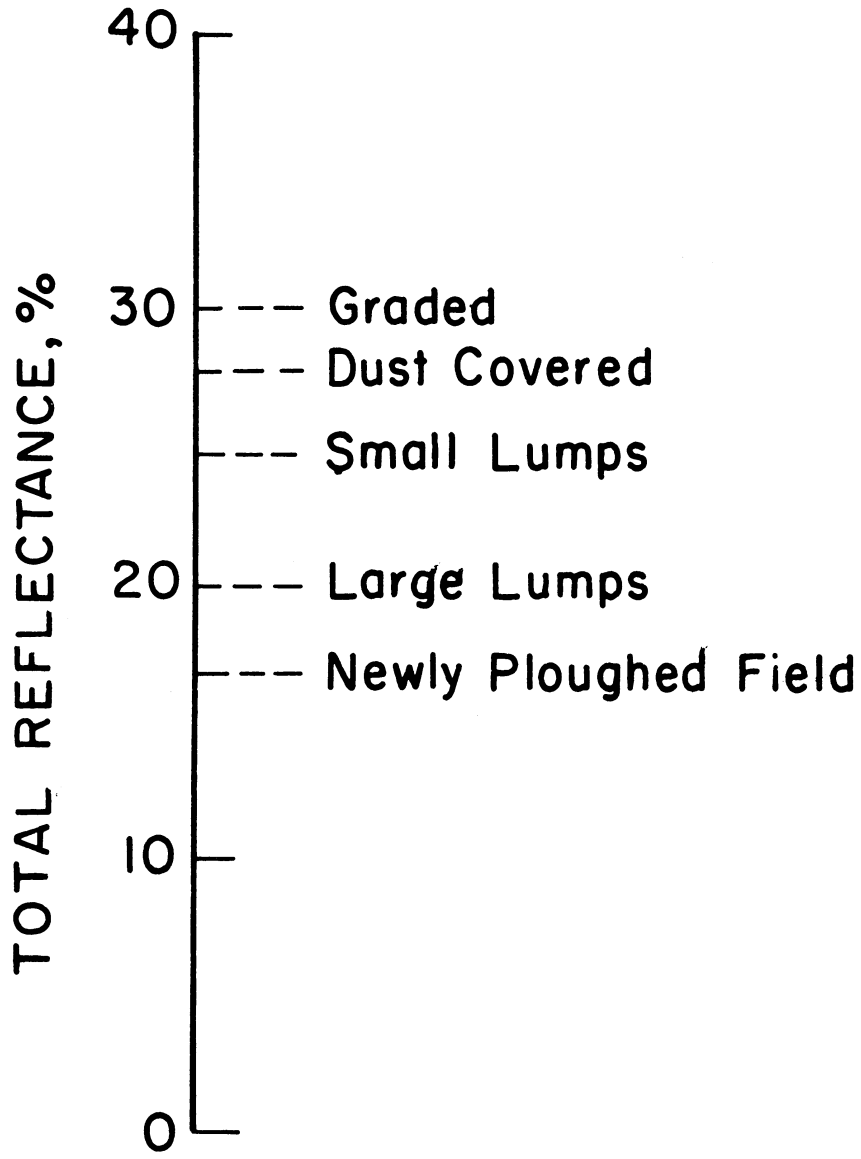

Figure 94. Dependence of total reflectance of clay soil on its surface condition.

wavelengths and thus implies a diurnal effect in the total reflectance of soil, with maximum value for low sun angles.

b. Vegetation

Figure 95 shows the range of typical values of total reflectance of different types of vegetation. Note that the range of values is not as great as for soils. The maximum value of total reflectance of vegetation appears to be about 25%. Again there is a diurnal variation (as can be inferred from the curves of Figure 90) with maximum value for low sun angles.

c. Water Basins

The reflectance of a smooth surface of pure water can be calculated from the Fresnel formula.

$$r = \frac{1}{2}\left[\frac{\sin^2(i-r)}{\sin^2(i+r)} + \frac{\tan^2(i-r)}{\tan^2(i+r)}\right] \qquad (92)$$

where $\frac{\sin i}{\sin r} = n = 1.33$

i = the angle of incidence

r = the angle of reflectance

n = the index of refraction.

Figure 96 (Reference 30) compares experimental data with data calculated according to the Fresnel formula. The decrease in total reflectance for small solar angles is due to the increase of scattered radiation relative to the direct sunlight. In part, the disagreement between experimental and calculated data is due to the influence of waves, water turbidity, and experimental error.

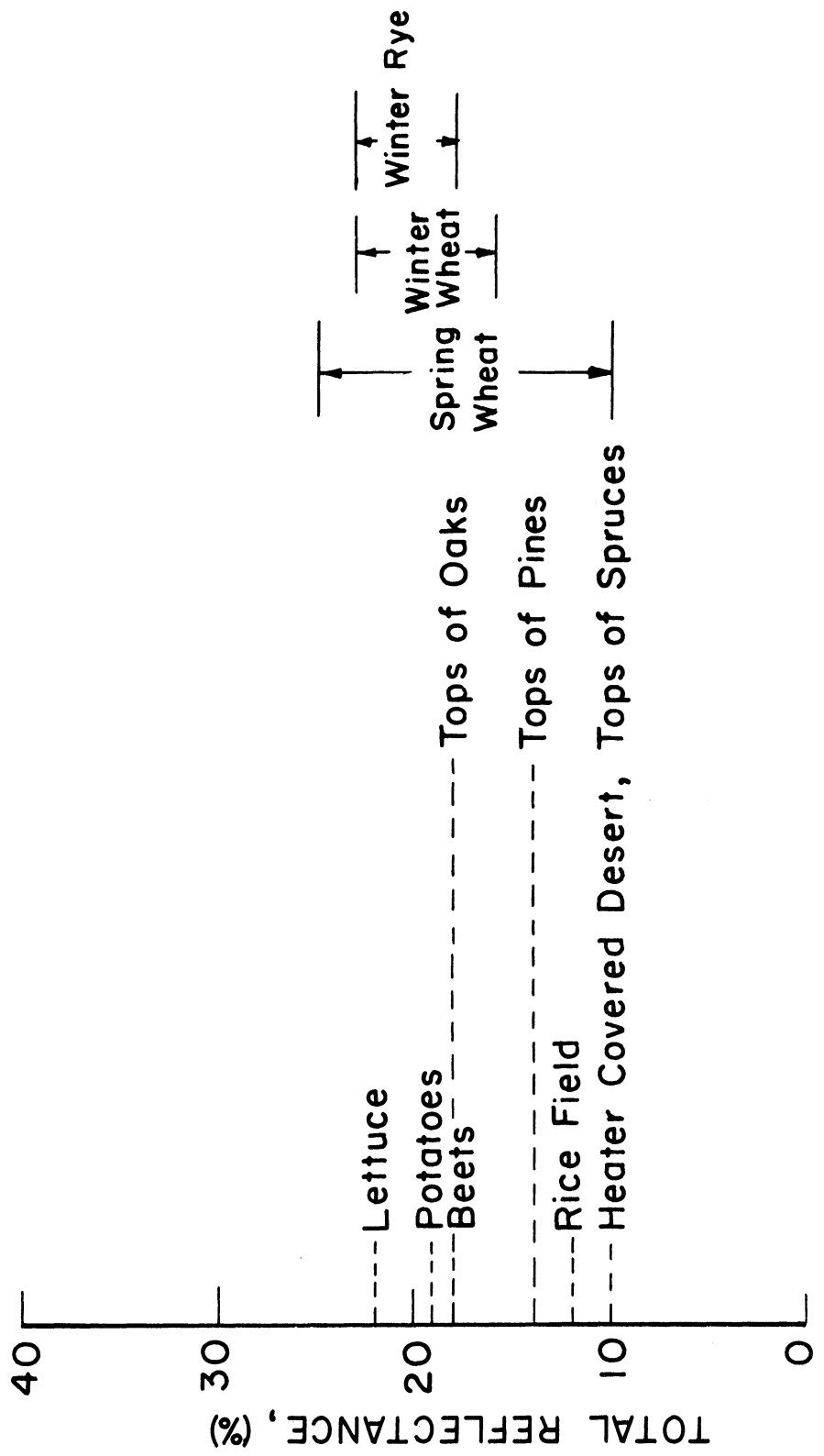

Figure 95. Total reflectance of vegetation.

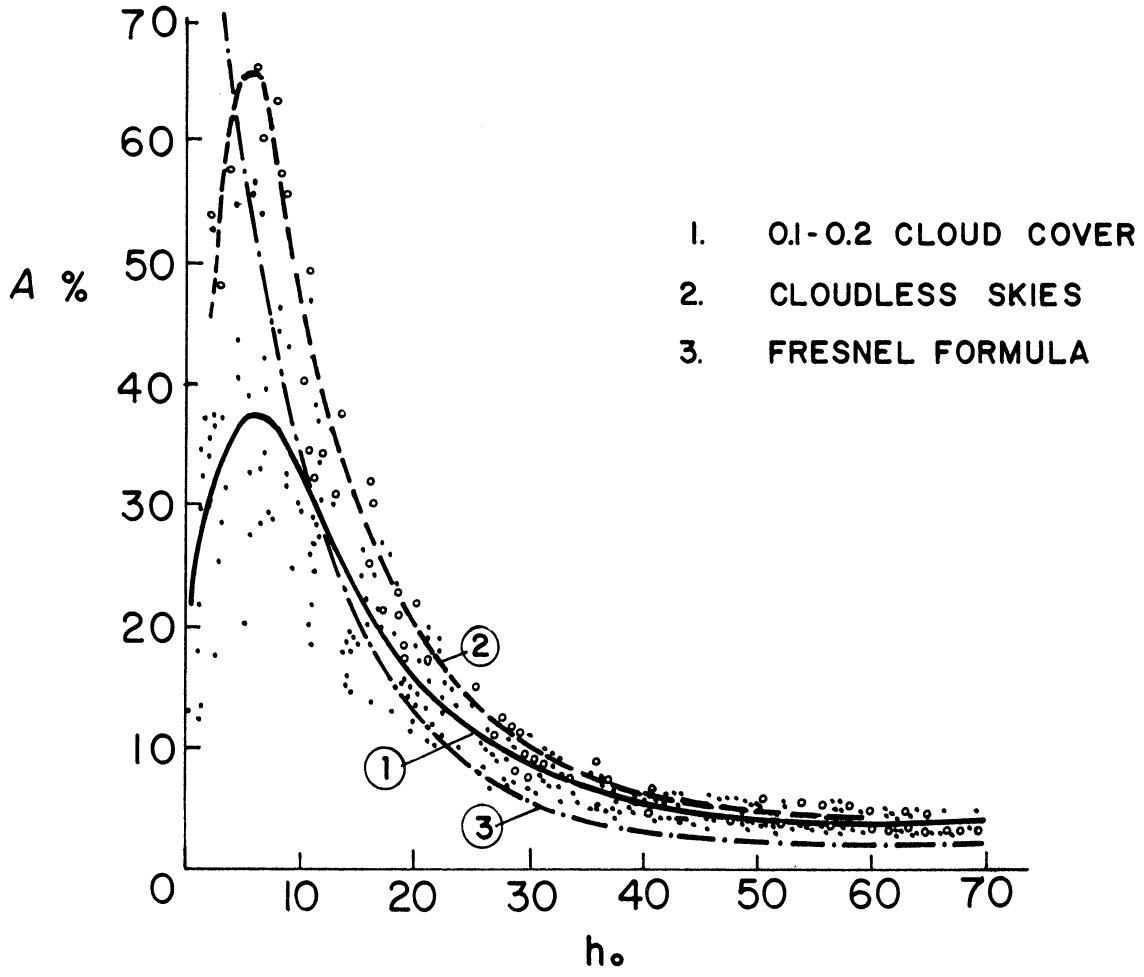

Figure 96. Total reflectance of water basins (after Kondratiev[30]).

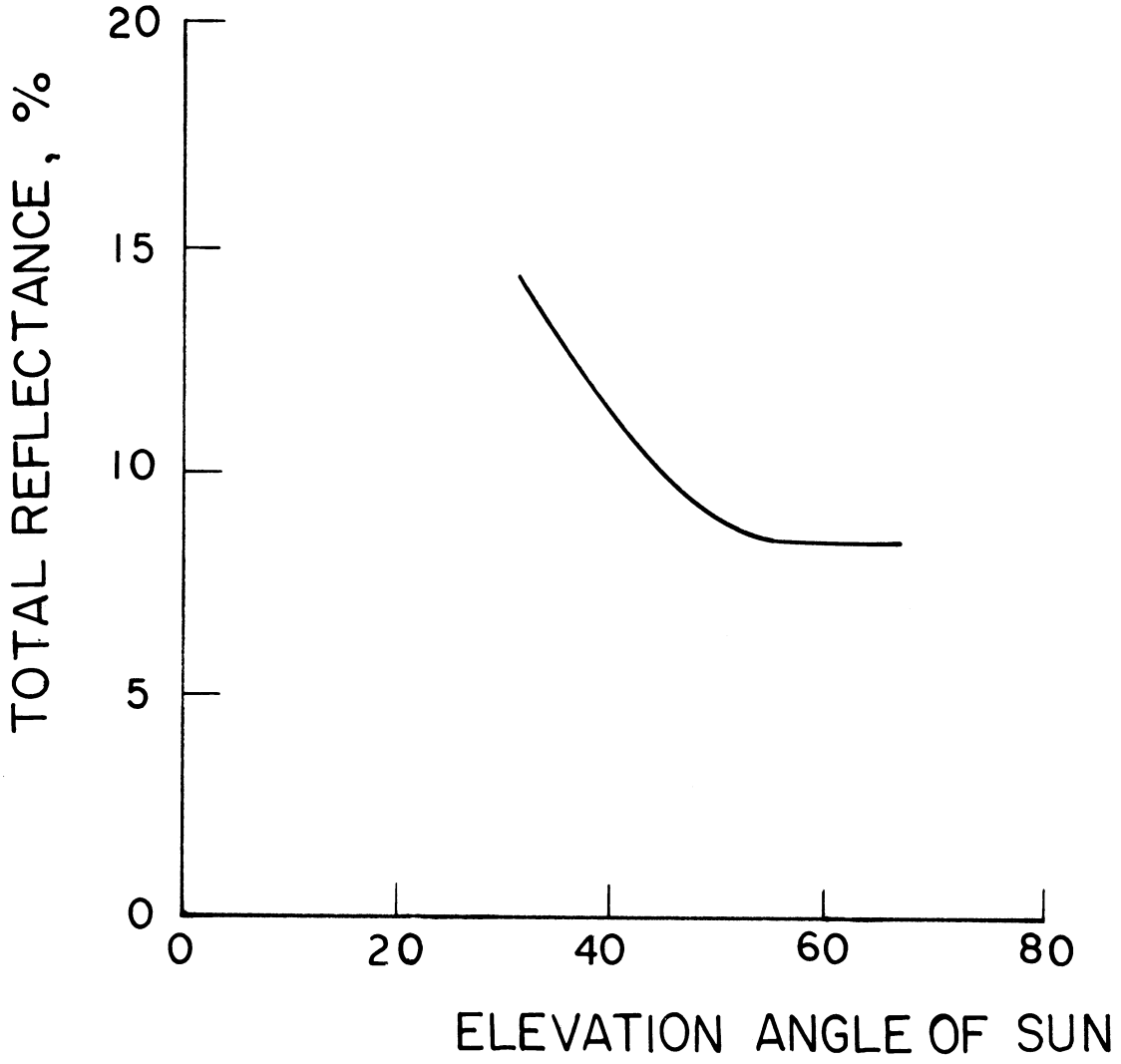

Figure 97. Variation of total reflectance of sea surface as a function of sun angle under stratus clouds (after Neiburger, et al.[45]).

The total reflectance of water basins is dependent on cloud cover conditions. Neiburger[45] has studied the reflection of the sea surface under overcast conditions. He observed total reflection of the sea surface for radiation transmitted below stratus clouds to be 10.5%. The observed variation of total reflectance under stratus clouds reproduced in Figure 97, indicates that the radiation under stratus clouds is not perfectly diffuse.

d. Snow and Ice

The total reflectance of snow varies over wide limits, depending on purity and surface conditions. Figure 98 (from Reference 30) shows this variability very clearly, with a range of values of 25-80% at one location. The mean value of total reflectance in the antarctic[30] is about 84%. Data by A. F. Spano[46] show 83% total reflectance for the antarctic polar plateau and 74% for the Ross Sea area for winter ice. Measurements by Kuz'min[30] indicated a total reflectance of 30-40% for sea ice in the White Sea area.

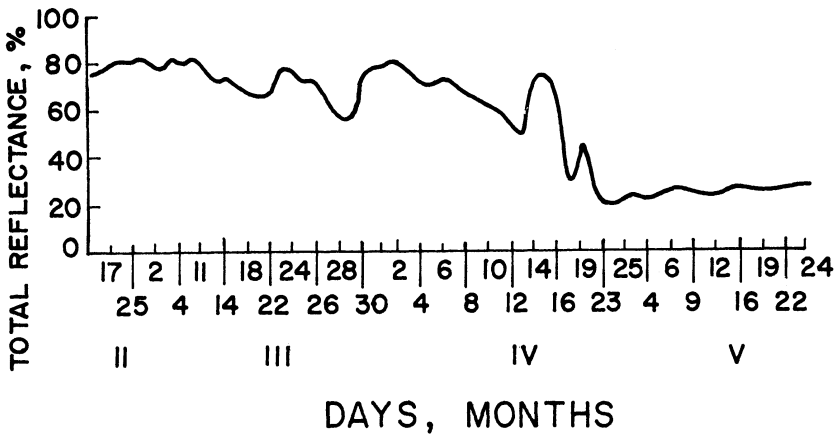

Figure 98. Change in total reflectance of snow cover with time (after Kondratyev[30]).

APPENDIX D

THE REFLECTANCE OF CLOUDS

1. SPECTRAL REFLECTANCE

Perhaps the earliest comprehensive study of cloud reflectance is that of Hewson,[47] who studied fogs of particles of fixed diameter and density. According to Hewson's data, the spectral reflectance is constant up to about 1.3 microns; in the longer wavelength regions there is a decrease of spectral reflectance with dips due to absorption by water vapor. A calculation by Novoseltsev[48] yielded similar results, see Figure 99. The spectral reflectance is constant to about 0.8 micron, with dips mainly due to water vapor absorption bands. Note that this curve is only a very approximate result for cloud spectral reflectance, since it has fixed size diameter and considers only water particles and not ice particles.

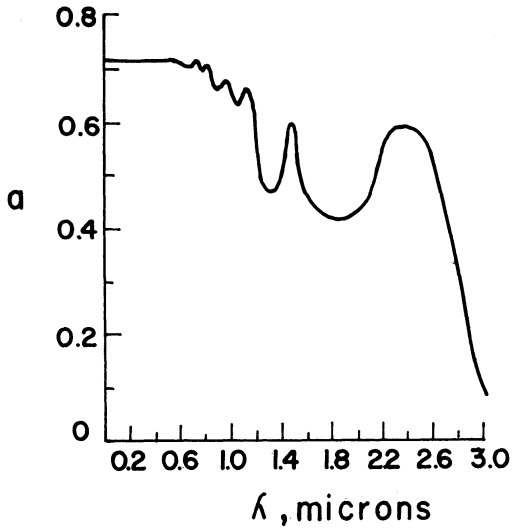

Figure 99. The spectral albedo for middle layer clouds (after Novoseltsev[48]).

2. ANGULAR DISTRIBUTION OF REFLECTANCE

The angular distribution of scattering from a water cloud with

realistic particle size distribution has been calculated by Deirmendjian.[49] Results for $\lambda = 0.45$ and 0.70 micron are shown in Figures 100 and 101 respectively. The figures show the intensity functions for parallel and perpendicular polarization as a function of scattering angle, i.e., the intensity of scattering of both polarizations for a small volume element of the cloud. The curves show a pronounced peak for scattering angle $\beta < 5°$, much brighter in the blue than in the red. As β increases, intensities fall, reach a minimum at $80 < \beta < 101°$. The intensity then increases as β increases, showing a fog how at 143° (with a hint of a smaller fog bow at 122° for $\lambda = 0.7$ micron). Finally the intensity has a secondary bright spot for $\beta = 180°$ (backscattering). Although this calculation does not represent cloud reflectance for a specific real type of cloud, we might expect to observe the salient features of this scattering pattern in cloud reflectance measurements.

3. TOTAL DIRECTIONAL REFLECTANCE

The classical measurement of cloud total reflectance is that of Aldrich.[50] He measured the total reflectance of a stratus cloud over land from a captive balloon. The cloud base varied from 1000-2000 feet during the measurements and the cloud top remained at 2600 feet. Aldrich reported a measured total reflectance of 0.78 independent of cloud thickness.

Measurements by Luckiesh[51] from an airplane indicated that the total reflectance varied from 0.36 for thin clouds to 0.78 for dense clouds of extensive area and great depth.

Neiburger[52] made measurements from a blimp over coastal stratus and obtained the results shown in Figure 102, showing the variation of total reflectance with cloud thickness. The maximum value of about 0.80

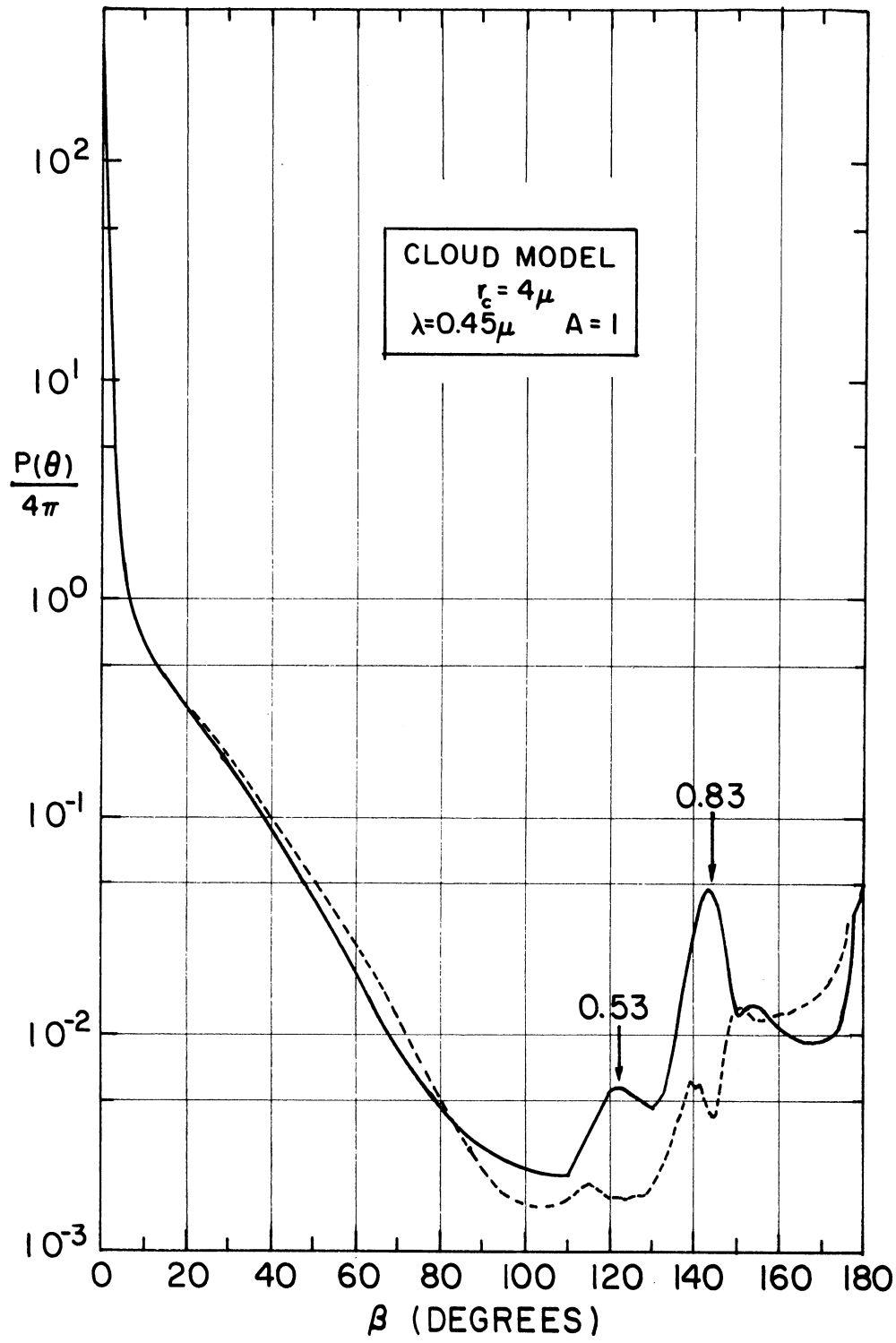

Figure 100. Intensity functions for water cloud illuminated by 0.45-micron radiation (after Deirmendjian[49]).

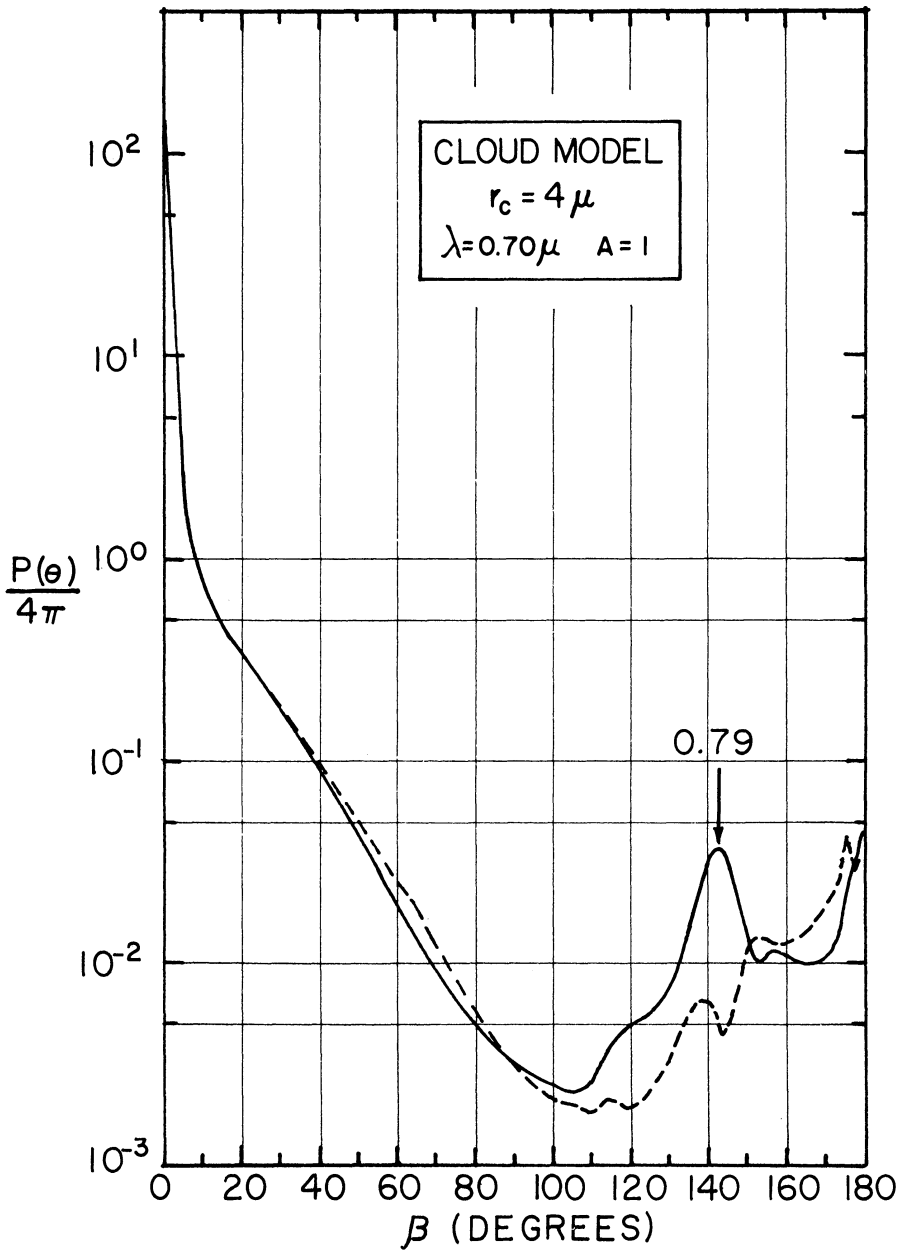

Figure 101. Intensity functions for water cloud illuminated by 0.70-micron radiation (after Deirmendjian[49]).

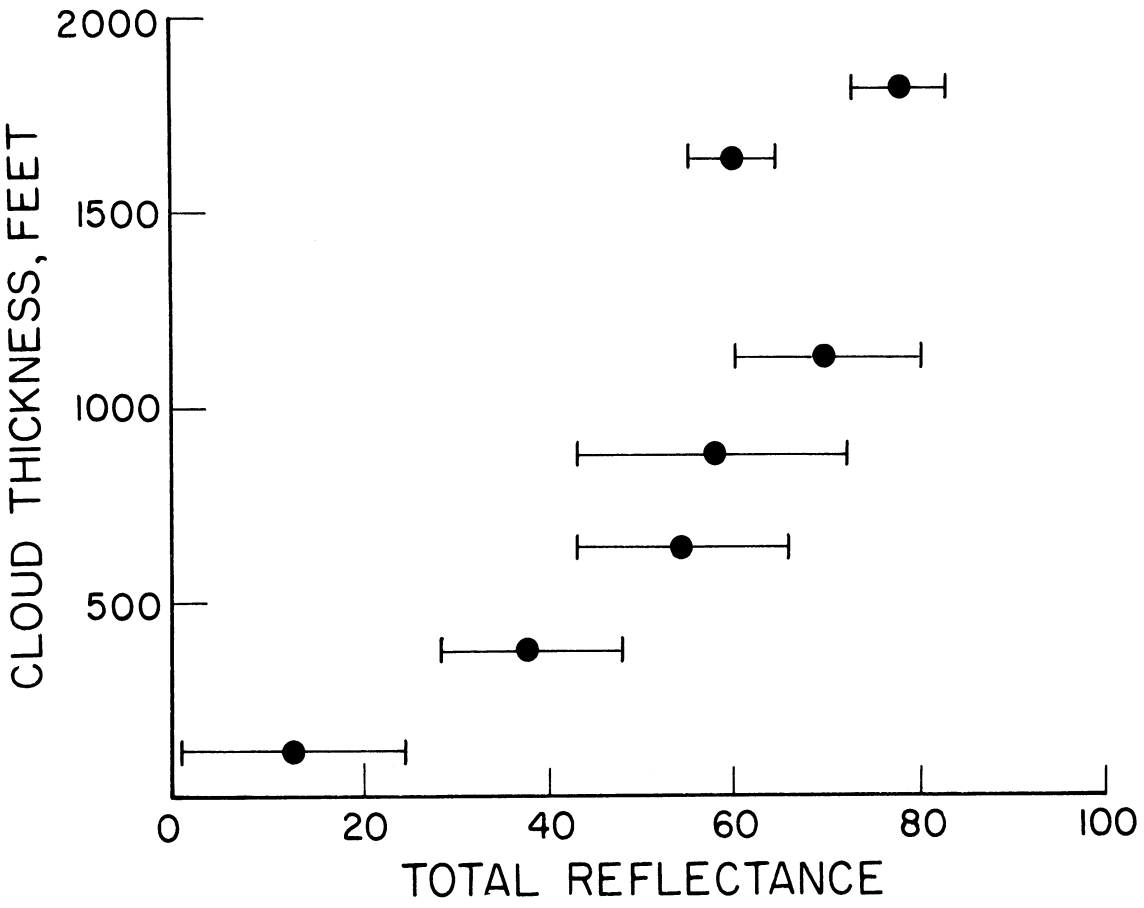

Figure 102. Total reflectance of coastal stratus cloud as a function of cloud thickness (after Neiburger[52]).

for very thick clouds agrees well with previous estimates, the variation of total reflectance with thickness is greatest for thin clouds.

Observations of N. I. Cheltsov[30] also show the dependence of cloud total reflectance with cloud thickness (see Figure 103). His data show reasonable agreement with that of Neiburger, and also show that cloud form has an influence on the total reflectance of clouds of a given thickness. Again, maximum values of about 0.80 were measured.

The dependence of total reflectance of clouds on the nature (reflectance) of the underlying surface is illustrated by the data in Table 24.[30]

TABLE 24

DEPENDENCE OF CLOUD TOTAL REFLECTANCE ON UNDERLYING SURFACE

10/10 (st, sc, ns)	Total Reflectance
Over ice clearings	0.70
Over water openings	0.32

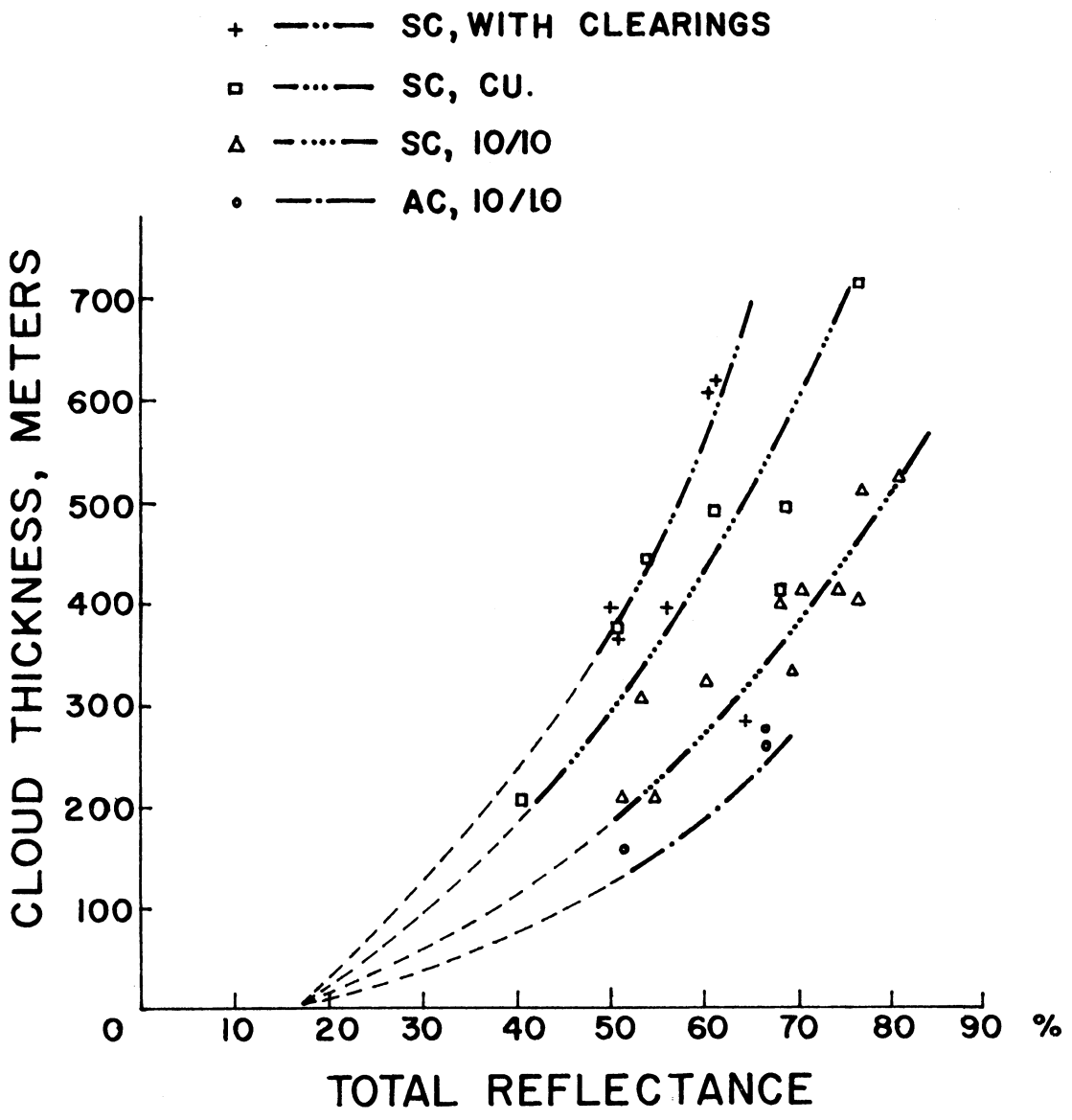

Figure 103. Dependence of cloud total reflectance on cloud thickness and cloud type (after Cheltser, see Ref. 30).

APPENDIX E

THE SCATTERING OF SOLAR RADIATION BY AIR MOLECULES AND AEROSOLS

1. MOLECULAR SCATTERING

Scattering by air molecules has been called Rayleigh scattering, after Lord Rayleigh who was first to successfully consider its theory.[53] More specifically Rayleigh scattering is the case of single, independent scattering by an agent satisfying the condition that the size parameter:

$$\alpha = \frac{2\pi r}{\lambda} < 0.1 \qquad (93)$$

where r = the radius of the scattering particle and λ = the wavelength of the radiation. The angular distribution of radiation scattered from an incident beam of radiance N_λ is described by a phase function $p(\cos\beta)$, where β is the scattering angle. The radiance of the scattered energy in the direction β is given by[53]:

$$dN_\lambda(\beta) = -K \frac{p(\cos\beta)}{4\pi} N_\lambda \, dm \quad \text{watts cm}^{-2} \text{ ster}^{-1} \text{ micron}^{-1} \qquad (94)$$

where: k_λ = the mass scattering coefficient

dm = the mass of a scattering element

For Rayleigh scattering in the atmosphere[55]:

$$k_\lambda = \frac{8\pi^3(n^2-1)^2}{3\lambda^4 N \cdot \rho} + \frac{6+3\delta}{7-3\delta} \qquad (95)$$

$$p(\cos\beta) = \frac{3}{4}(1 + \cos^2\beta) \qquad (96)$$

where n = the index of refraction of air

N = the molecular number density

ρ = the air density

δ = is the depolarization factor of air

The total loss of radiance is given by integrating $dN_\lambda(\beta)$ over the 4π solid angle, i.e.,

$$dN_\lambda = \int_{4\pi} dN_\lambda(\beta)d\Omega$$
$$= - k_\lambda N_\lambda dm \qquad (97)$$

since

$$\int_{4\pi} \frac{3}{16\pi}(1 + \cos^2\beta)d\Omega = 1 \qquad (98)$$

This theory provides a qualitative description of the brightness of the sky. Since the scattering coefficient is inversely proportional to the fourth power of the wavelength, the sky is blue. The angular distribution of scattered light is symmetric and for $\beta = 90°$, the scattered light amounts to one half of that scattered forward or backward. The brightness of the sky is determined by the angular distribution and the increase in scattering air mass near the horizon as compared to the vertical. However, for an accurate description of sky brightness, multiple scattering, and aerosol scattering must be considered.

A quantitative explanation of some of the observed features of the sky brightness was made possible by the development of the exact solution of the equation of radiative transfer, in a medium scattering according to Rayleigh's law, by Chandresekhar.[54] The extensive series of computations by Chandresekhar and Elbert,[56] Sekera and co-workers,[57,58] and Coulson[59,60] explained the main features of the radiation transmitted and reflected by a nonabsorbing, homogeneous, plane parallel atmosphere of moderate optical thickness τ, with Rayleigh scattering, and diffuse (Lambert) reflection at the surface. Calculations were made for the

entire upward and downward hemispheres for

$$\tau = 0.002, 0.05, 0.10, 0.15, 0.25, 0.50, 1.0$$

$$\cos\theta_o = 0.10, 0.20, 0.40, 0.60, 0.80, 0.92, 1.0$$

$$A = 0.00, 0.25, 1.00$$

where τ = optical thickness = $\int_{z_o}^{\infty} k_\lambda(z)\cdot\rho(z)dz$ (99)

k_λ = mass scattering coefficient

$\rho(z)$ = atmospheric density

θ_o = sun's zenith angle

A = total reflectance (albedo) of surface

z = altitude

These calculations clearly show the horizon brightening in the outgoing radiation (see Figure 104) and the dark part of the sky at about 90° from the sun. An integration of the upward flux over the entire hemisphere for incident radiation having the spectral distribution of the sun's radiation, for radiation wavelengths $0.32 < \lambda < 0.8$ micron, corrected by estimates of scattered radiation for $\lambda < 0.32$ micron and $\lambda > 0.8$ micron, yields a value of 7.6% for the earth's planetary albedo due to scattering by the clear atmosphere, decreased to 6.9% when corrected for ozone absorption.

Further studies of this same molecular scattering problem include those of Sekera[61] and Fraser[62] with Fresnel (specular) reflection at the surface and the work of Coulson, et al.,[63] using experimentally determined reflectance characteristics of red clay soil and white quartz sand for surface reflectance. Fraser's results include curves of surface total reflectance (albedo) vs. optical thickness (Figure

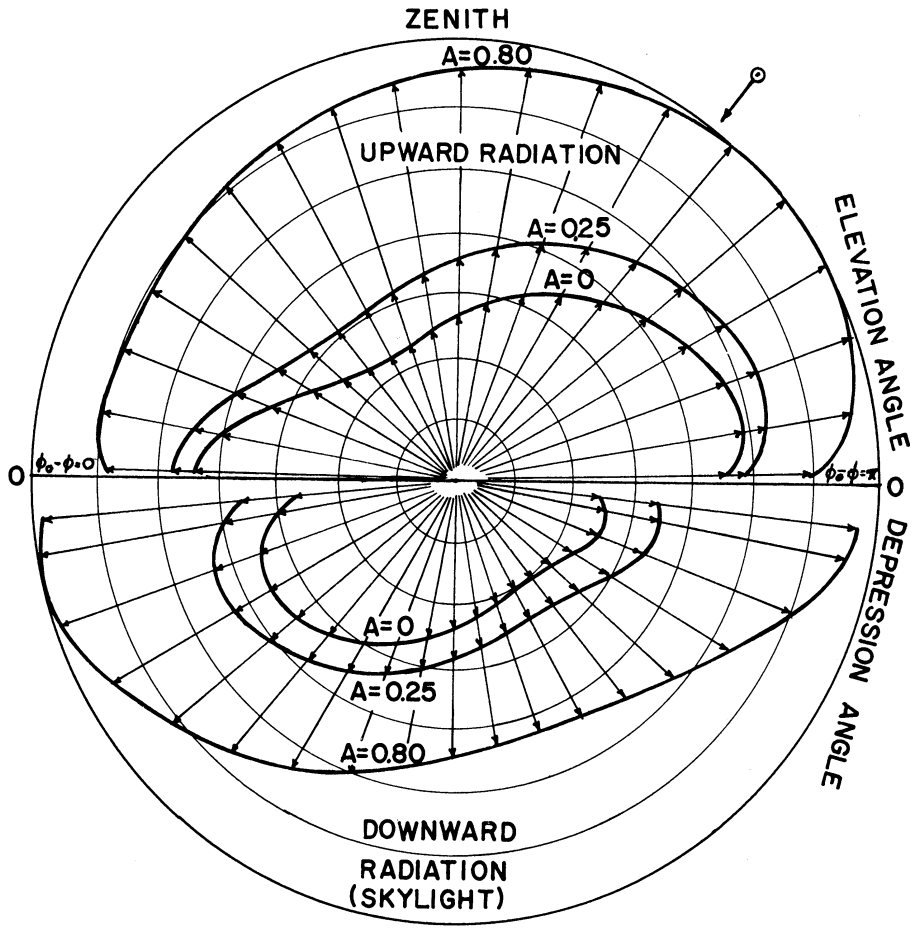

Figure 104. Distribution of intensity of light emerging from the top of the atmosphere and of the skylight in the principal plane, sun elevation 53°, optical thickness τ = 1.0, surface albedo A = 0,0.25 and 0.80 (after Coulson[59]).

105a) and the ratio of upward flux (Fresnel case) to upward flux (Lambert case) vs. optical thickness (Figure 105b). The figures show that, for solar zenith angles < 65°, the surface albedo is < 0.1, and the ratio is essentially unity. For larger zenith angles and for optical thickness < 0.5, the surface albedo increases and the ratio decreases. From Table 25 (after Coulson[60]), we see that normal optical thickness of the earth's molecular atmosphere < 0.5 corresponds to wavelengths > 0.644 micron. Thus the decrease of the ratio noted above applies only for wavelengths > 0.644 micron.

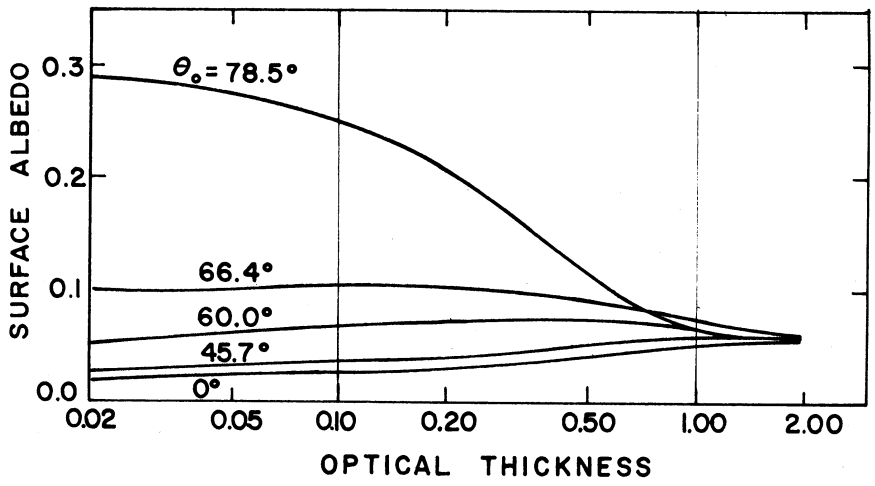

a.) SURFACE ALBEDO (FRESNEL CASE)

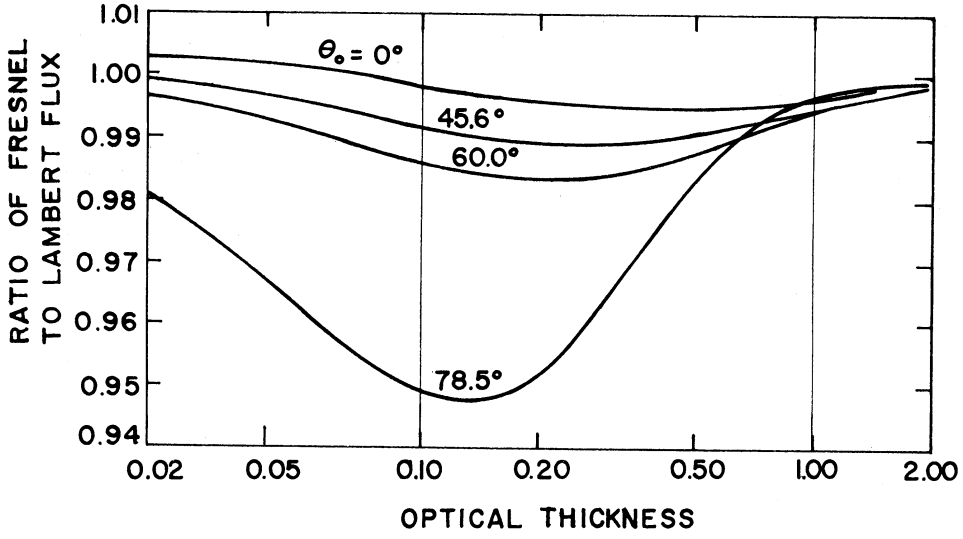

b.) FLUX RATIO.

Figure 105. Surface albedo and ratio of upward flux (Fresnel case) to upward flux (Lambert case) for nonabsorbing, homogeneous, plane parallel atmosphere with Rayleigh scattering (after Fraser[62]).

TABLE 25

WAVELENGTH DEPENDENCE OF NORMAL OPTICAL THICKNESS

OF EARTH'S MOLECULAR ATMOSPHERE ABOVE SEA LEVEL

(After Coulson[60])

τ	1.00	0.50	0.25	0.15	0.10	0.05	0.02
λ, microns	0.312	0.3715	0.4365	0.495	0.546	0.644	0.809

Coulson, et al.,[63] uses the surface reflectance data for white quartz sand and red clay soil (Figures 89a and 89c) in similar calculations. The results for red clay soil are shown in Figures 106a and 106b. The figures show relative intensities of five components and their sum, as a function of nadir angle in the principle plane. The components are:

I_s = radiation backscattered by the atmosphere, never reaching the earth's surface

I_{DD} = radiation transmitted directly through the atmosphere, reflected at the surface, and transmitted directly back through the atmosphere

I_{Dd} = radiation transmitted directly through the atmosphere, reflected at the surface, and transmitted diffusely back through the atmosphere

I_{dD} = radiation transmitted diffusely through the atmosphere, reflected at the surface, and transmitted directly back through the atmosphere

I_{dd} = radiation transmitted diffusely through the atmosphere, reflected at the surface and transmitted diffusely back through the atmosphere

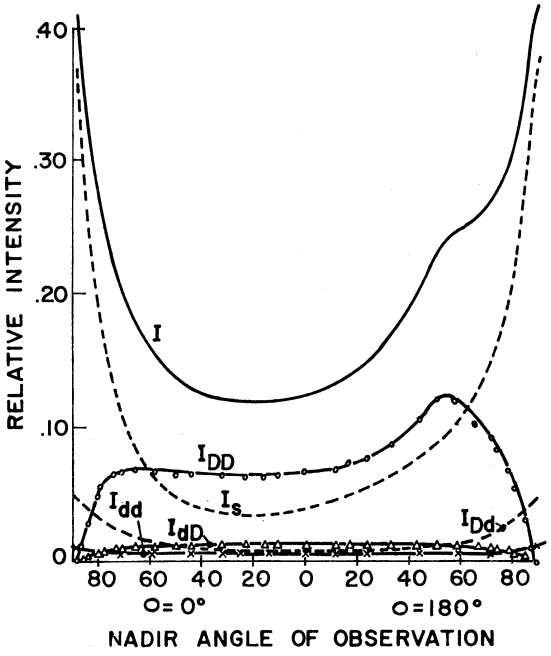

a.) λ =0.492 MICRONS (τ=0.15°), θ_o=53.1°.

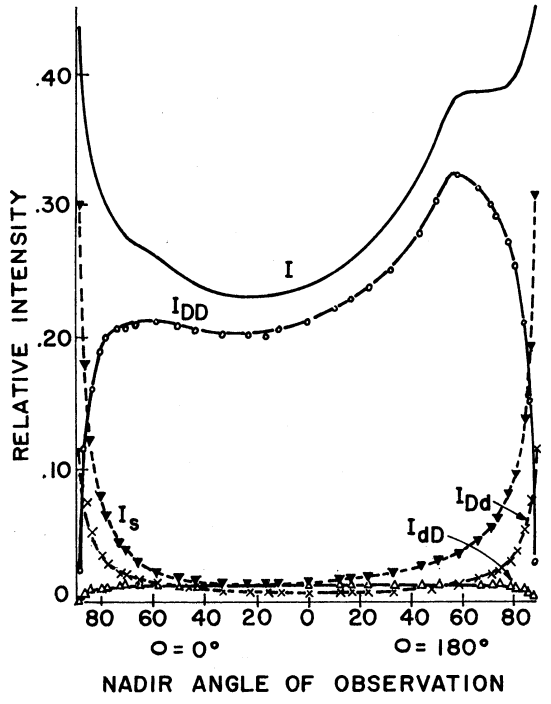

b.) λ =0.643 MICRONS (τ=0.05°), θ_o=53.1°.

Figure 106. Relative intensity of outward radiation for Rayleigh atmosphere with red clay surface (after Coulson[63]).

At 0.492 micron, the limb brightening of I_s dominates at large nadir angles, but for $\theta < 62°$, I_{DD} is $> I_s$. At 0.693 micron, the limb brightening of I_s still is evident, but I_{DD} is $> I_s$ for $\theta < 80°$. In both cases the integrated upward flux is dominated by I_{DD}.

Figures 107a, b show results for the white quartz and case. At 0.492 micron, limb brightening is still evident, at 0.643 micron the limb brightening only occurs in the forward direction ($\phi = 0$), the dominance of I_{DD} is complete for $\theta < 80°$. The maximum at $\theta = 85$ would be less pronounced in a spherical atmosphere. For $\theta_o = 0$, the nadir is brightest, with a gradual decrease of intensity with increasing nadir angle.

The program of calculations of this type is a continuing one, results for other types of surface reflectance are promised by the author. Results published so far indicate a pronounced dependence of outgoing radiation intensity on surface reflectance characteristics with a dominant role played by the I_{DD} component.

2. AEROSOL SCATTERING

The solutions for molecular scattering problems do not completely describe scattering in the real atmosphere. For example, the bright region immediately surrounding the sun, which is always observed in the clear sky, is not accounted for by molecular scattering theories and although the polarization of skylight is accounted for mainly by molecular scattering, details of polarization patterns indicate that real atmospheric scattering is governed by a law more complex than that of molecular scattering. In extremely clear atmospheres, at high altitudes, measured scattering patterns agree better with the molecular

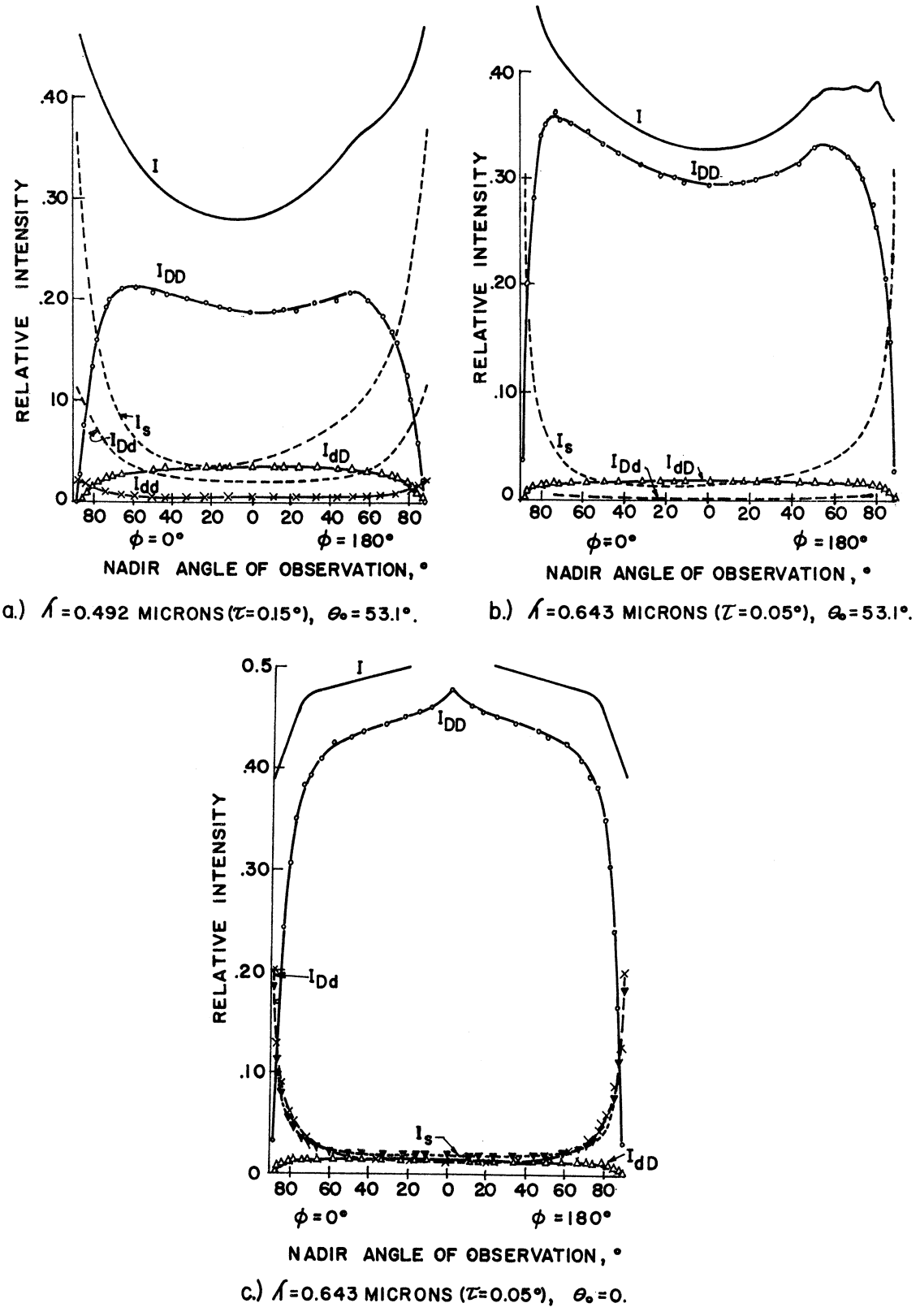

Figure 107. Relative intensity of outward radiation for Rayleigh atmosphere with white quartz sand surface (after Coulson[63]).

scattering patterns, than they do in the case of haze atmospheres near to the ground.

The deviations from molecular scattering are caused by aerosol scattering; for example, the bright "aureole" surrounding the sun is due to the very strong forward scattering of aerosol particles. Characteristics of the aerosol in the atmosphere, which must be known, are the size distribution, their distribution in space and the nature of the particles. The scattering process, i.e., angular dependence of scattered light must then be calculated.

The theory of scattering by spherical dielectric or absorbing particles has been developed by Mie.[64] The nature of the scattering process depends on the ratio of particle radius, r to radiation wavelength i.e., for $\alpha = \frac{2\pi r}{\lambda} < 0.1$, we have Rayleigh scattering; for $0.1 < \alpha < 40$, the Mie theory indicates sharp forward scattering. As α increases the infinite series which describe the scattering function converge more slowly, and only the advent of high speed computers has made solutions feasible. A large number of scattering functions for specific particle sizes and index of refraction now exists.[5]

The aerosol is composed of a mixture of particles. Junge[65] found, by direct measurements of the number and size of particles, that a continuous size distribution, from ions to giant nuclei up to 10 microns, exists. He described such a distribution with the formal relation:

$$dn(r) = N(r) \cdot dr = c \cdot r^{-\nu^*} \, d)\log r) \ cm^{-3}$$

or

$$dn(r) = 0.434 \cdot c \cdot r^{-(\nu^*+1)} dr \qquad (100)$$

where the constant c depends on the number of particles per cc, and values of ν^* are usually in the range $2.5 < \nu^* < 4$. Symbols in this equation are:

$n(r)$ = number of particles with size in range r to r + dr

$N(r) = \frac{dr(r)}{dr}$, cm^{-4}

ν^* = a constant.

Also, Volz[66] has shown by measurements of sky radiation, that the index of refraction for atmospheric aerosol was 1.5 instead of 1.33, the index of refraction of water, which had been used previously in the early computations.

The angular distribution of scattering of aerosol particles of a given size distribution must be found by integration over particle size. Rayleigh scattering is then added to the result. Many such scattering patterns have been computed (see Bullrich[67]). Strong forward scattering is due to many large particles, whereas small particles cause increased scattering at right angles.

For an explanation of sky brightness, an integration over wavelength must also be made. In addition multiple scattering and reflection from the earth's surface must be included in the calculations. Bullrich[67] considered single scattering with the change of scattering pattern with wavelength. Fiegelson, et al.,[68,69] considered multiple scattering, but at fixed wavelength only. The work of Bullrich is summarized in an extensive three volume set of tables published by the Air Force Cambridge Research Laboratories.[70] Results of Fiegelson's work are illustrated by Figures 108a and b. Figure 108a shows the brightness around the sun and the dark zone stretching from the anti-solar sky to the part of the sky below the sun. Figure 108b shows a

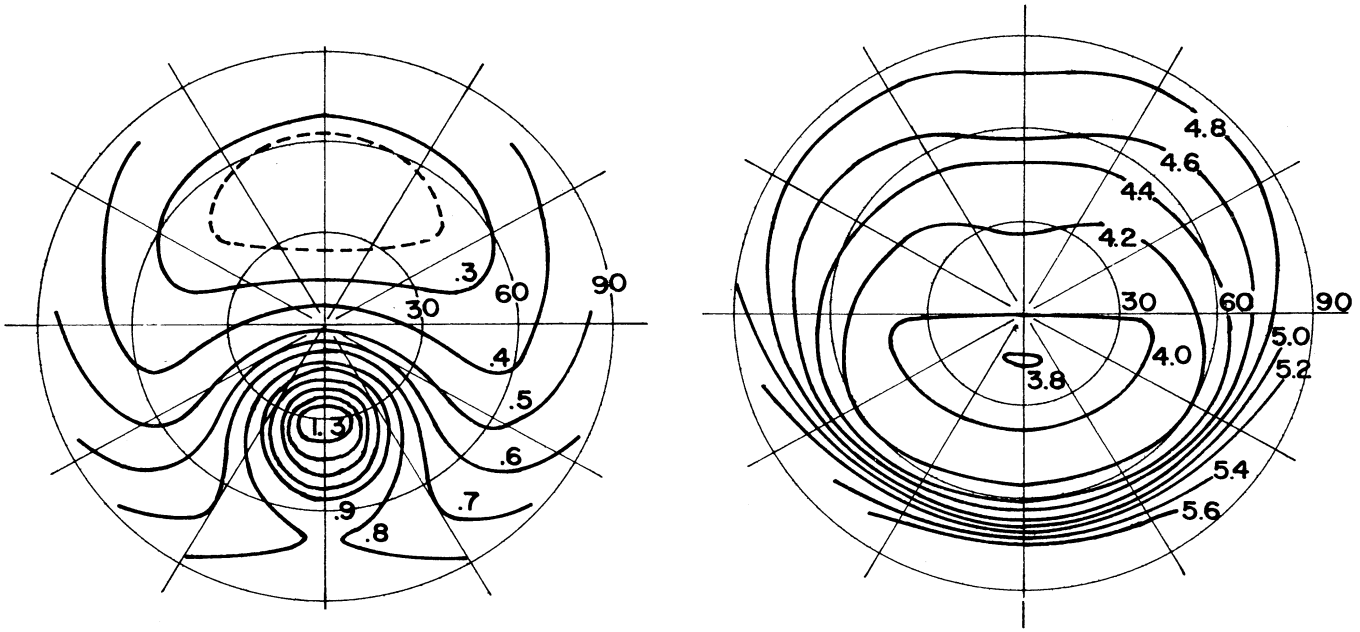

a.) RADIANCE OF THE SKY.

b.) RADIANCE OF THE EARTH PLUS ATMOSPHERE AS SEEN FROM OUTSIDE THE ATMOSPHERE.

Figure 108. Sky and earth radiance, for an atmosphere with optical depth 0.4, surface albedo 0.2 (Lambert), and aerosol scattering with five times as much forward as backscattering (after Feigelson, et al.[59]).

bright horizon in the forward direction, with a dark area in the region where a specular reflection could occur.

3. SUMMARY

The problem of scattering of solar radiation in the real atmosphere is not yet solved in all of its aspects. A complete solution must consider molecular and aerosol multiple scattering processes, aerosol particle size distribution as a function of altitude, selective absorption by air molecules, and the nature of reflectance at the earth's surface for all wavelengths of the incident solar radiation. Some solutions for problems considering a few of the above parameters have been made as described above.

APPENDIX F

F. ESTIMATES OF EARTH'S ALBEDO

Fritz[75] has attempted to evaluate the mean albedo of the entire earth, as well to establish how it is derived from various reflecting and scattering sources. The incoming solar radiation is divided up into three spectral ranges; ultraviolet ($0.2 < \lambda < 0.4$ micron), visible ($0.4 < \lambda < 0.75$ micron), infrared ($0.75 < \lambda < 4.0$ microns), containing 9%, 45%, and 46% of the incoming energy, respectively. The reflectance of the earth's surface, the atmosphere and clouds, in each of these three spectral regions is then calculated, so that, finally, values for a table such as Table 26a are obtained. The subscripts e, a, and c stand for earth surface, atmosphere, and clouds, respectively, and u, v, and i stand for ultraviolet, visible and infrared, respectively. The results were obtained in five steps, as follows:

1. Estimate 2% of solar radiation absorbed by ozone, in the ultraviolet. Therefore solar radiation reaching below the ozone layer arrives in the ratio 7:45:46 for the three spectral regions.
2. Use Abbot and Fowle's estimate of 2.3% of total radiation reflected back into space by earth surface features, i.e., $A_e = 2.3$. Divide A_e in the ratio 7:45:46, i.e., $A_{eu} = 0.1$, $A_{ev} = 1.1$, $A_{ei} = 1.1$.

3. Assume 14% of incoming solar radiation scattered back into space by cloud free atmosphere, and 5% by atmosphere above clouds, thus

$$A_a = 14(1-c) + 5 \cdot c$$

where c is the % cloud cover of the earth. Assuming c = 0.54, we have A_a = 9.1%. Divide this up in the ratio 2:4:1. Thus A_{au} = 2.6, A_{av} = 5.2, and A_{ai} = 1.3.

4. Assume Danjon's value of 39% for photometric albedo. Then $A_V = 0.45 \cdot 39 = 17.6$ and

$$A_{cv} = A_V - A_{ev} - A_{av} = 11.3$$

On the basis of cloud spectral reflectance

$$A_{cI} = 0.9\ A_{cv} = 10.2$$

$$A_{cu} = 7/45\ A_{cv} = 1.8$$

5. Thus we obtain the data of Table 26b. The earth's albedo is 35%, with an ultraviolet reflectance of 50%, visible reflectance of 39% (Danjon's photometric albedo) and infrared reflectance of 27%.

It is interesting to summarize this work in symbolic form, see Table 26c. Each of the nine basic quantities is given in terms of A_e, A_a or A_{cv}. A_e is estimated to by 2.3%, and A_a and A_{cv} are given by:

$$A_a = 14\ (1-c) + 5c = 14 - 9c$$

$$A_{cv} = A_V - 45/98\ A_e - 4/7\ A_a$$

TABLE 26

REFLECTION OF SOLAR RADIATION, %
(After Fritz[75])

		Ultraviolet	Visible	Infrared	Total
	Earth's Surface	A_{eu}	A_{ev}	A_{ei}	A_e
	Atmosphere	A_{au}	A_{av}	A_{ai}	A_a
(a)	Clouds	A_{cu}	A_{cv}	A_{ci}	A_c
	Total	A_u	A_v	A_i	A
	Solar Energy	9	45	46	100
	Earth's Surface	0.1	1.1	1.1	2.3
	Atmosphere	2.6	5.2	1.3	9.1
	Clouds	1.8	11.3	10.2	23.3
(b)	Total	4.5	17.6	12.6	34.7
	Solar Energy	9	45	46	100
	Reflectance	50	39	27	35
	Earth's Surface	$7/98A_e$	$45/98A_e$	$46/98A_e$	A_e
(c)	Atmosphere	$2/7A_a$	$4/7A_a$	$1/7A_a$	A_a
	Clouds	$7/45A_{cv}$	A_{cv}	$0.9A_{cv}$	$2.056A_{cv}$

where c is % cloud cover (in decimal form) and $A_v = 0.45\ D$; where D is Danjon's photometric albedo. Thus $A = A_e + A_a + 2.056\ A_{cv}$ substituting from above

$$A = .056A_e - 0.175A_a + 0.925D$$

or

$$A = .056A_e + 0.925D + 1.575c - 2.45 \qquad (101)$$

In the final analysis, Fritz's estimate of mean earth's albedo can be written as a function of A_e, D, and c. With $A_e = 2.3$, D = 39 (Danjon) and c = 0.54, we obtain

$$A = 0.129 + 36.073 + 0.851 - 2.45 = 34.6$$

His estimate thus is determined primarily by the Danjon value, with minor corrections due to the other factors. With Danjon's new estimate of D = 40%, we have for Fritz's A = 35.5%.

Houghton's[76] estimate of earth's albedo was obtained as a part of a calculation of the annual heat balance of the northern hemisphere. The computations were based on the following data:

1. Annual means, for North America, of total solar and sky radiation received at the surface (pyrheliometer data).
2. Smithsonian Astrophysical Observatory,[77] atmospheric transmission curves for clear sky scattering and absorption.
3. Cloud cover data by C.E.P. Brooks,[78] and C. F. Brooks,[79] Haurwitz and Austin,[80] and the Preliminary Climatic Atlas of the World.[81]

4. Surface reflectance data from Buttner,[82] Richardson,[83] Bartels,[84] Angstrom,[85] and many others.

5. Cloud absorption data by Fritz,[86] Neibeuger,[52] Hewson,[47] and Haurwitz.[87]

For each 10° latitude circle, albedo was calculated by a procedure which can be expressed by the following equation:

$$A = \frac{H_S - H'_A - H''_S}{H_S}$$

$$A = \frac{H_S - H'_A - H'_S \cdot R(c)(1-\rho_G)}{H_S} \qquad (102)$$

where

H_S = incident solar radiation outside of the atmosphere.

H'_A = radiation absorbed in the atmosphere with normal cloud cover.

H''_S = solar radiation at the surface with normal cloud cover.

H'_S = solar radiation at the surface with clear sky.

$R(c)$ = H''_S/H'_S, a function of cloud cover, c (derived from data for North America, applied world wide).

c = weighted cloud cover.

ρ_G = surface albedo.

Houghton's data is summarized in Tables 27a and 27b. His average albedo for the northern hemisphere shows remarkable agreement with Fritz's 35.5%.

London's[71] estimate of earth's albedo was obtained as a part of a study of atmospheric heat balance based on a rather detailed "realistic physical model" of the atmosphere. Vertical and latitudinal distribu-

TABLE 27

DATA USED TO OBTAIN ALBEDO OF NORTHERN HEMISPHERE

(After Houghton[76])

(a) Computed values (ly/day) of disposition of solar radiation incident on a clear atmosphere

		Latitude (deg. N)									
		0	10	20	30	40	50	60	70	80	90
Spring equinox	Outside atmosphere	892	879	839	771	682	573	446	305		
	Direct beam at surface	509	508	505	485	425	354	259	159		
	Diffuse at surface	93	90	83	72	66	61	53	43		
	Absorbed by atmosphere	198	190	169	142	123	99	82	61		
Summer solstice	Outside atmosphere	791	873	934	973	992	989	978	1010	1058	1076
	Direct beam at surface	434	495	545	588	608	609	600	593	609	609
	Diffuse at surface	89	93	95	95	98	97	98	110	124	128
	Absorbed by atmosphere	182	195	201	195	192	189	184	198	203	211
Fall equinox	Outside atmosphere	883	871	830	764	675	568	441	302	174	60
	Direct beam at surface	504	497	477	445	387	318	232	137	60	4
	Diffuse at surface	92	92	87	78	72	65	55	44	30	10
	Absorbed by atmosphere	196	192	182	162	143	122	100	78	60	44
Winter solstice	Outside atmosphere	842	731	603	461	318	175	49			
	Direct beam at surface	462	398	331	256	164	78	12			
	Diffuse at surface	95	83	69	52	42	27	9			
	Absorbed by atmosphere	194	170	135	100	71	45	19			
Annual mean	Outside atmosphere	850	838	801	743	668	576	469	406	369	353
	Direct beam at surface	477	475	465	444	396	340	270	225	197	176
	Diffuse at surface	93	89	83	74	70	62	55	51	48	48
	Absorbed by atmosphere	193	187	172	150	132	114	95	82	81	81

(b) Disposition of solar radiation (ly/day) with normal cloud cover.

Lat. (deg N)	Solar rad. at surface with clear sky	Weighted cloud cover	Solar rad. at surface with normal cloud	Surface albedo	Solar rad. absorbed at surface	Absorbed in normally cloudy atmos.	Total absorption	Planetary albedo
0	570	0.54	410	.071	381	192	573	.326
10	564	0.50	429	.080	395	183	578	.310
20	548	0.44	452	.098	408	166	574	.283
30	518	0.42	438	.110	390	142	532	.284
40	466	0.49	359	.102	322	122	444	.335
50	402	0.57	277	.092	252	100	352	.389
60	325	0.63	204	.091	185	76	261	.443
70	276	0.67	161	.168	134	58	192	.527
80	245	0.65	148	.36	95	52	147	.602
90	224	0.59	150	.56	66	51	117	.669
Mean 0–90	475	0.52	361	.100	325	136	461	.34

tions of temperature, pressure and relative humidity were prepared for each of the four seasons, as were latitudinal distributions of cloud cover of each of six types and of total cloud cover. The albedo calculations included consideration of ground reflectance; cloud scattering and absorption; the depletion of radiation due to scattering by air molecules, water vapor and dust particles; the absorption of the direct solar beam by ozone, water vapor, and dust; and the absorption of scattered radiation by water vapor and dust. Dust scattering and ground reflection data were based on Houghton's work all other calculations were new estimates by London and co-workers. The results, the distribution with latitude and season of planetary albedo in the northern hemisphere, is shown in Figure 109. The figure shows a minimum albedo of 27% in the subtropics in winter shifting poleward about 10° and increasing to 29% in summer. The higher albedos at high latitudes are due to increasing cloudiness and higher reflectivities in polar regions. The total planetary albedo averaged overall latitudes and seasons was about 35%, only a small variation with season was shown (35.6% in winter and 36.3% in summer). The contributions to the average total albedo were earth 4%, atmosphere 7%, and clouds 24%. With a mean cloudiness over the northern hemisphere of 51%, the mean albedo of clouds was 47%, and albedo of clear sky conditions (ground reflectance plus atmospheric scattering) was as shown in Table 28.

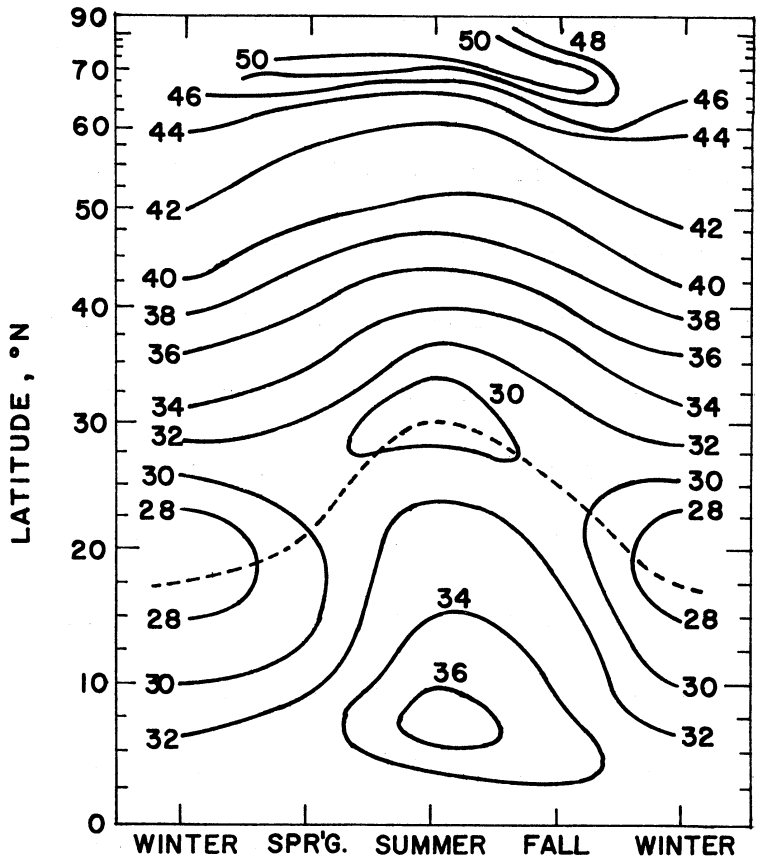

Figure 109. The seasonal distribution of the planetary albedo (%) (after London[71]).

TABLE 28

SEASONAL DISTRIBUTION OF PLANETARY ALBEDO COMPONENTS DUE TO ATMOSPHERIC SCATTERING AND GROUND REFLECTANCE (After London[71])

	Winter	Spring	Summer	Fall
Ground	9.0	7.4	5.0	6.0
Atm. Scattering	8.3	7.6	8.5	7.4
Total	17.3	15.0	13.5	13.4

Angstrom's[13] determinations of albedo are based on measurements by Drummond of the natural illumination of the sun and sky in South Africa.

After deriving a formula, from these data, to express the global illumination at sea level as a function of air mass and turbidity, he proceeded as follows:

1. He derived a photometric loss factor E, for the effect of the atmosphere on the incident solar flux, and then obtained average values $\bar{E}$, which were equal to 0.32 at the equator and 30° latitude, with a slight increase to 0.34 at higher latitudes.
2. A correction, for absorption, of 0.07 was applied, and an estimated factor of 0.035 was added for reflected energy reaching outer space. Thus the albedo in the photometric band, for clear sky, of 0.32-0.07+0.32 = 0.285 was found.
3. Another correction, adjusting for the difference in land and ocean reflectance, brought the photometric albedo to 0.295. This clear sky albedo is assumed to apply for the whole earth at 0.555 micron.
4. Using Danjon's photometric albedo of 0.39 for the earth and taking c = 0.52 in the relation

$$0.39 = (1-c)0.295 + c \cdot A_{cv}$$

gave $A_{cv} = 0.48$. Applying Hewson's spectral dependence of cloud albedo, gave $A_c = 0.46$ for the total spectral range.

5. From Danjon's photometric albedo measurements at three wavelengths, i.e.,

$$\lambda = 0.467 \qquad 0.543 \qquad 0.606$$

$$A_{v\lambda} = 0.48 \qquad 0.39 \qquad 0.315$$

the relation $A_\lambda = 1.03 - 1.19\lambda$ was found, and the photometric albedo for the range 0 to 0.7 micron was found to be

$$A_{0-0.7} = \frac{\int_{0.3}^{0.7} A_\lambda H_{S\lambda} d\lambda}{\int_{0.3}^{0.7} H_{S\lambda} d\lambda} = 0.41$$

The value of photometric albedo for clear sky $A'_{0-0.7}$ was found from

$$(1-c)A'_{0-0.7} + cA_c = 0.41$$

with $c = 0.52$ and $A_c = 0.46$. Thus:

$$A'_{0-0.7} = 0.355 .$$

6. An estimate of 15% more scattered energy for the entire spectral range was made, and the total clear sky albedo was found to be

$$A = \frac{0.355 \cdot 0.940 \cdot 1.15}{1.98}$$

where 0.940 is the incident solar energy in the range 0-0.7 micron at 1.98 is the solar constant.

7. The planetary albedo under average conditions of cloudiness was then

$$A = (1-0.52)0.195 + 0.52 \cdot 0.46 = 0.333$$

The second calculation made by Angstrom was a modification of Houghton's work. If we take 0.195 (instead of 0.135) as the albedo of the cloud free atmosphere, and use Houghton's cloud albedo of 0.55, we obtain a planetary albedo of 0.38. This implies that Danjon's photometric albedo should be 0.43 instead of 0.39. This second result is favored by Angstrom.

APPENDIX G

DESCRIPTION OF COORDINATE SYSTEMS USED

Coordinates	Reference	Figure	Application
Zenith angles: Θ_o, Θ Azimuth angles: ϕ_o, ϕ $\psi = \phi - \phi_o$	Zenith direction, QZ North direction, QN	1	Integration over (Θ, ϕ) to obtain directional reflectance $r_\lambda(\Theta_o, \phi_o)$ from bidirectional reflectance $\rho_\lambda(\Theta_o, \phi_o, \Theta, \phi)$.
Zenith angle: Θ_o Azimuth angle: ϕ'_o	Direction to sun, OS Line ON'	4a	Integration over sunlit hemisphere to obtain earth's albedo.
Colatitude: η Longitude: ζ	Line OP $\perp$ plane EOS Direction to observor: OE	5b	Bond's planetary albedo integration over that portion of sunlit hemisphere seen by observor.
Colatitude: η' Longitude: ζ'	North pole: N Greenwich meridian	10b	To specify geographical position on earth's surface.

REFERENCES

1. Bandeen, W. R., Halev, M., and Strange, I., "A Radiation Climatology in the Visible and Infrared From the TIROS Meteorological Satellites," NASA TN D-2534, National Aeronautics and Space Admin., Washington, D.C., June 1965.

2. House, F. B., "The Radiation Balance of the Earth From a Satellite," Ph.D. Dissertation, Univ. of Wisconsin, Dept. of Meteorology, 1965.

3. Edwards, D. K., "Measurement of Thermal Radiation Characteristics," Proceedings of the I.E.S. 1963 Annual Technical Meeting, pp. 417-424

4. Nicodemus, F. E., "The Directional Reflectance and Emissivity of an Opaque Surface," Applied Optics, 4, 767-773, No. 7 (July 1965).

5. vande Hulst, N. C., "Light Scattering by Small Particles," p. 12, J. Wiley and Sons, Inc., New York, 1957.

6. Thekaekara, M. P., "Survey of the Literature on the Solar Constant and the Spectral Distribution of Solar Radiant Flux," NASA Report SP-74, Washington, D.C., 1965.

7. Encylopedia of Science and Technology, p. 222, McGraw-Hill, New York, 1960.

8. Russell, H. N., "On the Albedo of the Planets and Their Satellites," Ap. J., 43, 173-196, No. 3 (April 1916).

9. Danjon, A., "Albedo, Color and Polarization of the Earth," Chapter 15, The Earth as a Planet-The Solar System, II, Univ. of Chicago Press, 1953.

10. Dubois, J., "The Variation of Brightness of the Moon's Earthshine in the Course of the Last Solar Cycle," L'Astronomie, pp. 242-246 (June 1965).

11. Bakos, G. A., "Measures of the Earthshine," Smithsonian Institution, Astrophysical Observatory, Special Report 162, August 1964.

12. Fritz, S., "The Albedo of the Planet Earth and of Clouds," J. Met., 6, 277-282 (August 1949).

13. Angstrom, A., "Atmospheric Turbidity, Global Illumination and Planetary Albedo of the Earth," Tellus, XIV, 435-450, No. 4 (1962).

14. Suomi, V. E., "The Thermal Radiation Balance Experiment on Board Explorer VII, Chapter 11, pp. 247-278, Juno II Summary Project Report Vol. III, Explorer VII, NASA, Marshall Space Flight Center, Huntsville, Alabama, 1960.

15. Hanel, R. A., "Radiometric Measurements From Satellites," Aerospace Eng., 34-39 (July 1962).

16. Wildey, R. L., "Photometry of the Earth From Mariner 2," J. Geo. Res., 69, 4661-4672, No. 21 (November 1964).

17. Hanel, R. W., "A Low-Resolution Unchopped Radiometer for Satellites," Am. Rocket Soc. J., 31, 246-250, No. 2 (February 1961).

18. Bartko, F., Kunde, V., Catoe, C., and Halev, M., "The TIROS Low Resolution Radiometer," NASA TN-D-614, GSFC, Greenbelt, Maryland, September 1964.

19. Bignell, K. J., "Heat-Balance Measurements From an Earth Satellite--An Analysis of Some Possibilities," Quart. J., Roy. Met. Soc., 87, 231-244 (April 1961).

20. Malkevich, M. S., Pokras, V. M., and Yurkova, L. I., "Measurements of Radiation Balance on the Satellite Explorer VII," translated by R. E. Daisley from Iskusstvennye Sputniki Zemli, No. 14, p. 105 (1962), Planet. Sp. Sci., 11, 839-865.

21. Widger, W. K. and Wood, C. P., "An Explanation of the Limitations to the Coverage Provided by TIROS," Weatherwise, 14, 230-237, No. 6, (December 1961).

22. Staff Members, "TIROS IV Radiation Data Catalog and User's Manual," Aeronomy and Meteorology Div., GSFC, NASA, December 1963.

23. London, J., "A Study of the Atmospheric Heat Balance," Final Report, Contract AF 19(122)-165, Research Division College of Engineering, New York University.

24. Astheimer, R. W., DeWaard, R., and Jackson, E. A., "Infrared Radiometric Instruments on TIROS II," J. Opt. Soc. Am., 51, 1386-1393 (1961).

25. Hummer, R. F. and Malinowski, F. R., "NIMBUS Five-Channel Scanning Radiometer," paper presented at Ninth National Infrared Symposium (IRIS), 6-8 May 1963, Dallas, Texas.

26. Data Book for NIMBUS Medium Resolution Infrared Radiometer (F-4)," Santa Barbara Research Center, Goleta, California, November 1964.

27. Bartman, F. L., "The Calibration of and Interpretation of Data From the 0.55-0.85 Micron and 0.2-4.0 Micron Channels of the F-1 and F-4 MRIR Radiometers," Univ. of Mich. Dept. of Aerospace Engineering Report 05863-9-T, Ann Arbor, Michigan, February 1966.

28. Holter, M. R., Nudelman, S., Suits, G. H., Wolff, W. L., and Zissis, G. J., "Fundamentals of Infrared Technology," p. 54, The McMillen Co., 1962.

29. Bandeen, W. R. and Strange, I., "A Two Year Study of the Planetary Heat Balance from TIROS 7 Radiation Data," paper presented at the 47th Annual Meeting of the American Geophysical Union, April 19-22, 1966, Washington, D.C.

30. Kondratyev, K. Ya., "Actinometry," NASA TT F-9712, Washington, D.C., November 1965 (translation of "Aktinometriya," Gidrometeorologicheskoye Izdatel'stvo, Leningrad, 1965).

31. Orr, D. G., Dwamik, S. E., and Young, L. M., "Reflectance Curves of Soils, Rocks, Vegetation and Pavement," Research Report No. 7746-RR, U.S. Army Engineer Research and Development Laboratories, Fort Belvoir, Virginia, 22 April 1963, AD 410588.

32. Ashburn, E. V. and Weldon, R. G., "Spectral Diffuse Reflectance of Desert Surfaces," JOSA, 46, 583-586, No. 8 (August 1956).

33. Gerharz, R. and Fischer, W. A., "Reflectance Measurements in the 0.6 to 2.5 Micron Part of the Spectrum," Technical Letter NASA-8, U.S. Dept. of Interior, Geological Survey (work performed under NASA Contract No. R-146), N66-21664.

34. Hovis, W. A., Jr. and Callahan, W. R., "Infrared Reflectance Spectra of Igneous Rocks, Tuffs and Red Sandstone From 0.5 to 22 Microns," Goddard Space Flight Center, Greenbelt, Md., N66-23428.

35. Kropotkin, M. A. and Kozyrev, B. P., "Study of the Reflection Spectra of Natural and Synthetic Materials in the 0.7-100 Micron Range," Optics and Spectroscopy, 17, 136 (1964).

36. Coulson, K. L., "Effects of Reflection Properties of Natural Surfaces in Aerial Reconnaissance," Applied Optics, 5, 905-916, No. 6 (June 1966).

37. Kondratyev, K. Y., Mironova, Z. F., and Otto, A. N., "Spectral Albedo of Natural Surfaces," Pure and Applied Geophysics, 59, 207-216, No. 3 (1964).

38. Gates, D. M., et al., "Spectral Properties of Planets," Applied Optics, 4, 11-20, No. 1 (January 1965).

39. Coulson, K. L., Bouricius, G. M., and Gray, E. L., "Optical Reflection Properties of Natural Surfaces," J. Geo. Res., 70, 4601-4611, No. 18 (September 15, 1965).

40. Duntley, S. G., et al., "Visibility," Applied Optics, 3, 549-598, No. 5 (May 1964).

41. Boileau, A. R. and Gordon, J. I., "Atmospheric Properties and Reflectances of Ocean Water and Other Surfaces for a Low Sun," Applied Optics, 5, 803-813, No. 5 (May 1966).

42. Gordon, J. I. and Church, P. V., "Overcast Sky Luminances and Directional Luminous Reflectances of Objects and Backgrounds Under Overcast Skies," Applied Optics, 5, 919-923, No. 6 (June 1966).

43. Knowles Middleton, W. E. and Mungall, A. G., "The Luminous Directional Reflectance of Snow," JOSA, 42, 572-579, No. 8 (August 1952).

44. Kondratyev, K. Y. and Manolova, M. P., "Angular Distribution of Radiation Intensity Reflected by Natural Underlying Surfaces," Leningrad University Bulletin, No. 10, pp. 52-58 (1957).

45. Neiburger, M., "The Reflection of the Diffuse Radiation by the Sea Surface," Trans. Am. Geoph. Union, 29, 647-652, No. 5 (October 1948).

46. Spano, A. F., "Results of an Airborne Albedo Program in Antarctica," 1963, Monthly Weather Review, 93, 697-703, No. 11 (Nov. 1965).

47. Hewson, E. W., "The Reflection, Absorption, and Transmission of Solar Radiation by Fog and Cloud," Quart. J. Roy. Meteor. Soc., 69, 47-62, No. 298 (January 1943).

48. Novoseltsev, Y. P., "Spectral Reflectivity of Clouds," NASA TT F-328, Translation of "Spektrolnaya Otrazhatelnaya Oblakov," Trudy Glavnoy Geofizicheskoy Observatoiri Imeni A. I. Voyykova, No. 152, pp. 186-191 (1964).

49. Diermendjian, D., "Scattering and Polarization Properties of Water Clouds and Haze in the Visible and Infrared," Applied Optics, 3, 187-196, No. 2 (February 1964).

50. Aldrich, L. B., "The Reflecting Power of Clouds," Smithsonian Misc. Coll., 69, No. 10 (1919).

51. Luckiesh, M., "Aerial Photometry," Astrophys. J., 49, 108-130 (1919).

52. Neiburger, M., "Reflection, Absorption and Transmission of Insolation By Stratus Clouds," J. Meteor., 6, 98-104 (1919).

53. Lord Rayleigh, Scientific Papers (Cambridge England, 1899), pp. 87, 104, 518.

54. Chandrasekhar, S., "Radiative Transfer," Dover Publications, New York, p. 5, 1960.

55. Elterman, L., "Atmospheric Attenuation Model, 1964, in the Ultraviolet, Visible and Infrared Regions for Altitudes to 50km," AFCRL Environmental Research Paper No. 46, Office of Aerospace Research, USAF, L. G. Hanscom Field, Mass. (1964).

56. Chandrasekhar, S. and Elbert, D., "The Illumination and Polarization of the Sunlit Sky on Rayleigh Scattering," Trans. Am. Phil. Soc., New series, 44, 643, Part 6 (1954).

57. Sekera, Z. and Ashburn, E. V., "Tables Relating to Rayleigh Scattering of Light in the Atmosphere," NAVORD Report 2061, U.S. Naval Ordnance Test Station, Inyokrn, Calif., 1953.

58. Sekera, Z. and Blanch, G., "Tables Relating to Rayleigh Scattering of Light in the Atmosphere," Sci. Report No. 3, Contract AF 19-(133)-239, Air Force Cambridge Research Center (1952).

59. Coulson, K. L., "Characteristics of the Radiation Emerging From the Top of a Rayleigh Atmosphere," Plan. and Space Sci., 1, 265-284, No. 4 (September 1959).

60. Coulson, K. L., Dave, J. V., and Sekera, Z., "Tables Related to Rayleigh Scattering of Light in a Plane Parallel Atmosphere," Univ. of Calif. Press, Berkeley, 1960.

61. Sekera, Z., "The Effect of Sea Surface Reflection on the Sky Radiation," Union Geodesique Geophys. Intem. Monogram., 10, 66 (1961).

62. Fraser, R. S., "Effect of Specular Ground Reflection on Radiation Leaving the Top of a Planetary Atmosphere," AIAA Thermophysics Specialist Conference, Monterey Calif., Sept. 13-15, 1965, Paper No. 65-664.

63. Coulson, K. L., Gray, E. L., and Bouricious, G.M.B., "Effect of Surface Reflection on Planetary Albedo," ICARUS, 5, 139-148 (1966).

64. Mie, G., Ann. Physik, 25, 377 (1908).

65. Junge, C. E., "Gesetzmassigkeiten der Grossenverteilung Atmospharischer Aerosole uber dem Kontinent," Ber. Deut. Wetterd., U.S. Zone, No. 35, p. 261 (1952).

66. Volz, F., "Optik der Trapfen," Hand Buch der Physik, Vol. VIII, Chap. 14, p. 822.

67. Bullrich, K., "Scattered Radiation in the Atmosphere and the Natural Aerosol.," Advances in Geophysics, 10, 101-261, Academic Press, New York (1964).

68. Fiegelson, E. M., Malkevich, M. S., and Kogan, S. Y., "Calculations of the Brightness of Light in the Case of Anisotropic Scattering, Part I," Transactions of the Institute of Atmospheric Physics No. 1, Academy of Sciences, USSR, Press, Moscow (1958). Translated from the Russian, Consultant's Bureau Inc., New York (1960).

69. Astroshenko, V. S., Fiegelson, E. M., Glazova, K. S., and Malkevich, M.S., "Calculation of the Brightness of Light in the Case of Anisotropic Scattering, Part II," Transactions of the Institute of Atmospheric Physics No. 3, Academy of Sciences USSR, Press, Moscow (1962). Translated from the Russian, Consultant's Bureau, New York (1963).

70. deBary, E., Brown, B., and Bullrich, K., "Tables Related to Light Scattering in a Turbid Atmosphere," Vol. I, AFCRL-65-710(I), Air Force Cambridge Research Laboratories, L. G. Hanscom Field, Bedford, Mass., Sept. 1965, Vol. II, AFCRL-65-710(II), Sept., 1965, Vol. III, AFCRL-65-710(III), Sept. 1965.

71. London, J., "A Study of Atmospheric Heat Balance," Dept. of Meteorology and Oceanography, Final Report on Contract AF 19(122)-165, AFCRL-TR-57-289, July 1957.

72. Abbot, C. G. and Fowle, F. E., Annals of the Astrophysical Observatory of the Smithsonian Institution, II (1908).

73. Simpson, G. C., "Some Studies on Terrestrial Radiation," Mem. Roy. Meteor. Soc., Vol. II, No. 16, pp. 69-95 (1928); also Vol. III, No. 21 (1928); Vol. III, No. 23 (1929).

74. Bauer, F. and Philips, H., "Der Warmeshaushalt der Luftdruck der Norbhalbkugel in Januar und Juli and zur Zeit der Aquinoktien und Solstitien," I Mitteilung. Gerl. Beitr. 2, Geophysik, 42, 160-207 (1934).

75. Fritz, S., "The Albedo of the Planet Earth and Clouds," J. Meteor., 6, 277-282 (Aug. 1949).

76. Houghton, H. G., "On the Annual Heat Balance of the Northern Hemisphere," J. Meteor., 11, 1-9, No. 1 (Feb. 1954).

77. Smithsonian Meteorological Tables, 5th Rev. Ed., Washington, D.C., 1939.

78. Brooks, C.E.P., "The Mean Cloudiness Over the Earth," Mem. Roy. Meteor., Soc. 1, No. 10, pp. 127-138 (1927).

79. Brooks, C. F., et al., "Climatic Maps of North America," Cambridge, Harvard Univ. Press. (1936).

80. Haurwitz, B., and Austin, J. M., "Climatology," New York, McGraw-Hill Book Co., 1944).

81. Preliminary Climatic Atlas of the World (Anonymous)(1943).

82. Buttner, K., 1929: Messungen der Sonnen und Himmelstrahlung im Flugzeug, Meteor. Z., 46, 525-527 (1929).

83. Richardson, L. F., "Measurement of Water in Clouds," Proc. Roy. Soc. London, A, 96, 19-31 (1919).

84. Bartels, J., "Die Strahlung und Ihre Bedeutung Fur das Luftlrule der Nordhalbkugel im Januar und Juli und zur Zeit der Aquinoktien und Solstein, Gerlands. Beitr. Geophysik, 41, 160-207 and 45, 82-132 (1934, 1935).

85. Angstrom, A., "On the Albedo of Various Surfaces of Ground," Geograf. Ann., 7, 323-342 (1925).

86. Fritz, S., "Scattering and Absorption of Solar Energy by Clouds," Cambridge, Mass. Inst. of Tech. (Sc.D. thesis), 1953.

87. Haurwitz, B., "Insolation in Relation to Cloud Type," J. Meteor., 5, 110-113 (1948).

88. Bartman, F. L., Surh, M. T., and Whybra, M. G., "Long Term Integrity of the TIROS 5-Channel Radiometer Visible Channel Characteristics," University of Michigan, Dept. of Aero. and Astro. Engr. Report No. 03615-13-T, Ann Arbor, Mich., December 1963.

89. Bartman, F. L., Chaney, L. W., Titus, P. A., and Whybra, M. G., "Infrared and Visible Radiation Measurements by Radiometer and Interferometer on High Altitude Balloon Flights at 34-Km. Altitude," Paper presented at International Symposium on Radiation Processes, Leningrad, USSR, August 5-12, 1964.

90. Bartman, F. L., Chaney, L. W., and Surh, M. T., "Reflectance of Kodak White Paper," University of Michigan, Dept. of Aero. and Astro. Engr. Report No. 05863-5-T, Ann Arbor, Mich., April 1964.

91. Malinowski, F. R., "Investigation of F-1 MRIR," SBRC report on Contract NAS 5-757, 2 November 1964, Goleta, California.

92. Landsberg, H., "Climatology," in Handbook of Meteorology, F. A. Berry, Jr., et al., New York, McGraw-Hill Book Co., 1945, pp. 927-997.